EXPERIMENTAL AND NUMERICAL STUDIES OF JET IMPINGEMENT COOLING ENHANCEMENT

by

Abdel Rahman Sameeh Hasan Salem

A Dissertation Submitted in

Partial Fulfillment of the

Requirements for the Degree of

Doctor of Philosophy

in Engineering

at

The University of Wisconsin-Milwaukee

May 2023

ABSTRACT

EXPERIMENTAL AND NUMERICAL STUDIES OF JET IMPINGEMENT COOLING ENHANCEMENT

by

Abdel Rahman Sameeh Hasan Salem

The University of Wisconsin-Milwaukee, 2023
Under the Supervision of Professor Ryoichi S. Amano

Jet impingement is a cooling method used to efficiently cool gas turbine blades and other engine components. In jet impingement cooling, fluid jets travel perpendicular to the hot surface through nozzles and impinge on the surface with high velocity to dissipate the thermal load. Internal cooling of gas turbine blades is commonly performed with impingement cooling and serpentine channels. Besides gas turbine blades, the other turbine components such as turbine guide vanes, rotor disks, and combustor walls can be cooled using high-momentum air jets. Additionally, jet impingement is not only limited to gas turbine cooling, since it is also applicable for electronic-chip cooling, hot metal sheets cooling, paper and fabric drying, as well as many other applications.

As providing compressed cooling air can be quite expensive, this study is focused on optimizing the cooling air characteristics to maximize heat transfer and enhance cooling efficiency. The study incorporates three scopes; the first highlights the main geometrical and flow aspects that affect the cooling performance and can potentially influence the design of the cooling circuits. These geometrical and flow factors include Reynolds number (Re), jet-to-target spacing -also known as stand-off distance (Z/D)-, jet array configuration (in-line and staggered), and jet-to-jet

spacing (S/D) with an intermediate crossflow condition (double exit case), where the spent air has a bidirectional exit. A range of Reynolds number (Re) of 2,500 – 12,500 was investigated for air jets issued from a 5×5 square nozzle array and correlated with the Nusselt number (Nu) for laminar and turbulent flow regimes. It was found that the increase in Reynolds number (Re) resulted in a higher stagnation Nusselt number (Nu), where it peaked underneath the middle row of jets for the intermediate crossflow scheme (bi-directional exit). A detailed comparison of different stand-off distances (Z/D) of 3, 5, and 7.5 for each flow case showed a reduction in both line-averaged and area-averaged Nusselt number (Nu) as the stand-off distance (Z/D) increased. The increased stand-off distance results in a higher entrainment of the surrounding air that causes the loss of jets' momentum.

Jet configuration was also explored by comparing in-line and staggered nozzle arrays operating at the same conditions of Reynolds number (Re_j) and stand-off distance (Z/D). It was concluded that the capability of achieving higher heat transfer rates of the in-line nozzle configuration is higher than the staggered one, especially at shorter stand-off distances (Z/D). In in-line arrays, the jet rows tend to protect each other from the crossflows interacting with the main jet streams and weakening them, due to the shorter distance given to air crossflow to accelerate before striking the next row of jets. However, in the staggered arrangement, the influence of the crossflow is higher as the crossflow accelerates further and directly impacts the jets. Additionally, jet interactions were also investigated through jet-to-jet spacing (S/D) as manipulating the spacing between the jets can change how each two neighboring jet streams interact with one another. It was concluded that as the open area ratio (A_o) decreases, the heat transfer performance decreases due to the enlarged area that the nozzles are required to cover.

The second scope of this study deliberates the jet-to-jet interactions and the accumulation of the crossflow as the spent air migrates downstream before exiting the fluid domain. The crossflow accumulation usually causes a decay in the Nusselt number and, hence, reduces the overall cooling performance. This study investigated several crossflow mitigation techniques for a maximized crossflow condition (single exit case), where the spent air has a unidirectional exit. Firstly, by attaching small and easy-to-manufactured crossflow diverters to protect jet streams from upstream crossflows and, therefore, enhance heat transfer performance. The investigations comprised three diverter shapes of cylindrical, rectangular, and ribbed type with heights of 25%, 50%, and 75%, as a percentage of jet-to-target (Z/D) spacing denoted as Quarter-Length (QL), Half-Length (HL), and Three-Quarter-Length (TQL), respectively. Secondly, by extending the jets, where the jet shells were extended in the flow field, where the jets were either of a fixed height of 1.5D (EXTF) or with a variable height of 0 - 2D (EXTV). Results considered the increase in Nusselt number (Nu) along with the associated pressure loss and showed a net enhancement of up to 5.2%, 3.1%, and 3.8% for cylindrical, rectangular, and ribbed-type diverters, respectively. Additionally, the EXTF showed the highest net heat transfer enhancement among all other techniques. It offered an average of 13.4% net enhancement while the EXTV offered 10.4%. Thirdly, by manipulating the jet diameters in a 5×5 in-line array where the jet diameters were varied according to three scenarios of 5%, 10%, and 20% increase towards the spent air exit. The variable jet diameter showed a minimal enhancement of Nusselt number (Nu) not exceeding 2.09 % for the 5% increase in the jet diameter, while it adversely affected the heat transfer for other scenarios.

The third scope is to experimentally study the effect of rotation on the temperature surface profile under three rotational speeds (rpm) and three different Reynolds numbers (Re) in the turbulent flow regime and under non-uniform heat flux conditions. It was concluded that as the rotational speed increased, the jet diversion was increased due to the increased tangential force component. This diversion in jets was minimized as the jets' momentum increased (increase in jet Reynolds number (Re)).

Overall, most of the study scopes involved developing numerical CFD codes using StarCCM+ software to validate the experimental results so that the same model can be used to numerically investigate other geometries and aspects. Improving a reliable CFD model with an acceptable level of accuracy and simulation convergence time led to eliminating the need to conduct expensive and complicated experiments. The k-ε turbulence model was used due to its robustness and fast convergence time. As this study explored a wide range of thermofluidic parametric analyses of jet impingement, resolving turbulence scales was not a priority, and the steady state assumption while modeling turbulence is suitable for the application. Additionally, post-processing techniques for analyzing thermal images were heavily implemented to handle, process, and present the results.

Dedicated to my parents, my siblings, and my fiancé,
for their unconditional love, support, and encouragement

TABLE OF CONTENTS

LIST OF FIGURES

LIST OF TABLES

NOMENCLATURES

SYMBOLS

A_{foil}	Target plate surface area
A_o	Open area ratio
C	Regression multiplier coefficient
$C_{1\varepsilon}$	Turbulence model coefficient 1
$C_{2\varepsilon}$	Turbulence model coefficient 2
$C_{3\varepsilon}$	Turbulence model coefficient 3
C_{μ}	Turbulence model multiplier coefficient
D	Jet diameter
f	Friction factor
g	Gravitational acceleration
G_b	buoyancy forces Turbulent kinetic energy generation
G_k	Velocity gradients Turbulent kinetic energy generation
Gr	Grashof number
h	Convective heat transfer coefficient
I	Measured electric current
k	Turbulence kinetic energy
K	Air thermal conductivity
L	Characteristic length
m	Regression exponent
$\dot{m}$	Total measured mass flowrate

N	Total number of jets
Nu	Nusselt Number
$\overline{Nu_L}$	Line averaged Nusselt number
$\overline{Nu_s}$	Surface averaged Nusselt number
P_b	Turbulent kinetic energy production due to buoyancy
P_k	Turbulent kinetic energy production due to mean velocity shear
Pr	Prandtl number
P_T	Total pressure
q''	Heat flux
Ra	Rayleigh number
Re	Reynolds number
S/D	Normalized jet-to-jet distance
S_k	User defined turbulent kinetic energy sink
t	Time scale
T	Temperature
$\overline{T_s}$	Surface average temperature
u	Velocity component
u^+	Friction velocity
$\overline{U}$	Mean velocity component
$\grave{U}$	Time-dependent velocity component
V	Measured voltage drop
X	Streamwise direction

X/D	Normalized streamwise distance
Y	Streamwise direction
Y_M	Non-homogonous dilatation effect term
$Y+$	Nearest wall distance measured in viscous lengths
Z	Flow direction
Z/D	Normalized stand-off distance

GREEK SYMBOLS

α	Heat transfer performance parameter
β	Air coefficient of thermal expansion
δ	Uncertainty operator
ε	Turbulence dissipation rate
ε_m	Emissivity
η	Heat transfer parameter
μ	Air dynamic viscosity
μ_t	Turbulent eddy viscosity
ν	Kinematic viscosity
ρ	Air density
σ_k	Turbulence model coefficient
σ	Stefan-Boltzmann constant
τ	Shear stress
Φ	Mass flux
$\overline{\Phi_{row}}$	Row-averaged jet mass flux

$\overline{\Phi_{Total}}$	Total-averaged jet mass flux

SUBSCRIPT

a	Ambient
b	Baseline
$f.c$	Forced convection
gen	Generated due to target plate resistivity
i, in	Inlet
j	Jet
$n.c$	Natural convection
o, out	Outlet
rad	Radiation
R	Rotation
s	Surface
S	Stationary

ABBREVIATIONS

CFM	Cubic feet per minute
CYL	Cylindrical shaped
EXTF	Fixed-Height Extended Jets
EXTV	Variable-Height Extended Jets
HL	Half-Length
IQR	*Inter-Quartile Range*
MW	Megawatt

QL	Quarter-Length
REC	Rectangular shaped
RIB	Ribbed shaped
RNG	Renormalization Group
rpm	Revolution per minute
SCFM	Standard cubic feet per minute
TIT	Turbine Inlet Temperature
TQL	Three-Quarter Length

ACKNOWLEDGEMENT

There was only a place for one name on the cover of this thesis. However, this work could not be completed without the tremendous help and support that enlightened my way during my PhD battle.

First and foremost, I would like to thank God; he has given me faith and strength throughout all difficulties. Secondly, I would like to express my deepest gratitude to my advisor, Professor Ryoichi S. Amano, for his valuable guidance, unstoppable support, and faith in me. I am thankful for every piece of information I learnt from him, every fruitful discussion, and every resource he provided me with. I would also like to thank my doctoral committee, Professor John Reisel, Professor Ilya Avdeev, Professor Istvan Lauko, and Professor Wilkistar Otieno, for their time, their patience, and their valuable feedback and insights into my research.

I would like to express my immeasurable appreciation to my lovely family. To the first love of my life, the best lady in the world, my mother Fatima Musallam. To the most faithful person on earth, my father Sameeh Salem, who passed away picturing me as a doctor. To all my siblings and to my lovely fiancé Aya Nabeel.

Words cannot express my sincere gratitude to those who were always there for me, those whom I learnt a lot from, Dr. Mohamed Abousabae, Mr. Ibrahim Soliman, Dr. Mohammad Qandil, Mr. Mohamed Maache, and, last but not least, Dr. Ahmad AbdelHadi. To all my friends and colleagues that the space doesn't allow me to mention their names, yet their names are engraved in my heart, indeed.

"Whatever Your Mind Can Conceive and Believe, It Can Achieve!"

CHAPTER 1: INTRODUCTION

1.1 Jet Impingement Cooling Description

Jet impingement is a cooling method that removes heat loads from an impingement surface by directing high-velocity and high-momentum jets. These jets can be either gas or liquid, or even a two-phase flow. Impinging jets can cool down or heat up the impinging surface, whichever suits the application better. The cooling jets can vary in their types, while confined and unconfined jets are the most common types. The confined jets involve a confining wall to surround the flow stream when the impingement occurs. The confined impinging jets are suitable for small space designs, while the unconfined ones can be simply designed and fabricated. Multiple jet regions can be distinguished in a confined jet impingement. The potential core is formed near the tip of the nozzle as seen in Figure 1-1 and Figure 1-2.

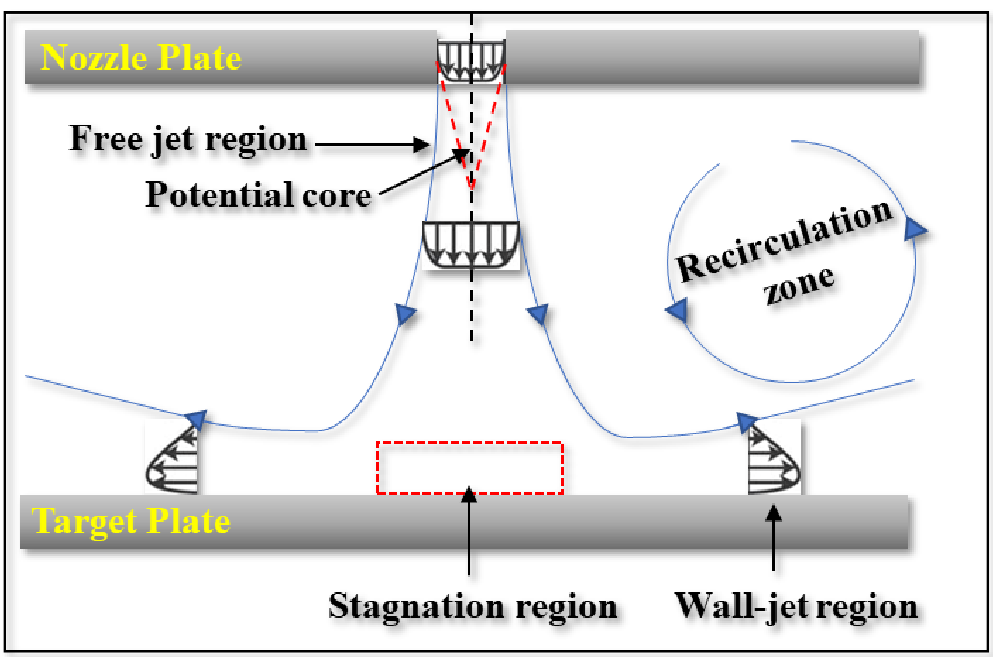

Figure 1-1: Jet physics

The flow in this region is free of flow entrainment from the surrounding (no mixing occurs). In this region, the velocity profile is almost uniform, and typically has a length of 4 to 6 diameters. It ends when the mean velocity falls below 95% of the exit velocity measured at the tip of the nozzle.

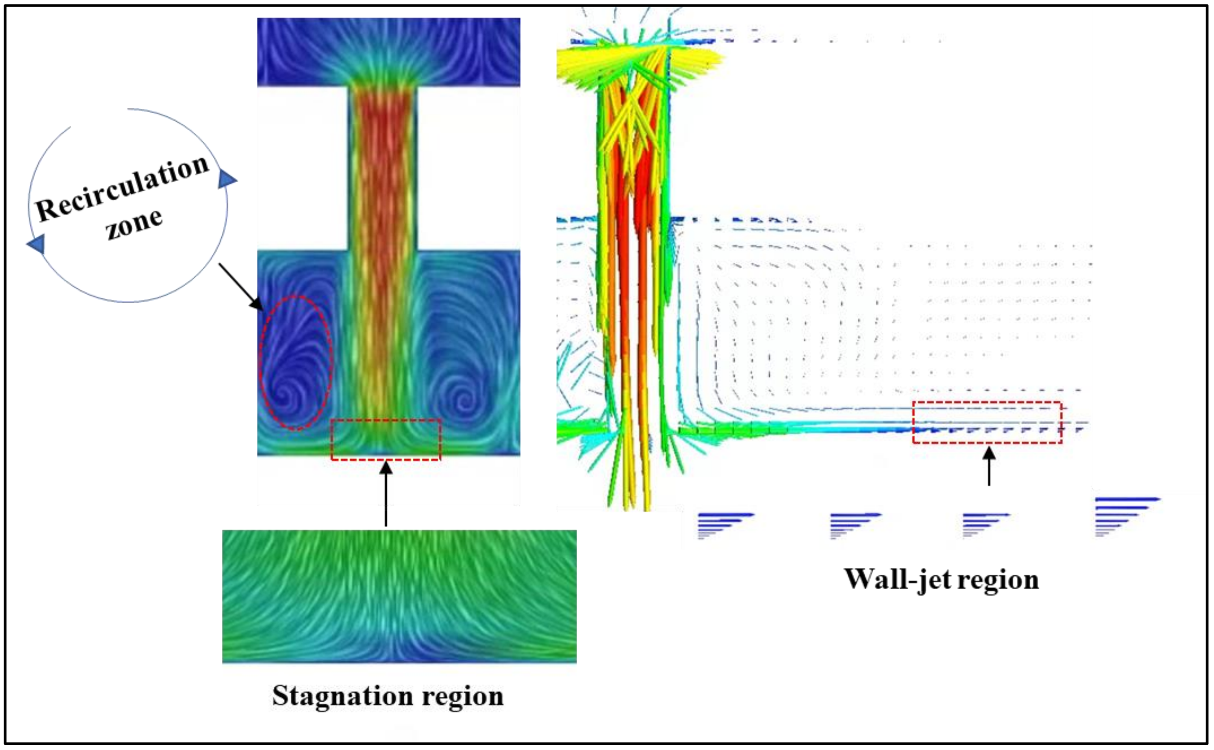

Figure 1-2: Velocity vectors explaining jet physics

As the jet travels further, surrounding air entrains into the main jet flow and reduces its velocity, until it impinges on the surface and forms a stagnation region. In this region, the velocity rapidly vanishes, and the static pressure suddenly increases (see Figure 1-3). Shear driven region is formed near the walls (known as the jet wall region), where the axial flow boundary layer is formed and developed near the walls. Multiple jets can interact with one another, when two streams are moving in opposite directions, an upwash flow results in the recirculation zone between the jets.

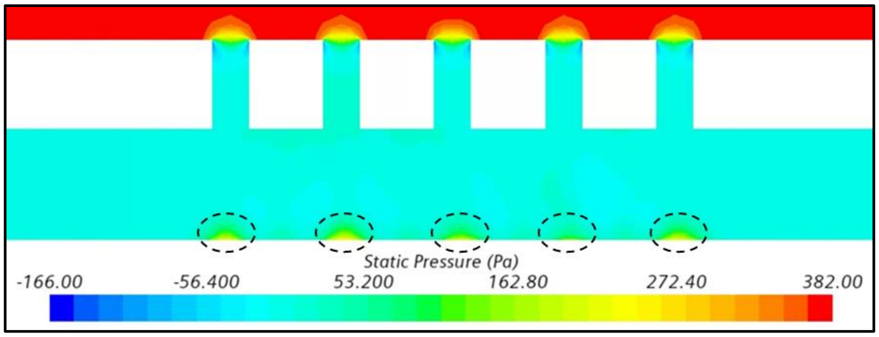

Figure 1-3: Static pressure increase in the stagnation regions

Nowadays, continuous development of the technology can be seen through the tremendous efforts in optimizing jet impingement cooling performance, as well as the huge investments in Computational Fluid Dynamics (CFD) to properly understand heat transfer and fluid flow. Current unique applications of jet impingement cooling involve power electronics, military applications, and solar photovoltaic cells [1] [2] [3]. The next sections discuss the developments of the gas turbine as a major jet impingement cooling application.

1.2 Gas Turbine Historic Background and Development

The gas turbine is one of the components that form the gas power cycle. Efforts have been made to develop the gas turbine and to enhance its efficiency. One of those successful efforts was completed back in 1903 when the first gas turbine was invented by the Norwegian inventor Aegidius Elling. Elling's model was successfully able to generate more power than needed to run its own components, using both a rotary compressor and a turbine. Gas turbines had not become industrialized until 1939 when a 4 MW unit was fully operated in a power station in Switzerland. The turbine back then was developed and engineered by a Swiss group of engineering companies named Brown, Boveri & Cie. (BBC). It was reported that the unit's efficiency peaked at 17.4% when operating at 3,000 rpm, and a Turbine Inlet Temperature (TIT) of 550 °C (1,022 °F).

Meanwhile in the United States of America, General Electric (GE) engineered its first gas turbine in 1949, which was used at Oklahoma gas and electric Company. Although the design-rated power was 3.5 MW, GE's turbine exceeded that by a wide margin. Between 1949 and 1952, it was reported that a 4.2 MW average power was reached with an efficiency of around 17%. A year after, GE included twin intercoolers and recuperators in the 5 MW units installed in Vermont. As gas turbines received much development in pressure ratios, TIT, and coating materials, two 25 MW gas turbines were put in service in a combined cycle by the Austrian utility provider Newag.

Gas turbines entered the cargo industry in 1969 with the LM2500 model developed by GE. The turbine is used to power the Callaghan cargo ship while using a 16-stage compressor with inlet guide vanes and 6 variable stator stages. It also entailed two turbine stages in the high-pressure section that were exhausted into a 6-stage free power turbine.

Combustion in gas turbines also received huge attention. In 1978, BBC reported that the combustion should take place under lean conditions and air and fuel should be separated from the combustion process. In other words, fuel and air should be premixed before delivery to the combustor. The need to reduce the Nitrogen Oxides (NO_x) emissions led to the dry-low NO_x premix combustion at the 420 MW unit installed in a power plant in Dusseldorf, Germany, by BBC back in 1984. Further development led to the increased gas turbine's efficiency of 42.5% as a simple cycle. After then, it was converted to a combined cycle in 1992, with a 147 MW unit installed by Virginia Electric and Power Company (VEPCO). An increased firing temperature of 1,425 °C (2,600 °F) was reached by GE in 2003 when a single shaft combined cycle plant operated in Wales. Siemens achieved the highest turbine efficiency in 2011 when it broke the 60% limit in Germany.

Nowadays, gas turbine efficiency is boosted to 65% as GE successfully commissioned a 1.4 GW combined cycle in Malaysia. Turbines now produce much less NO_x with higher TIT as most of the turbines benefit from the advances in additive manufacturing and material developments [4] [5].

1.3 Gas Turbine Components

A gas turbine -like other internal combustion engines- consists mainly of 4 main steps. The turbine set can be divided into two main sections, which are the cold and the hot sections. The cold section includes the air intake and the compression stages, whereas the combustion and exhaust stages form the hot section. The main gas turbine components can be seen in Figure 1-4 [6].

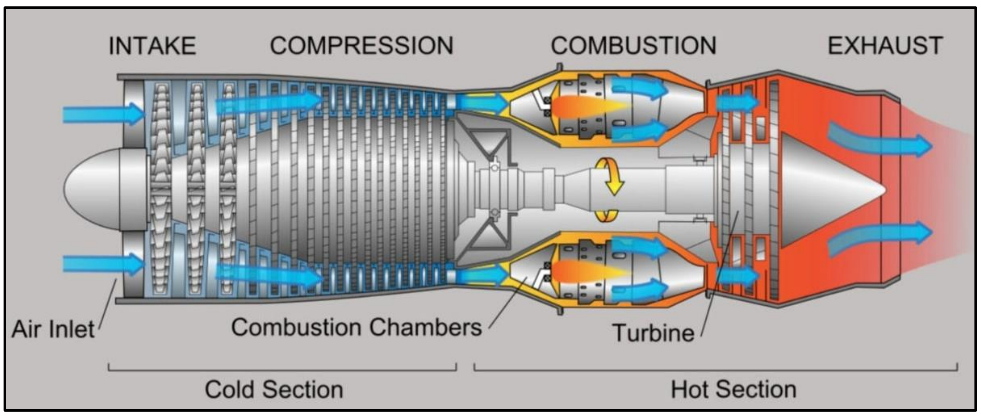

Figure 1-4: Gas turbine major components [6]

1.3.1 Compressor

Initially, gas turbines utilized centrifugal compressors that were limited to low-pressure ratios. Modern gas turbine compressors are axial-flow type ones where higher-pressure ratios can be achieved. The axial compressor receives and discharges the flow in the axial direction. Compressors usually contain multiple rotor blade stages and multiple stator vanes in between as shown in Figure 1-5 [7]. Air pressure increases as the air is passing through the compressor stages.

There will also be a slight temperature increase across the stages. Air leaves the compressor and enters the diffuser where the flow velocity is converted to static pressure. The airflow is then routed to the combustor inlet.

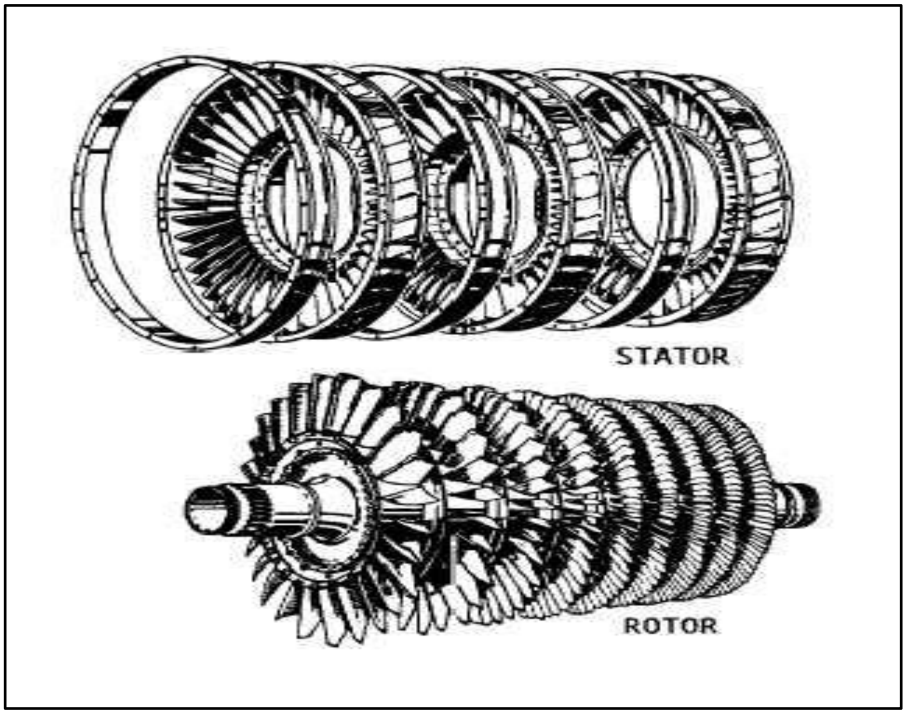

Figure 1-5: Compressor's rotor and stator blades [7]

1.3.2 Combustor

Combustor receives the high-pressure air that must be split into two main streams. One of the streams (the primary flow) is routed to the primary zone where optimized fuel is injected and mixed with the combustion high-pressure air. The other stream (the secondary air) is routed through the combustor casing to complete the combustion as shown in Figure 1-6 [8]. The rest of the secondary air is then introduced to the dilution zone to cool down the exhaust so that it can be delivered to the turbine blades at a temperature that the blades can withstand.

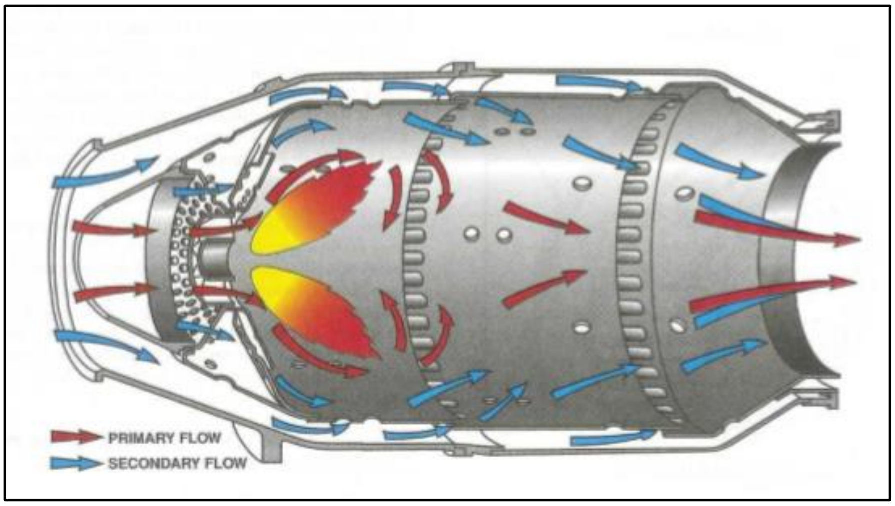

Figure 1-6: Gas turbine combustor [8]

1.3.3 Turbine

The turbine is where the kinetic energy of the hot gasses stream is converted into mechanical energy. The stream of hot gases expands through multiple turbine phases. A part of the expansion usually occurs in the high-pressure phase where the turbine is used to drive the compressor, while the load is usually connected to the low-pressure turbine. The turbine is similar to the compressor since it also consists of rows of stationary blades followed by rotating blades. However, the order of the stationary and rotating blades is different. In the compressor, energy is added to the gas by the rotor blades while stator vanes convert it to static pressure. In the turbine, the stationary vanes increase the gas velocity while the rotor blades extract the hot gas energy [9].

1.4 Problem Statement and Objectives

Gas turbines can be found in multiple industries, such as aircraft and aerospace applications, power generation industries, marine industries, and many others. These machines are subjected to continuous development to enhance their efficiency, extend their life spans, and provide safer operating conditions. The Turbine Inlet Temperature (TIT) plays a significant role in increasing the thermal efficiency of a turbine. Most of the nowadays turbines operate at TIT of 1,375 – 1,425 °C (2,500 – 2,600 °F). Turbine internal components -especially blades- are limited to temperatures where they can durably operate. Also, temperature variations inside the turbine can cause thermal stresses which ultimately lead to a shorter operating lifetime or even thermal failures. Since most turbines operate at temperatures higher than what blades and other components can withstand, introducing cooling methods to cool down turbine parts becomes essential to ensure a safe operation. The temperature of the combustion products that leave the combustor and enter the turbine is nonuniformly distributed among turbine parts. Elevated temperatures and non-uniformity are the biggest enemies that cause excessive thermal loads on turbine blades and other parts. Due to the blade rotation, the centrifugal force shifts the peak temperature of the combustion products towards the tip region of the blade. A typical average radial temperature distribution can be seen in Figure 1-7 [10].

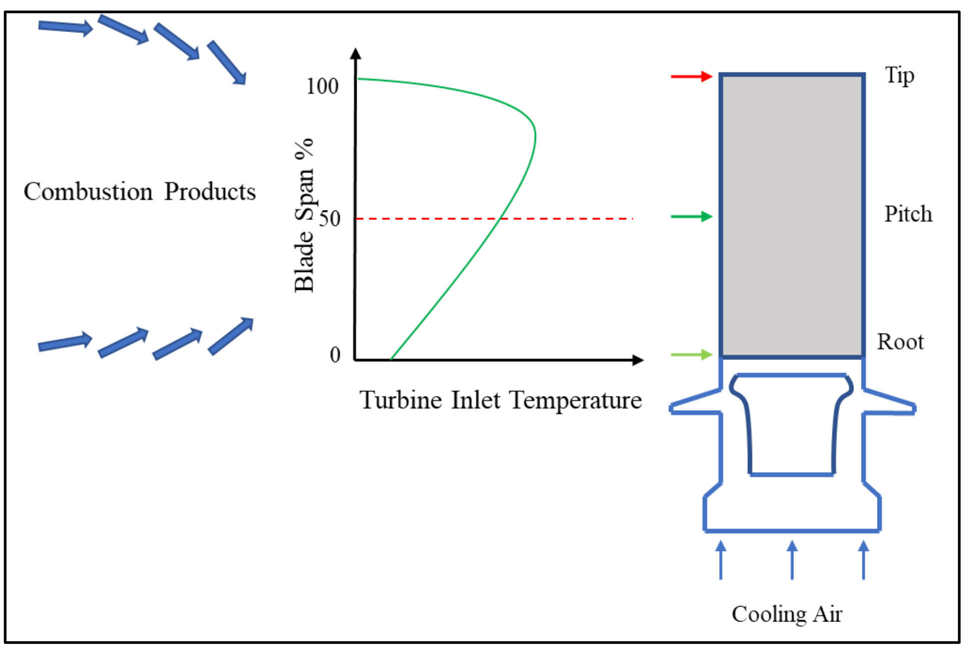

Figure 1-7: Average radial temperature distribution on a turbine blade

Turbine blades are subjected to multiple sophisticated cooling methods to cool down all blade regions. Cooling air passes through internal channels to remove the heat across the blade walls by convection. Multiple serpentine channels are designed to have the cooling airflow from the hub to the tip of the blade. Film cooling is achieved by allowing the air to establish an insulating layer between the hot gases and the blade, which is also a common cooling method for combustor liners. A part of the cooling air travels toward the blade trailing edge where short pins are utilized due to space limitations and exit through holes.

Jet impingement cooling is among various cooling techniques that offers high cooling efficiency. Air is blasted from a tiny hole (nozzles) on the inner surface of the turbine rotor blade. Since blade leading edges experience the highest temperatures compared to the mid chord and blade root, they require more cooling to handle higher heat loads. The high-velocity jets remove the heat from the areas where high temperatures are expected and even temperature distribution is preferred to be maintained. Also, structure constraints on the rotor blade under high rotation and high centrifugal loads make jet impingement cooling the only preferred method to cool down the blade's leading edge.

To summarize the problem statement, thermal efficiency and power output can be improved by increasing the turbine inlet temperature. Although the increased turbine inlet temperature can increase thermal efficiency, it can also cause thermal stresses on the various turbine components. The blade leading edge is among the main regions where higher temperature and greater temperature non-uniformity occur. This suggests the urge needs to optimize and control various jet impingement cooling parameters to enhance heat transfer.

The fundamental goal of this research is to offer additional perspective on the table to contribute to the never-ending research that aims to enhance jet impingement cooling technology. Thus, achieving the highest convective heat transfer coefficient by manipulating the main geometrical and physical parameters. This study is also focused on improving the mixing mechanisms to exchange heat actively and more efficiently with the hot boundaries using the turbulent flow nature. Additionally, since crossflows are formed as the coolant air initially strikes the heated boundary and travels towards the exits, they can heavily interact with jet cores and weakens the jet potential core. This research tries to explore methods to mitigate and treat the negative crossflow effects, and it also touches base with the rotational effects on the cooling air flow field. Finally, this thesis may offer a research guide and a suitable computational methodology for the researchers to investigate similar problems and issues in the future.

1.5 Motivation

Jet impingement cooling technology is selected to be the scope of this study because it can provide the highest heat transfer coefficient augmentation compared to all other internal cooling methods. Jet impingement cooling is needed and implemented in many industrial applications and is not only limited to gas turbine cooling [11] [12]. From rocket launcher, high-density electronic chips, metal sheets, and paper, to fabric drying, jet impingement cooling can be found among these applications and more due to its nature and capability of removing a large amount of heat. One of the interesting jet impingement cooling implementations is shown in Figure 1-8 as semi-conductor cooling. The complexity of conducting experiments has been overcome by fabricating and installing two test rigs (One for the stationary and one for the rotating blade) that simulate the active cooling method on a heated plate. Extreme and non-safe operating conditions are simulated by the Computation Fluid Dynamics (CFD) which is an effective engineering approach that is used to simulate the action of thermos-fluid in a system.

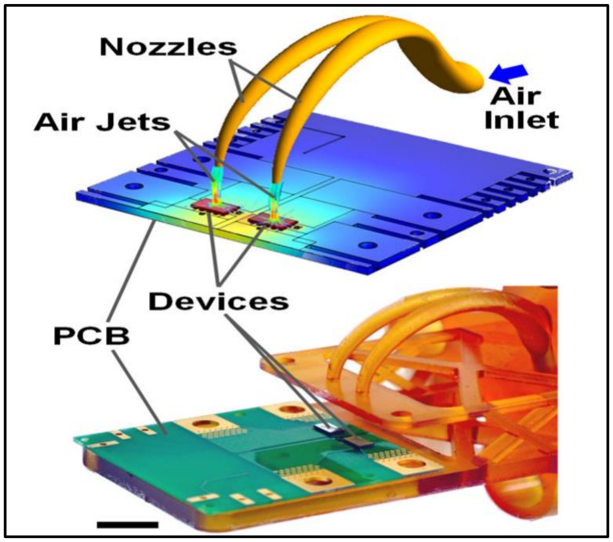

Figure 1-8: Gallium nitride semi-conductor on a circuit board cooling using jet impingement [12]

1.6 Research Resources

The research is conducted at the University of Wisconsin-Milwaukee (UWM) laboratories and facilities by utilizing the following resources:

- UWM labs located at Engineering and Mathematical Sciences (EMS) and University Services and Research Building (USRB).
- UWM High-Performance Computing (HPC) units that provide more than 2,700 computational cores, 11.5 TB RAM, and over 725 TB storage.
- UWM libraries.
- UWM Machine Shop and 3D printing facility.
- SOLIDWORKS, CREO, PYTHON, MATLAB, FLIR thermal studio, and STAR CCM+ software.

CHAPTER 2: LITERATURE REVIEW

A gas turbine engine requires high-temperature and high-pressure cycles to achieve higher efficiency and power density. The cooling of turbine blades and vanes is done with a combination of internal cooling and film cooling. Internal cooling is performed through a combination of impingement cooling and serpentine channels. Thermodynamically, it is an expensive process as the coolant needs compression with as high as 40% of the coolant supplied from the compressor. Developing cooling capabilities to gain a higher turbine inlet temperature requires a greater understanding of the physics of airflow behavior. Below is a summary of the most recent research and advancement in the technology:

2.1 Reynolds Number, Stand-Off Distance, Arrays, and Pressure Considerations

Reynold's number, jet-to-target plate distance (also known as stand-off distance), nozzle array spacing, and target surface geometry are among the critical geometrical and physical factors that affect the effectiveness of jet impingement cooling. Lee et al. studied the effect of Reynolds number, stand-off distance, and nozzle array spacing along with both streamwise and spanwise directions [13]. It was reported that the heat transfer rate is directly proportional with jet Reynold's number and inversely with jet-to-target distance Similar Nusselt number distribution was observed regardless of the stand-off distance and Reynold's number where the peaks are periodically decreased towards the streamwise direction. Xing et al. utilized the liquid crystal method to explore the effects of the stand-off distance [14]. Their study covered stand-off distances of 1 to 5 jet diameters with Reynolds number varying between 15,000 and 35,000 under three crossflow schemes. They found that the stand-off distance of 3 jet diameters outperformed all other spaces for all crossflow schemes. Short stand-off distances do not allow the jets to fully develop.

Research efforts have been made to discover the effect of the nozzle array patterns. Metzger et al. favor the in-line arrays over the staggered ones as they provide better heat transfer rates [15]. Wae-hayee et al. reported a 13% - 20% higher average Nusselt number corresponding to the inline nozzle arrays over staggered ones both experimentally and numerically [16]. Florschuetz et al. also investigated in-line and staggered nozzle array patterns for multiple stand-off distances and Reynolds numbers [17]. They reported significantly higher Nusselt numbers at a stand-off distance of 1 than the values of 2 and 3 for high hole density configuration. They also observed a higher crossflow velocity (directly upstream of each jet) compared to the staggering arrays where the crossflow is slower and nearly uniform. Miao et. al. investigated the effect of crossflow exit direction on the heat transfer characteristics. Cooling air was issued from inline and staggered round jets impinging on a flat plate. Parallel, hybrid, and counter crossflow directions were investigated for Reynolds numbers ranging from 2,440 to 14,640, and stand-off distances of 1, 3, and 6. They concluded that hybrid orientation creates smaller pressure drop and achieves higher Nusselt numbers [18].

Five confined staggered circular jets were utilized by San et. al. to study the jet-to-jet spacing effect on heat transfer characteristics [19]. They observed fewer jet interactions effect at a larger jet-to-jet spacing and small jet-to-target spacing which enhances the Nusselt number and heat transfer effectiveness. Also, for staggered nozzle arrays, the stagnation Nusselt number associated with the center jet significantly decreases with the increased ratio of jet plate width to jet diameter According to San et al. [20]. Similar observations were reported numerically by Wang et al. [21]. Brevet et al. presented a correlation for the influence of stand-off distance, jet Reynolds number, and jet-to-jet spacing utilizing thermal imaging techniques on a heated flat surface [22]. They observed a maximum heat transfer performance at a stand-off distance of 3. San et al. examined both width-to-jet diameter and length-to-jet diameter ratios [23]. They correlated the stagnation Nusselt number with these ratios as exp $[-0.044(W/D) - 0.011(L/D)]$. Similar results have been reported by many other researchers [24] [25] [26].

2.2 Jet Shape Effects

Manipulating jet shapes is a perspective of the aerodynamic performance of the cooling medium flowing through them. Elongated orifices have been compared to round orifices by Nuntadusit et al. where the same jet exit area was set while changing the orifice aspect ratio [27]. They reported minimum crossflow effects when the aspect ratio of the jet is 4 compared to the cases where the aspect ratio was 1 (the typical circular jet) and 8 (more of a slot shape). Another comparison between circular and elliptical nozzle shapes has been conducted by Keenan et al. showed an increased heat transfer rate for short stand-off distances [28]. Another comparison between the square, rectangular, and circular orifice shapes with different aspect ratios of 1 – 20 showed better performance in the square orifice shapes at larger axial distances in the same experimental conditions [29]. Lobed geometries have also received considerable attention [30] [31]. One of the efforts has been made experimentally by Martin et. al. who introduced two-lobed geometries operating at Reynold's number of 10,000 to 50,000 [31]. They reported a 10% increase in Nusselt number at the stagnation point compared to the circular nozzles. Conjugated convective heat transfer has been studied by Guan et al. on a conical wall cooled by chevron nozzles. Multiple chevron lengths (with respect to nozzle diameter) of 0.1, 0.2, and 0.3 and a penetration depth of 0.1, 0.15, and 0.2. They reported a larger normal velocity, and more vortices are introduced downstream of the chevrons, leading to improving the heat transfer rates [32]. The pressure fluctuation causes a great deal of unsteadiness in the film coolant flow, which significantly degrades the performance of film cooling [33]. Zimmer et al. [34] investigated jet impingement cooling with 55 impingement jet arrays and stand-off distance Z/D =3. They reported that the heat transfer enhancement leans to either equivalent or degraded to steady flow conditions due to the natural unsteadiness in coolant flow due to wake passing. According to Herwig et al. the rapid changes to the turbulent flow field have a significant effect on unsteady jets [35]. Jet shapes have been studied by many researchers [36] [37] [38] [39].

2.3 Jet Inclination Effects

In contrast to orthogonal jet impingement, researchers have investigated oblique jet impingement. Circular inclined jets have been investigated by Ingole et al. over a wide range of Reynold's numbers (2,000 – 20,000) [40]. Jet to target plate inclination of 15 – 75 degrees was used to understand cooling performance in such conditions. Their results showed a low average Nusselt number at 15 because of the detachment of the coolant from the target surface during operation. Another numerical study was done by Bhagwat et. al to investigate jet inclination on heat transfer characteristics [41]. A sharp decrease in Nusselt number was observed toward the uphill due to the severe loss of momentum. They also observed uneven temperature distribution that results in extreme thermal stresses. Planar particle image velocimetry was utilized by Zhang et al. to monitor normal and oblique impinging jet development for a wide range of angles of inclination of 90, 60, 45, and 30 [42]. They observed increased eccentricity of stagnation points as the inclination angle decreased. Also, the deflection of the wall jet was observed at larger inclination angles which leads to a faster decay in the tangential velocity at the wall. Inclination angles of 0, 15, 30, and 45 for liquid jet impingement were considered by Baghel et al. [43]. The higher inclination angle (>30) achieved significantly higher Nusselt numbers compared to the orthogonal jets (0). Similar observations were reported by many other researchers [44] [45]. Heat and fluid flow characteristics of a single oblique jet had been studied by Tong et al. [46]. The local stagnation Nusselt number was found to be asymmetrical where the shifting increased as the jet inclination increased. Varying the jet inclination in the range of 15°-90° along with a stand-off distance of 2-12 was experimentally reviewed by Pawar & Patel. An increase in the heat transfer asymmetry was also observed as the inclination angle dropped. Additionally, it was found that the displacement of stagnation Nusselt number seemed to be more sensitive to the inclination angle, especially at the shorter stand-off distances. However, in angles less than 30°, the heat transfer might be reduced due to the fluid disengagement from the substrate during the flow [47].

2.4 Swirling Jets

The swirling magnitude of the jets can affect their momentum. Several research efforts have been made to investigate swirling jets. Among these efforts, Nuntadsuit et al. utilized twisted tape inserts inside the nozzle pipe to generate swirling jets to study the flow and heat transfer characteristics [48]. Different twist ratios were experimentally examined at a fixed stand-off distance. They observed two main streams formed by the presence of the twisted tapes where the jet separation is increased as the twist number increases. Swirling jets can result in high heat transfer compared to cylindrical jets at a low nozzle-to-target distance. However, as Z/D increases, the heat transfer from swirling jets decreases, while cylindrical jets remain relatively unchanged. This is due to the expansion of the swirling jet at higher, while the cylindrical jet retains its potential core. Additionally, obliquely impinging swirling jets have reduced stagnation zones due to the asymmetric arrangement of the swirl passages in relation to the target surface [49]. A study done by Fawzy et al. on the compound cooling unit of a swirl enhancements strategies stated that the increase in Reynolds number from 10,000 to 25,000, at a fixed temperature ratio, will enhance the heat transfer significantly and rise Nusselt number to 99.7%, whereas the increase in the temperature ratio from 0.65 to 0.95 will result in an 11% increase in Nusselt number, at constant Reynolds number [50]. Additional swirling jets research efforts have been made by many other researchers [51] [52] [53].

2.5 Curved Surfaces

Heat transfer analysis on the non-flat (convex and concave) surfaces has been conducted due to the urge to understand the gas turbine's leading edge cooling mechanism. Due to the nature of the surface, the stagnant air over the leading edge carries huge thermal loads that need to be treated. Early studies have been conducted to adequately remove the high heat loads and ensure better gas turbine performance and durability [54]. Heat transfer analysis on a concave semi-cylindrical surface using a row of air jets was performed by Fenot et al. [55]. They concluded a minor increase in Nusselt number in the impingement region. The authors also noticed confinement of the jet's flow that has two consequences: stagnation of the adiabatic wall temperature and decrease of Nusselt number distribution. The effects of surface relative curvature numbers were studied using liquid crystals by Cornaro et al. [56]. They observed a dependency between the intensity and the location of stagnation Nusselt number and the Reynolds number, and the jet exit-to-surface distance due to the boundary layer. Furthermore, Selimefendigil and Öztopb researched the effects of a non-uniform magnetic field and jet inclinations over an elastic curved surface [57]. They reported a 7% fluctuation in Nusselt number as the amplitude of the magnetic field is varied. Singh et al. investigated jet impingement cooling on a circular cylinder with a constant heat flux boundary. They also reported an increase in stagnation Nusselt number as the stand-off distance decreased [58]. Other research efforts utilized different techniques and included both stationary and rotational experiments and numerical domains over curved surfaces [59] [60].

2.6 Crossflow Mitigation

Other passive techniques were also used to minimize the crossflow effects and enhance heat transfer rates. Crossflow could be diverted away from the issued jets by using U-shaped rips (diverters), as per Madhavan et al. [61]. Another study on crossflow reduction found that using a corrugated structure in the impingement cooling method led to an increase in heat transfer of approximately 11% [62]. Implementing the diverters significantly increased mass flux as they protect the jet core from the crossflow and, therefore, a 9-15% increase in heat transfer rates. Yeranee et al. attached air-induced ducts to the end of the pipe nozzle to increase the jet's turbulence intensity [63]. Heat transfer enhancement of up to 6% was observed using the air-induced ducts, especially at larger stand-off distances. A corrugated wall and variable height extended jets were examined by Esposito et al. [64]. In dense jet arrays, they reported an enhancement of 40-50% of the variable extended jets compared to the baseline design of jets. He et al. studied the heat transfer enhancement resulting from different crossflow diverter shapes. They reported a net heat transfer enhancement of up to 14.7% under a range of Reynolds numbers of 3,500 – 14,000 [65]. Other surface features, including chevron and wedged shape, were utilized by Parbat et al. to provide protection to the jets against the crossflow [66]. The wedged surface showed a higher pressure drop of 30%, while the chevron caused a much less pressure drop. Similarly, anti-crossflow impingement structures were developed such that the corrugated jet plane enlarges the sectional area for crossflows without changing any other parameter [67]. Terzis et al. varied the jet diameter of narrow impinging channels to regulate the crossflow [68]. Five inline jets with a 10% increased (or decreased) diameter towards the channel exit were tested at two Reynolds numbers. Increasing the jet diameter towards the channel exit showed better heat transfer performance due to less crossflow development compared to the baseline (constant jet diameter) and the decreased one. Similar observations have been concluded by Fechter et al. [69].

2.7 Rotation Effects

For most gas turbine cases, it needs to be cooled as it rotates. The rotation can influence the flow field due to the Coriolis and gravitational forces. Many research efforts have been made in this area. Among these efforts, Hong et al. investigated the mass and heat transfer of a rotating jet impingement cooling channel using an impingement array and impingement/effusion array [70]. They reported significant deflection when the channel is rotated along the leading-edge direction due to the jet deflection and the spreading phenomenon. A numerical investigation done by Lu et al. found that the rotation can cause the flow field to become distorted which will increase the average Nusselt number as the rotational speed increases. Consequently, increasing the rotational speed can improve the uniformity of heat transfer performance [71]. Hua et al. studied the effect of the rotation angle at constant stand-off distance and jet hole diameter [72]. They reported significant variation in the jet mass flux when the angle between the jet and the rotating plane was in the range of 90° – 135°. However, when the angle increased, further deterioration of the stagnation heat transfer was observed due to the induced jet diversion. Deng et al. focused on the Coriolis and buoyancy forces at different Reynolds and rotation numbers. They reported specific values of rotation number after which the buoyancy forces cannot be neglected. However, when the rotation number exceeds a certain value (rotation number of 0.42), the heat transfer is no longer affected by the rotation. Another threshold of Reynolds number was set by Safi et al. who examined the effect of rotation over a wide range of Reynolds numbers (up to 30,000) and rotational speeds between 0 to 750 rpm [73]. They reported insignificant rotation effects as the flow increased and, hence, the Reynolds number increased. Li et al. examined the effect of channel orientation from 90 - 180 degrees in a rotating impingement cooling channel [74]. Reynolds number varied between 5,000 and 15,000 while the maximum jet rotation number was set to be 0.24. Changes in mass flow distribution were observed due to the Coriolis forces that generate large vortices at angles between 90 to 135 degrees.

The buoyancy and density ratio effects on a rotating cooling u channel has been investigated by Saravani et al. [75]. It was concluded that heat transfer rates are sensitive to the buoyancy force. Higher buoyancy force was induced as the rotation number increased, which led to a significant increase in heat transfer rates. Nourin et al. compared hemispherical and leaf-dimpled channels to the smooth-wall channel [76]. They reported strong vortex rolls in the flow created by the dimples leading to up to 18% higher heat transfer rate. Additionally, Nourin et al. combined the dimpled channel with guide vanes of different geometries [77] . It was concluded that some of the studied geometries can lead to additional heat transfer enhancement. Similarly, Saravani et al. investigated several guide vanes designs on the bend section of a two-pass cooling channel with 45° ribs [78]. All their designs achieved higher heat transfer rates at the bend region. Also, the pressure drop in the bend region was reduced when the guide vanes were present. Kumar et al. conducted numerical studies on a two-pass cooling channel equipped with rib turbulators (60° V-rib, inverted 60° V-rip, and combination of both) and bleed holes of different designs [79]. It was found that the combination of 60° inverted V-ribs on the inlet section with 60° V ribs on the outlet along with bleed holes outperformed all other designs in terms of heat transfer rates.

2.8 Thesis Outline, Novelty, and Material Organization

The overall outline of this thesis is to bring another perspective to the table on the jet impingement cooling topic. It was firstly, establishing a platform to properly understand heat transfer mechanisms and fluid flow structures of a stationary heated target plate. The heated target plate mimics a blade or any heated object experiencing a uniform heat flux condition. This platform relies on utilizing an experimental test rig that accommodates most of the geometrical features discussed on this thesis. Additionally, the experimental work led to developing and continuously enhancing numerical CFD codes to simulate and predict heat profile and flow characteristics by numerically solving Navier-Stokes equations. The numerical solver offers a reliable solution for cases at higher temperatures and cooling air flows. The novelty in this part can be seen through exploring a wide range of variables and correlating them together to determine the chief factors that can influence the design of the cooling circuit as well as a robust numerical solver that considers a good level of solution accuracy with minimal computational resources.

The study of minimizing the crossflow adverse effects on cooling efficiency has not been investigated enough in the literature. This part offers a complete comparison of crossflow effects minimization through multiple passive techniques. It also considers the associated pressure loss and accounts for the net heat transfer enhancement. Additionally, the height effect of the crossflow diverters has not been previously investigated in the literature.

Finally, the available literature lacks temperature monitoring on a non-uniform heat flux condition and during rotational operation. Therefore, a new test rig along with a wireless method of monitoring the temperature while the whole setup is rotating was initiated. The rotational investigation can be carried out to explore other flow behaviors under the rotation influence.

There will be eight (8) chapters organized as follows:

Chapter 1: Briefly introduces gas turbine development over the years, highlights the major gas turbine components, and states the problem and the research objectives, motivation, and research resources.

Chapter 2: Includes a literature survey to review the previous work done by researchers all over the world in the jet impingement area. It presents the main objectives, methodologies, findings, and conclusions that have influenced this research.

Chapter 3: Presents the research methodology that describes the experimental test rig designs and components including cooling and heating circuits, temperature measuring and monitoring, experiment procedures, and calibration. It also discusses the theory and governing equations, experiments uncertainty and error analysis, as well as data post-processing techniques.

Chapter 4: Introduces the numerical solver aspects including turbulence modeling, geometry domain, boundary conditions, solution models, mesh and solution-mesh dependency, solution stability and solution-stopping criteria. It also concludes the results and compares the experimental and the numerical results.

Chapter 5: Discusses the main geometrical parameters that affect and influence the cooling circuit performance including the effects of Reynolds number, jet-to-target spacing, jet configuration, and jet-to-jet spacing.

Chapter 6: Explores various crossflow mitigation techniques to protect jet cores and enhance the cooling efficiency including jet protection via crossflow diverters, jet protection via extended jets, and varying jet diameter along the streamwise direction. It also presents the corresponding pressure drop to the enhancement of the cooling efficiency.

Chapter 7: Initiates a new experimental setup that can be used to study the jet impingement cooling under rotational conditions. It also discusses various force components effects on heat transfer and cooling air flow field.

Chapter 8: Summarizes the main research findings, provides takeaway notes, and suggests further recommendations to carry on investigating jet impingement cooling and enhancing the current test facility and the computational methodologies and techniques.

Appendices I-XV: Provide complete sets of figures, tables, and codes for heatmaps, Nusselt number, and data acquisition.

CHAPTER 3: METHODOLOGY

3.1 Stationary Test Rig Description

3.1.1 Test Rig Overview

The stationary test rig was designed to study the jet impingement cooling geometrical and physical parameters for gas turbine blades leading edge and all other suitable jet impingement cooling applications. Manipulating variables such as coolant flow rate, heat flux, nozzle shape, and nozzle-to-target (Z/D) spacing are the key factors that drove the design of the test rig to accommodate the implementation of these variables. The test reg entails mainly a confined chamber with a square cross-section of 235 mm in length and width, while the height is 115 mm as shown in Figure 3-1.

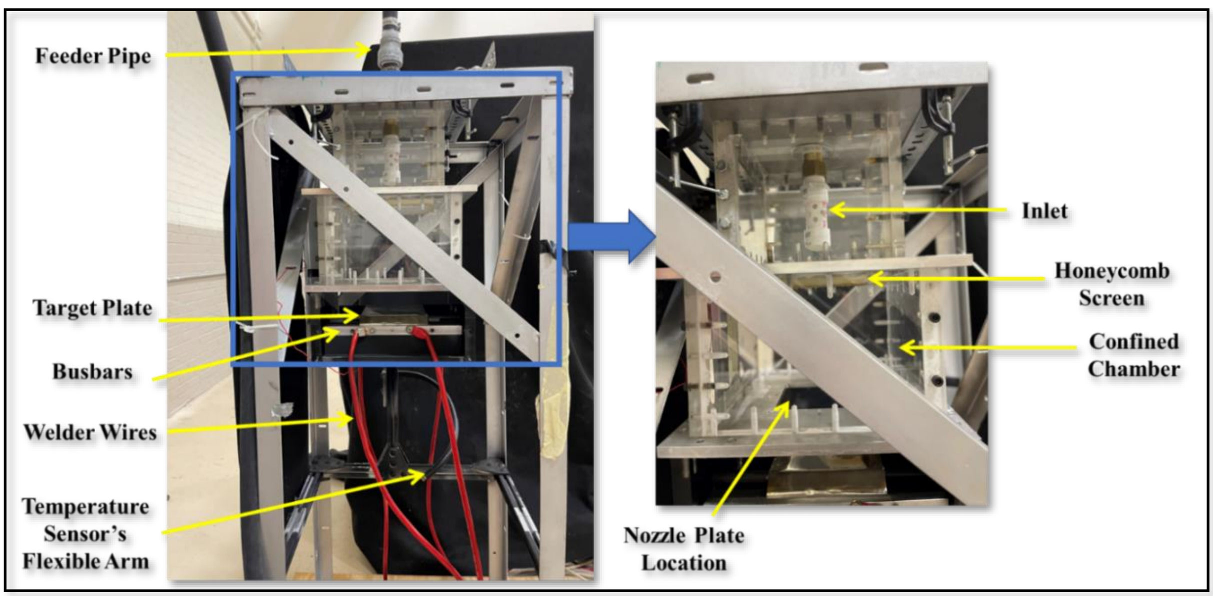

Figure 3-1: Test rig overview

The confined (pressurized) chamber receives the cooling air from the main half-an-inch feeder pipe. An aluminum air straightener honeycomb screen was placed downstream of the confined chamber. It is meant to straighten, stabilize, and distribute the incoming cooling airflow in one direction. The flow is routed through the nozzle plate where the impingement jets are issued. The confined chamber has an opening in the bottom where different nozzle plates can be mounted, such that the cooling performance for a variety of nozzle plate designs can be tested. A thermal camera is mounted on a flexible arm to capture the temperature distribution on the backside surface of the SS 304 foil. Figure 3-2 shows an exploded view of the test rig.

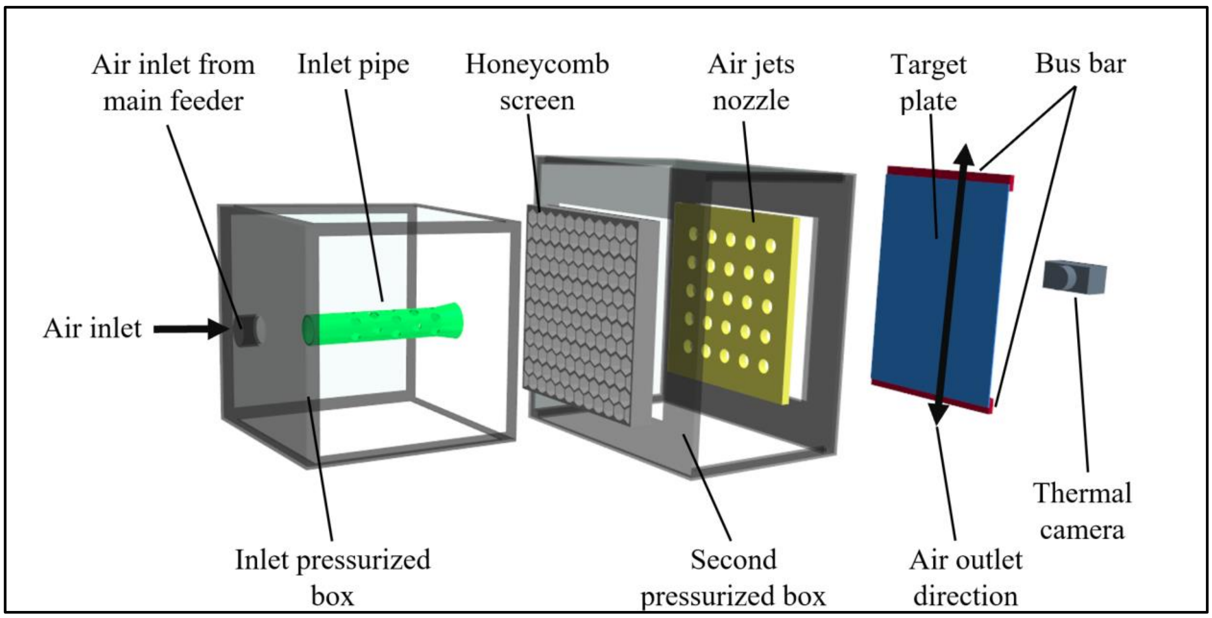

Figure 3-2: Test rig exploded view

3.1.2 Target Plate and Nozzle Plate

The scope of the experiment is a 2 mm-thick stainless-steel foil grade 304. Stainless Steel grade 304 is made of an iron-chromium-nickel alloy blend. The selection of stainless steel as the target plate was due to its corrosion resistance, high electric resistivity, and ease of form. The back surface of the foil has a square cross-section with a 10 cm × 10 cm and is black painted by a high emissive 2-μm acrylic-based Krylon Ultra-FLAT paint. The highly emissive black paint (emissivity of 0.95) ensures accurate surface temperature monitoring.

Multiple nozzle plates are tested throughout this study to examine different parameters. A sample of these plates is shown in Figure 3-3, where both machining and 3D printing methods were employed to build the nozzle plates. Although the steel machined parts provide better surface finish and rigidity against the airflow transferring through them, 3D printed samples are less expensive and easier to machine with higher dimensions accuracy. The nozzle plates are 12 × 12 cm where the holes (jets) are centered to generate the high momentum jets so that they perpendicularly strike on the target plate. As shown in Figure 3-4, the distance between the nozzle plate and the target plate can be manually adjusted.

Figure 3-3: Nozzle plate samples

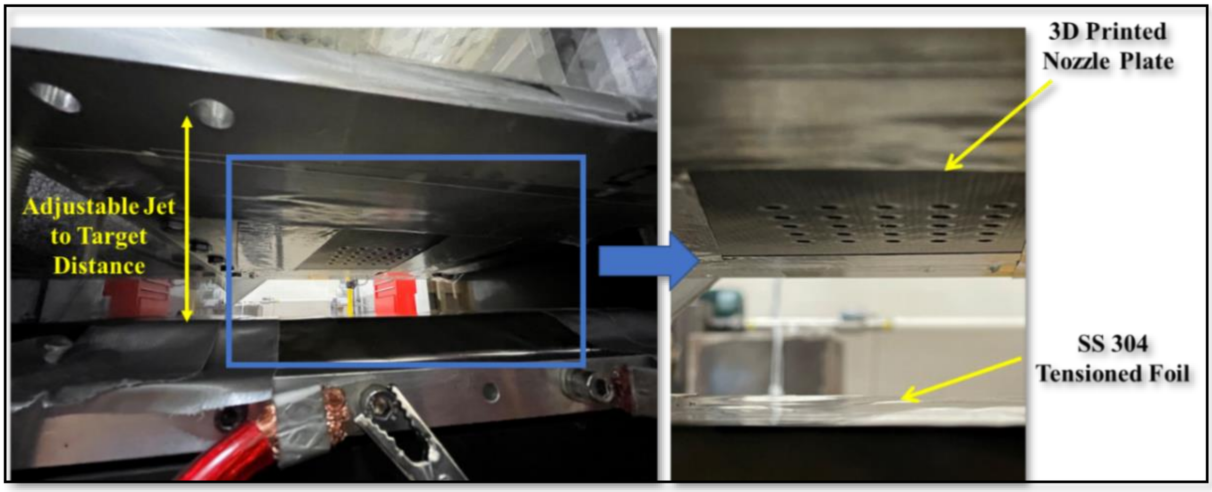

Figure 3-4: Test rig close-up

3.1.3 Airflow Circuit and Measurement

The heated target plate is cooled by atmospheric air issued from EG & G ROTRON (Model DR202Y9) blower that can produce a maximum airflow of 52 SCFM [80]. The coolant airflow is controlled by a gate valve the excess airflow is bypassed from the system by manually adjusting the gate valve opening. The gate valve is installed downstream of the blower and upstream of ALICAT SCIENTIFIC's M-5SLPMD/5M flow meter [81]. The flow meter measures not only the flow but also the temperature and the pressure. The flow meter circuit is shown in Figure 3-5.

3.1.4 Heat Flux Source

Due to safety concerns, an indirect method of heating was used where the target plate was connected to a DC power source. The power source leads were directly connected to brass busbars to which the SS 304 foil is connected. Brass busbars are known for high electric conductivity and efficient power distribution, and they efficiently distribute electric power to the clamp interface (The busbar-foil interface).

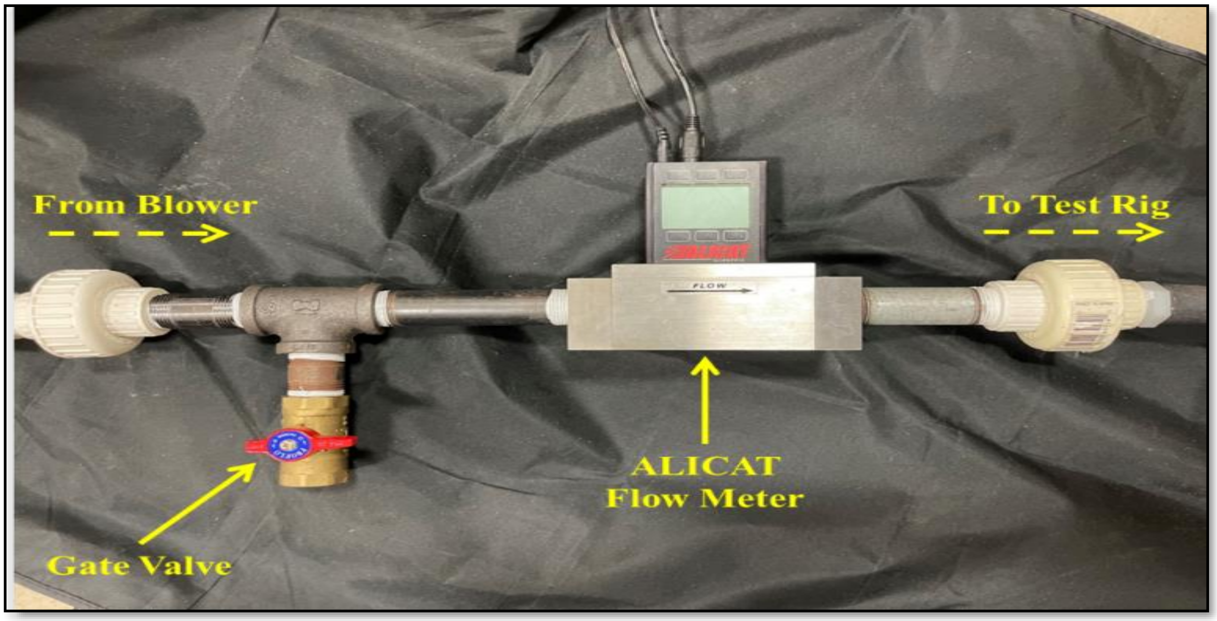

Figure 3-5: Flow meter circuit

Electric current transfers from one busbar to the other, and herby current passes through the foil. When an electric current passes through the foil, heat is generated due to the foil's electric resistivity. The voltage drop across the foil was measured by a FLUKE digital multimeter. The current and voltage measurements were collected and used to estimate the heat flux that the target plate is subjected to.

3.1.5 Temperature Measurement and Monitoring

The channel formed between the front side of the target plate and the nozzle plate is narrow. Therefore, measuring the front surface's temperature was quite difficult. A non-contact method (shown in Figure 3-6) is used to capture the temperature distribution of the target plate's back side using a FLIR A35 temperature sensor. The sensor detects a small temperature difference of 50 mK. The sensor resolution is 320 × 256 pixels with a fixed focus of 60 HZ Image frequency, and a temperature range of –25 °C to 100 °C with 5% accuracy [82]. Research IR 3.0 software developed by FLIR was used to extract the temperature profiles. After then, PYTHON codes were implemented to post-process the captured images. The post-processing procedure was done by extracting the surface temperature profiles. It also enhances the thermal camera calibration and eliminates image distortion.

Figure 3-6: FLIR A35 IR temperature sensor

3.2 Experiment Preparations and Calibration

Initial test runs have been performed to calibrate all systems and reduce all potential errors in measurements. Each system was separately calibrated and tested to ensure safe and smooth operation while measurement errors are also minimized.

3.2.1 Target Plate and Nozzle Plate

Target plates have a wide range of designs and dimensions to accommodate various studies and variables that will be discussed in the next chapters. The designs consist mainly of a 5×5 square array of nozzles (A total of 25 holes). All designs were carried out using SOLIDWORKS software. Nozzle plates vary in hole dimensions, hole arrangement (inline and staggered), jet-to-jet spacing, and others such as extended holes and crossflow diverters. The machined or the 3D-printed nozzle plates were tested to ensure a smooth surface finish. Any leftover material that can interfere with the flow field was scrubbed and removed. By using Stratasys Fortus 400 mc FDM 3D printer, a resolution of 127 to 330 microns is expected, and therefore the dimensions are guaranteed. A sample of the nozzle plate with jet extensions is shown in Figure 3-7.

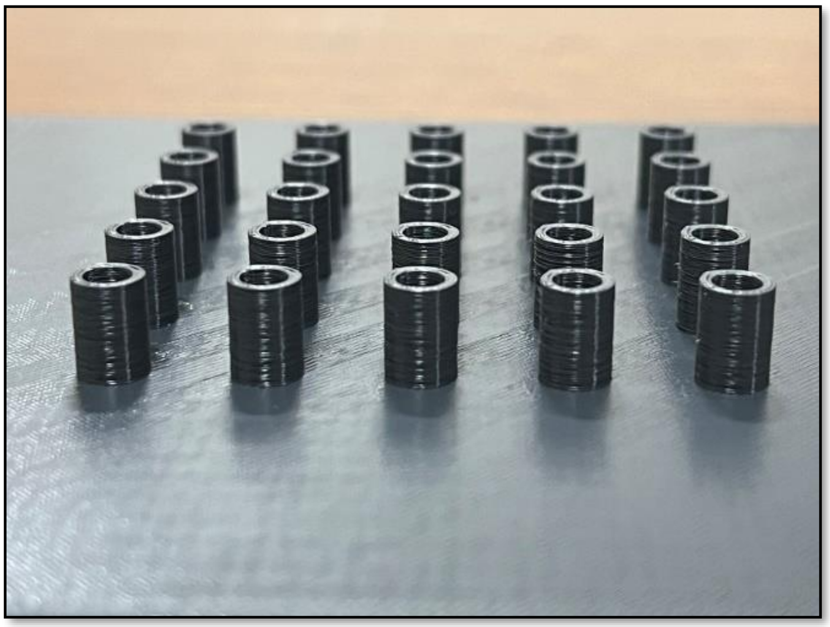

Figure 3-7: 3D-printed nozzle plate sample

The target plate is formed from SS 304. The foil is tensioned and connected to the busbars. The tensioned foils mitigate any deflections or deformations that can occur due to the heat generated within the foil. The back surface of the foil is prepared and cleansed with Alcohol before applying multiple paint layers. The foil is visually inspected to ensure there are no unpainted spots and the consistency of the painted surface finish.

3.2.2 Heating System

Electric power was supplied through the welder wires that were connected to the busbars. As depicted in Figure 3-8, the current measurement was taken via apparatus screen, while a FLUKE multimeter measured voltage drop across the target plate to estimate the heat supplied to the target plate.

Due to safety concerns, although the wilder can provide up to 160 Amps, the current was limited to 60 Amps for safety reasons. The corresponding average measured voltage drop was as low as 1.4 V. Voltage drop was measured multiple times at different experimental conditions and the mean recorded voltage value was considered in heat flux calculations.

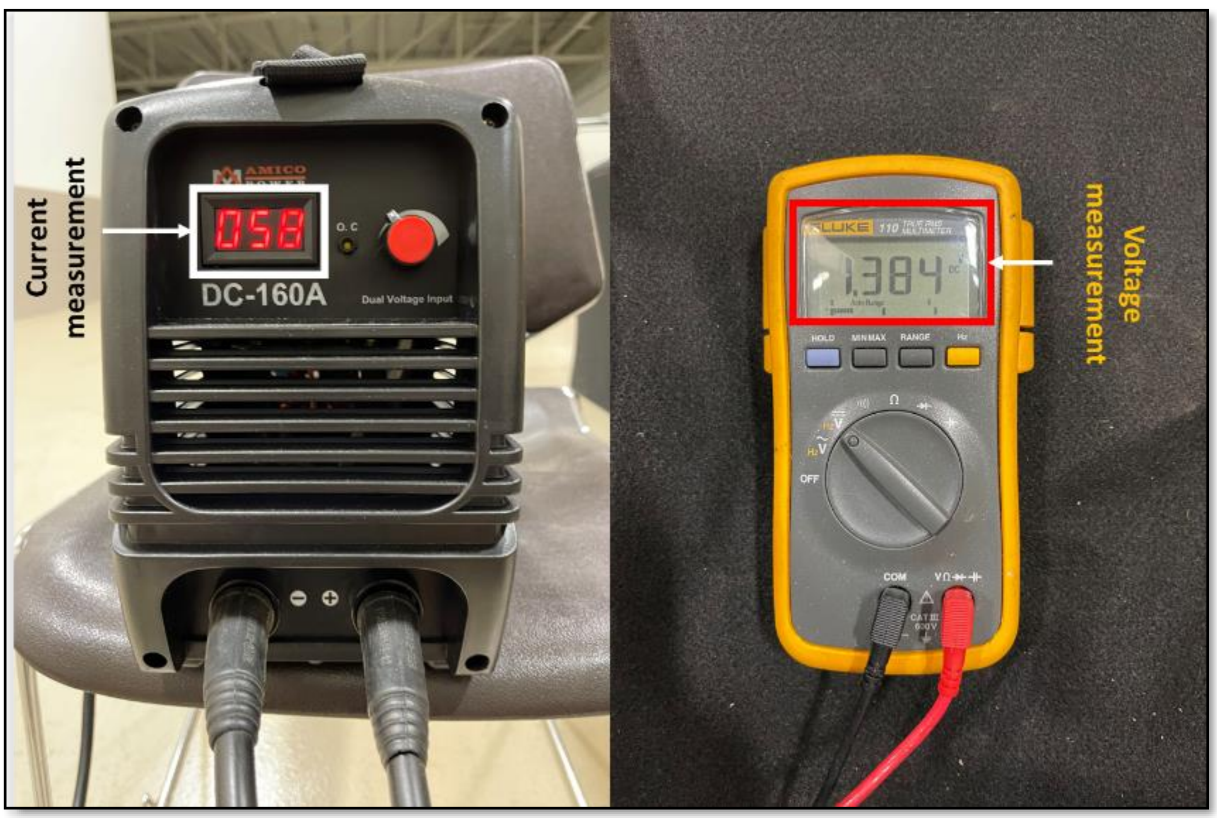

Figure 3-8: Current and voltage measurement

The time needed for the target plate to reach the steady state condition should be evaluated before running the experiment. Constant current was supplied while the temperature was being monitored. The temperature became steady and uniform after around 1 minute as shown in Figure 3-9, which compares the surface temperature profile at different time steps. The constant temperature indicated a very minor change in temperature as the heating continued, while uniform temperature means that the temperature was the same everywhere on the target place surface. The steady state conditions were reached around 50 seconds after the heating started. Therefore, one minute of heating is considered in all experiments.

3.2.3 Cooling System

Cooling air mass flowrate, temperature, and pressure are the main variables that must be calibrated. Proper airflow rate and temperature measurements can lead to better boundary conditions defined in the numerical simulations. This will also lead to better matching between the experimental and numerical results. Both airflow rate and temperature were measured by ALICAT SCIENTIFIC's M-5SLPMD/5M flow meter. The measurements were validated against a handheld FLUKE flowmeter and temperature thermometers. Similar to the calibration of the heating system, the steady-state temperature after cooling must be achieved. It can be seen from Figure 3-10, that the jet cores were completely developed, and the temperature profile became independent of time after one minute of cooling.

3.2.4 Thermal Imaging

The temperature profile was captured via a FLIR A35 thermal camera (temperature sensor). The camera is mounted at the end of a flexible arm, and the arm is repositioned such that the camera field of view captures all target plate domains. This position is kept fixed in all experiment runs. Emissivity values and camera-to-body distance are set through Research IR 3.0 software as shown in Figure 3-11. Prior to data collection, the camera lens is cleaned as per the manufacturer's user guide. A focus tool is also mounted on the camera to improve capturing the temperature profile.

3.3 Experiment Procedures and Approach

After the calibration of all systems, the test begins by turning on the DC power source. The current was preset at 58 Amps, and the corresponding voltage drop across the target plate was measured. Electric current was continuously supplied for 1 minute until the steady state temperature was reached. After then, the cooling started with a preset cooling air flowrate. The cooling air temperature and flowrate were measured through the ALICAT flowmeter. The measurements of the current and voltage drop across the target plate were employed to evaluate the heat flux. Thus, electrical energy that was dissipated to the target plate can be calculated from equation 3-1:

$$q''_{gen} = \frac{V\ I}{A_{foil}} \tag{3-1}$$

Where q''_{gen}: Heat generated due to target plate resistivity, V: Measured voltage drop, I: Measured current, and A_{foil}: Target plate surface area.

Different heat transfer mechanisms are responsible for dissipating the heat away from the target plate surface. Most of the generated heat is transferred through forced convection due to the high momentum jets impinging on the surface. Radiation and natural convection represent a small portion of the heat rejection where heat is dissipated from the back side of the target plate by natural convection, and both the back and the front side by radiation.

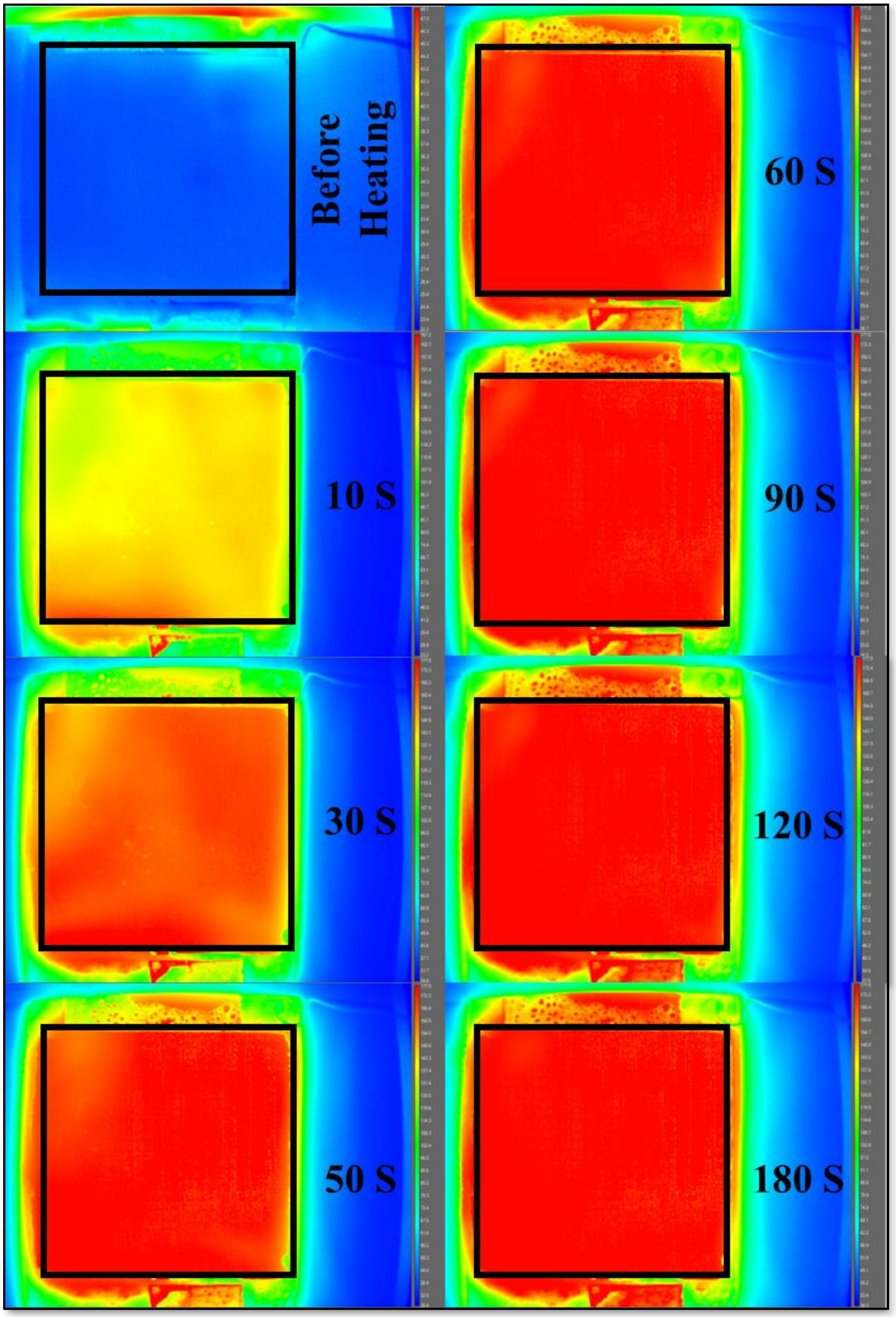

Figure 3-9: Temperature profile variation with time in the heating phase

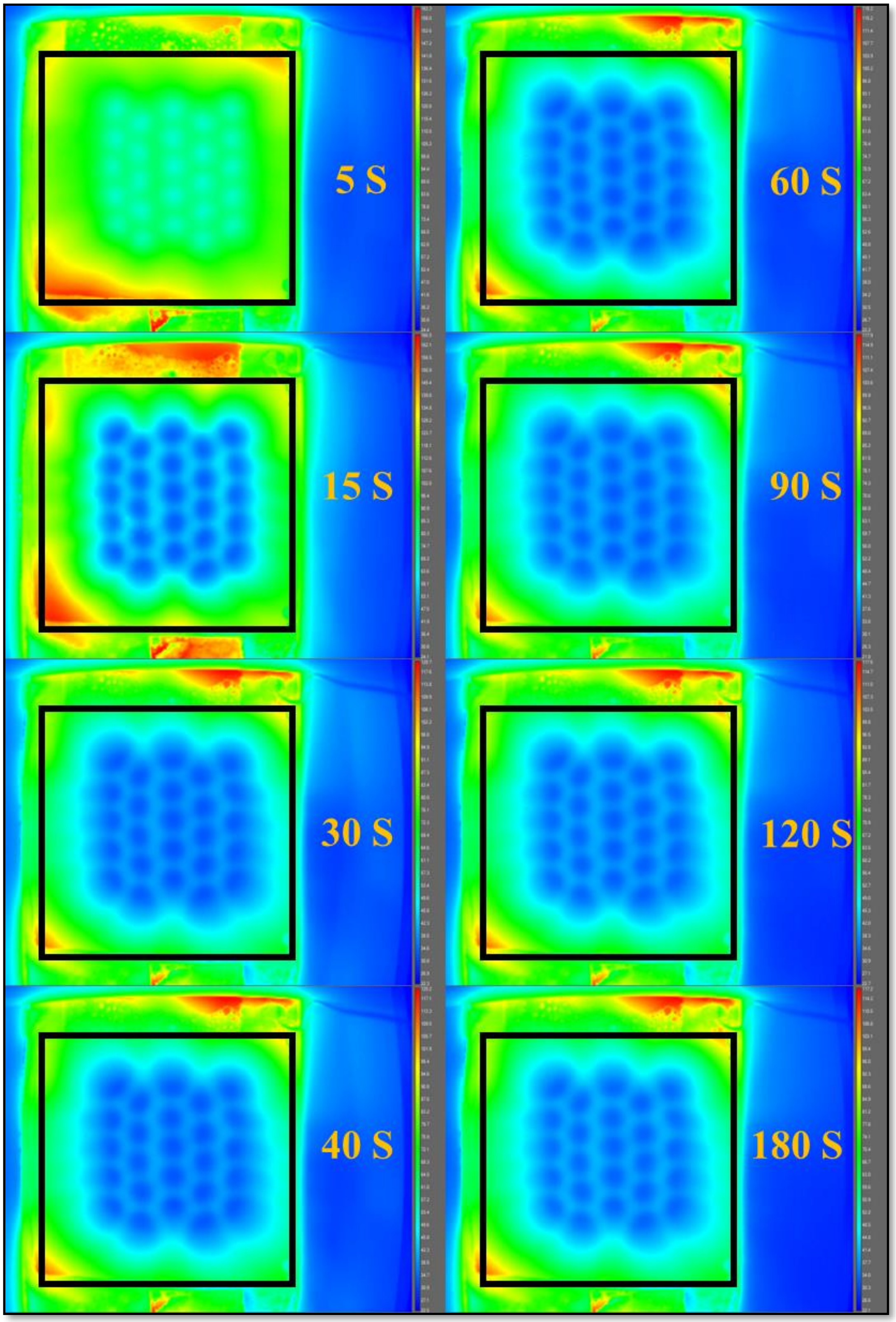

Figure 3-10: Jet cores development with time in the cooling phase

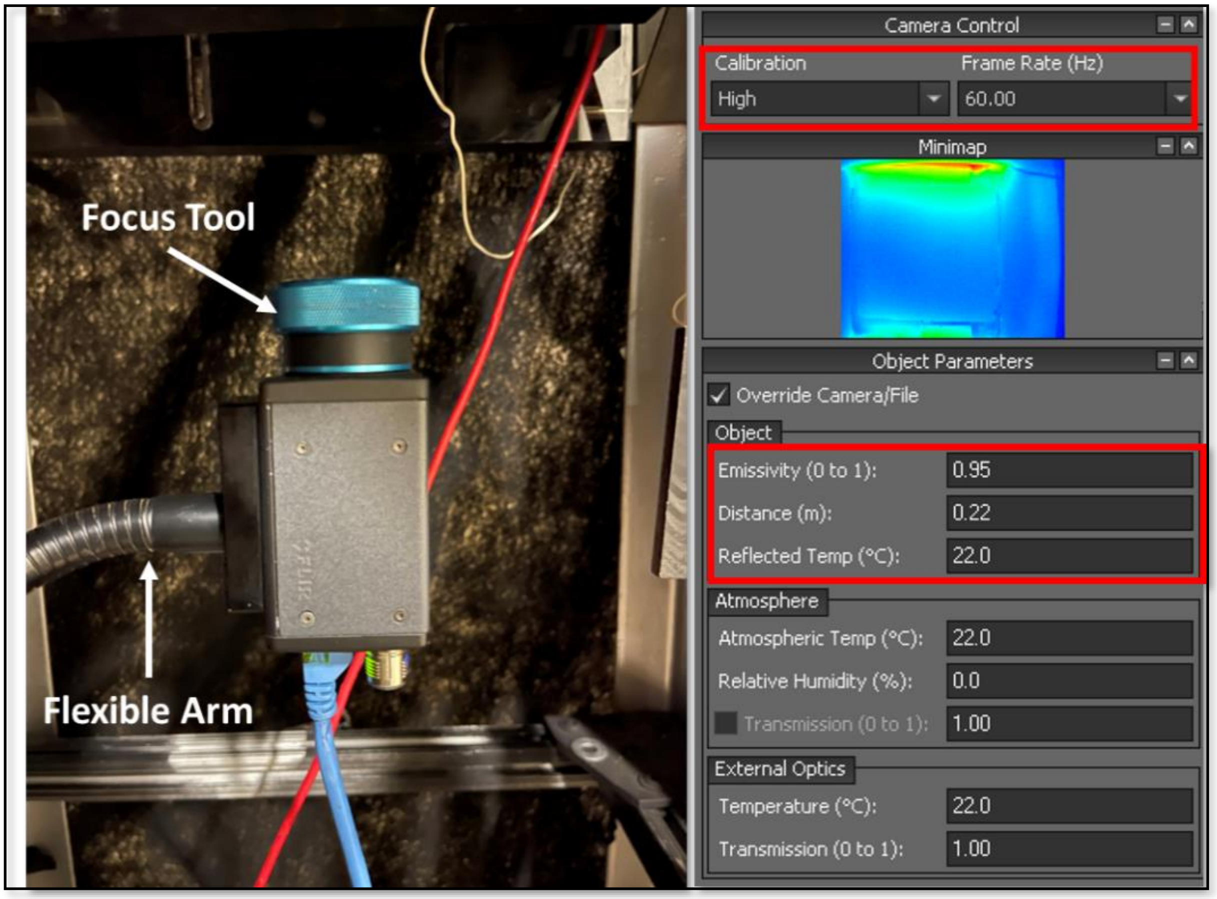

Figure 3-11: Thermal camera calibration

The radiative heat can be either absorbed or reflected by air molecules or absorbed by the test rig's metallic structure and the black curtain covering the test rig. The radiation heat transfer does not dominate other heat transfer mechanisms at low temperatures. Figure 3-12 represents the heat transfer mechanisms that dissipate the heat from the target plate. Therefore, the heat flow can be represented as in equations 3-2 and 3-3:

$$q''_{gen} = q''_{f.c} + q''_{rad\ (back\ and\ front\ sides)} + q''_{n.c\ (back\ side)} \quad \text{3-2}$$

$$q''_{gen} = h\,(T_s - T_j) + \sigma\varepsilon_m(T_s^4 - \ T_j^4) + h_{n.c}\ (T_s - T_a) \quad \text{3-3}$$

Natural convection heat transfer coefficient is calculated from equation 3-4:

$$h = \frac{Nu\,K}{L} \qquad 3\text{-}4$$

Where Nu is evaluated from McAdams's relation in equation 3-5:

$$Nu \;=\; 0.27\,Ra^{1/4} \qquad 3\text{-}5$$

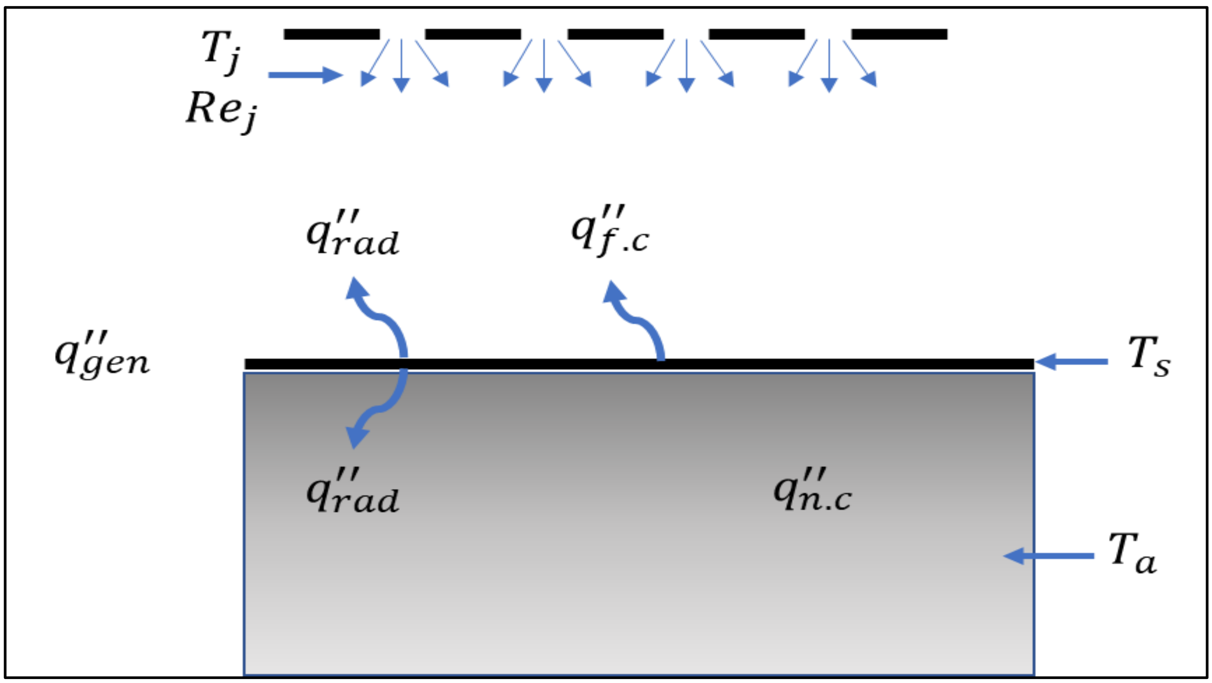

Figure 3-12: Target plate heat transfer mechanisms

Where Rayleigh and Grashof numbers are expressed in equations 3-6 and 3-7:

$$Ra \;=\; Gr\,Pr \qquad 3\text{-}6$$

$$Gr \;=\; \frac{\beta g \rho^2 L^3}{\mu^2}\,(Ts - Ta) \qquad 3\text{-}7$$

Therefore, by rearranging and substituting the terms, the connective heat transfer coefficient is estimated by 3-8:

$$h_{\,n.c} = \frac{0.27\,\left(\frac{\beta g \rho^2 L^3}{\mu^2}\,(T_s - T_a)\,P_r\right)^{1/4}}{L} \qquad 3\text{-}8$$

All air properties were evaluated at the film temperature which is the arithmetic mean between the surface and the air bulk temperature.

Based on different operating scenarios of heat flux and coolant airflows, the radiation and natural convection combined losses are accounted for approximately 20% on average. A 20% natural convection and radiation losses are a good match with the reported results reported by Zimmer et al. and Schroder et al. [83] [84]. They reported that the radiation and natural convection losses accounted for 14% and 6-8% of the total heat flux, respectively. Due to the difficulty of measuring the flow from each jet, the total airflow is assumed to be divided equally in all 25 jets. Equation 3-9 calculates the average jet Re_j considering the mean nozzle flow rate:

$$Re_j = \frac{4\ \dot{m}}{N\ \pi\ \mu\ D} \tag{3-9}$$

Nusselt number is the ratio of the convective to the conductive heat transfer. Nu can be used to characterize the active cooling along the foil surface; the higher the Nu is, the larger the heat dissipation is achieved. It can be represented as shown in equation 3-10:

$$Nu = \frac{h\ D}{K} \tag{3-10}$$

3.4 Experiment Uncertainty and Error Analyses

The errors in Nusselt number (Nu) and Reynolds number (Re_j) are estimated based on the parameters involved in their expressions. Manufacturer calibration uncertainties were used when provided. However, conservative estimates were used for individual settings when uncertainties were not given. The uncertainty of the Nusselt number (Nu) can be calculated using equation 3-11.

$$\delta Nu = \sqrt{\sum \left(\frac{\partial Nu}{\partial x}\ \delta x\right)^2} \qquad 3\text{-}11$$

Equation 3-10 can be decomposed into the main variables that contribute to the Nusselt number (Nu) uncertainty as below:

$$Nu = \frac{V\ I\ D}{Sx\ Sy\ k\ Ts - \ Sx\ Sy\ k\ Ta} \qquad 3\text{-}12$$

Substituting equation 3-12 in equation 3-11 yields:

$$\delta Nu = \sqrt{(}\left(\frac{\partial Nu}{\partial V}\ \delta V\right)^2 + \left(\frac{\partial Nu}{\partial I}\ \delta I\right)^2 + \left(\frac{\partial Nu}{\partial D}\ \delta D\right)^2 + \left(\frac{\partial Nu}{\partial Sx}\ \delta Sx\right)^2 + \left(\frac{\partial Nu}{\partial Sy}\ \delta Sy\right)^2 + \left(\frac{\partial Nu}{\partial Ts}\ \delta Ts\right)^2 + \left(\frac{\partial Nu}{\partial Ta}\ \delta Ta\right)^2 + \left(\frac{\partial Nu}{\partial k}\ \delta k\right)^2) \qquad 3\text{-}13$$

And similarly, for Re_j:

$$\delta Re_j = \sqrt{\sum \left(\frac{\partial Re_j}{\partial x}\ \delta x\right)^2} \qquad 3\text{-}14$$

$$\delta Re_j = \sqrt{\left(\frac{\partial Re_j}{\partial \dot{m}}\ \delta \dot{m}\right)^2 + \left(\frac{\partial Re_j}{\partial D}\ \delta D\right)^2 + \left(\frac{\partial Re_j}{\partial \mu}\ \delta \mu\right)^2} \qquad 3\text{-}15$$

The uncertainties in the Nusselt number (Nu) and Reynolds number (Re_j) were ±4.15%, and ±1.09%, respectively, as listed in Table 3-1. The error in Nusselt number (Nu) values is dependent on the surface temperature; it increases as the temperature increases.

Table 3-1: Experiment uncertainty

Item (x)	Quantity	Units	δItem (δx)
V	1.38	V	0.005
I	58	A	0.5
D	4	mm	0.0635

S_x	100	mm	0.1
S_y	100	mm	0.1
T_s	Varies	°C	0.05
T_a	24.85	°C	0.005
K	0.026	W/m.°C	0.0005
$\dot{m}$	Varies	Kg / S	9.9×10^{-6}
μ	1.86×10^{-5}	Pa.S	9.8×10^{-6}
Uncertainty in $\boldsymbol{Nu}$ (δNu)			**$\pm$ 1.14 or 4.15%**
Uncertainty in $\boldsymbol{Re_j}$ ($\boldsymbol{\delta Re_j}$)			**$\pm$ 48.84 or 1.09%**

3.5 Data Post Processing

Captured images were post-processed by a PYTHON code (see APPENDIX O for full script). Images were cropped to accurately extract the temperature profile of the target plate domain that is only 10 × 10 cm. A spreadsheet was also extracted that includes one temperature reading in each pixel of the camera field of view. The heatmap transformation is depicted in Figure 3-13, while the post-processing workflow is summarized below:

3.5.1.1 Importing Data Tables and Formatting Structure

First, a procedure was carried out to standardize the formatting of temperature tables obtained from FLIR Camera and StarCCM+. The required temperature table format is shown in Table 3-2:

Table 3-2: Standard table formatting for data post-processing

Row/Column	1	2	...	N
1	(1,1)	(1,2)	…	(1, N)
2	(2,1)	(2,2)	…	(2, N)
.	.	.	…	.
.	.	.	…	.
.	.	.	…	.
M	(M,1)	(M,2)	…	(M, N)

3.5.1.2 Cropping and Filtering Data Tables

Temperature data tables were cropped from the experiment and StarCCM+ so the same pixel area can be captured, which corresponds to the heated target plate area. After cropping, temperature outliers in the data were filtered out (Extreme temperatures on the edges) that deviated too much from the surface average temperature. Finally, if necessary, temperature tables were adjusted by transposing them so that the used air outlets are the same for the experiment and CFD tables.

3.5.1.3 Generating Heat Maps

Heat maps were generated for the experiment and the CFD temperature tables by normalizing the temperature values from data tables according to a color bar standard. Then, every pixel temperature was projected for the corresponding location on the heat map 2D plane.

3.5.1.4 Calculating Surface and Line Averages

This step started by calculating the temperature averages along the used air outlets, which reduced the dimensions of the temperature data table from (M rows and N columns) to (N columns). After that, the spanwise distance along the used air outlet was normalized to generate non-dimensional distances (e.g: X/D). Nusselt line averages were then calculated by calculating the Nusselt number for every temperature line average point according to equation 3-10.

3.5.1.5 Generating Box Plots

Box plots were generated to compare the behavior across different spanwise distances on the air nozzle. This step started by calculating the line average Nusselt number as outlined before, then grouped the results by selecting unique combinations of normalized stand-off distances (Z/D) and normalized spanwise distances (S/D). Each of these groups has four different flows Reynolds number constituents (2,500, 3,000, 4,000, and 4,500). After that, each group's box plot was constructed by calculating the minimum, maximum, interquartile range (IQR), mean, and median.

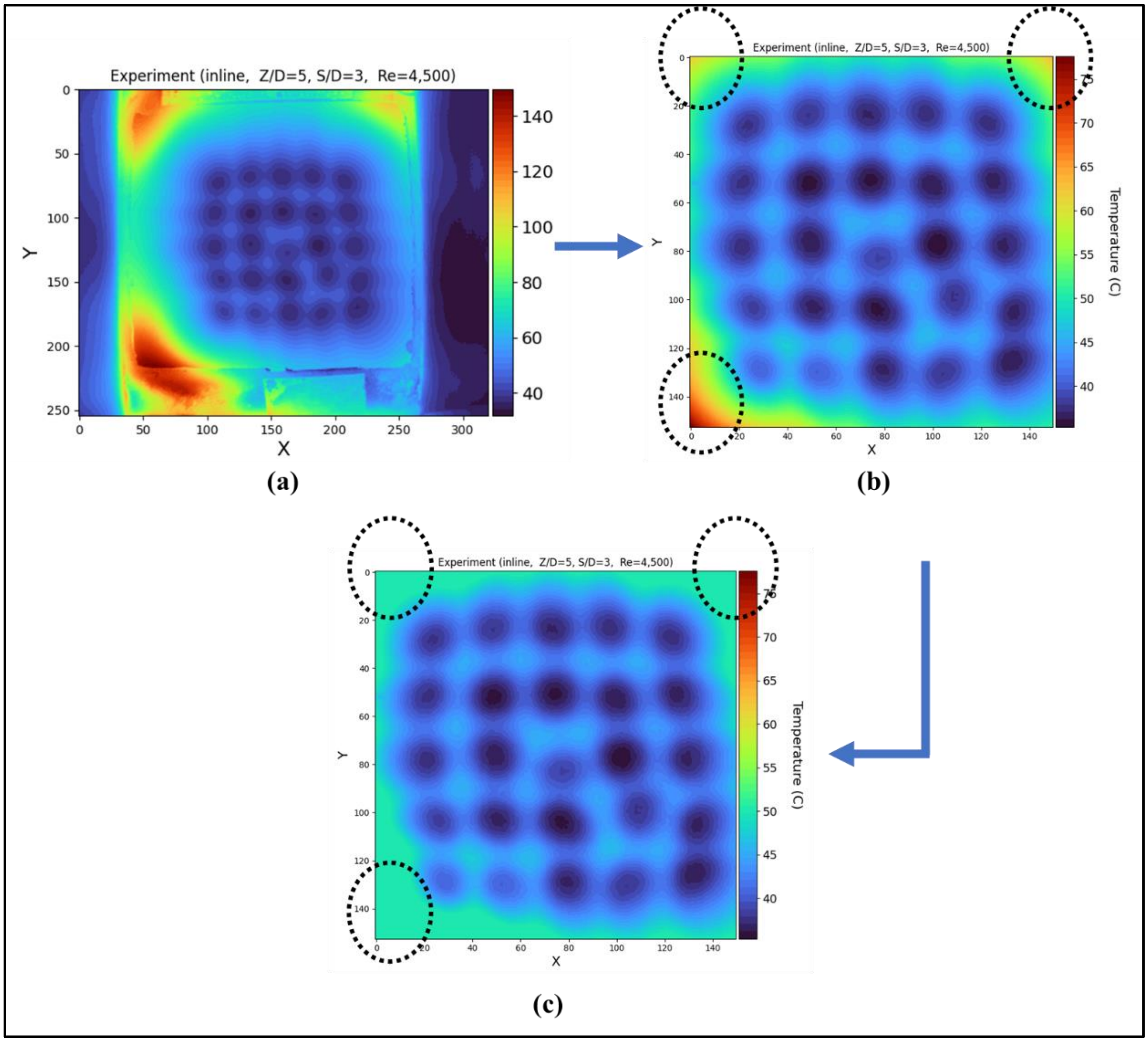

Figure 3-13: Thermal image transformation, (a) raw image, (b) cropped image, and (c) filtered image

CHAPTER 4: NUMERICAL MODELING AND VALIDATION

The experiment was simplified such that 25 cooling holes impinge on a flat plate surface. The test was conducted to cover a range of Reynolds numbers of (2,500, 3,000, 4,000, and 4,500). Reynold numbers of up to 10,000 were accomplished via CFD. The results include studying and manipulating the variables that could enhance the heat transfer mechanism.

4.1 Numerical Solver and Governing Equations

4.1.1 Turbulence Model

Turbulence fluctuations in the flow field occur in both space and time scales. These fluctuations occur in many different space and time scales, making predicting the flow field behavior complicated.

The high kinetic energy of some fluid field regions can easily overcome the fluid's viscosity-damping action and therefore, disturb the main flow field. The turbulence causes plenty of fluctuations that affect the mean flow field properties (such as velocity, temperature, pressure, etc.). Turbulence is maximized as the damping effect is minimal due to the low fluid viscosity and as the fluid inertial forces increase, as portrayed by the non-dimensional Reynolds number. High Reynolds numbers indicate dominant kinetic energy (Inertial forces) compared to the viscous forces. Navier-Stokes equations govern the physics of the fluid flow field. These equations are applicable to both laminar and turbulent flow regimes. The continuity, momentum, and energy equations are expressed in equations 4-14-2, and 4-3, respectively [85] [86]:

$$\frac{\partial \rho}{\partial t} + (\nabla \cdot \rho u) = 0 \qquad \text{4-1}$$

$$\rho \frac{Du}{Dt} = -\nabla p + \mu \nabla^2 v + \rho g \qquad \text{4-2}$$

$$\rho \, C_p \frac{DT}{Dt} = -[\nabla \, . \; q] - [\left(\frac{\partial \, ln \, \rho}{\partial \, ln \, T}\right)_p \frac{DP}{Dt} - (\tau : \nabla)] \qquad \text{4-3}$$

Reynolds Averaged Navier-Stocks (RANS) models decompose the flow field properties into two main components: time-averaged and fluctuating component. As shown in Figure 4-1, velocity (U as a function of both time and space) can be divided into a time-averaged component (mean velocity $\overline{\text{U}}$ as a function of space only) and a time-dependent component Ù as a function of both space and time) as expressed in equation 4-4.

$$U\,(x,t) = \overline{U}\,(x) + \grave{U}\,(x,t) \qquad \text{4-4}$$

The RNG k-epsilon (k-ε) model is a member of the RANS family where all the effects of turbulence are modeled. The K-epsilon (k-ε) model was initially developed by Jones and Launder [87] and formed into a two-equation model to solve for Turbulent Kinetic Energy (TKE) and Turbulence Dissipation Rate (TDR) as shown in equations 4-5 and 4-6:

$$\frac{\partial(\rho k)}{dt} + \frac{\partial(\rho u_i k)}{\partial x_i} = \frac{\partial}{\partial x_j}\left((\mu + \frac{\mu_T}{\sigma_k})\frac{\partial k}{\partial x_j}\right) + G_k + G_b - \rho\varepsilon - Y_M + S_k \qquad \text{4-5}$$

$$\frac{\partial(\rho \varepsilon)}{dt} + \frac{\partial(\rho u_i \varepsilon)}{\partial x_i} = \frac{\partial}{\partial x_j}\left((\mu + \frac{\mu_T}{\sigma_\varepsilon})\frac{\partial \varepsilon}{\partial x_j}\right) + \frac{C_{1\varepsilon}\varepsilon}{k}(G_k + C_{3\varepsilon}G_b) - \frac{C_{2\varepsilon}\rho\varepsilon^2}{k} + S_\varepsilon \qquad \text{4-6}$$

This model assumes that the turbulent shear stress is related to the mean rate of strain via turbulent viscosity. The turbulent eddy viscosity is calculated through 4-7:

$$\mu_t = C_\mu \frac{\rho k^2}{\varepsilon} \qquad \text{4-7}$$

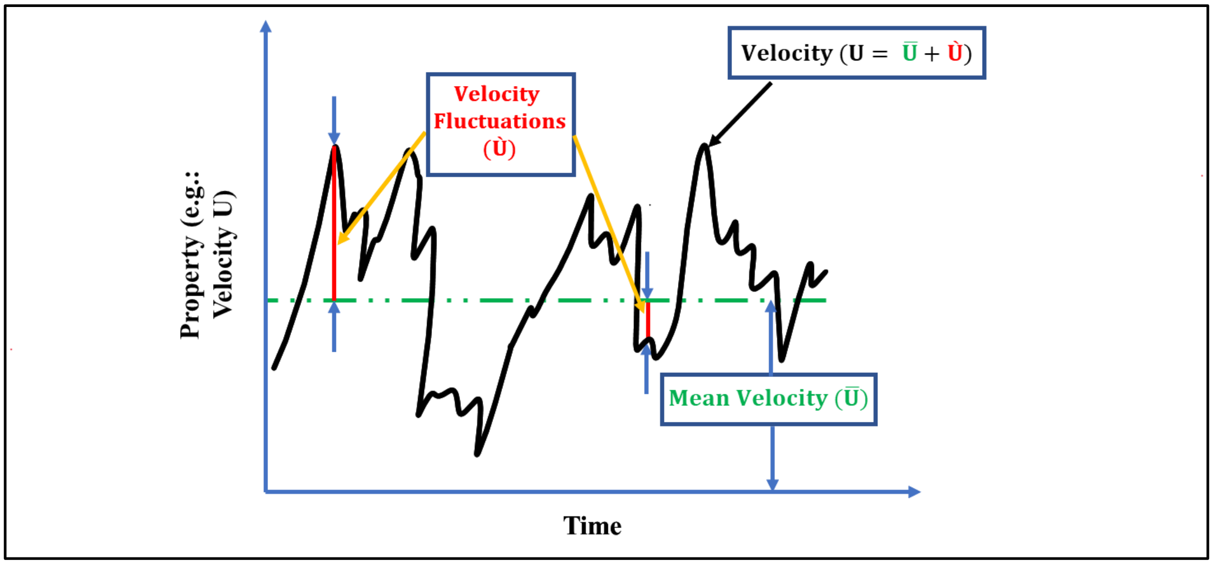

Figure 4-1: Velocity components as an example of RANS decomposition

Where, μ_t is the turbulent eddy viscosity, ρ is the fluid density, and C_μ is the multiplier coefficient (0.09). The RNG k-ε model is known for its robustness and fast convergence time. Also, the RNG k-epsilon model is a good entry model that is robust, non-stiff, as well as does not need a lot of work in terms of initial conditions and stability considerations. Moreover, the simulated case includes relatively low temperature and pressure fields and does not involve geometry curvatures or significant adverse pressure gradients. Hence, the model assumptions are deemed suitable for this application. As this study explores a wide range of thermofluidic parametric analysis of jet impingement, resolving turbulence scales is not a priority, and the steady state assumption while modeling turbulence is suitable for the application.

4.1.2 Geometry, Boundary Conditions, and Computational Domain

The computational study was performed employing The Star CCM+ software to model the flow and heat transfer interactions. The confined chamber, the nozzle plate, and the heated foil all together, form the area of focus, which is designed using SolidWorks software according to the physical setup dimensions and characteristics, as shown in Figure 4-2.

The mass flow rate is specified as the top chamber's boundary condition where air at lab temperature enters and is then routed through the nozzle. Air issued from nozzles strikes -perpendicularly- the target plate. A constant heat flux boundary condition is defined on the target plate. When air impinges the target plate, it migrates towards the exits where a pressure outlet boundary condition is defined. Non-slip condition is defined on the nozzle walls, the target plate wall, as well as the pressurized chamber walls.

4.1.3 Mesh and Mesh Independence Study

Discretizing the entire fluid domain into small cells (nodes) is important in validating the results. Governing equations are numerically solved in these cells, and the results can vary according to the mesh. Mesh properties play a significant role in the solution's accuracy. Although finer mesh results in more accurate solutions, it requires more expensive computational time and cost. Mesh refinement should be done in stages until the solution is not affected by the mesh (independent). Multiple mesh variables are manipulated, and the results are compared and validated against the experimental results. Mesh study steps are summarized below:

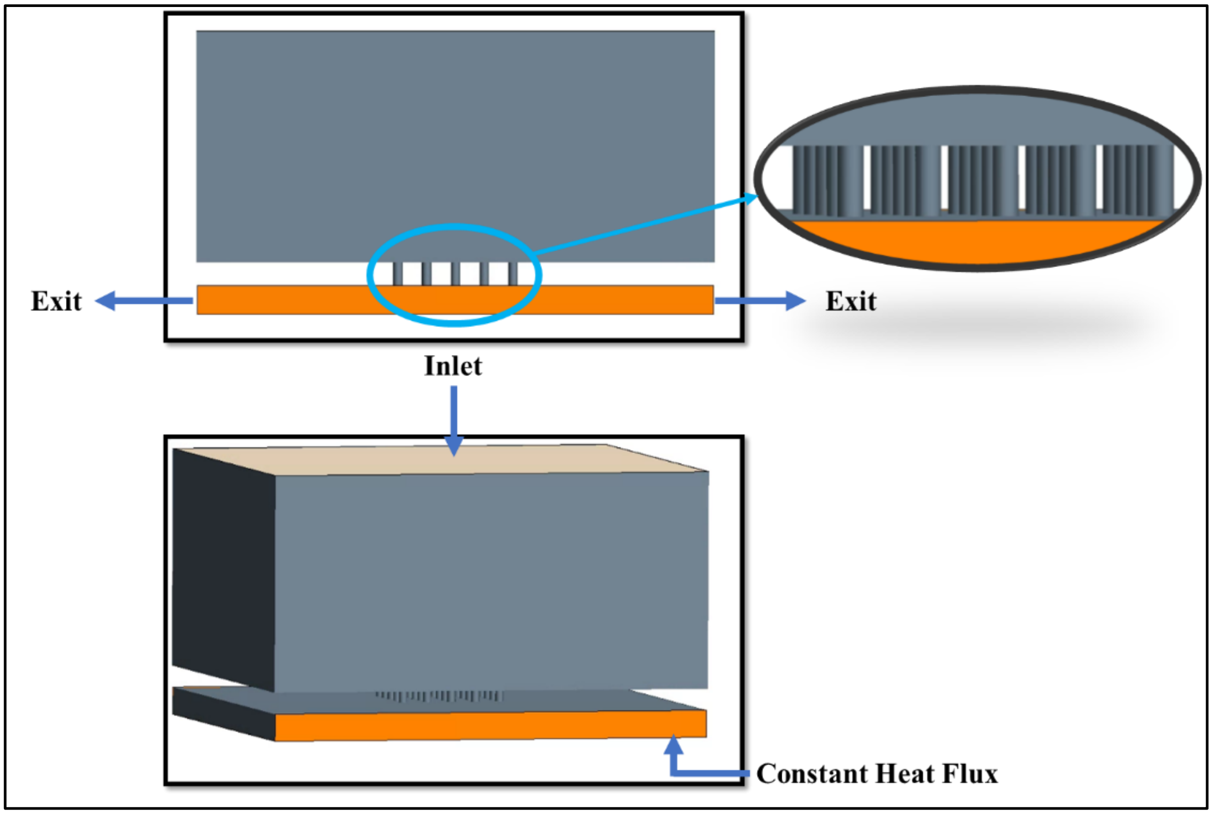

Figure 4-2: Geometry and boundary conditions

4.1.3.1 Meshing Models

A trimmer model is used to generate hexahedral-shaped cells that are distributed in the volumetric domain. The trimmer model is accompanied by a prism layer mesher where prismatic layers are generated near the walls to improve the accuracy of the solution. The reason is that all main flow properties heavily depend on resolving the temperature and velocity gradients near the walls in the viscous sublayer in a flow boundary layer (hydrodynamic and thermal boundary layers). In the case of a coarse mesh, gradients can be miscalculated and therefore, the solution becomes less accurate. The surface is meshed using surface remesher models.

4.1.3.2 Cell Size and Prism Layer Manipulation

The main goal of the mesh independence study is to select a mesh configuration where the solution is not affected by any mesh refining. The bas cell size is manipulated along with the number of prismatic layers near the walls. It is worth mentioning that wall functions are introduced in all generated meshes to enhance the solution of the steeper gradients near the wall. Two-layer all y+ treatment model uses blended wall functions that emulate the low-wall treatment for fine meshes, and the high-wall treatment for coarse meshes. Wall y+ provides a relationship between the friction velocity (u^{+}), absolute distance from the wall to the cell (y), and kinematic viscosity (ν) as described by equation 4-8.

$$y^{+} = \frac{\mathrm{y}\, u^{+}}{\nu} \tag{4-8}$$

In the viscous sublayer, the viscous effects dominate the flow, and Reynolds shear stress is negligible. Turbulence stress dominates the fluid in the logarithmic layer where the flow is fully turbulent. The buffer layer is the transitional region between the viscous-dominated region and turbulence-dominated region as shown in Figure 4-3. It is desired to keep the wall y+ as low as 1 so that the boundary layer is adequately modeled.

The entire computational domain is discretized in a way that smaller cell sizes are generated near the area of interest (bottom chamber) where more turbulence and wall effects are expected, while a relatively coarse mesh is constructed where the flow is routed to the area of interest as shown in Figure 4-4 and Figure 4-5.

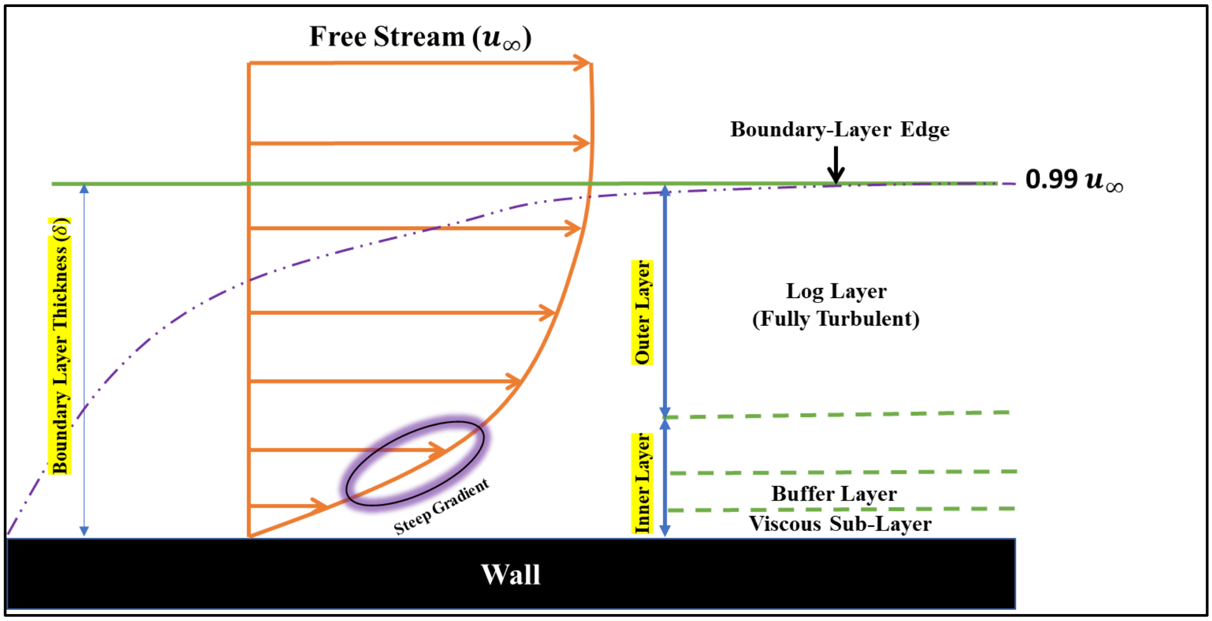

Figure 4-3: Boundary layer and near the wall treatment

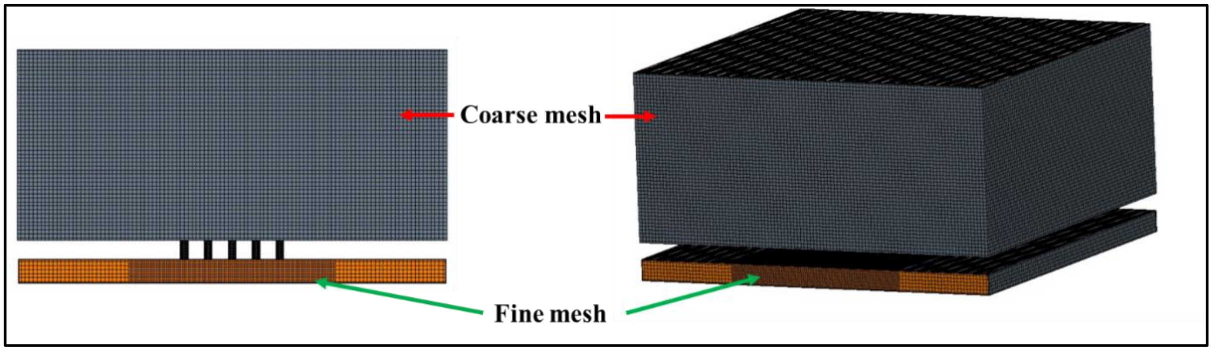

Figure 4-4: Volume mesh with refinement near the area of interest

The mesh is gradually refined as the base size is reduced from 4 mm to 0.8 mm. Temperature profile and maximum wall y+ are captured. The criteria for selecting the mesh are to get the optimum matching in terms of surface temperature and surface temperature profile, and to keep the wall y+ close to 1.

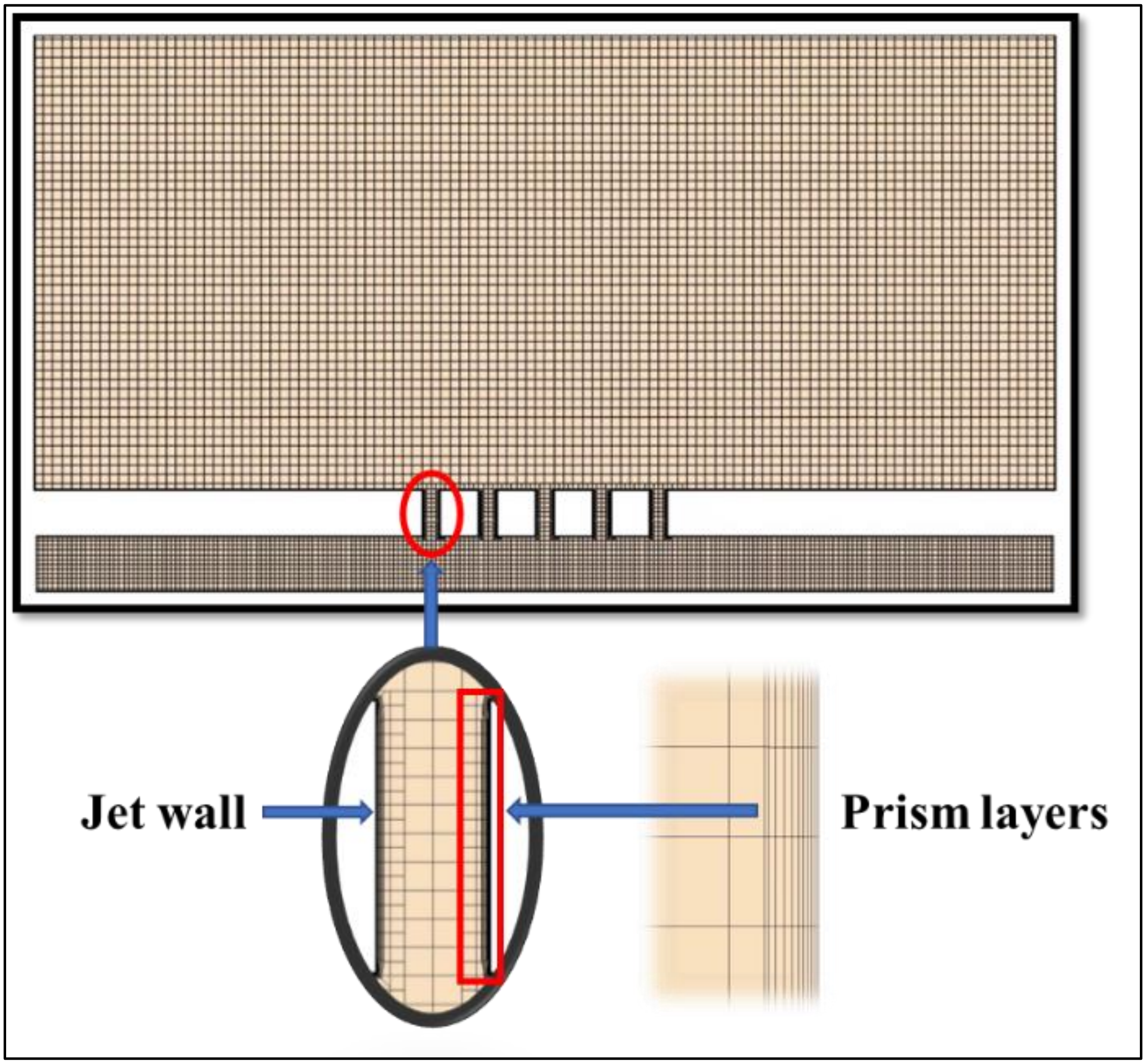

Figure 4-5: Mesh cross-sectional scene and prism layers

In the first trial, mesh refinement is done while using only 2 prismatic layers across all cell sizes. Line average temperature is converted into Line-averaged Nusselt number ($\overline{Nu_L}$) and is compared to the experimental results as shown in Figure 4-6. The profile tends to decrease as the mesh becomes more refined and the smaller cell base sizes of 0.8 mm and 1 mm provide a decent prediction of the temperature profile. However, the profile was still overpredicting the temperature almost everywhere on the surface and the wall y+ was still relatively high.

The other manipulated factor was the number of prismatic layers while keeping the same cell sizes. Better approximation was observed when more prismatic layers are introduced for the same cell size as shown in Figure 4-7. The number of prism layers was increased to 5 and 10. The temperature profile (represented by $\overline{Nu_L}$) was enhanced and the resulting solution from each cell size is closer compared to the case where only 2 prism layers are used. Slight differences were observed across cell base sizes of 2, 1.5, 1, and 0.8 mm.

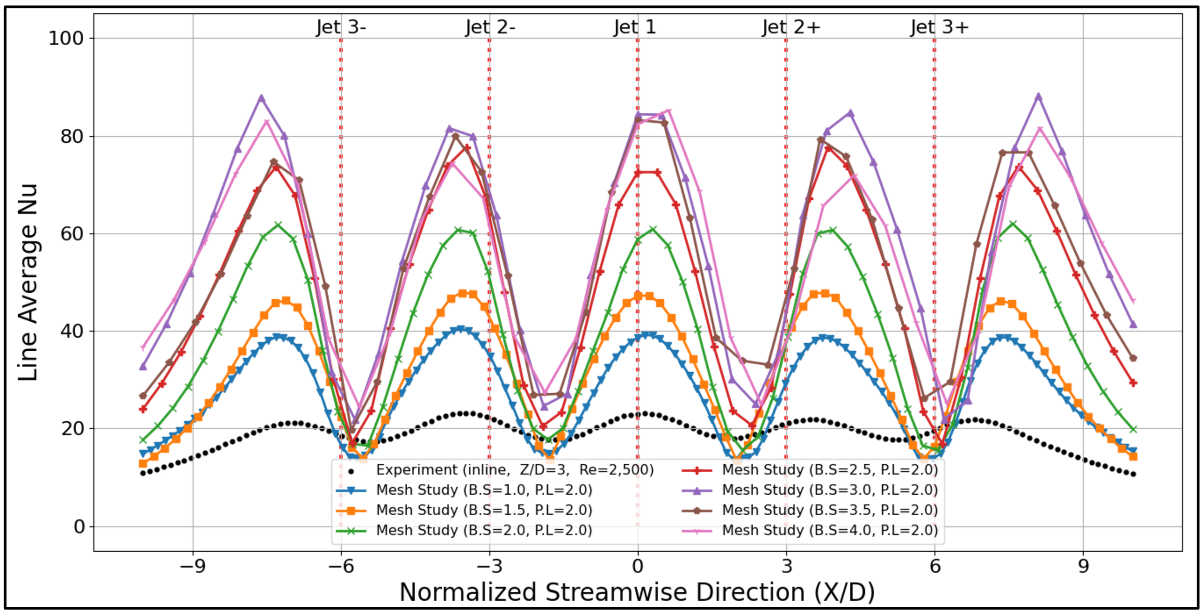

Figure 4-6: $\overline{\boldsymbol{Nu_L}}$ profile for meshes with 2 prism layers

One more step is conducted to check the solution dependency on the mesh. The most refined meshes (base sizes of 2, 1.5, 1, 0.8 mm) with 10 and 12 prism layers are introduced and compared to each other as depicted in Figure 4-8. It can be clearly seen that all meshes provide similar solution and the temperature no longer depend on the mesh. Since higher inlet mass flow conditions are expected to induce more turbulence and therefore increase the wall $Y+$ values and considering the computational time and cost associated with the finer meshes, the mesh with a 2 mm base size and 10 prism layers is selected to simulate all cases. All mesh details are summarized in Table 4-1.

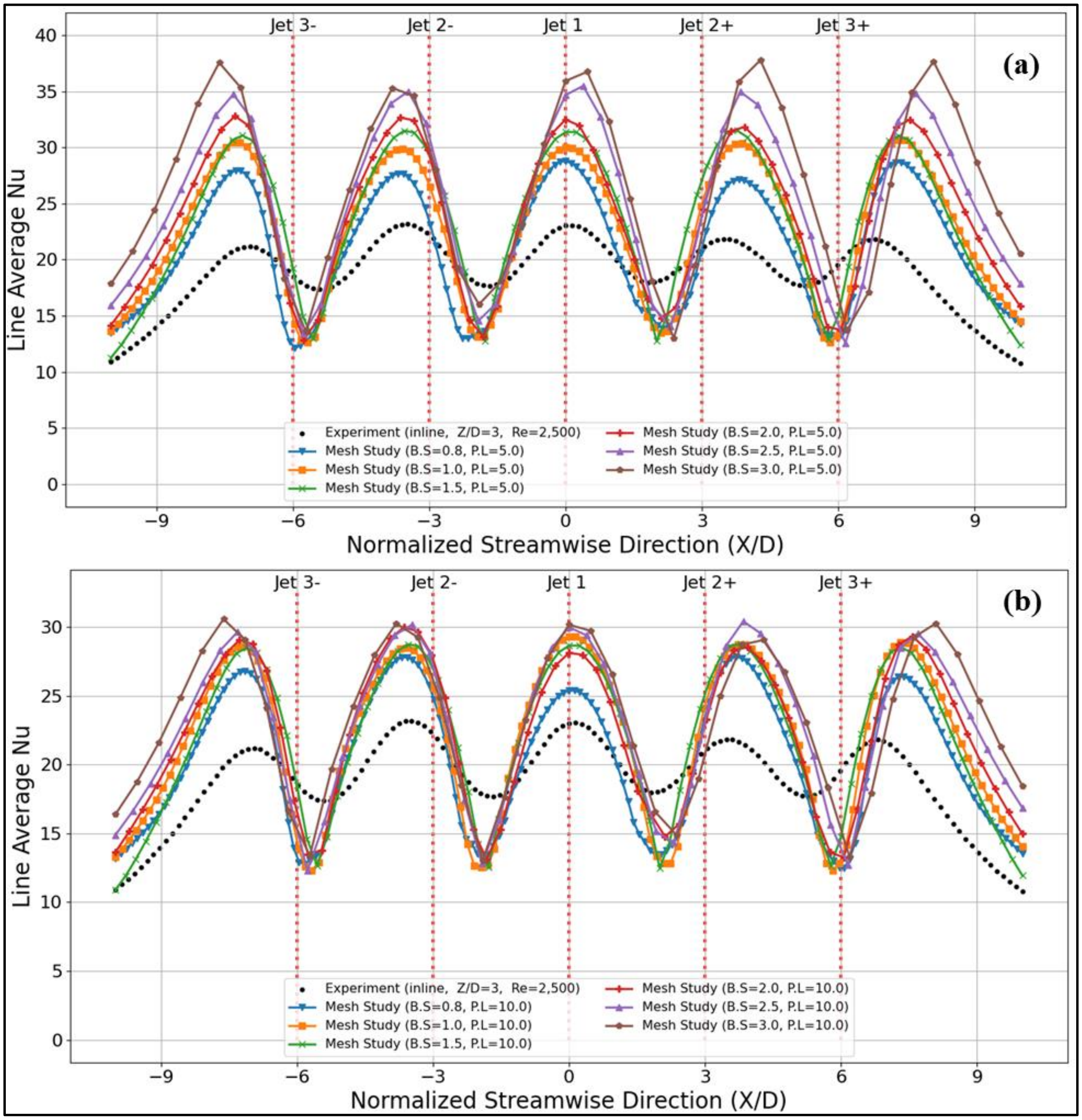

Figure 4-7: $\overline{\boldsymbol{Nu_L}}$ profile for meshes with (a) 5 prism layers, (b) 10 prism layers

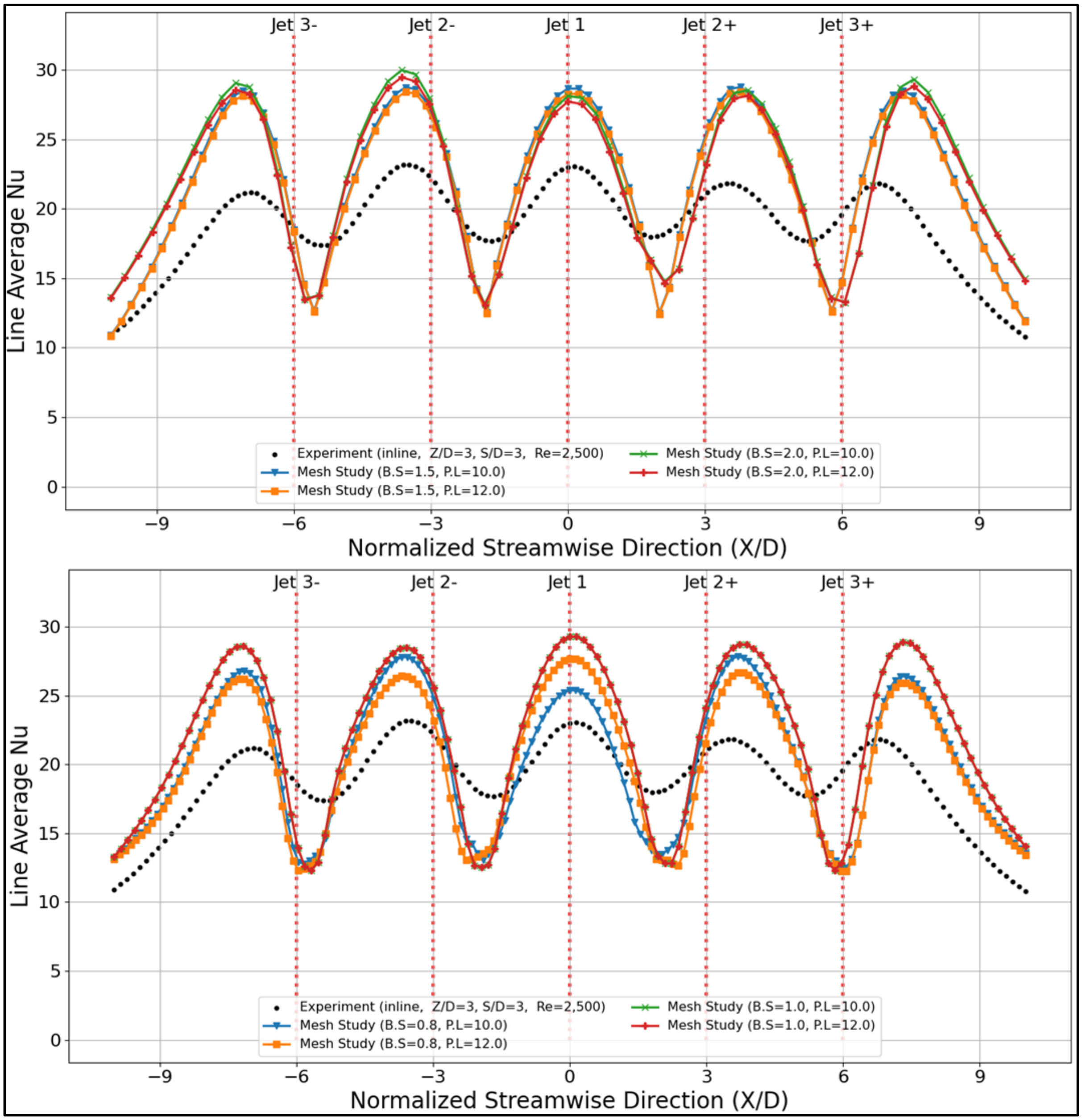

Figure 4-8: Comparison of the finer meshes with 10 and 12 prism layers

Table 4-1: Summary of mesh study

Mesh base size (mm)	**Number of Prism layers**	**Max Wall $Y+$**	**Total cells (Million)**	$\overline{T_s}$ **(°C)**
4.0	2	9.1	0.17	32.95
	5	3.5	0.26	41.57
	10	1.5	0.38	44.32
	12	1.0	0.45	44.52
3.5	2	9.4	0.25	33.40
	5	3.3	0.41	41.59
	10	1.4	0.53	44.01
	12	0.9	0.62	44.37
3.0	2	6.7	0.37	33.02
	5	2.9	0.51	40.87
	10	1.2	0.75	42.65
	12	0.8	0.88	42.90
2.5	2	6.0	0.6	34.52
	5	2.7	0.8	41.63
	10	1.1	1.1	43.07
	12	0.7	1.3	43.41
2.0	2	5.2	1.1	36.95
	5	2.3	1.5	42.47
	10	0.8	2	43.53
	12	0.5	2.2	43.71
1.5	2	4.2	2.5	39.22
	5	2.1	3	42.95
	10	0.7	4	44.02
	12	0.5	4.4	44.18
1.0	2	3.3	7.6	40.92
	5	1.4	8.8	43.31
	10	0.4	10.6	43.96
	12	0.3	11.4	43.96
0.8	2	3.1	14.7	42.86
	5	1.2	16.5	44.73
	10	0.3	19.4	45.20
	12	0.2	20.5	45.40

4.1.3.3 Solution Convergence, Stability, and Stopping Criteria

Solution convergence is rapidly reached as shown in Figure 4-9. The Residuals fall after the 700th iteration and plateau below 10^{-3} (Except for the continuity and energy as they plateau below 10^{-1}). The surface average temperature is also monitored for each iteration for up to 2,500 iterations. At the 200th iteration, it fluctuates around 314.6 K where almost no changes are observed as depicted in Figure 4-10. Although the solution converges fast, the 2,500 iterations will be carried out for all other simulations.

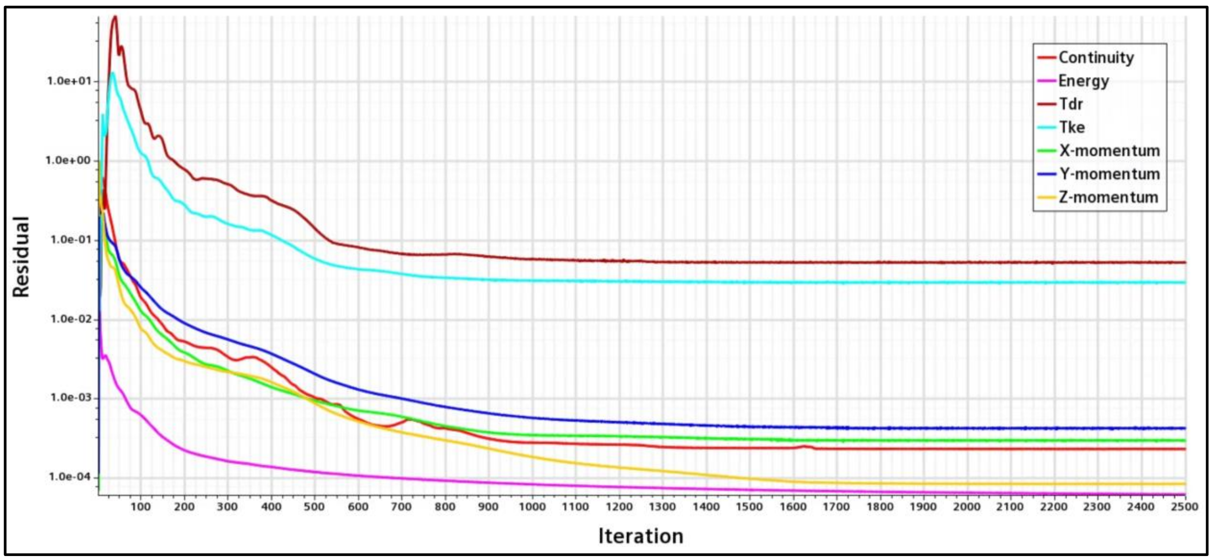

Figure 4-9: Solution residuals

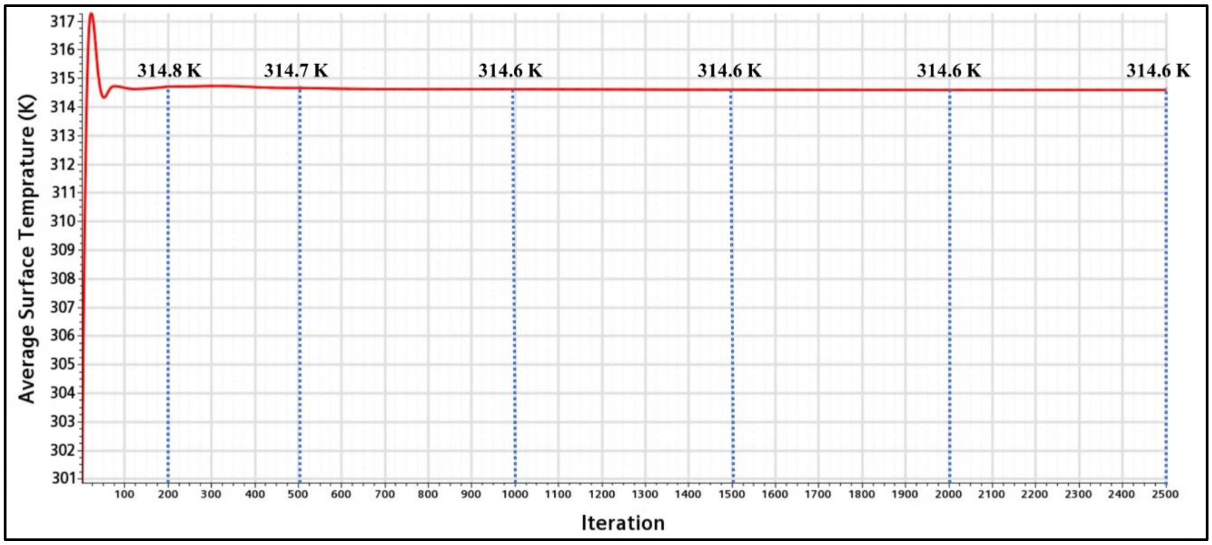

Figure 4-10: Solution progression and stability

4.1.4 Physical Model Conditions and Additional Models

The following models are used to govern the fluid flow and enhance the solution:

- Three-dimensional: designed to work on three-dimensional meshes.
- Gas: single-phase model where air is selected as the domain material.
- Constant density: density is defined as constant and does not change with temperature or any other factors.
- Mesh gradients: Used in several places in the volume mesh
- Segregated flow: invokes the segregated solver to solve each of the momentum equations in turn, one for each dimension. The momentum and continuity are linked with a predictor-corrector approach.
- Segregated fluid temperature: Solves the total energy equation with temperature as the solved parameter.

- Cell quality remediation identifies the poor-quality cells and then modifies the gradients in these cells and the neighbor cells to improve the solution robustness.
- Turbulent flow.
- Steady flow.
- k-ε turbulence model.
- Realizable k-ε turbulence model.
- Wall distance.
- Two-layer All y+ wall treatment (hybrid near wall treatment): a wall treatment is the set of near-wall modelling assumptions. Hybrid treatment that attempts to emulate the high- wall treatment for coarse meshes and the low-y+ wall treatment for fine meshes.

4.2 Baseline Model

The baseline nozzle plate model was created as an inline array of 5×5 that forms 25 total jet holes. A constant hole diameter (D) was set to be 4 mm with a 1.5 mm length as depicted in Figure 4-11. The inline configuration implies that each row (or column) is equally spaced in both directions. These directions are noted as streamwise (X) and spanwise direction (Y). The streamwise direction is the axis where the flow travels towards the test rig exit after impinging the target plate, whereas the spanwise direction is the axis where the flow is blocked by walls. The spacing between each consecutive row or column was normalized against the jet diameter and set at three times the diameter (S = $3D$). The jet height (Z) is the distance between the jet tip and the target plate was normalized against the jet diameter and was set at three times the D (Z=$3D$). Airflow was experimentally varied to achieve Jet Reynolds numbers (Re_j) of up to 4,500. Jet Reynolds number

(Re_j) was calculated assuming the main flow in the feeder piped is distributed equally across all 25 holes. CFD simulations were carried out to cover a higher Re_j of up to 10,000.

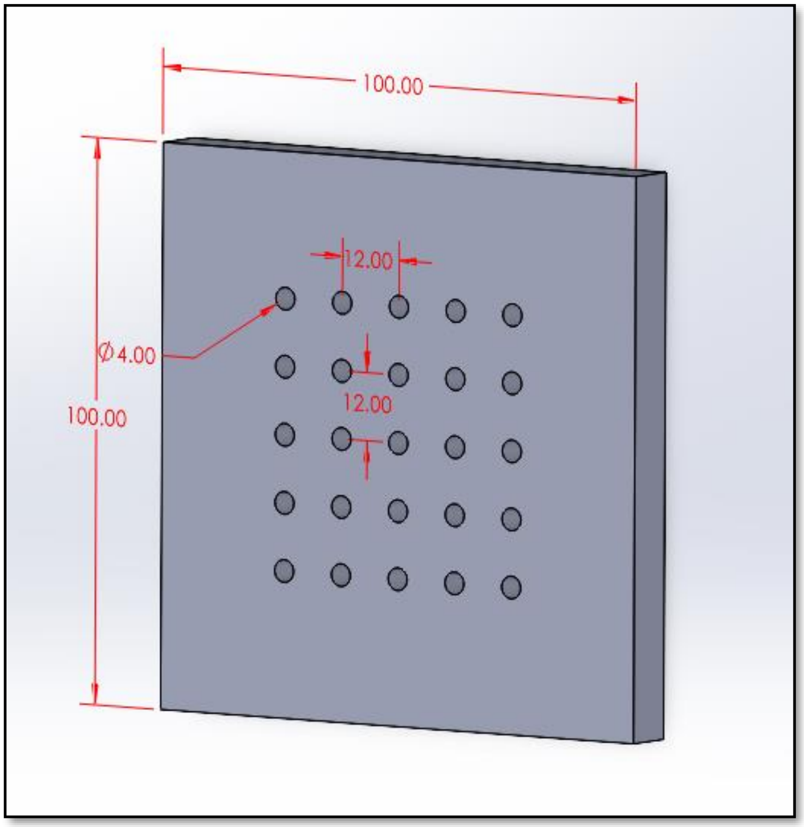

Figure 4-11: Baseline nozzle plate design and dimensions (in mm)

4.3 Validation, Surface Averaged, and Line Averaged Approximations

As an example, the operating conditions of Re_j of 4,500 and a jet-to-target spacing (Z/D= 3) were considered. For this case, a comparison of the processed experimental and numerical heat maps can be seen in Figure 4-12, while some other selected heat maps can be found through APPENDIX A to APPENDIX D sections. Some distortion can be seen in the experimental heat map due to the continuous rapid heating-cooling procedures. The temperature in the intermediate locations between the jets is higher in the CFD compared to the experiment. This is because, in the experiment, heat is generated inwardly as the busbars are heated first and then the electric current moves towards the center of the target plate. On the other hand, a constant heat flux condition that was implemented in the CFD implies a uniform heat generation in each computational cell.

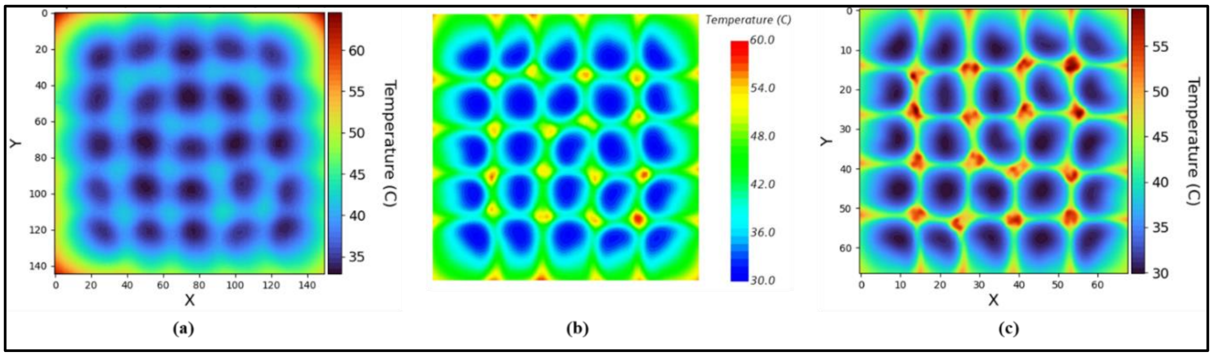

Figure 4-12: Heat maps for $\boldsymbol{Re_j}$ = 4,500 and $\boldsymbol{Z/D}$ = 3, (a) processed exp, (b) raw CFD, and (c) processed CFD

The experimental results were validated using the surface average and the line average techniques. In the surface average, each point (pixel in experiment or cell in CFD) on the target plate is averaged, yielding a single temperature value ($\overline{T_s}$) and then used to calculate the surface averaged Nusselt number ($\overline{Nu_s}$). In the line average technique, $\overline{Nu_L}$ was evaluated from the average temperature for each grid column along the spanwise direction. In both techniques, Nu was evaluated from equation 3-10.

A comparison between the experiment and the CFD in terms of $\overline{T_s}$ and $\overline{Nu_s}$ showed that the CFD numerical solver approximated the temperature with a good match to the experiment where the errors in $\overline{T_s}$ is 5.36% as listed in Table 4-2. $\overline{Nu_L}$ plot is depicted in Figure 4-13.

Table 4-2: $\overline{T_s}$ and $\overline{Nu_s}$ comparison for Re_j = 4,500 and Z/D = 3

Case	$\overline{T_s}$ (°C)	$\overline{Nu_s}$
Experiment	40.08	27.48
CFD	37.93	35.04
$\overline{T_s}$ (E%)	**5.36**	

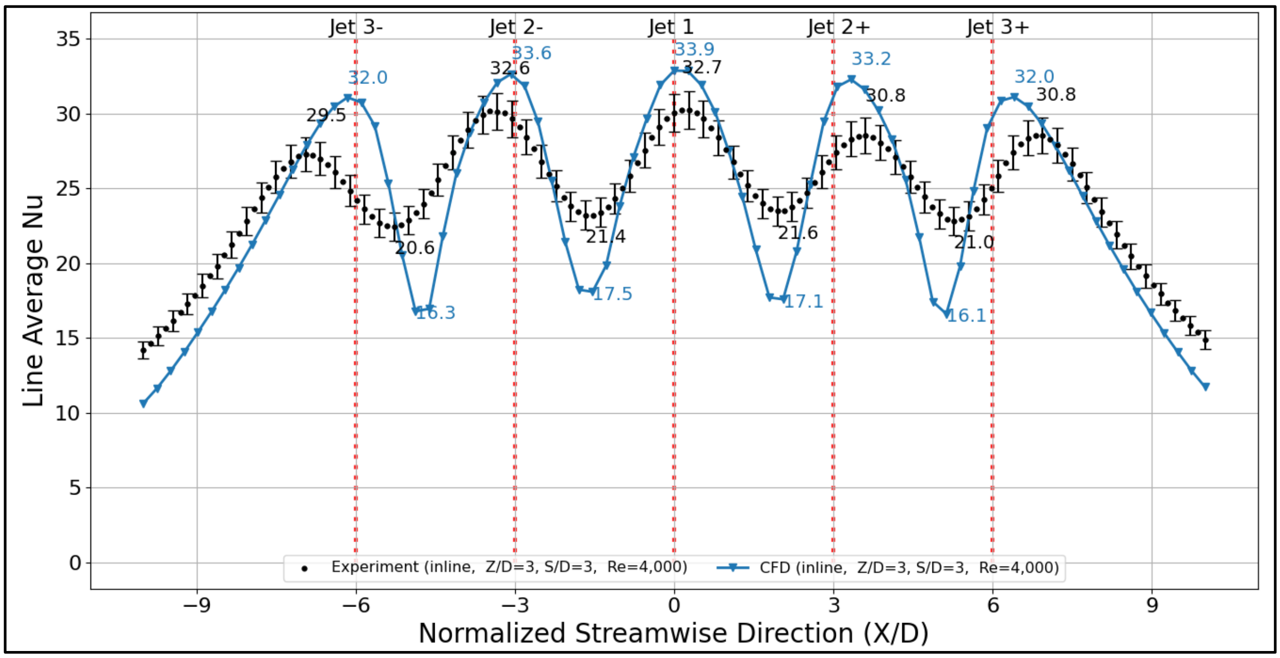

Figure 4-13: Experimental and CFD $\overline{Nu_L}$ for Re_j = 4,000, and Z/D = 3

CHAPTER 5: GEOMETRICAL ANALYSIS: REYNOLDS NUMBER, STAND-OFF DISTANCE, AND JET ARRAY EFFECTS

This chapter provides details of different geometrical considerations on an array of jet impingements. The main goal of this chapter is to provide a complete guide to the effect of the influencing parameters that may guide the design and help in understanding the physics behind all observations.

5.1 Effect of Reynolds Number (Re_j) on Nusselt Number (Nu)

The Reynolds number ($\mathrm{Re_j}$) was changed by varying the main airflow and was calculated assuming the flow is equally distributed across all holes, as noted in equation 3-9. Regardless of the experimental conditions and configuration, the increased $\mathrm{Re_j}$ will ultimately result in heat transfer enhancement represented by the Nusselt number. The highest local Nusselt number (Nu) was observed at the stagnation points underneath the jet cores as shown in Figure 5-1. This pattern indicates more active cooling at the impingement jets' impact locations. The shifting in the Line-averaged Nusselt number $\overline{\mathrm{Nu_L}}$ secondary peaks is due to the crossflows that interact with the jet core and shift it away downstream (Jet 2+ and Jet 2-), as shown in Figure 5-2. Cooling degradation can also be noticed for the jets far from the middle row of jets (Jet 3+ and 3) as an effect of the crossflow accumulation. Furthermore, Z/D = 3 and 7.5 also followed the same trend. $\overline{\mathrm{Nu_L}}$ plots can be found through APPENDIX E to APPENDIX H. Table 5-1 summarizes the effect of $\mathrm{Re_j}$ on the cooling performance. All reported results follow the same pattern and the CFD approximations are in good match with the experimental results with a maximum $\overline{T_s}$ error of 11.66 % (Case of Inline, $\mathrm{Re_j}$ = 3,000, and Z/D = 5).

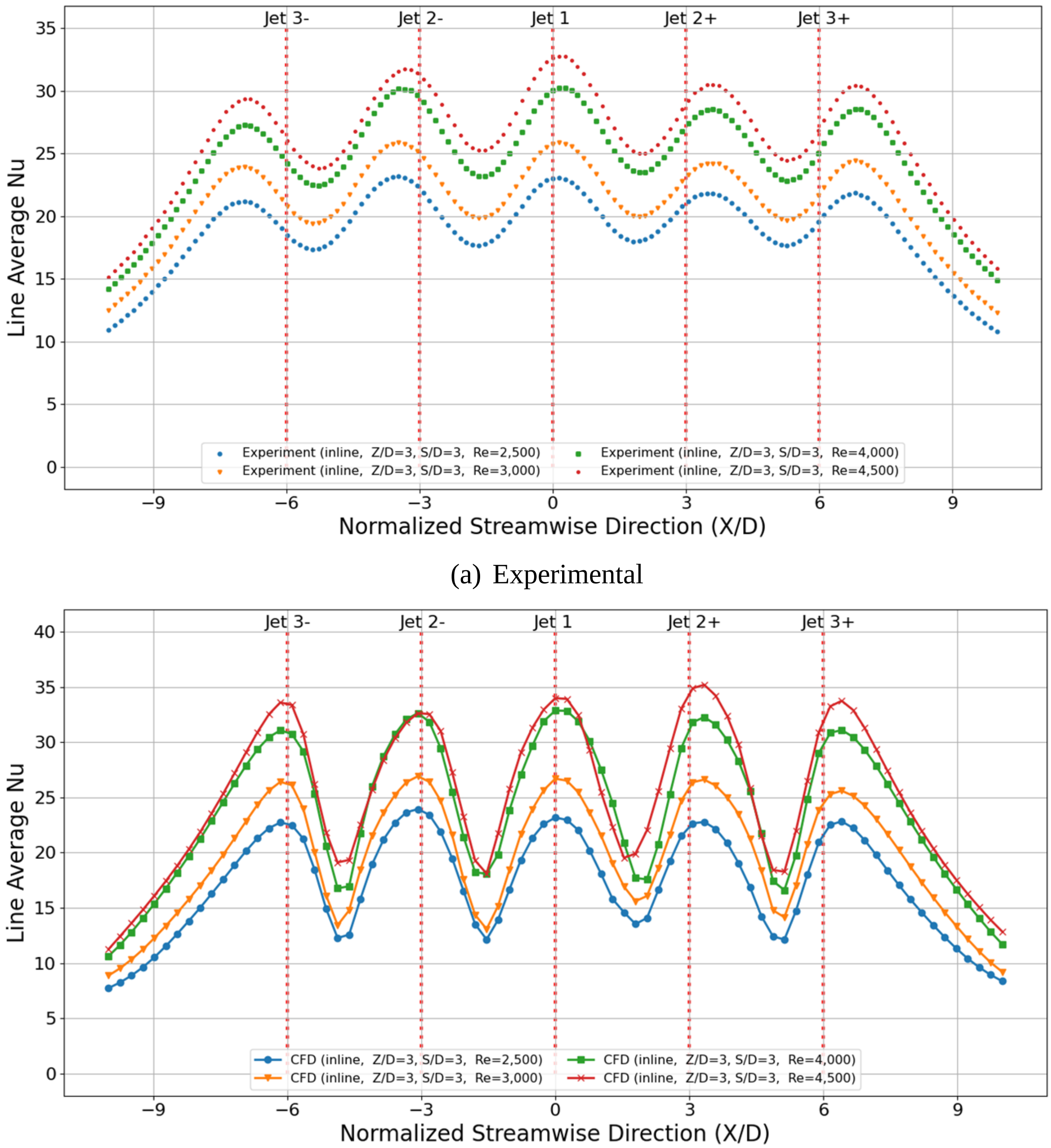

(b) CFD

Figure 5-1: Experimental and CFD $\boldsymbol{Re_j}$ effect on $\overline{\boldsymbol{Nu_L}}$ for $\boldsymbol{Re_j}$ = 2,500 – 4,500, and $\boldsymbol{Z/D}$ = 3

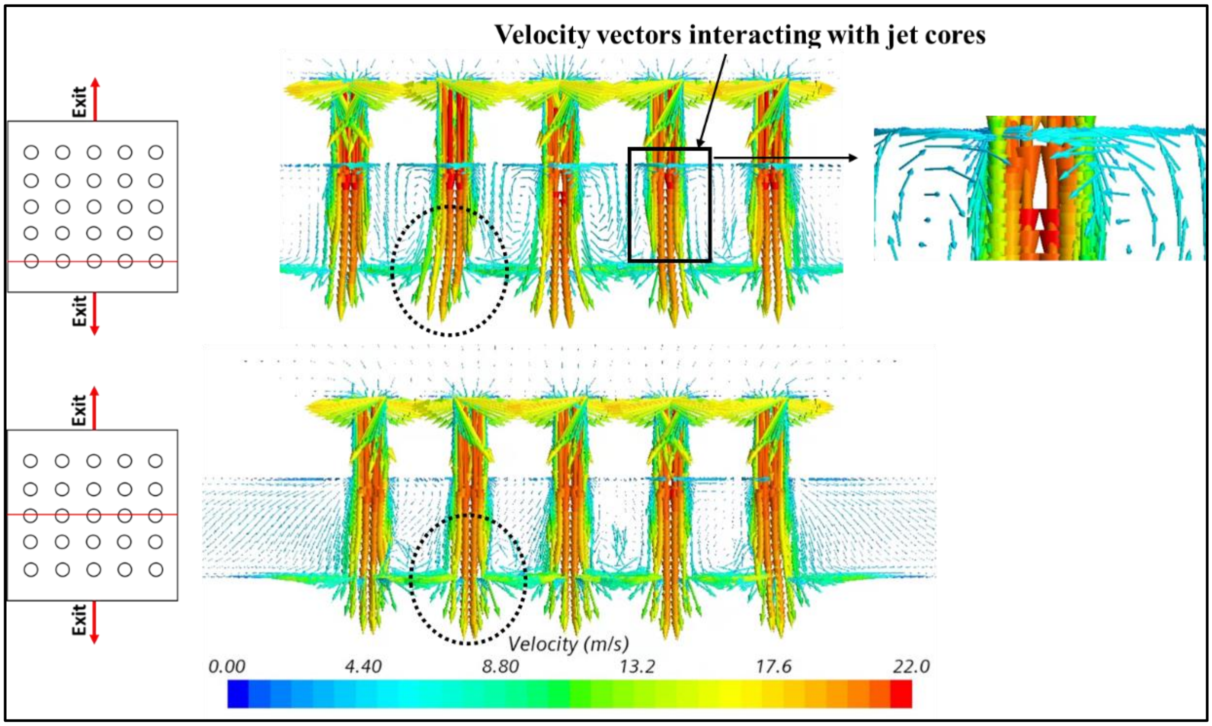

Figure 5-2: Velocity vectors interacting with jet cores for $\boldsymbol{Re_j}$ = 4,000 and $\boldsymbol{Z/D}$ = 3

Table 5-1: $\overline{T_s}$ and $\overline{Nu_s}$ comparison summary for inline configuration at different $\boldsymbol{Re_j}$ and $\boldsymbol{Z/D}$

Z/D	Re_j	Exp $\overline{T_s}$ (C°)	CFD $\overline{T_s}$(C°)	Exp $\overline{Nu_s}$	CFD $\overline{Nu_s}$	$\overline{T_s}$ E%
3.0	4,500	40.08	37.93	27.48	35.04	5.36
	4,000	41.13	38.60	25.72	33.30	6.15
	3,000	43.80	41.23	22.10	27.89	5.87
	2,500	46.14	43.54	19.76	24.43	5.64
5.0	4,500	43.56	40.01	22.07	30.09	8.15
	4,000	45.45	41.29	19.95	27.63	9.15
	3,000	49.75	43.95	16.48	23.38	11.66
	2,500	53.47	47.36	14.34	20.02	11.43
7.5	4,500	45.77	41.91	19.26	25.89	8.43
	4,000	48.80	43.57	16.69	23.31	10.72
	3,000	53.71	49.33	13.81	17.63	8.15
	2,500	58.18	56.46	11.93	13.84	2.96

To correlate the Nusselt number with the Reynolds number, a power regression model was used for the entire range of Reynolds numbers between 2,500 to 12,500. The regression model assumes that the Nusselt number is only a function of the Reynolds and Prandtl numbers. Since the Prandtl number is not expected to be sensitive to the range of temperature in this study, equation 5-1 and Figure 5-3 can represent the correlation as :

$$\mathrm{Nu} = \mathrm{C}\, Re^{m} \qquad \text{5-1}$$

Fitting the surface averaged Nusselt number against the Reynolds number with a power regression model showed that the exponent m equals a value of 0.5673 while the multiplication coefficient equals 0.1934. These results match with the literature reported by Weigand and Spring in their review paper [88].

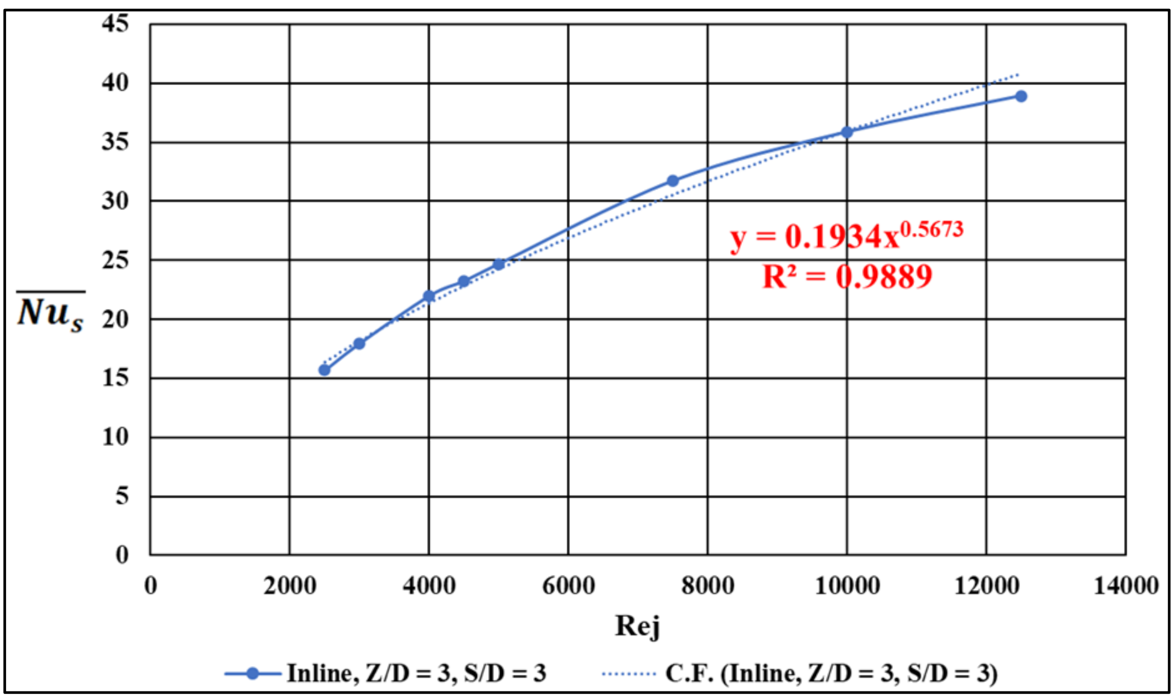

Figure 5-3: Power regression model for $\boldsymbol{Re}$ effect

5.2 Jet-to-Target Spacing Effect

The vertical distance between the tip of the nozzle and the target plate significantly affects the heat transfer performance. As the jet path increases, it allows more surrounding air to entrain the main jet stream, losing the jet's momentum. The entrainment increases and becomes more severe at higher Reynolds numbers. Short stand-off distances (less than three) were not considered because having a fully developed flow is unlikely to be guaranteed. In the fully developed flow jets, the boundary layer grows enough such that the effect of the walls becomes less noticeable. Also, there will be difficulty in conducting the experiment due to the mounting of the target plate at a shorter distance that is close to the nozzle plate.

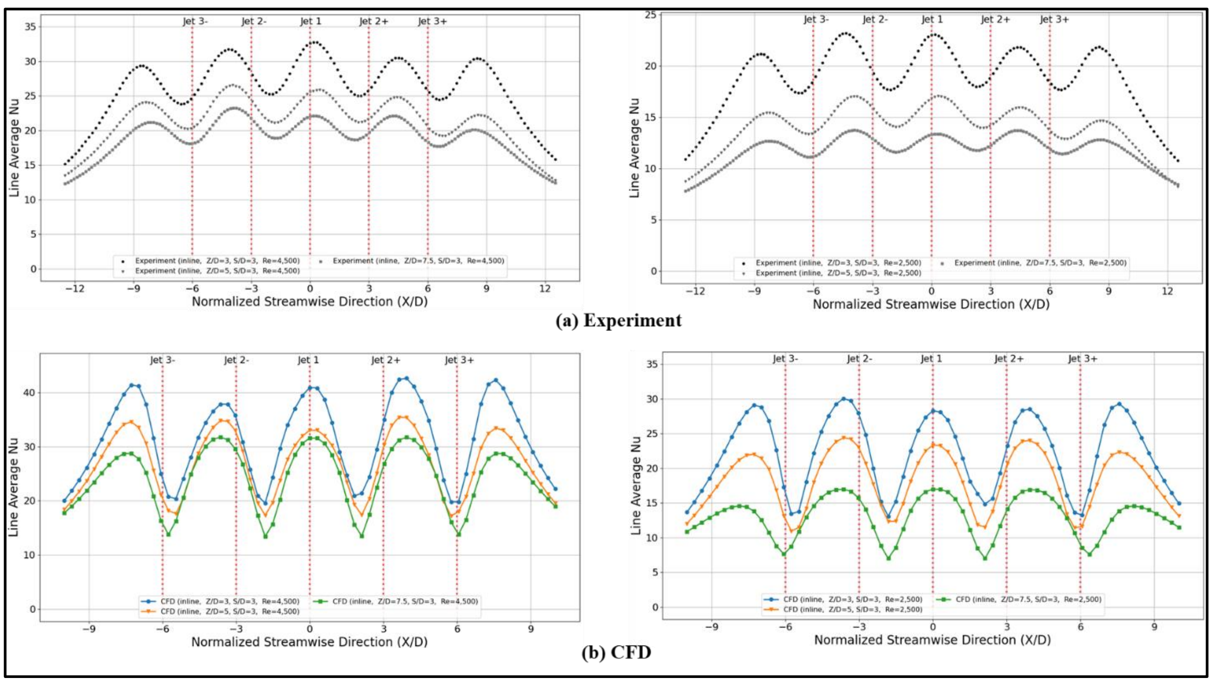

Figure 5-4: Experimental and CFD $\boldsymbol{Z/D}$ effect on $\overline{\boldsymbol{Nu_L}}$ for $\boldsymbol{Re_j}$ = 4,500 and 2,500

The effect of varying jet-to-target spacing was experimentally investigated by considering three Z/D values of 3, 5, and 7.5. A constant Re_j was introduced across all Z/D to examine the influence of the stand-off distance. As an example, $\overline{\mathrm{Nu}_\mathrm{L}}$ plots for inline configuration at $\mathrm{Re_j}$ of 4,500 are presented in Figure 5-4, while the rest $\mathrm{Re_j}$ values can be found in APPENDIX G and APPENDIX H.

The results generally showed a slight decrease in $\overline{\mathrm{Nu}_\mathrm{L}}$ for the same flow rate as the Z/D increases. Jet active cooling regions were shifted further downstream as the Z/D increased due to the higher crossflow accumulations that interact more with the jet cores and each pair of jets prior to the impingement. Also, jet deflections become more noticeable as Re_j increases. The jet deflection observation was made by comparing velocity contours at different Z/D. Figure 5-5 compares between Z/D of 3, 5, 10, and 15 where higher deflections occurred at Z/D 10 and 15 while little deflections at shorter Z/D (3 and 5). A summary of the Z/D effect is tabulated in Table 5-2 and Figure 5-6 for inline jet configurations.

Table 5-2: $\overline{\boldsymbol{T_s}}$ and $\overline{\boldsymbol{Nu_s}}$ comparison summary for inline configuration at different $\boldsymbol{Re_j}$ and $\boldsymbol{Z/D}$

$\boldsymbol{Re_j}$	$\boldsymbol{Z/D}$	**Exp** $\overline{\boldsymbol{Nu_s}}$	**CFD** $\overline{\boldsymbol{Nu_s}}$
4,500	3.0	27.48	35.04
	5.0	22.07	33.30
	7.5	19.26	27.89
4,000	3.0	25.72	24.43
	5.0	19.95	30.09
	7.5	16.69	27.63
3,000	3.0	22.10	23.38
	5.0	16.48	20.02
	7.5	13.81	25.89
2,500	3.0	19.76	23.31
	5.0	14.34	17.63
	7.5	11.93	13.84

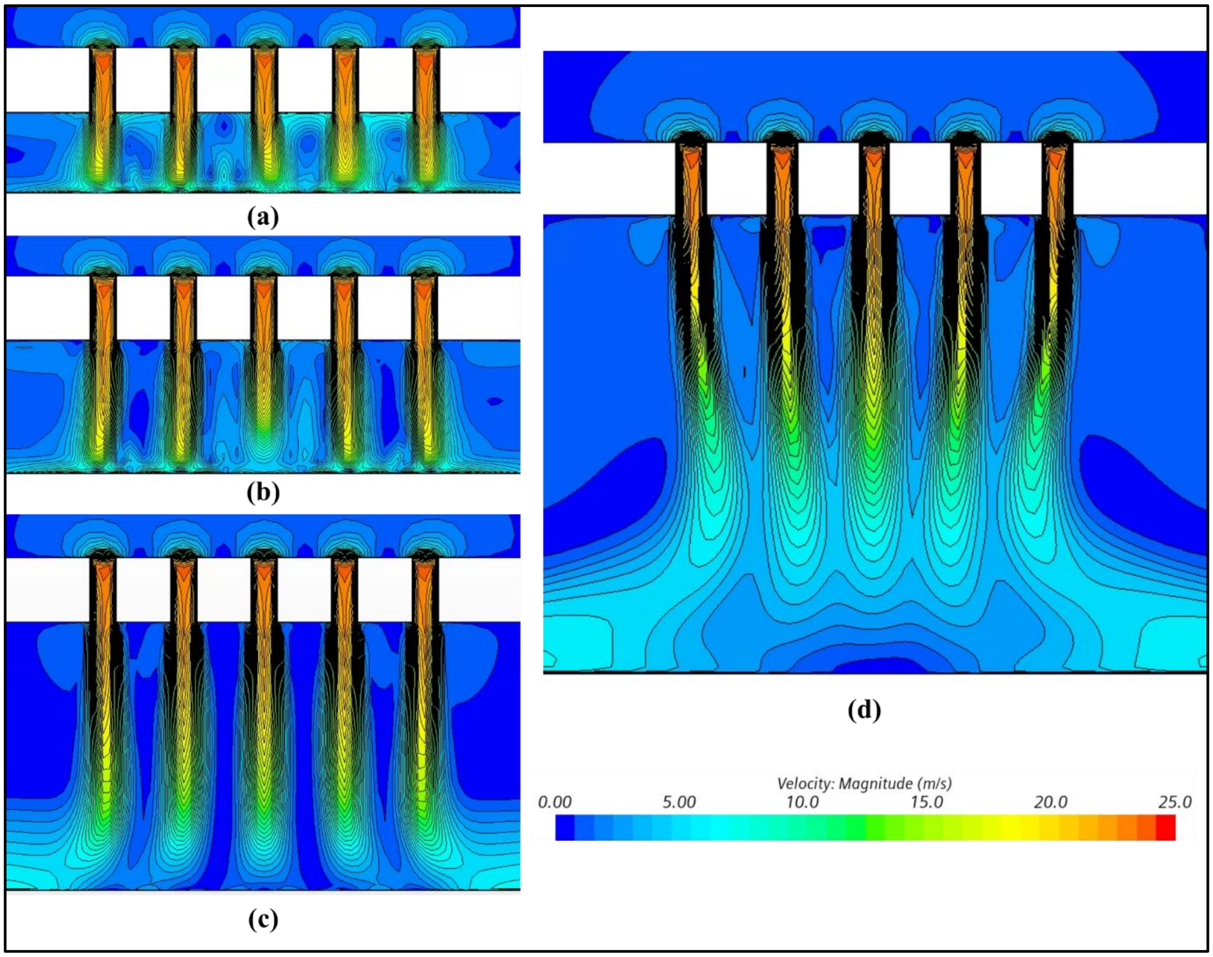

Figure 5-5: Jet redirection represented by velocity contours at $\boldsymbol{Z/D}$ of (a) 3D, (b) 5D, (c) 10D, and (d) 15D

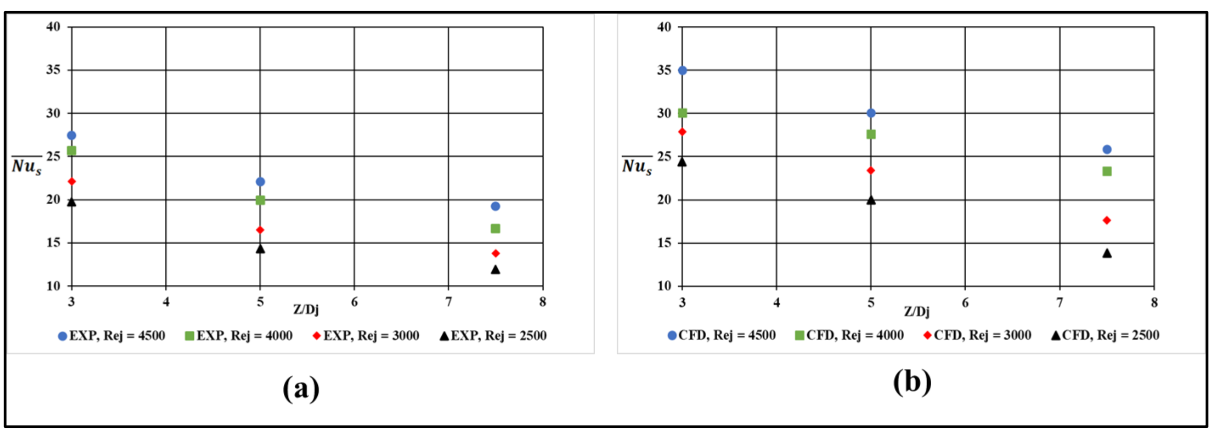

Figure 5-6: $\boldsymbol{Z/D}$ effect on $\boldsymbol{\overline{Nu_s}}$ for $\boldsymbol{Re_j}$ = 2,500 – 4,500, (a) experimental, (b) CFD

5.3 Jet Configuration Effect

This study compares the inline and the staggered arrangement of the 25 jets. A schematic of the nozzle plate for both cases can be found in Figure 5-7. Similar operating conditions of Reynolds number and stand-off distance were used to eliminate any variability in these factors. For the staggered array, similar observations to the inline configurations have been made in regard to the Reynolds number and the stand-off distance. The increase in Reynolds and the decrease in the stand-off distance each attributed to higher Nusselt number values. Therefore, the effects of Z/D and $\mathrm{Re_j}$ are not discussed in this section. The Surface averaged Nusselt number results for the experiment and the CFD are summarized in Table 5-3.

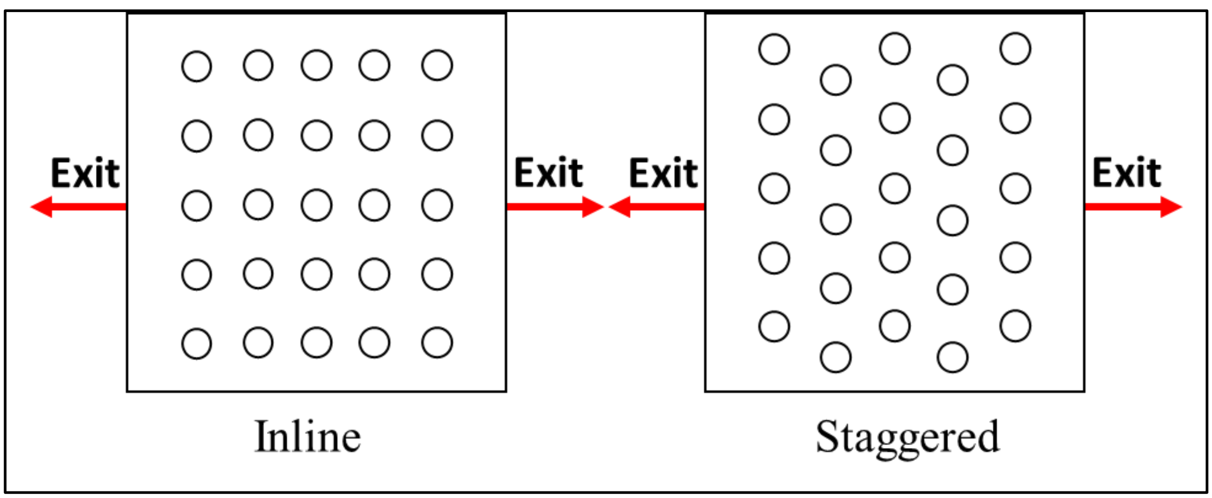

Figure 5-7: Inline and staggered arrays nozzle plates

With a margin of error of up to 11.66%, there was a good agreement between the experimental and the numerical results. Slight differences can be noticed when the staggered array is compared to the inline one. A Line-averaged Nusselt number comparison between the inline and the staggered jet arrays is depicted in Figure 5-8.

Table 5-3: $\overline{T_s}$ and $\overline{Nu_s}$ comparison summary for staggered configuration at different Re_j and Z/D

Z/D	Re_j	Exp $\overline{T_s}$ (C°)	CFD $\overline{T_s}$(C°)	Exp $\overline{Nu_s}$	CFD $\overline{Nu_s}$	$\overline{T_s}$ E%
3.0	4,500	42.34	40.66	23.69	30.83	5.36
	4,000	43.42	41.88	22.43	28.79	6.15
	3,000	47.13	45.57	18.73	23.91	5.87
	2,500	50.28	48.65	16.55	20.94	5.64
5.0	4,500	41.67	42.89	24.69	26.75	8.15
	4,000	45.05	44.39	20.37	24.77	9.15
	3,000	49.32	48.06	16.84	20.87	11.66
	2,500	53.72	51.33	14.30	18.16	11.43
7.5	4,500	46.12	44.35	19.06	23.02	8.43
	4,000	46.77	46.09	18.54	20.95	10.72
	3,000	51.13	51.67	15.36	16.40	8.15
	2,500	55.07	58.52	13.33	12.99	2.96

The Nusselt number profile shows that the inline configuration performs slightly better than the staggered arrays, especially at shorter stand-off distances. This is due to the more protection of the jets from the upstream row of jets as the spent air crossflow is given less distance to accelerate before striking the next row of jets. In the staggered arrangement, the influence of the crossflow is higher as the crossflow accelerates and directly impacts the jets.

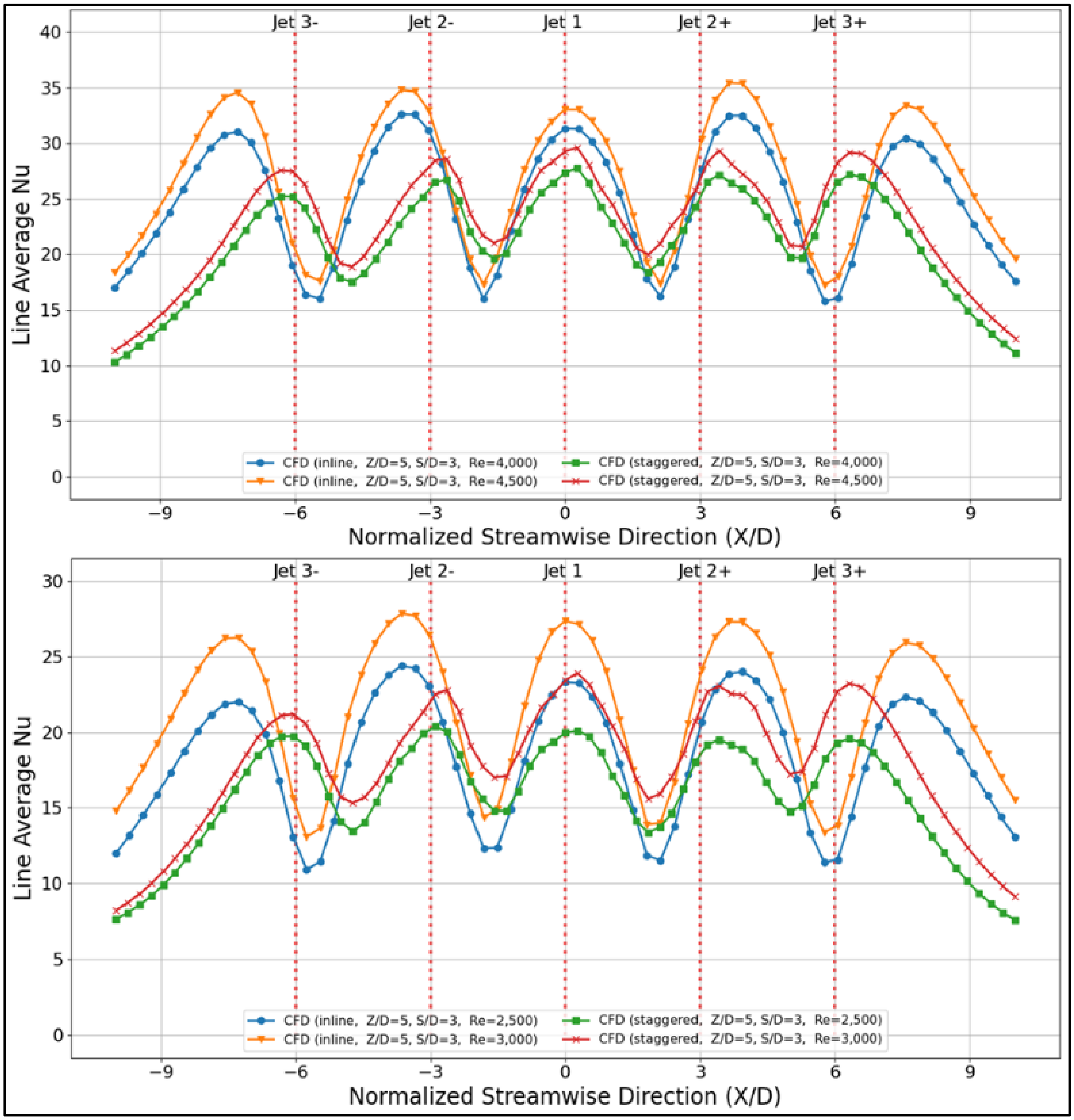

Figure 5-8: Inline and staggered arrays $\overline{\boldsymbol{Nu_L}}$ comparison for $\boldsymbol{Re_j}$ = 2,500 – 4,500

5.4 Jet to Jet Spacing Effect

The jets are distributed as a rectangular array of equal jet-to-jet spacing along both the streamwise and the spanwise directions in an inline configuration. The jet spacing is defined as the distance between each of two consecutive jet centers as shown in the schematic in Figure 5-9. Two methods are explored to investigate the jet-to-jet spacing effect. These methods were conducted either by varying the target plate area and separating the nozzles further apart or by fixing the area while introducing more nozzles with a smaller diameter at a constant flow rate.

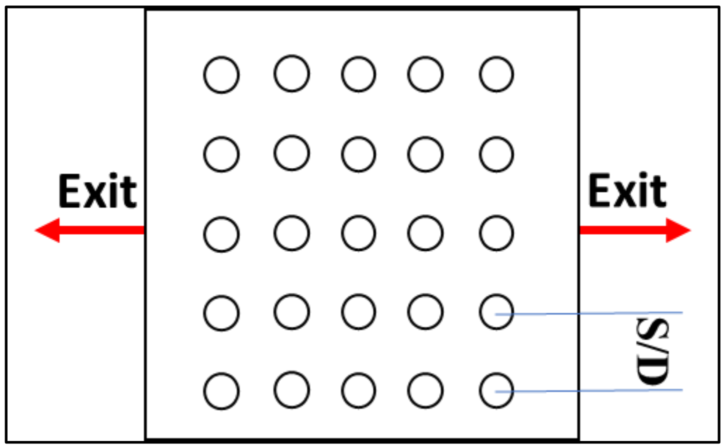

Figure 5-9: Schematic of jet-to-jet spacing for inline nozzle plate

5.4.1 Variable Target Area

In the variable target area, the area of the target plate is enlarged as the jets are separated further from each other. Three scenarios have been investigated with normalized jet-to-jet spacings of 2, 3, and 5, as summarized in Table 5-4.

Table 5-4: Open area ratios for different S/D spacings

S/D Case	Target Area Covered (L × W) in mm	A_o
2	48 × 48	0.136
3	72 × 72	0.061
5	120 × 120	0.022

The open area ratio (A_o) is defined as the ratio of the total area of the nozzles that covers a specific target plate area. From the Line-averaged Nusselt number profiles shown in Figure 5-10. As the open area ratio decreases, the heat transfer performance decreases because of the larger area that the nozzles cover. Comparing the stagnation Nusselt number for all cases shows that at S/D = 2, the Nusselt number peaked slightly below 30, while it did not exceed a value of 25 for both S/D of 3 and 5. It is recommended to optimize this parameter as decreasing the jet-to-jet spacing might cause more severe jet interaction that eventually weakens the coolant momentum.

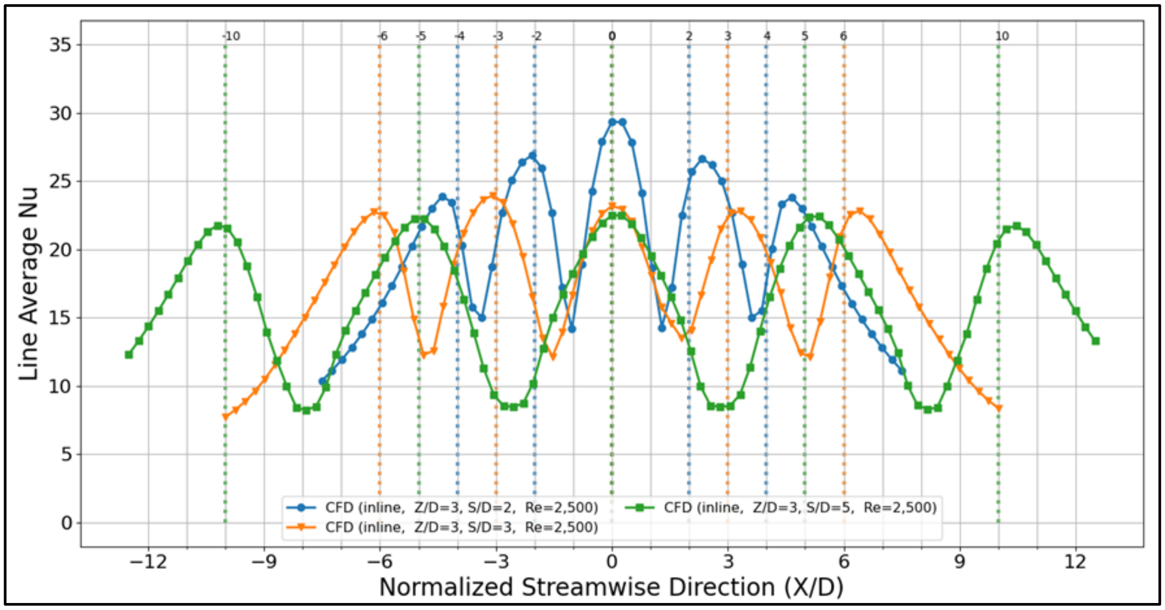

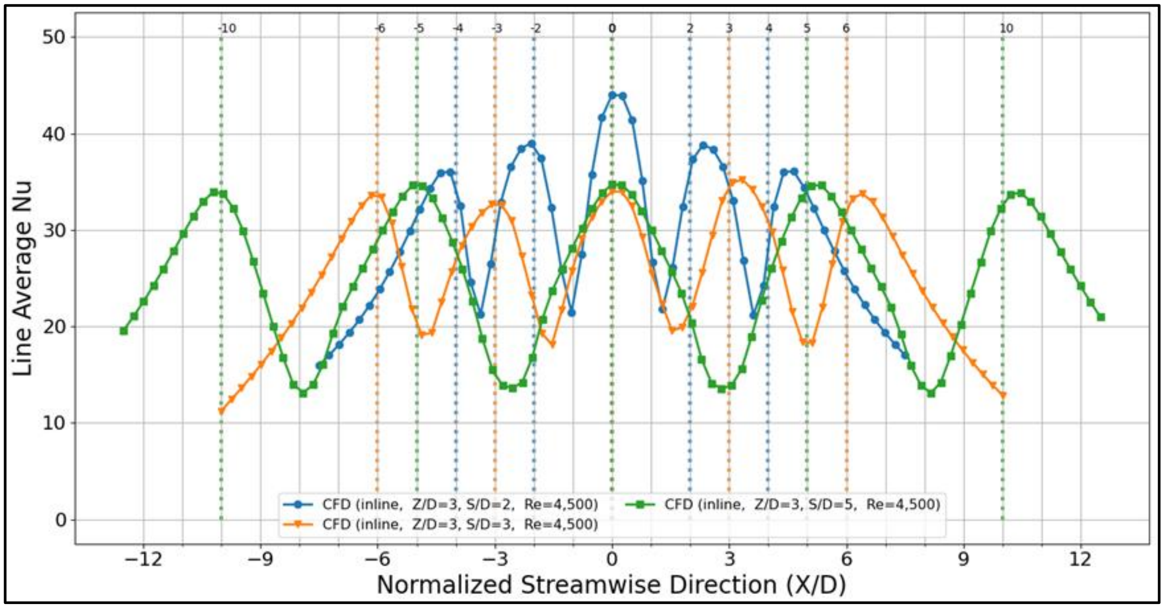

Figure 5-10: $\overline{\boldsymbol{Nu_L}}$ profiles for jet-to-jet spacing comparison at $\boldsymbol{Z/D}$ = 3, $\boldsymbol{Re_j}$ = 2,500 and 4,500

5.4.2 Variable Number of Jets with Constant Air Flow

The same open area ratio (A_o) was kept constant while the jet-to-jet spacing was changed by adjusting the nozzle diameter. As an example, to achieve a jet-to-jet spacing of 2, the entire area of the target plate was utilized to equally distribute the nozzles in a way where the distances between the jet centers is also equal to the distance from the side jets' centers to the sides of the target plate. This design criteria required adjusting the distribution than that was used in the previous section. As a result, a square array of 25 jets represented the S/D of 4, a square array of 36 jets represented the S/D of 5, and a square array of 81 jets represented the S/D of 2. Since the flow rate was kept constant, there was differences in Reynolds number as shown in Table 5-5.

Table 5-5: Variable number of jets design

Array	**Jet-to-jet spacing (S/D)**	Re_j
5×5	4	9,720
6×6	3	6,750
9×9	2	3,000

For the same flow rate, the heat transfer performance increased when the jet array is less packed. The comparison can be claimed unfair as Reynolds number was becoming a factor. The main finding out of this section was that a more uniform surface temperature was observed when the jets were more packed. The Line-averaged Nusselt number for the abovementioned cases is shown in Figure 5-11.

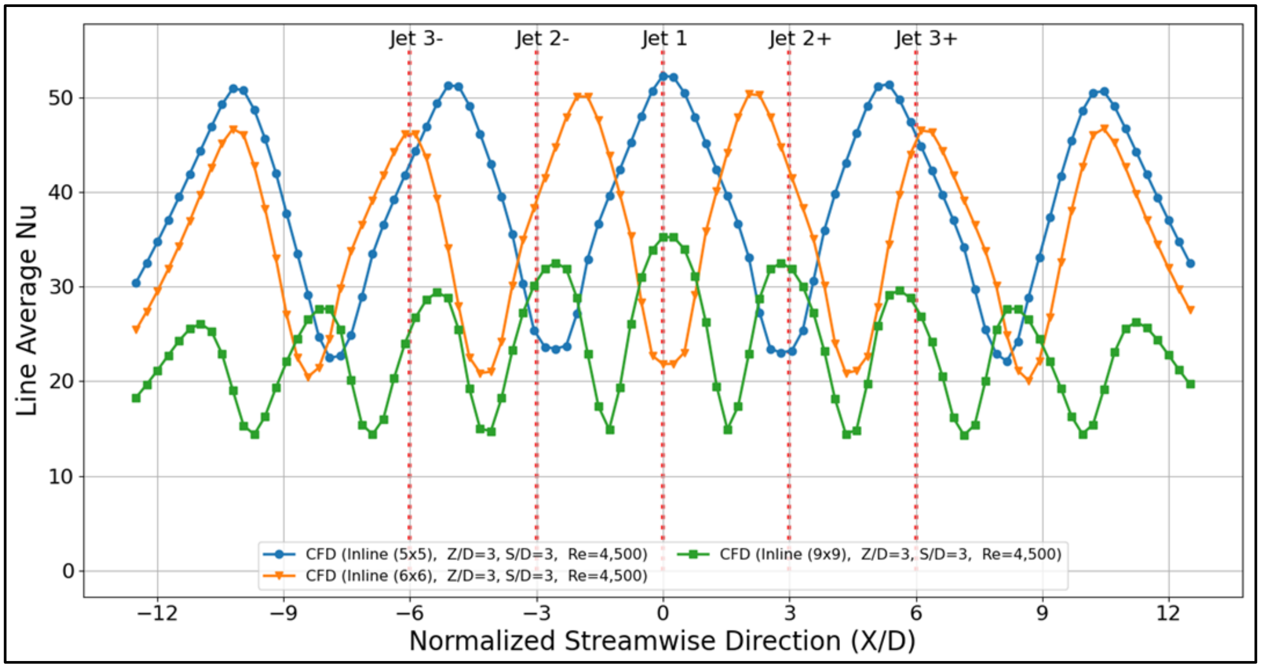

Figure 5-11: $\overline{\mathrm{Nu_L}}$ profiles for jet-to-jet spacing comparison at Z/D = 3, $\mathrm{Re_j}$ = 4,500 and 4,500 for different number of jets

5.5 Geometrical Effects Summary

In this study, the main geometrical features that affect jet impingement cooling has been experimentally and numerically studied to investigate the heat transfer characteristics on a double exit crossflow scheme. A range of Reynolds number of 2,500 – 12,500 was covered to study the effect of Reynolds number on the heat transfer performance and to correlate the Nusselt number with the Reynolds number for turbulent flow regime.

The increase in Reynolds number commonly resulted in a higher stagnation Nusselt number, where it peaked underneath the middle row of jets. The side rows of jets experienced higher spent air crossflows that resulted in redirecting and bending the jet flow streamline. Hence, it led to a degradation in Nusselt number along the streamwise direction. A cooling regression exponent (m) was found to match the available literature.

A comparison of different stand-off distances for each flow case showed a reduction in both Line-averaged and area-averaged Nusselt number as the stand-off distance increased. This was justified by the entrainment of the surrounding air that causes the loss of jets' momentum. Furthermore, jet Active cooling regions were shifted further downstream as the stand-off distance increases due to the higher crossflow accumulations that interact more with the jet cores and each pair of jets prior to the impingement.

It was also concluded that the in-line nozzle configuration is capable of achieving higher heat transfer rates, especially at shorter stand-off distances. This is due to the more protection of the jets from the upstream row of jets as the spent air crossflow is given less distance to accelerate before striking the next row of jets. In the staggered arrangement, the influence of the crossflow is higher as the crossflow accelerates and directly impacts the jets. The jet-to-jet spacing effect was also studied. It was concluded that as the open area ratio decreases, the heat transfer performance decreases because of the larger area that the nozzles cover.

Since the crossflow causes a great deal of jet distortion, bending, and Nusselt number degradation, it is worth looking methods to minimize its effects. Therefore, the next chapter addresses the crossflow effects and proposes solutions to control and minimize them.

CHAPTER 6: CROSSFLOW MITIGATION

Jet-to-jet interactions result in the accumulation of crossflow as the spent air migrates downstream, which usually causes a decay in the Nusselt number and reduces the overall cooling performance. In this chapter, several crossflow mitigation techniques are investigated to protect jet cores from upstream crossflows and, therefore, enhance heat transfer performance.

6.1 Jet Protection and Crossflow Mitigation via Crossflow Diverters

6.1.1 Proof of Concept Stage

The accumulation of the crossflow as it migrates downstream can result in undesirable decay in the Nusselt number. Cylindrical-shaped crossflow diverters are attached to the nozzle plate in a trial to prove the concept of diverting the crossflows away from the jet cores. The outer radius of the diverter is 4 mm and has a thickness of 1 mm. The diverters have a fixed height 1.5D as shown in Figure 6-1.

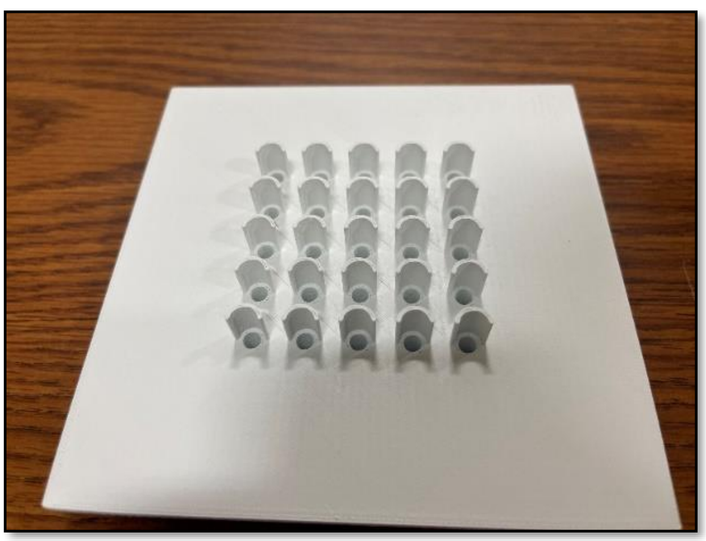

Figure 6-1: Cylindrical crossflow diverter design

As the name implies, these geometries tend to protect the jet core and divert the crossflow accumulation away from the downstream jet cores. Figure 6-2 compares the baseline geometry and the semi-circular crossflow diverters in terms of the temperature distribution on the target plate. The jets are significantly less deflected in the case of the crossflow diverters. This can also be seen in the velocity distribution field shown in Figure 6-3. Therefore, it is expected that these diverters can enhance the heat transfer efficiency.

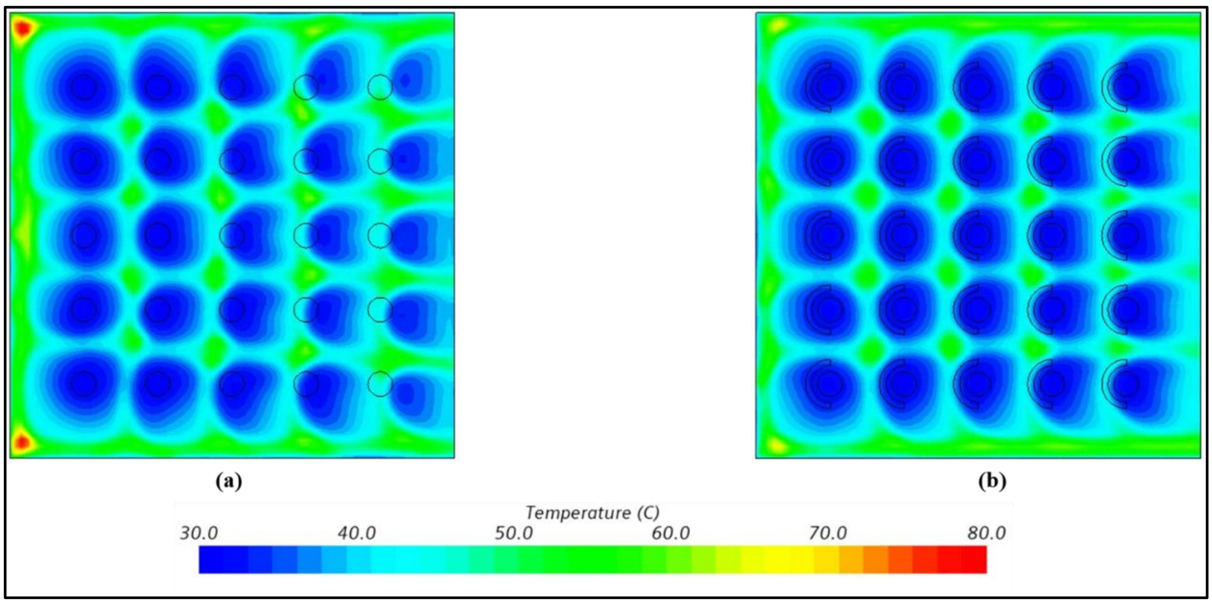

Figure 6-2: Raw CFD heat maps at $\boldsymbol{Re_j}$ = 4,500 and $\boldsymbol{Z/D}$ = 3, (a) baseline, (b) cylindrical crossflow diverter

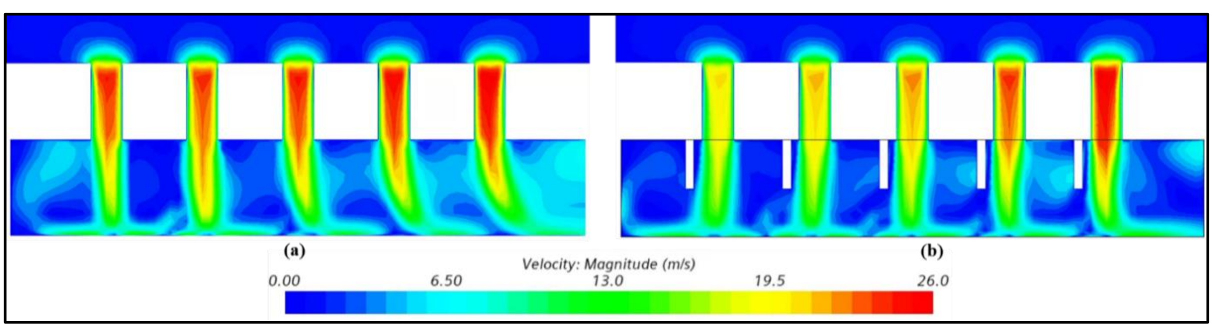

Figure 6-3: Middle row velocity field at $\boldsymbol{Re_j}$ = 4,500 and $\boldsymbol{Z/D}$ = 3, (a) baseline, (b) cylindrical crossflow diverter

To quantify for the crossflow effects, the axial mass flux entering the jet core field was normalized against the jet mass flux according to equation 6-1:

$$\frac{\Phi_c}{\Phi_j} = \frac{\dot{m}_c\, A_c}{\dot{m}_j\, A_j} \qquad \text{6-1}$$

As depicted in Figure 6-4, a lower mass flux ratio was observed for the crossflow diverter case compared to the baseline case, which is another evidence that the diverter could enhance the heat transfer performance on the target plate. The difference between the mass flux ratio is expected to increase as the streamwise direction extends, meaning that more jets are employed along the streamwise location.

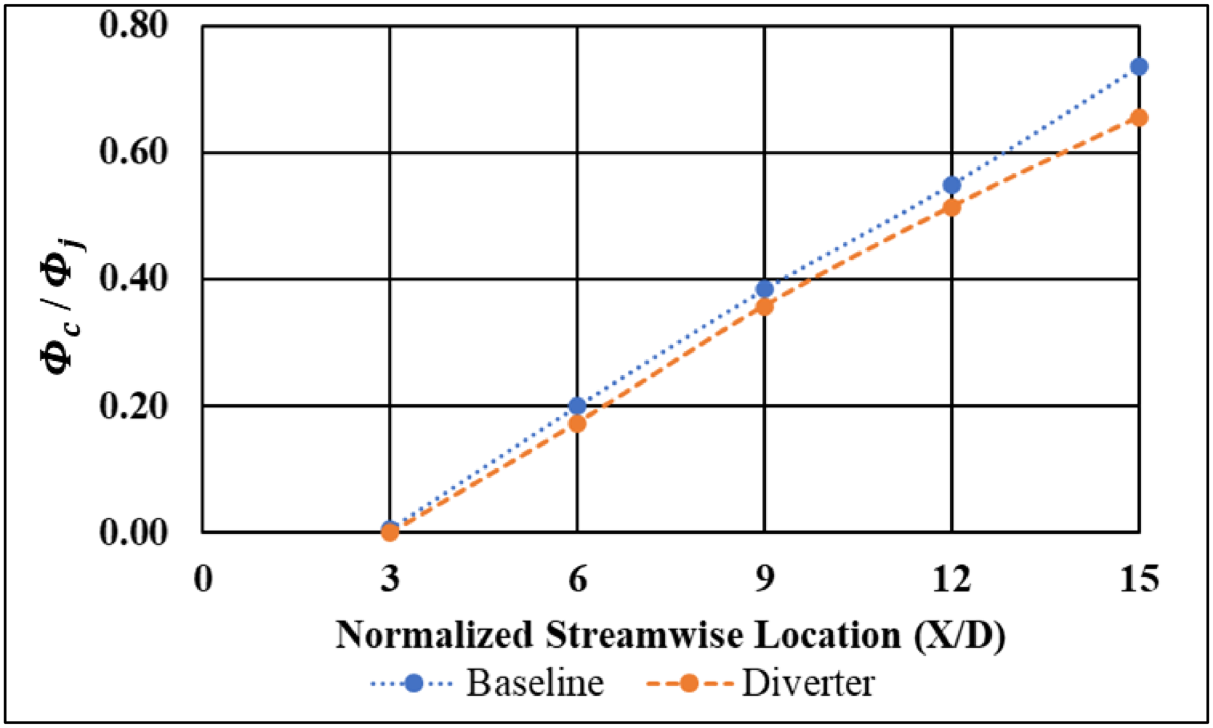

Figure 6-4: Crossflow to jet mass flux ratio at $\boldsymbol{Re_j}$ = 4,500 and $\boldsymbol{Z/D}$ = 3

6.1.2 Crossflow Diverters Results

Furthermore, in this study, the heat transfer performance of three crossflow diverter shapes is evaluated under a Reynolds number of 2,500 – 10,000. The effect of the height of the diverters on both heat transfer performance and the associated pressure loss penalty was evaluated and optimized. The net heat transfer enhancement is introduced through a heat transfer parameter (η) to account for both enhancement in Nusselt number and pressure loss penalty that leads to high pumping power requirements.

Three different diverter shapes (cylindrical, rectangular, and ribbed) are numerically evaluated. All diverters are placed directly below the jet holes and are located 3 mm apart from center to center as are the 4 mm-diameter jet holes. Diverters are 1-mm thick and vary in height as a percentage of the stand-off distance (Z/D) that is the vertical height from the nozzle tip to the target surface. The stand-off distance is set at three times the jet diameter (D = 4 mm) while the diverter heights are Quarter (QL), Half (HL), and Three-Quarters (TQL). A sample of the diverters can be seen in Figure 6-5.

6.1.3 Visual Comparison via Heat Maps

A sample of the generated heatmaps for a coolant flow Re_j equal to 10,000 is shown in Figure 6-6. It can be clearly seen that the cooling performance tends to decay as the flow migrates downstream. The downstream jets are weakened because of the accumulation of crossflows that interact with the jet columns. When the diverters are present, the cooling performance downstream of the active cooling region is less diminished.

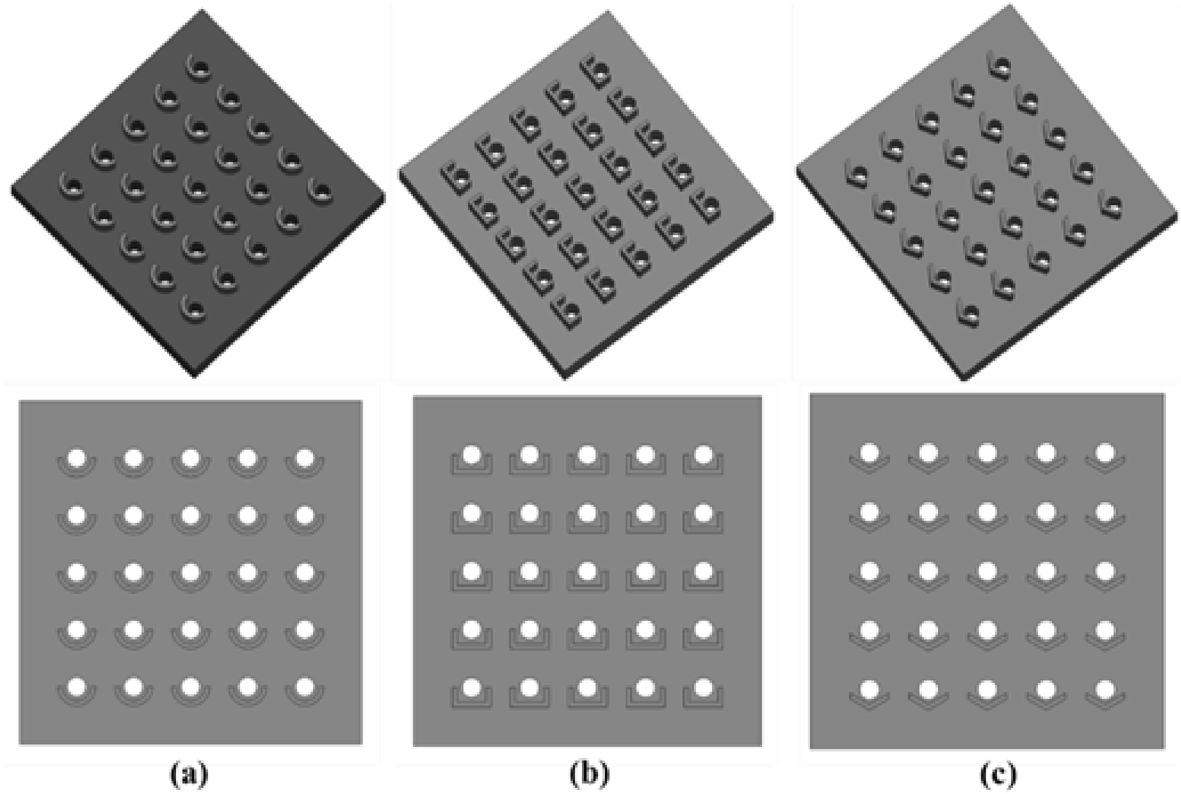

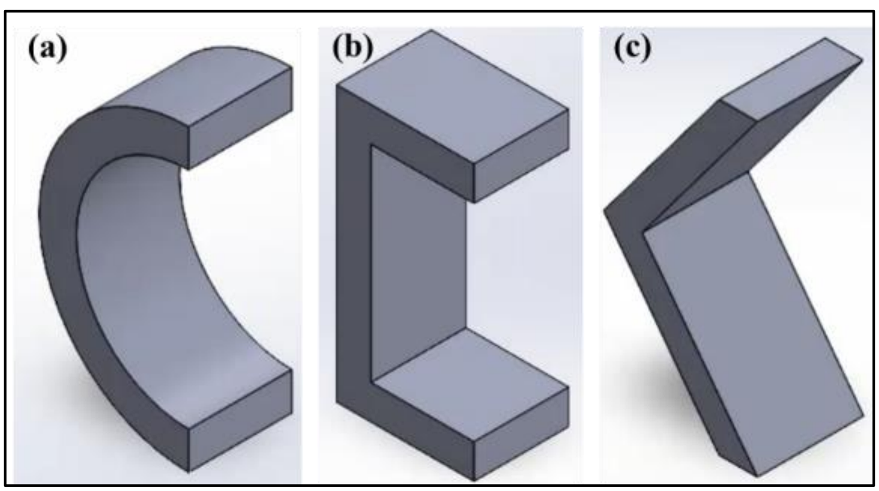

Figure 6-5: Diverter shapes, (a) CYL, (b) REC, and (c) RIB

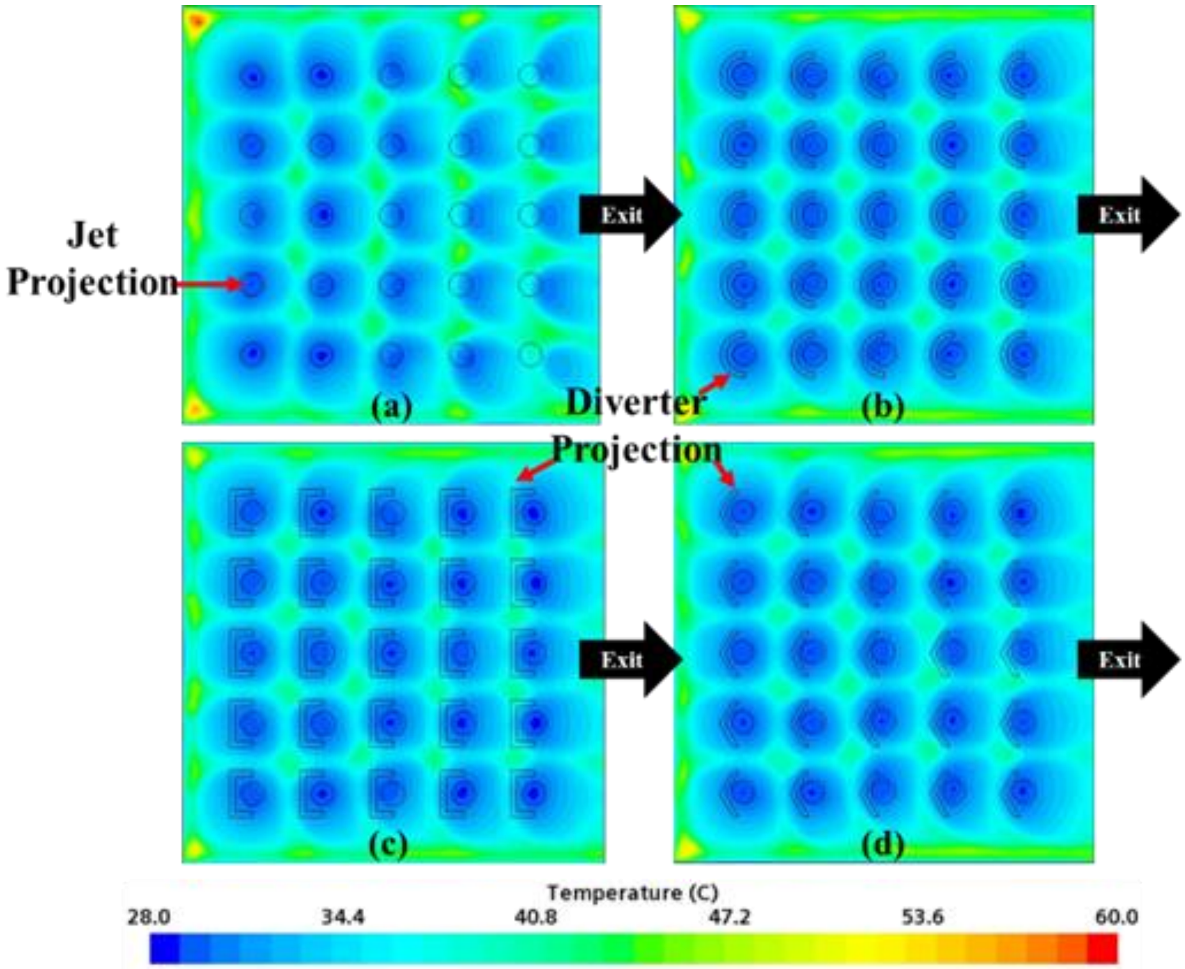

Figure 6-6: CFD heat maps at $\boldsymbol{Re_j}$ = 10,000 and TQL diverter for, (a) baseline, (b) CYL, (c) REC, and (d) RIP

In addition, compared to the baseline case, these downstream locations experience less shifting toward the exit in terms of peak Nusselt Number ($\overline{Nu_L}$).

6.1.4 Line-Averaged and Surface-Averaged $\boldsymbol{Nu}$

The heat transfer performance was evaluated via the line-averaged Nu as Figure 6-7 compares the line-averaged Nusselt Number ($\overline{Nu_L}$) of the baseline model (where no diverters are attached) with different diverter configurations for single-exit setups (to the right-hand side). The rest of the Line-averaged Nusselt number can be found in Appendix I, Appendix J, and Appendix K.

Moreover, the enhancement peaked at an average of 12%, 10.7%, and 11.3% for cylindrical, rectangular, and ribbed shapes, respectively. It can also be noticed that the cylindrical shape outperforms other shapes at shorter diverter heights. Figure 6-8 summarizes the enhancement of $\overline{Nu_s}$ for all crossflow diverter shapes. The details can be found in Table 6-1, Table 6-2, and Table 6-3.

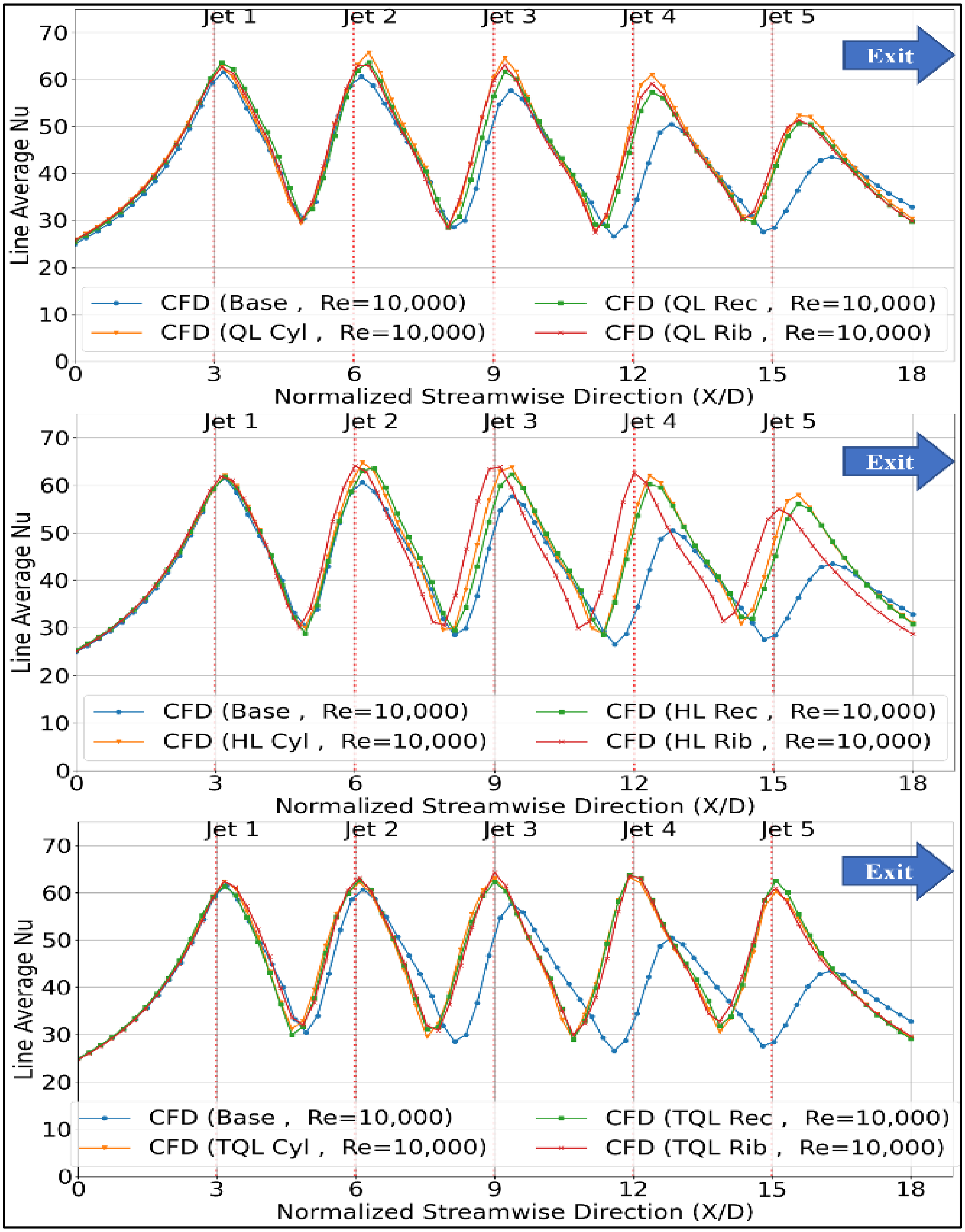

Figure 6-7 : Line-averaged $\boldsymbol{Nu}$ distribution at $\boldsymbol{Re_j}$ = 10,000 for different crossflow diverter heights: (a) CYL, (b) REC, and (c) RIB

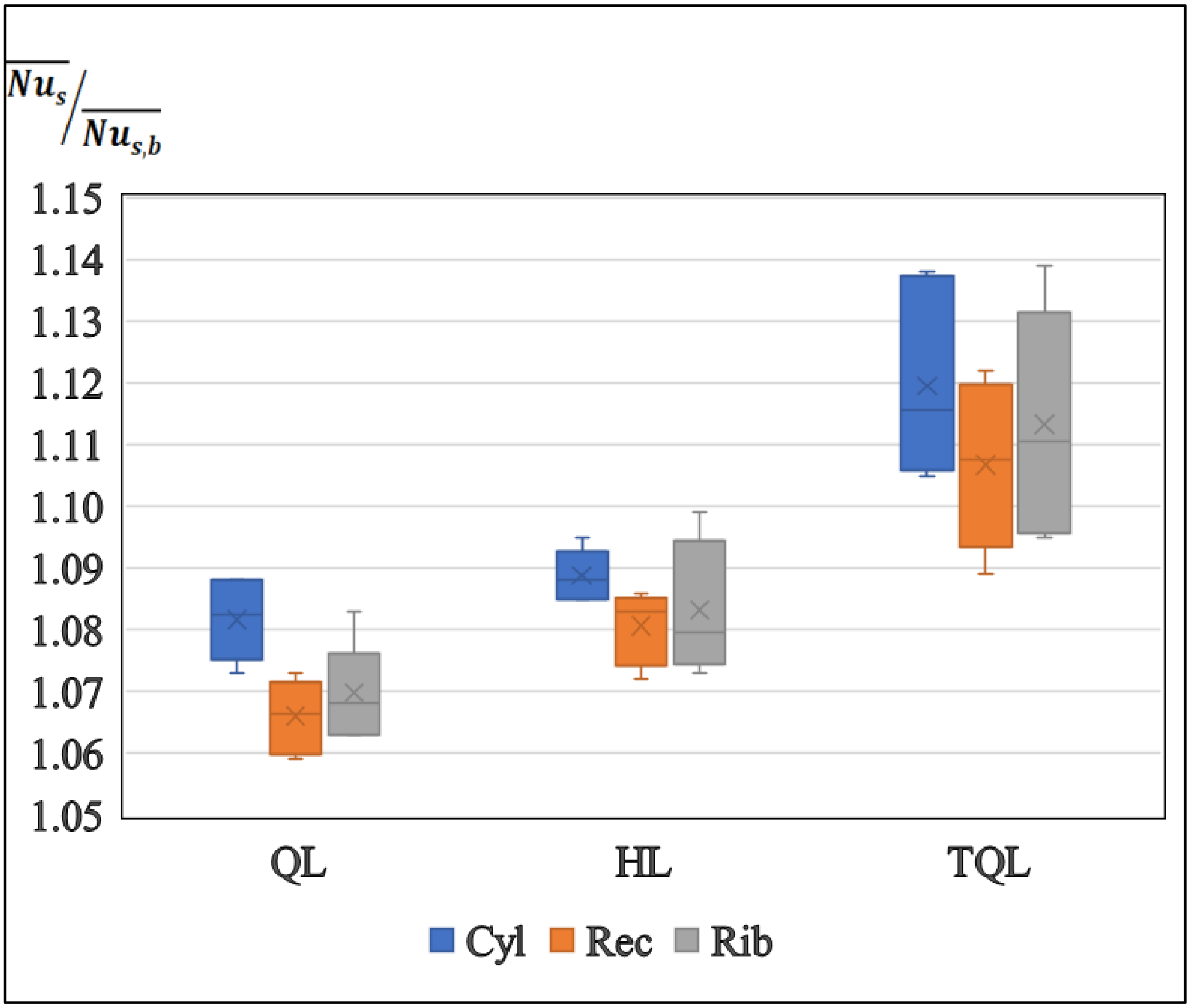

Figure 6-8 : Boxplots summary of normalized $\overline{\boldsymbol{Nu_s}}$ for all diverters

Table 6-1: Normalized $\overline{\boldsymbol{Nu_s}}$ for cylindrical diverters

$\boldsymbol{Re_j}$	$\overline{Nu_s}/\overline{Nu_{s,b}}$		
	QL	**HL**	**TQL**
2,500	1.088	1.095	1.137
3,500	1.088	1.092	1.138
4,500	1.086	1.088	1.120
5,500	1.079	1.085	1.111
7,500	1.076	1.088	1.105
10,000	1.073	1.085	1.106
Avg:	**1.081**	**1.089**	**1.120**

Table 6-2: Normalized $\overline{Nu_s}$ for rectangular diverters

$\boldsymbol{Re_j}$	$\overline{Nu_s}/\overline{Nu_{s,b}}$		
	QL	**HL**	**TQL**
2,500	1.073	1.086	1.122
3,500	1.069	1.084	1.119
4,500	1.071	1.072	1.111
5,500	1.064	1.085	1.104
7,500	1.060	1.082	1.095
10,000	1.059	1.075	1.089
Avg:	**1.066**	**1.081**	**1.107**

Table 6-3: Normalized $\overline{Nu_s}$ for ribbed diverters

$\boldsymbol{Re_j}$	$\overline{Nu_s}/\overline{Nu_{s,b}}$		
	QL	**HL**	**TQL**
2,500	1.083	1.099	1.139
3,500	1.074	1.093	1.129
4,500	1.071	1.084	1.116
5,500	1.065	1.073	1.105
7,500	1.063	1.075	1.096
10,000	1.063	1.075	1.095
Avg:	**1.070**	**1.083**	**1.113**

6.1.5 Friction Factor and Velocity Flow Fields

The friction factor is another important factor in quantifying the extent to which the diverters might increase the coolant pumping requirements. The existence of the diverter causes additional flow resistance and requires higher pressure to drive the flow. Hence, the total pressure drop in the cooling channel was evaluated from the difference in the total pressure at the nozzle array inlet ($P_{T,in}$) and the channel outlet ($\Delta P_{T,out}$) as shown in equation 6-2:

$$\Delta P_T = P_{T,in} - \Delta P_{T,out} \qquad 6\text{-}2$$

Total pressure drop values were used to estimate the associated non-dimensional friction factor as described in equation 6-3:

$$f = \frac{2\ D\ \Delta P_T}{\rho\ u_{out}^2 L} \qquad 6\text{-}3$$

To quantify the pressure drop penalty associated with the diverters, the friction factor (f) was normalized against the corresponding baseline model friction factor (f_b). Figure 6-9 summarizes the normalized friction factor values for all cases. The details can be found in Table 6-4, Table 6-5, and Table 6-6.

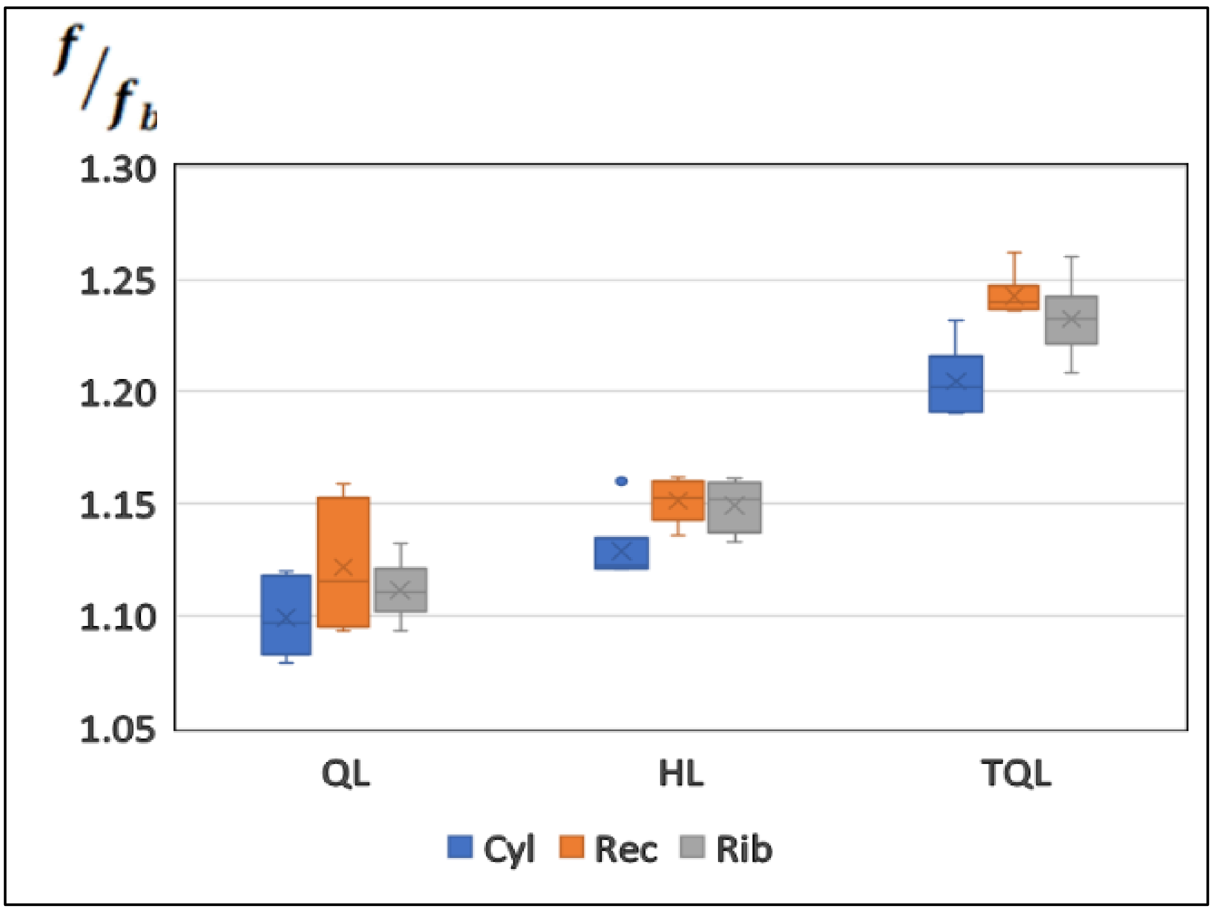

Figure 6-9: Boxplots summary of normalized friction factor for all diverters

Table 6-4: Normalized friction factor for cylindrical diverter

Re_j	f/f_b		
	QL	**HL**	**TQL**
2,500	1.084	1.124	1.191
3,500	1.079	1.121	1.190
4,500	1.105	1.121	1.198
5,500	1.089	1.126	1.210
7,500	1.117	1.121	1.206
10,000	1.120	1.160	1.232
Avg:	**1.099**	**1.129**	**1.204**

Table 6-5: Normalized friction factor for rectangular diverter

Re_j	f/f_b		
	QL	**HL**	**TQL**
2,500	1.159	1.159	1.241
3,500	1.150	1.146	1.237
4,500	1.119	1.136	1.238
5,500	1.093	1.145	1.236
7,500	1.096	1.162	1.242
10,000	1.112	1.159	1.262
Avg:	**1.122**	**1.151**	**1.243**

Table 6-6: Normalized friction factor for ribbed diverter

Re_j	f/f_b		
	QL	**HL**	**TQL**
2,500	1.115	1.133	1.260
3,500	1.093	1.138	1.236
4,500	1.105	1.150	1.235
5,500	1.106	1.154	1.230
7,500	1.117	1.161	1.208
10,000	1.132	1.159	1.226
Avg:	**1.111**	**1.149**	**1.232**

The diverters induce additional flow resistance yielding higher jet velocities closer to the exit than near the blocked boundary. Figure 6-10 shows the velocity contours of all diverter cases at the same Reynolds number of 10,000. The velocity tends to increase at the downstream jet (jet 5). Additionally, to represent the flow velocity distribution, the jet mass flux was averaged across each row of jets along the streamwise direction (denoted as $\overline{\Phi_{row}}$) and normalized against the jet mass flux across all jets (denoted as $\overline{\Phi_{Total}}$).

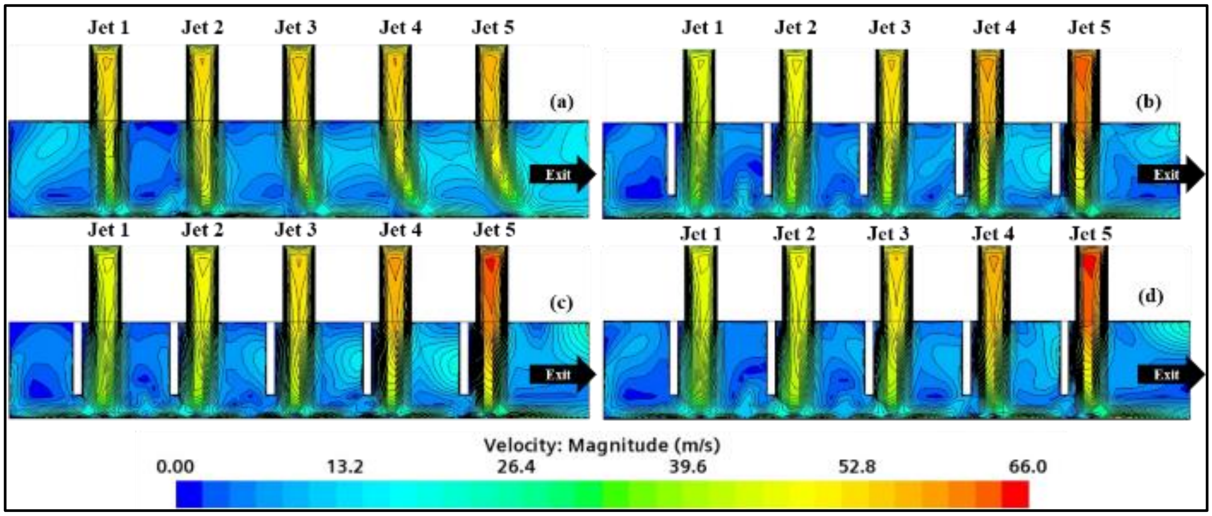

Figure 6-10: Streamwise velocity contours at Re = 10k and TQL diverters: (a) baseline, (b) CYL, (c) REC, and (d) RIB.

When no diverters were attached, the jet mass flux slightly varied between 0.98 – 1.05. More non-uniform mass flux distributions with higher variations of 0.87 – 1.17 were observed for all diverters, with negligible differences across all diverter shapes. Mass flux was calculated from equation 6-4, and the distribution can be found in Figure 6-11.

$$\Phi = \frac{\dot{m}}{A} \qquad (6\text{-}4)$$

6.1.6 Net Heat Transfer Enhancement

The enhancement in heat transfer performance can be correlated to the pressure drop penalty to quantify the net enhancement. The heat transfer parameter proposed by Fan et al. [89] was used to correlate the desired Nu enhancement with the increased coolant pumping requirements due to the undesired pressure loss. The heat transfer parameter is defined in equation (6-5):

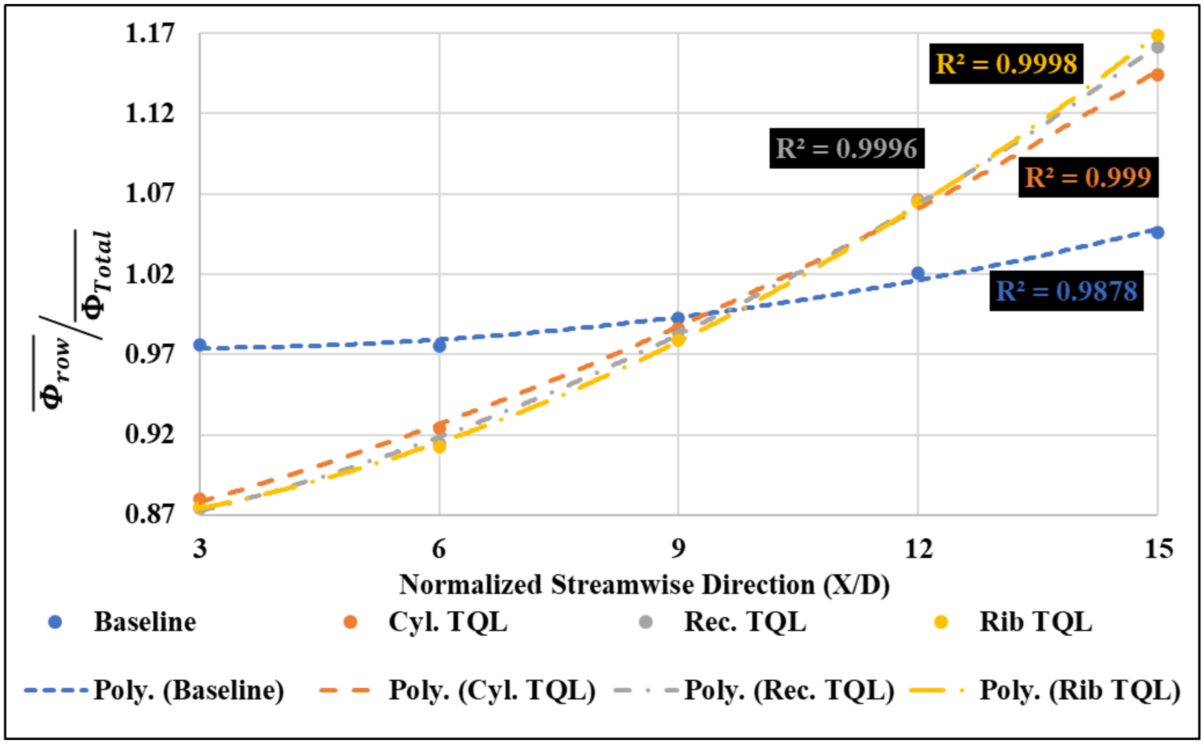

Figure 6-11: Row-averaged to total-averaged jet mass flux ratio for $\boldsymbol{Re_j}$ =10,000 and TQL diverters

$$\eta = \frac{\overline{Nu}/\overline{Nu_b}}{\left(f/f_b\right)^{1/3}} \qquad \text{6-5}$$

As summarized in Table 6-7, Table 6-8, and Table 6-9, all diverters showed an above unity heat transfer parameter when normalized against the baseline model. The average net enhancement ranged from 3.3% for QL rectangular diverter to 5.2% for TQL cylindrical diverter. Furthermore, the cylindrical-shaped diverter outperformed all other shapes followed by the rib-shaped diverter. The rectangular-shaped diverter has the least favorable aerodynamic characteristics and it led to the least heat transfer enhancement. There was also no clear trend between the jet diverter height and heat transfer parameter.

Table 6-7: Heat transfer parameters ($\boldsymbol{\eta}$) for cylindrical diverter

$\boldsymbol{Re_j}$	$\boldsymbol{\eta}$		
	QL	**HL**	**TQL**
2,500	1.059	1.054	1.073
3,500	1.061	1.051	1.074
4,500	1.050	1.047	1.055
5,500	1.049	1.043	1.043
7,500	1.037	1.047	1.038
10,000	1.034	1.033	1.032
Avg:	**1.048**	**1.046**	**1.052**

Table 6-8: Heat transfer parameters ($\boldsymbol{\eta}$) for rectangular diverter

$\boldsymbol{Re_j}$	$\boldsymbol{\eta}$		
	QL	**HL**	**TQL**
2,500	1.022	1.034	1.044
3,500	1.021	1.036	1.043
4,500	1.031	1.028	1.035
5,500	1.033	1.037	1.028
7,500	1.028	1.030	1.019
10,000	1.022	1.024	1.010
Avg:	**1.026**	**1.031**	**1.029**

Table 6-9: Heat transfer parameters ($\boldsymbol{\eta}$) for ribbed diverter

$\boldsymbol{Re_j}$	$\boldsymbol{\eta}$		
	QL	**HL**	**TQL**
2,500	1.044	1.055	1.054
3,500	1.042	1.047	1.052
4,500	1.036	1.035	1.041
5,500	1.030	1.023	1.031
7,500	1.025	1.023	1.030
10,000	1.020	1.024	1.023
Avg:	**1.033**	**1.034**	**1.038**

6.2 Jet Protection and Crossflow Mitigation via Extended Jets

6.2.1 Proof of Concept Stage

The developing flow zone where the surrounding air entrains into the jet reduces the jet's velocity. The extension of the jets towards the target plate would serve two purposes. Similar to the crossflow diverters discussed in the previous sections, it is meant to protect the jet cores from the upstream spent air crossflow. Additionally, allowing more distance for the flow to develop such that the peak jet velocity and momentum would increase. The initial designs are divided in two techniques. These techniques employ a shell (tube) around the nozzles with either fixed or variable heights. Initial results showed that both techniques can enhance the heat transfer effectiveness compared to the baseline model. The downstream jets tend to be more protected from the spent air crossflow as shown in Figure 6-12.

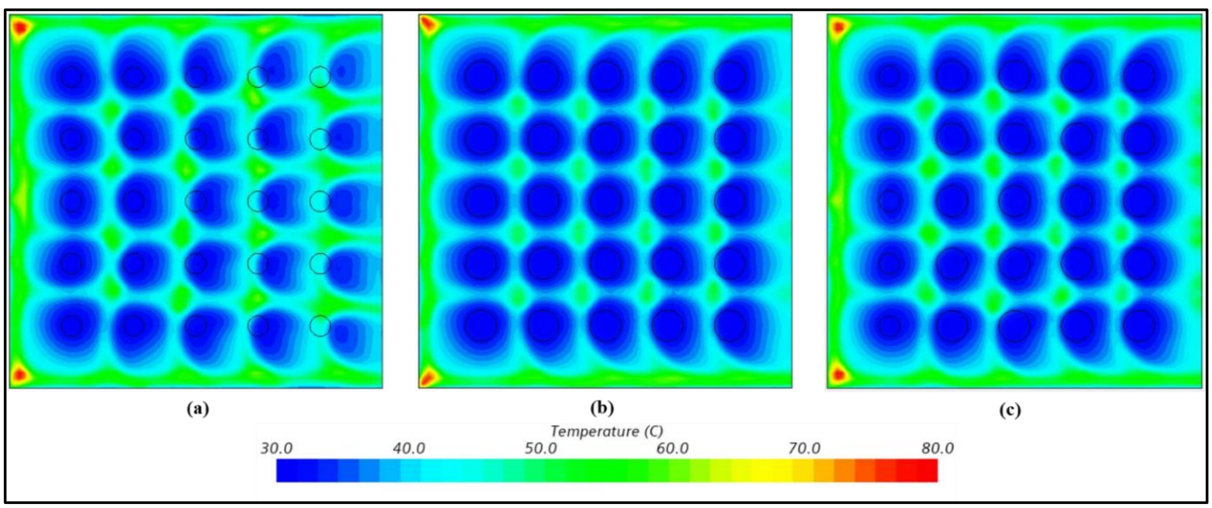

Figure 6-12: Raw CFD heat maps at Re_j = 4,500 and Z/D = 3, (a) baseline, (b) EXTF, and (c) EXTV

In this study, the heat transfer performance of the above-mentioned extended jets is evaluated under a Reynolds number of 2,500 – 10,000. The effect of fixed and variable extended jets on heat transfer performance and the associated pressure loss penalty was evaluated. The net heat transfer enhancement is introduced to account for both enhancement in Nusselt number and pressure loss penalty that leads to high pumping power requirements.

To minimize the spent air interference with the jets, a 3-mm radius with 1-mm thickness shells are employed to protect the jet core from the crossflow. The EXTF geometry has a fixed height of one and a half times the jet diameter (1.5 D) which is equivalent to HL case in the previous study of crossflow diverters. On the other hand, the EXTV geometry was designed to compare the pressure loss and the flow field structures. It starts with a no-jet extension in jet row number 1 to two times the diameter (2 D) in jet number 5. The geometries for both techniques are shown in Figure 6-13.

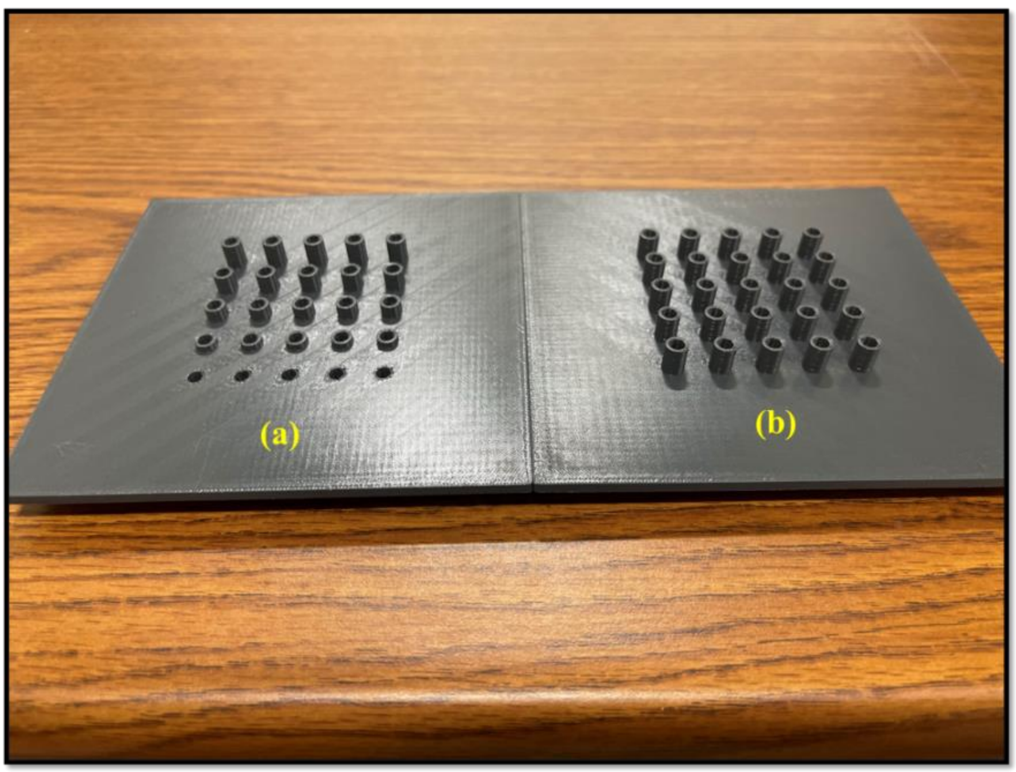

Figure 6-13: Extended jets design, (a) variable, (b) fixed

6.2.2 Line-Averaged and Surface-Averaged Nu

The heat transfer performance was evaluated via the line-averaged Nu as Figure 6-14 compares the line-averaged Nusselt Number ($\overline{\mathrm{Nu}_{\mathrm{L}}}$) of the baseline model with extended jets of fixed height (EXTF) and of variable height (EXTV) configurations for single-exit setups (to the right-hand side). The rest of the Line-averaged Nusselt number can be found in Appendix L.

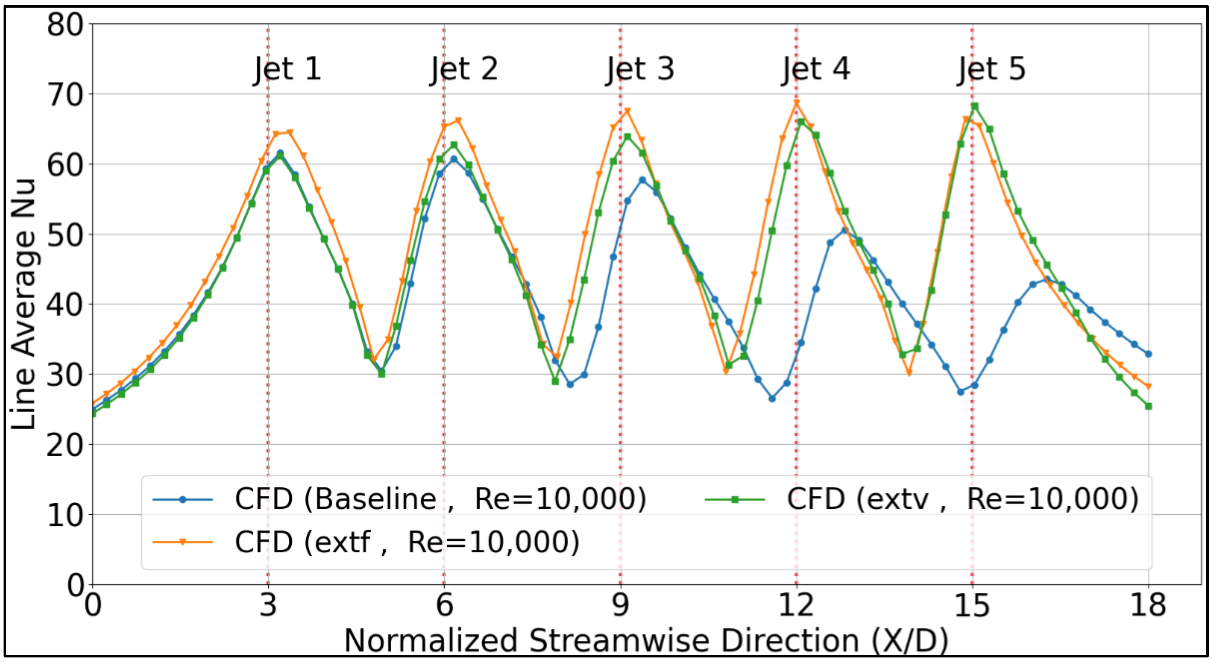

Figure 6-14 : Line-averaged $\boldsymbol{Nu}$ distribution at $\boldsymbol{Re_j}$ = 10,000 for fixed and variable extended jets

In jet row number 1, the stagnation Nusselt number was slightly higher for the EXTF case compared to the baseline and the EXTV models. The stagnation Nusselt number peaked at the 4$^{\text{th}}$ jets row for the EXTF and at the 5$^{\text{th}}$ jets row for the EXTV. Also, the stagnation Nusselt number was continuously deteriorating for the baseline model, and starting from the third jets row, the crossflow influence was more noticeable, resulting in both weakened and shifted jets. The stagnation Nusselt number for all jet rows is summarized in Table 6-10.

Table 6-10: Stagnation $\overline{Nu_L}$ for extended Jets

Jet Row Number	Stagnation $\overline{Nu_L}$		
	Baseline	**EXTF**	**EXTV**
Jet Row #1	61.9	64.7	61.4
Jet Row #2	60.7	66.3	62.8
Jet Row #3	57.7	67.7	63.9
Jet Row #4	50.6	68.7	66.1
Jet Row #5	43.4	66.3	68.4

For both jet extension techniques, the $\overline{\mathrm{Nu}_s}$ was enhanced with an average of 18.2% and 15.7% for the EXTF and the EXTV, respectively. It can also be noticed that the enhancement decreases with the Reynolds number as a result of the accelerated spent air and the higher turbulence charge nearby the path of the jet when they freely travel toward the target plate.

Across all Reynolds numbers, the EXTF outperformed the EXTV. This can be justified by the more uniform pattern of the pipes, and as they are fixed in height, they allow the same distance for the crossflow to accelerate before being blocked by the jet shells. Furthermore, since only the last row of jets in the EXTV provides a longer distance for the jet to developing compared to the EXTF, more jet development was achieved for the EXTF in the first four rows of jets. The detailed normalized Nusselt number can be found in Table 6-11.

Table 6-11: Normalized $\overline{Nu_s}$ for extended jets

Re_j	$\overline{Nu_s} / \overline{Nu_{s,b}}$	
	EXTF	**EXTV**
2,500	1.235	1.195
3,500	1.211	1.179
4,500	1.190	1.166
5,500	1.171	1.151
7,500	1.150	1.134
10,000	1.136	1.119
Avg:	**1.182**	**1.157**

6.2.3 Friction Factor and Velocity Flow Fields

Similar to the diverters, the extended jets also induce additional flow resistance yielding higher jet velocities closer to the exit than near the blocked boundary. Additionally, the flow is less uniformly distributed across all 5 jets as there is an increase in the downstream jets' mass flux. This is due to the less pressure differential between the inlet of the jet and the exit of the channel. Table 6-12 summarizes the normalized friction factor for both EXTF and EXTV where the EXTV slightly causes higher pressure drops (an average of 15.4% compared to 13.1% for the EXTF).

Table 6-12: Normalized friction factor for extended jets

Re_j	f/f_b	
	EXTF	**EXTV**
2,500	1.133	1.161
3,500	1.128	1.151
4,500	1.129	1.147
5,500	1.125	1.149
7,500	1.132	1.141
10,000	1.140	1.173
Avg:	**1.131**	**1.154**

6.2.4 Net Heat Transfer Enhancement

The enhancement in heat transfer performance can be correlated to the pressure drops penalty to quantify the net enhancement. The heat transfer parameter was defined in equation (6-5). As summarized in Table 6-13, both designs showed an above unity heat transfer parameter when normalized against the baseline model. The average net enhancement for the EXTF and EXTV are 13.4% and 10.4%, respectively.

Table 6-13: Heat transfer parameters ($\boldsymbol{\eta}$) for extended jets

Re_j	η	
	EXTF	**EXTV**
2,500	1.184	1.137
3,500	1.163	1.125
4,500	1.143	1.114
5,500	1.126	1.099
7,500	1.104	1.085
10,000	1.087	1.061
Avg:	**1.134**	**1.104**

6.3 Jet Protection Through Variable Jet Diameter Along the Streamwise Direction

Three jet diameter configurations were conducted to study their effects on heat transfer and flow field characteristics. Jet diameters were varied along the streamwise direction to minimize the crossflow effects. To regulate the crossflow accumulations, the jets diameters are increased along the streamwise direction, starting from the smallest to the largest diameter. The jet diameter varied according to three scenarios of 5%, 10%, and 20% increase towards the exit, as shown in Figure 6-15 and Table 6-14. The average jet diameter at each row was used to evaluate the Line-averaged Nusselt number, while the average jet diameter was used for the surface-averaged Nusselt number. Furthermore, as the jet diameter changes, the Reynolds number is no longer constant across all jets. Hence, the mass flow rate that corresponds to a specific Reynolds number in the baseline case was used for the variable jet diameter case and denoted as that specific Reynolds number.

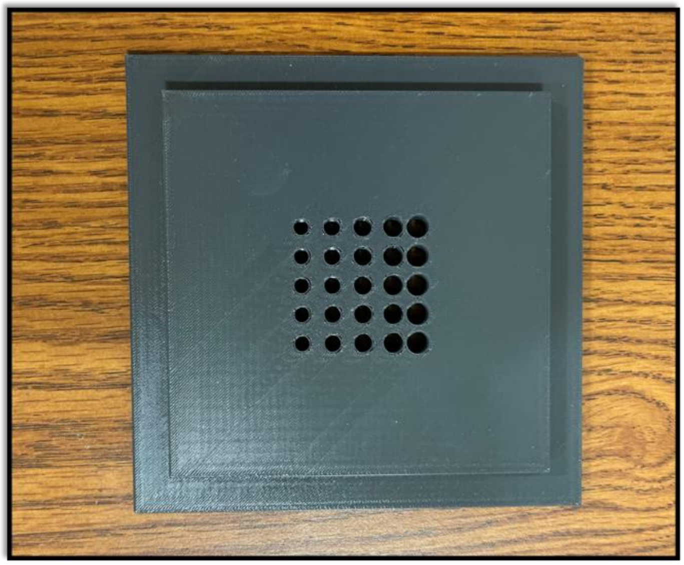

Figure 6-15: Variable jet diameter, 10% increase

Table 6-14: Variable Jet Diameter (VJD) diameter range

Case	Diameter (D) Range (mm)
Baseline	4
5% increase towards the exit	3.6 – 3.8 – 4.0 – 4.2 – 4.4
10% increase towards the exit	3.2 – 3.6 – 4.0 – 4.4 – 4.8
20% increase towards the exit	2.4 – 3.2 – 4.0 – 4.8 – 5.6

6.3.1 Visual Comparison via Heat Maps and Flow Field

The target plate temperature profile shown in Figure 6-16 shows the differences between the three-variable jet diameters mentioned earlier. Slight differences were observed between the 5% and the 10% cases, while in the 20% case, the wall temperature was reported to have a much higher temperature. This is due to the small diameter of the first row of jets resulting in less velocity and momentum of the first row of jets. The velocity profiles can be seen in Figure 6-17.

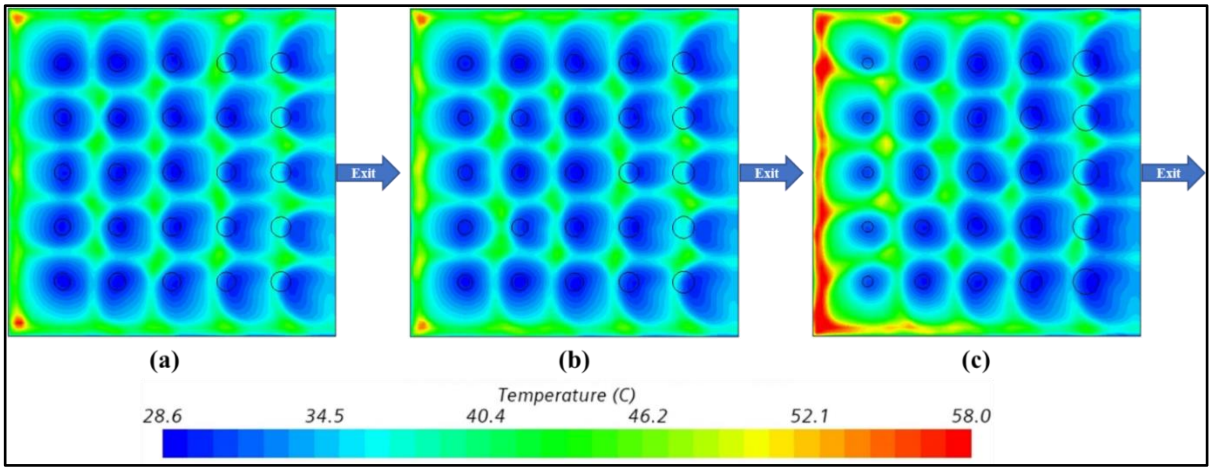

Figure 6-16: Raw CFD heat maps for VJD at $\boldsymbol{Re_j}$ = 10,000 and $\boldsymbol{Z/D}$ = 3, (a) 5%, (b) 10%, and (c) 20%

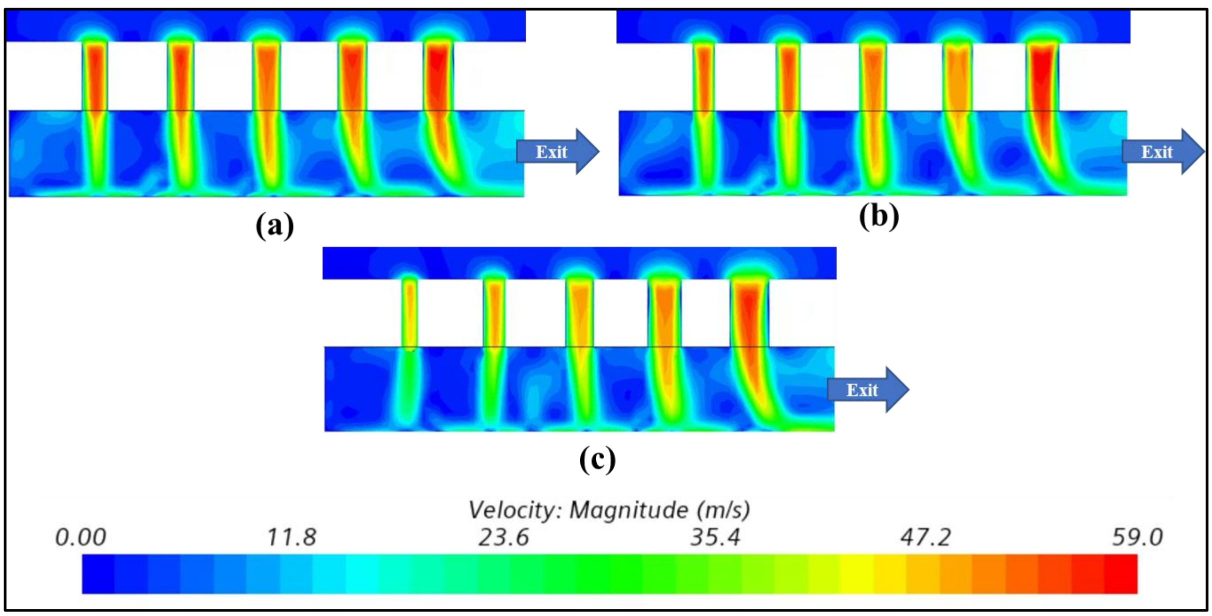

Figure 6-17: Velocity profiles for VJD at $\boldsymbol{Re_j}$ = 10,000 and $\boldsymbol{Z/D}$ = 3, (a) 5%, (b) 10%, and (c) 20%

6.3.2 Line-Averaged and Surface-Averaged $\boldsymbol{Nu}$

A sample of the Line-averaged Nusselt number for the single exit case (to the right-hand side) at Re_j of 10,000 is shown in Figure 6-18. At the first row, the baseline case showed the highest heat transfer rate as it has the largest diameter. Starting from the third row (jet 3), all cases achieved higher Nusselt numbers. The stagnation points are less shifted as the jet diameter increases further. Overall, varying the jet diameter has shown a minimal effect on the Nusselt number. The surface averaged Nusselt number for all cases is summarized in Figure 6-19. Both cases with 5% and 10% jet diameter increase showed an average of 2.09% and 2.07% in the surface-averaged. On the contrary, as the jet diameter further increased, it adversely affected the heat transfer and led to less thermal uniformity. It reduced the surface averaged Nusselt number by 2.76% compared to the baseline.

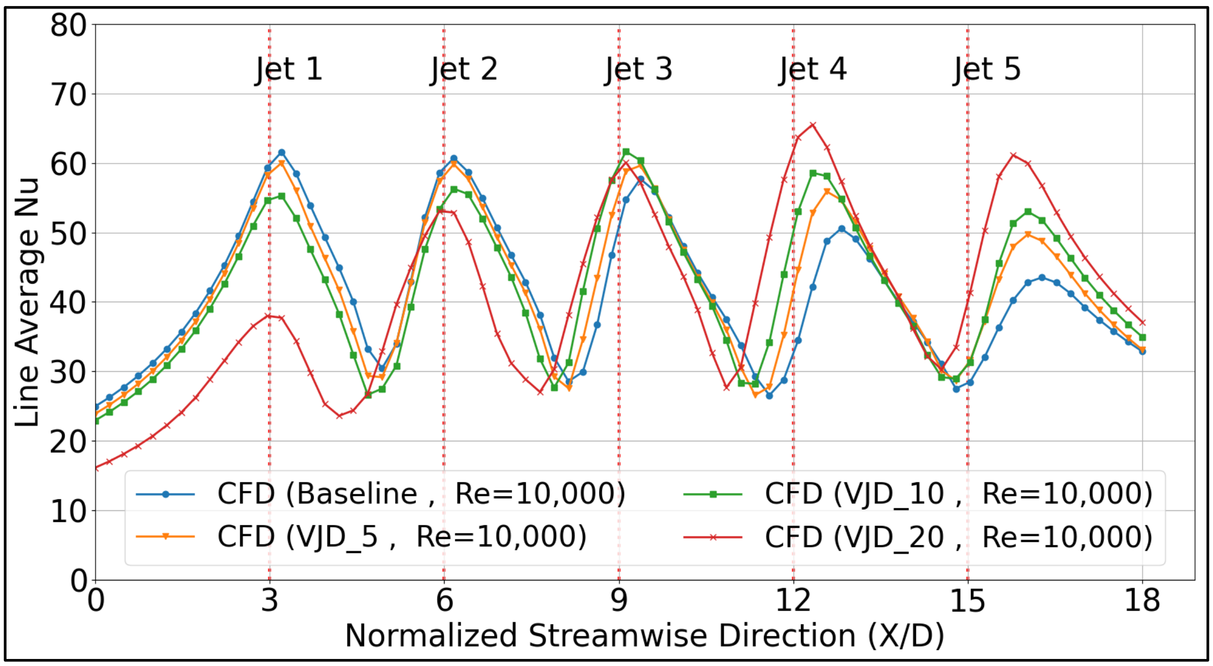

Figure 6-18: Line-averaged $\boldsymbol{Nu}$ distribution at $\boldsymbol{Re_j}$ = 10k for 5%, 10%, and 20% VJD

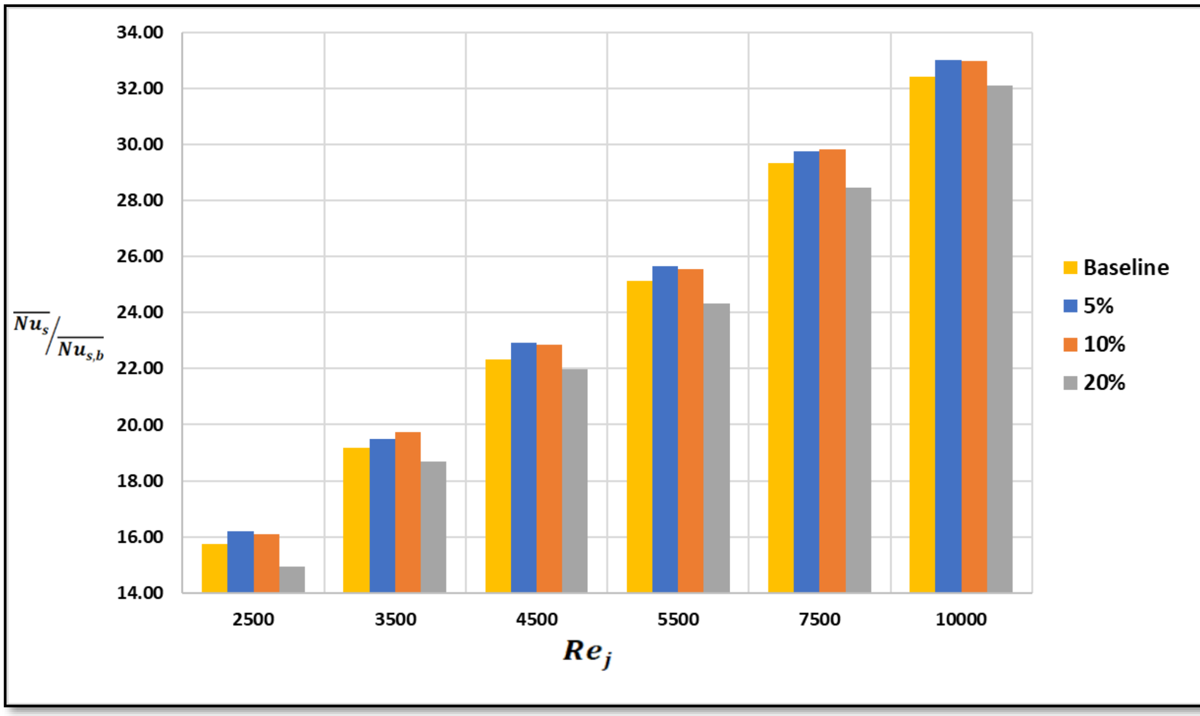

Figure 6-19: Summary of 5%, 10%, and 20% VJD

6.4 Crossflow Mitigation Summary

In this study, several crossflow mitigation techniques were investigated. Two methods were achieved by attaching small and easy-to-manufactured crossflow diverters and circular jet extension to protect jet cores from upstream crossflows and, therefore, enhance the heat transfer performance. The third technique was carried out by varying the jet diameter towards the channel exit. Three diverter shapes (cylinder, rectangle, and rib type) and two jet extensions (fixed height extended jets (EXTF) and variable height extended jets (EXTV)) were studied within a 25-jet array under laminar and turbulent flow regimes (Re of 2,500 – 10,000). Furthermore, three jet diameter increments of 5%, 10%, and 20% were examined. The crossflow diverters and the extended jets affected the heat transfer performance such that the line-averaged Nusselt number distributions showed higher values compared to the baseline case. They also showed less to no shifted stagnation points at the downstream jets, where jet distortion is the most severe in the baseline case due to jet-to-jet interactions and the buildup of the crossflow. One drawback was the jet mass flux being less uniform than the baseline model. However, the Nusselt number peaks were not affected by the variation of the air mass flux.

As the diverter was extended further into the flow field, more jet protection was achieved across all diverter shapes. The enhancement in Nusselt number peaked at an average of 10.5%, 11.3%, and 11.3% for cylindrical, rectangular, and ribbed shapes, respectively. The extension of the diverters' height posed an additional pressure drop that was quantified by normalizing the friction factor. For the extended jets, the enhancement in the Nusselt number peaked at an average of 18.2 and 15.7 for the EXTF and the EXTV, respectively. The EXTV posed a slightly higher pressure drop.

As higher-pressure drops require higher pumping powers to drive the flow, heat transfer parameter was introduced to correlate the desired enhancement in the Nusselt number with the pressure loss penalty. All diverters and extended jets showed above-unity values indicating that the enhancement in the Nusselt number dominated the pressure drop. The TQL cylindrical diverter offered a 5.2% increase in the net heat transfer performance, which outperformed all other diverter shapes and heights. Overall, the cylindrical-shaped diverters showed better flow aerodynamics as they smoothly diverted the crossflows to form channels between every two rows of jets. This behavior was concluded according to the friction factor and flow pressure contours. Finally, the rectangular diverters were outperformed by cylindrical and ribbed, which is reasonable due to the less favorable aerodynamics due to the sharp edge geometry.

The EXTF showed the highest net heat transfer enhancement among all other techniques. It offered an average of 13.4% net enhancement while the EXTV offered 10.4%. Not only the extended jets showed higher net heat transfer enhancement, but they also resulted in less pressure drops and higher heat transfer with better mass flux distribution across all jet rows and more uniform heat loads. Finally, all heat transfer effectiveness results of net heat transfer enhancement for QL, HL, and TQL, can be found in Figure 6-20, Figure 6-21, and Figure 6-22, respectively.

As the TQL cylindrical diverter showed the best heat transfer and flow field characteristics, a comparison between the extended jets and the TQL cylindrical diverter is shown in Figure 6-23. The comparison showed that the extended jets further enhance the heat transfer with less pressure drop penalty.

The variable jet diameter showed a minimal enhancement of Nusselt number not exceeding 2.09 % for the 5% increase in the jet diameter, and therefore no pressure loss analysis was performed. Also, as the jet diameters increased by 20%, they showed an adverse effect leading to a non-uniform heat distributions and less heat transfer rates of 2.76%.

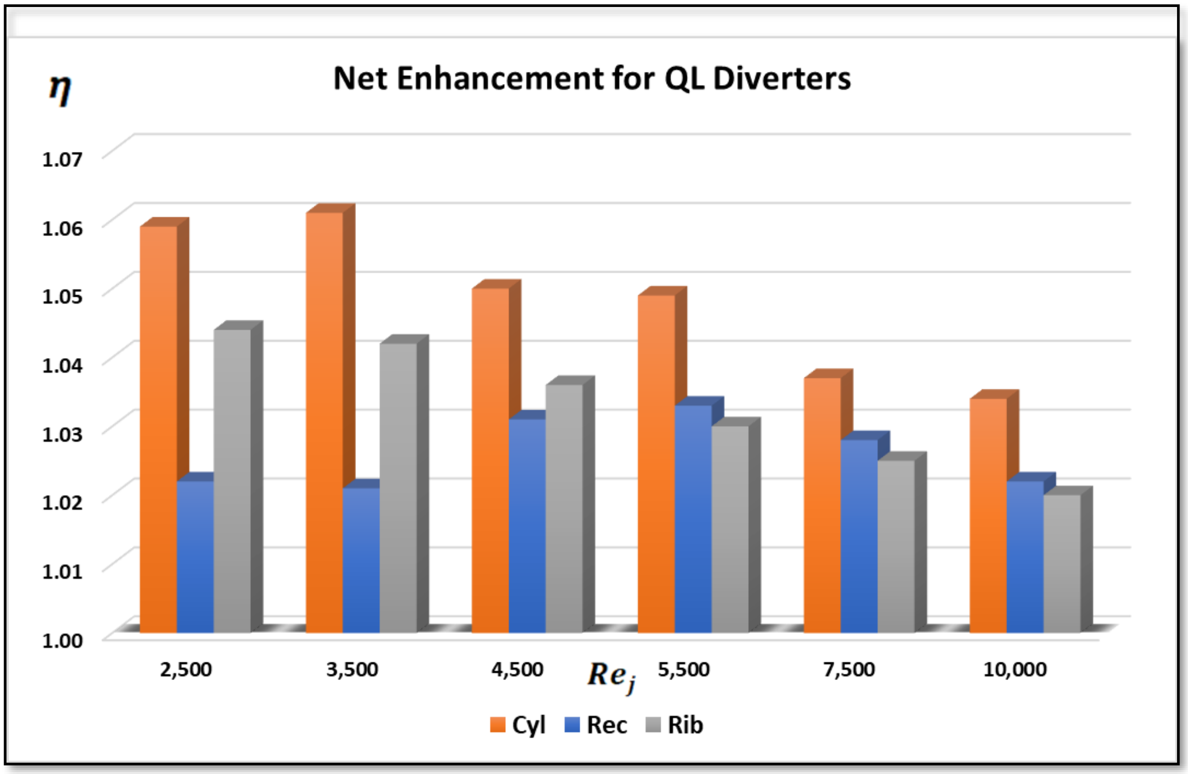

Figure 6-20: Summary of heat transfer effectiveness parameter for QL diverters

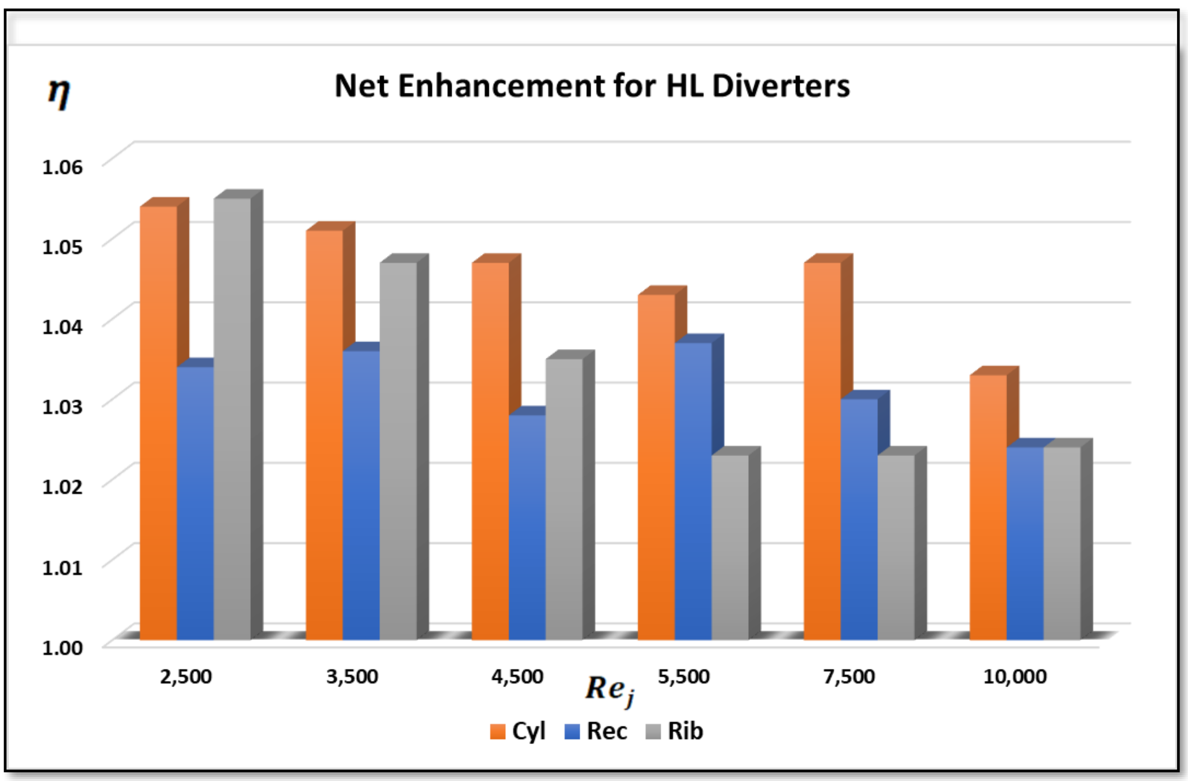

Figure 6-21: Summary of heat transfer effectiveness parameter for HL diverters

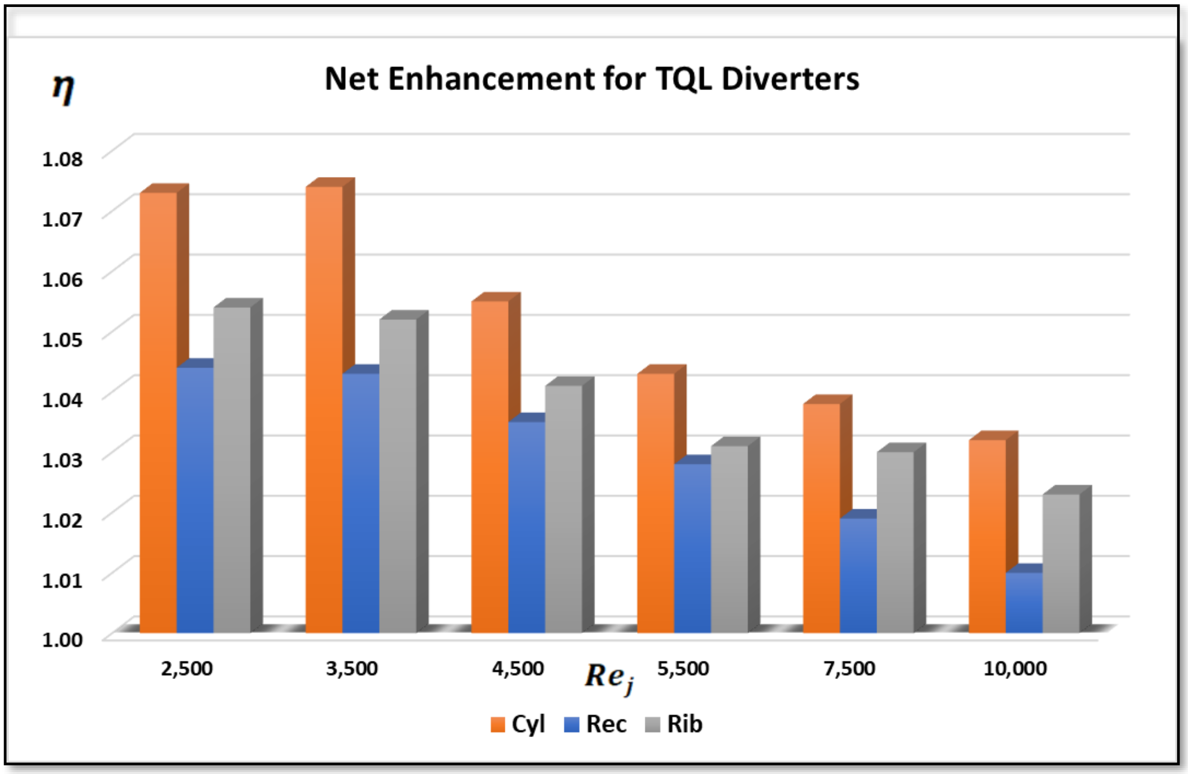

Figure 6-22: Summary of heat transfer effectiveness parameter for TQL diverters

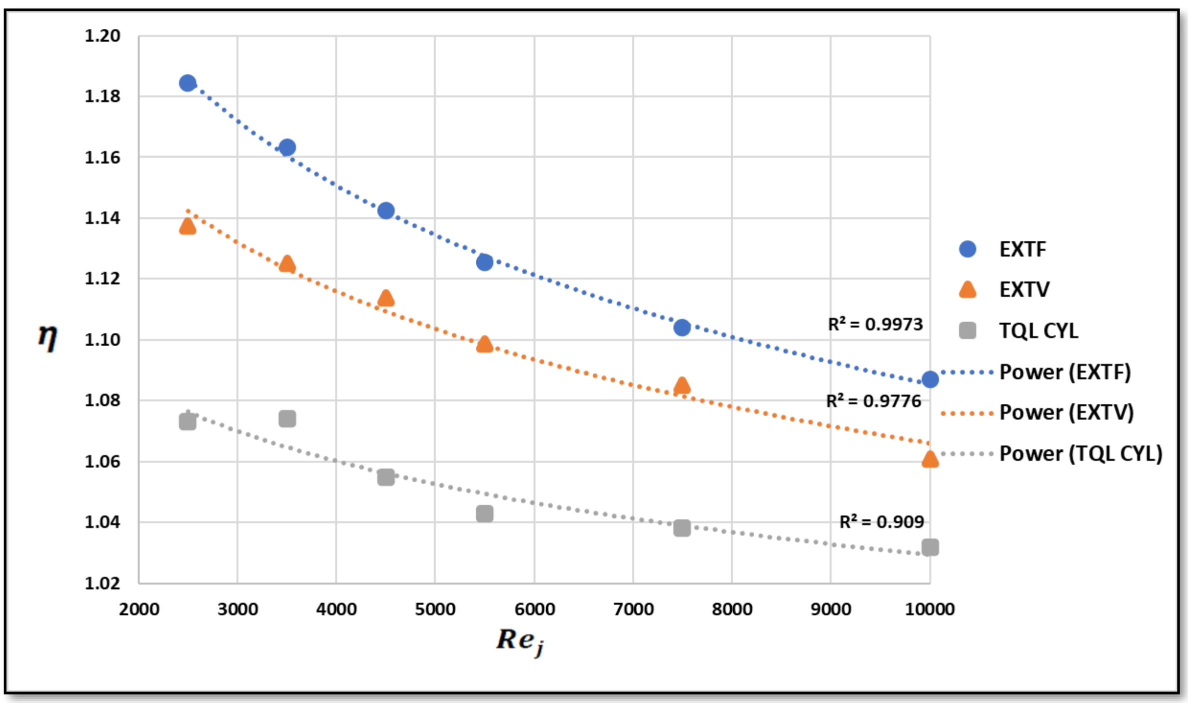

Figure 6-23: Overall heat Transfer comparison

CHAPTER 7: ROTATION ANALYSIS

7.1 Rotational Test Rig Description

Apart from the stationary test rig discussed earlier in Chapter 3, another test rig was used to investigate the effect of rotation on jet impingement heat transfer and flow field structure. The cooling channel was initially designed and built at the University of Wisconsin-Milwaukee to study the cooling performance of a two-pass U-shaped channel as shown in Figure 7-2.

Figure 7-1: Rotating channel

The experimental test rig was modified to study the effects of rotation on jet impingement cooling as shown in Figure 7-2. The coolant air is provided by a 2.4 HP centrifugal blower that can deliver a maximum of 120 CFM. The blower can be controlled by a Variable Frequency Drive (VFD) controller where the cooling air flow can be adjusted by varying the frequency of the blower's motor. A VP FlowScope digital flowmeter is connected to the cooling air feed line downstream of the blower to measure the flow entering the shaft and feeding into the rotating arm [90]. The flowmeter can measure a flow of up to 3,500 CFM with a flow temperature of up to 60 °C. The shaft (where the cooling air travels) is rotated by a three-phase 7.5 HP belt-driven induction motor with a max rpm of 1,770. The motor is also connected to its own VFD to regulate its speed so that it delivers the desired rpm. The motor is connected to a pulley mounted around the shaft.

An electric strip heater manufactured by "Omega" was used to mimic the hot target plate surface [91]. The heater is mounted perpendicular to the jet plate. The jet plate consists of a 3×5 array with 4-mm diameter jets. The jets are separated by a three-diameter length (S/D = 3), while the stand-off distance (Z/D) was set at 5.5 D. The current is supplied by an autotransformer to manipulate the heat generated on the heater surface. The backside of the heater is black painted by a high emissive 2-μmm acrylic-based Ultra-FLAT Krylon paint. The highly emissive black paint (emissivity of 0.95) ensures accurate surface temperature monitoring.

A wireless thermal camera type FLIR ONE EDGE PRO is mounted on the rotating channel behind the target plate [92]. It rotates with the same inertial frame with respect to the target plate, therefore, it captures the surface temperature profile during operation. The thermal camera provides a resolution of 640×480 pixels and measures temperature with an accuracy of ±3°C (5.4°F) or ±5%.

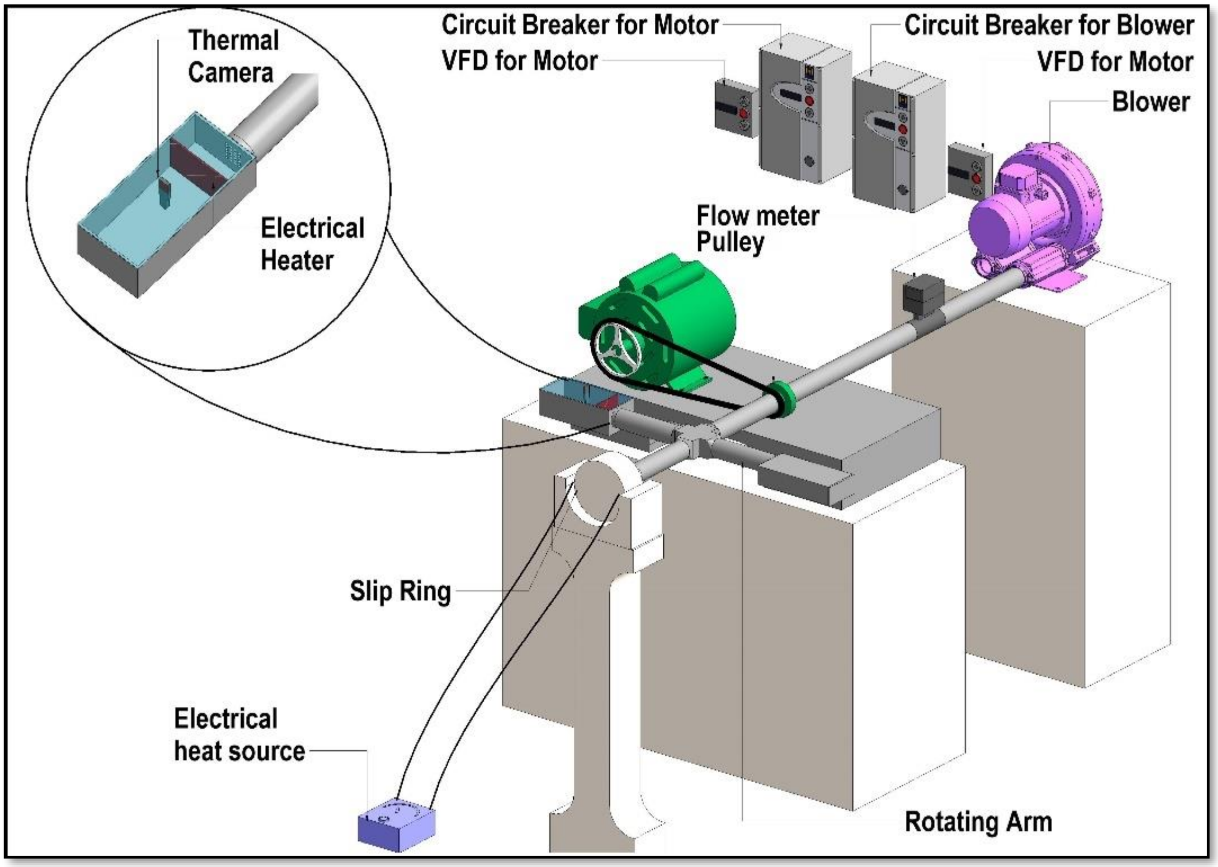

Figure 7-2: Modified rotational test rig

Stress analysis was performed at the early stages of the test rig design to ensure safe operation. Both sides of the rotating arm are balanced to minimize the vibration that can lead to a failure in the system. Additionally, the entire setup is located inside a wooden cage with a steel frame, such that the rotation occurs inside the cage.

7.2 Methodology and Test Sequence

The test sequence was initialized by heating the strip heater to the steady state temperature. When the steady state condition is reached, no further change in the temperature profile was noticed. The autotransformer that provides the electric current was set at 80% of its full voltage resulting in a 117 V and 1.6 Amps. Although these setting were kept constant across all test runs, there were some variations in the temperature profile of the target plate due to the variation in the heater's response, the ambient temperature, and other experimental variables and conditions. The heat flux was non-uniformly applied on the target plate such that higher temperatures are shifted towards the exit of the crossflow as shown in Figure 7-3. The reason behind that was to mimic a more realistic heat distribution as the leading-edge experiences higher thermal loads compared to the trailing edge. Due to the difficulty of obtaining the same exact heat profile in each run, a comparison will be made upon a set of two thermal images. The first image will represent the cooling performance of a stationary case until the system reached a stationary steady state condition. After then, the system is rotated, and another thermal image is captured when the rotational steady state condition was reached. The test sequence is summarized in Figure 7-4.

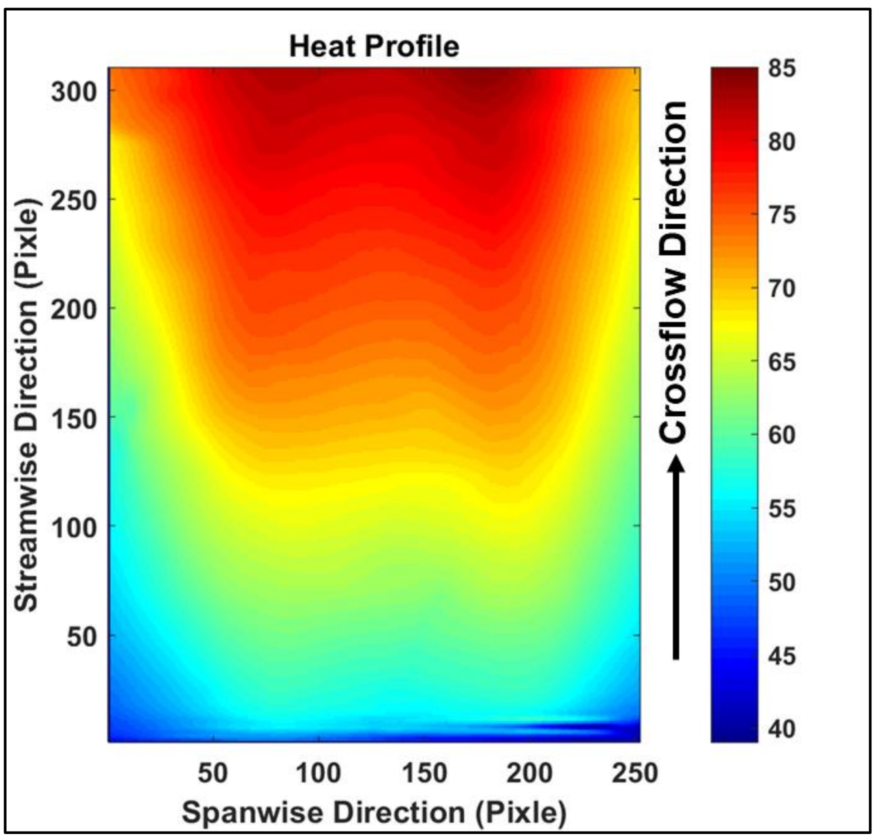

Figure 7-3: Non-uniform heat flux profile on the target plate

Heating	Stationary Cooling	Rotational Cooling
• Setting the required voltage and current for the strip heater. • Monitoring and capturing the surface temperature profile until the steady-State condition is reached (The strip heater's temperature does not rise beyond this point).	• Running the air blower and setting the required frequency on the VFD controller panel. • Measuring the cooling air properties during operation (flow and temperature). • Capturing a thermal image to extract the surface temperature profile when stationary steady-state condition (after ~ 90 seconds).	• Heating and cooling are continued at the previous settings. • Running the induction motor at the desired rpm by varying the frequency on the motor's VFD controller panel. • Capturing a thermal image to extract the surface temperature profile when rotational steady-state condition (after ~ 90 seconds).

Figure 7-4: Rotational test sequence summary

The cooling flow rate measured by the flowmeter was to calculate jet's Reynolds number as shown in equation 7-1.

$$Re_j = \frac{4\,\dot{m}}{N\,\pi\,\mu\,D} \qquad 7\text{-}1$$

To evaluate the heat transfer performance, the Nusselt number was calculated from equation 7-2:

$$Nu = \frac{h\,D}{K} \qquad 7\text{-}2$$

Where the convective heat transfer coefficient (h) can be evaluated from the heat balance as follows:

$$h = \frac{q''_{gen}}{T_s - T_j} \qquad 7\text{-}3$$

Where T_s is the surface temperature and T_j is the jet temperature that was measured by the flowmeter. Since each set of data compares the stationary and the rotational cases, there will be two values of the convective heat transfer coefficients. The target plate's surface temperature measured at the stationary steady state condition ($T_{S,S}$) was used to calculate the stationary convective heat transfer coefficient (h_S), while the target plate's surface temperature measured at the rotation steady state condition ($T_{S,R}$) was used to calculate the rotation convective heat transfer coefficient (h_R) as follows:

$$h_S = \frac{q''_{gen}}{T_{S,S} - T_j} \tag{7-4}$$

$$h_R = \frac{q''_{gen}}{T_{S,R} - T_j} \tag{7-5}$$

Substituting equations 7-4 and7-5 in equation 7-2 yields expressions for the stationary and the rotational Nusselt numbers, Nu_S and Nu_R, respectively, as follows :

$$Nu_S = \frac{q''_{gen}\, D}{k\,(T_{S,S} - T_j)} \tag{7-6}$$

$$Nu_R = \frac{q''_{gen}\, D}{k\,(T_{S,R} - T_j)} \tag{7-7}$$

To evaluate the net change in Nusselt number, the rotational Nusselt number (Nu_R) was normalized against the stationary one (Nu_S) where q''_{gen}, D, and k are canceled out as follows:

$$Nu_R / Nu_S = \frac{T_{S,S} - T_j}{T_{S,R} - T_j} \tag{7-8}$$

7.3 Results and Discussion

Before studying the rotational effects on heat transfer, a baseline was created using a stationary case where the target plate was initially cooled with no rotation. When the steady state temperature profile was reached, the rotation began, and another thermal image was captured and compared against the stationary case. Therefore, for each case, two images were taken and analyzed together.

Each rotational thermal image was denoted as RX-Y, where X indicates the rotational speed (rpm) while Y represents the cooling air flowrate. Similarly, the stationary thermal images were named as SX-Y following the same naming procedure. Although there was no rotation, X was used to distinguish the stationary image corresponding to the specific X rotational value. Three different rpms of 36, 72, and 144 were investigated at three different cooling air flowrates. These flowrates resulted in a fully turbulent flow condition represented by a Reynolds number of (9,484), (16,676), and (28,492) The jet temperature was measured by the flowmeter and by neglecting the slight increase of the temperature as the flow travels from the feedline and reached to the exit of the nozzles. Also, as the flow increased, the recorded jet temperature varied from 18.3 °C to 22.9 °C for the minimum and the maximum flow, respectively. The complete legend of all cases can be found in Table 7-1.

Table 7-1: Rotation cases legend and details

<table>
<tr><th>Condition</th><th>Cooling air flowrate CFM (m^3/s)</th><th>Re_j</th><th>Recorded cooling air temperature (°C)</th><th>Rotational speed (RPM)</th><th>Abbreviation</th></tr>
<tr><td rowspan="9">Stationary</td><td rowspan="3">14.40 (0.006796)</td><td rowspan="3">9,484</td><td rowspan="3">18.3</td><td rowspan="9">N. A</td><td>S1-A</td></tr>
<tr><td>S2-A</td></tr>
<tr><td>S3-A</td></tr>
<tr><td rowspan="3">25.32 (0.011950)</td><td rowspan="3">16,676</td><td rowspan="3">19.6</td><td>S1-B</td></tr>
<tr><td>S2-B</td></tr>
<tr><td>S3-B</td></tr>
<tr><td rowspan="3">43.26 (0.020416)</td><td rowspan="3">28,492</td><td rowspan="3">22.9</td><td>S1-C</td></tr>
<tr><td>S2-C</td></tr>
<tr><td>S3-C</td></tr>
<tr><td rowspan="7">Rotation</td><td rowspan="3">14.40 (0.006796)</td><td rowspan="3">9,484</td><td rowspan="3">18.4</td><td>36</td><td>R1-A</td></tr>
<tr><td>72</td><td>R2-A</td></tr>
<tr><td>144</td><td>R3-A</td></tr>
<tr><td rowspan="3">25.32 (0.011950)</td><td rowspan="3">16,676</td><td rowspan="3">19.8</td><td>36</td><td>R1-B</td></tr>
<tr><td>72</td><td>R2-B</td></tr>
<tr><td>144</td><td>R3-B</td></tr>
<tr><td>43.26 (0.020416)</td><td>28,492</td><td>22.9</td><td>36</td><td>R1-C</td></tr>
</table>

		72	R2-C
		144	R3-C

7.3.1 Temperature Profile Analysis

A set of two heatmaps was used to extract the surface temperature profile. A sample of the generated heat maps is shown in Figure 7-5. The heat maps were post-processed and reproduced using a MATLAB script that reads the temperature profile from the original image that was converted to readable data (spreadsheet). The spreadsheet provides a temperature reading at every pixel in the thermal image. The MATLAB script is capable of cropping, rotating, and processing the distortion in the images. Additionally, better color pallets can be applied for better data representation. Figure 7-6 shows a sample of a raw and a regenerated thermal image.

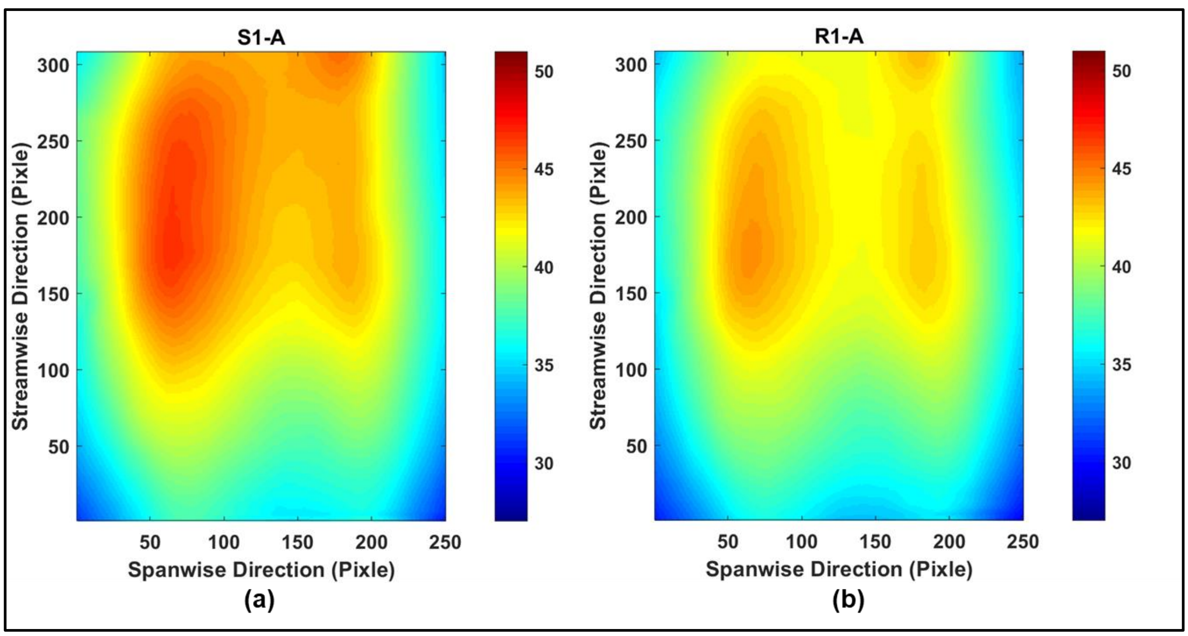

Figure 7-5: Thermal image set comparing stationary to the rotation

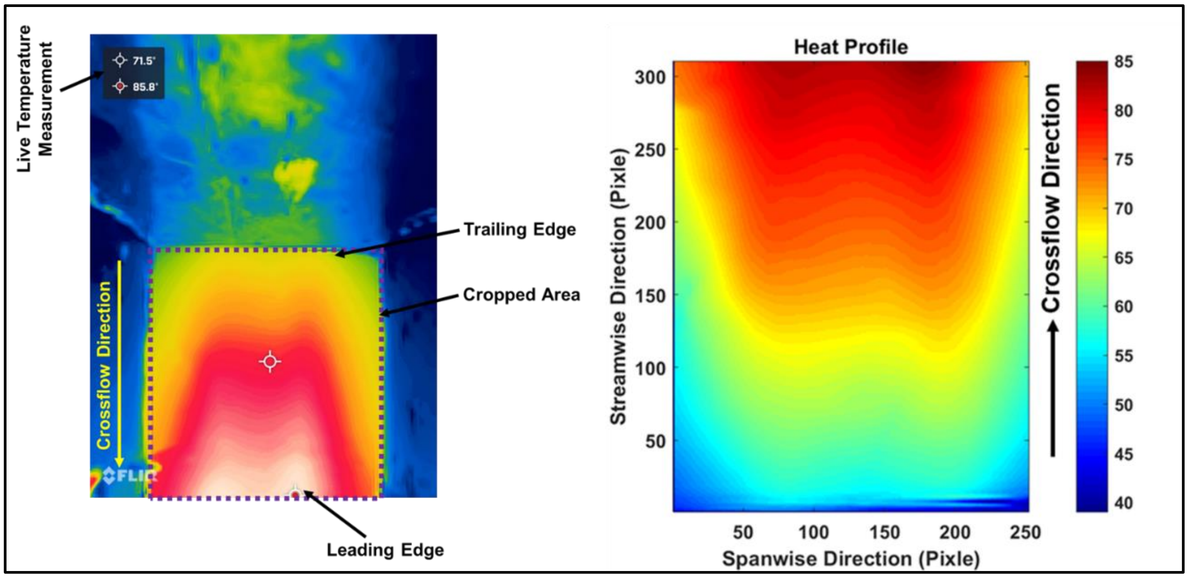

Figure 7-6: Thermal image reproduction, left: raw image, right: regenerated image

Line-averaged temperature profiles at different rotation speeds (rpms) and Reynolds number can be seen through Figure 7-7, Figure 7-8, and Figure 7-9. Generally, the temperature corresponding to the rotational cases slightly increased compared to the stationary cases towards the trailing edge as the rotation diverted the jets further towards the leading edge. The jet diversion is not only caused by the crossflow momentum. The rotational motion of the volume of the fluid between the exit of the nozzle and the surface of the target plate results in centrifugal and tangential force components. The tangential force component acts along the streamwise direction where it increases as the rotational speed increases. Hence, the comparison of different rotational speeds at the same Reynolds number shows higher temperature variation at the leading edge. However, the increase of the jets' momentum as the flow increases has a damping effect on the jet diversion. This observation can be made when comparing the higher flow Reynolds numbers at the same rotational speed.

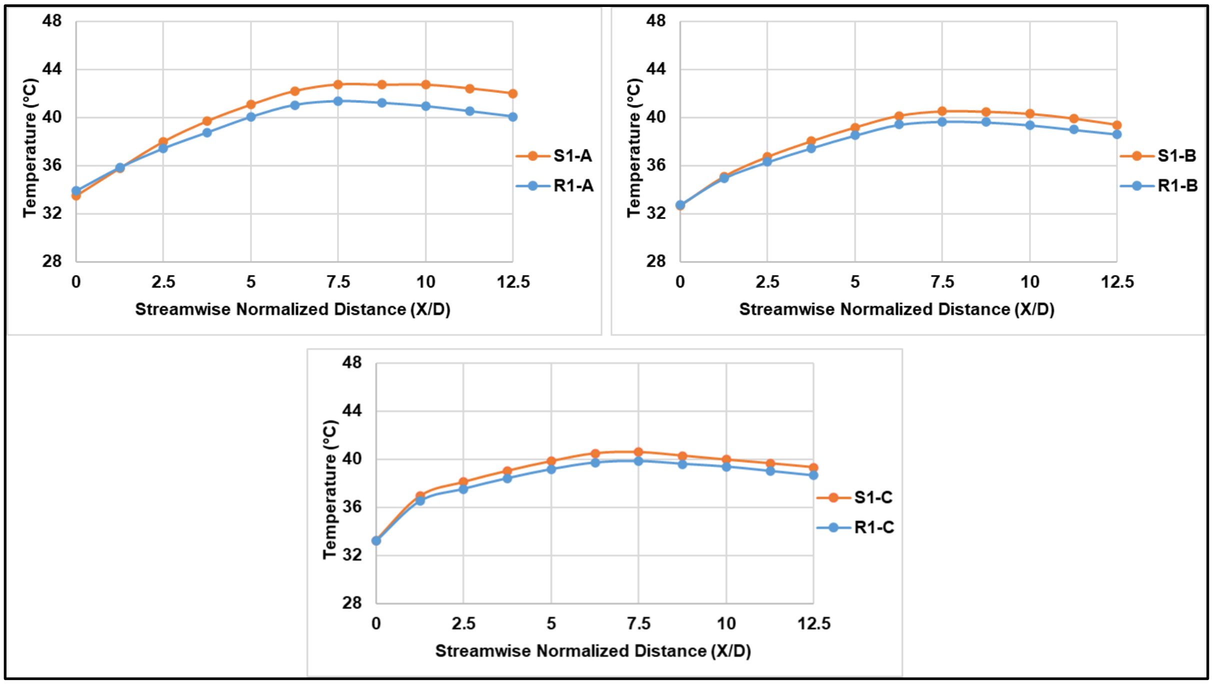

Figure 7-7: Line-averaged temperature profile comparison at R1 and different $\boldsymbol{Re_j}$

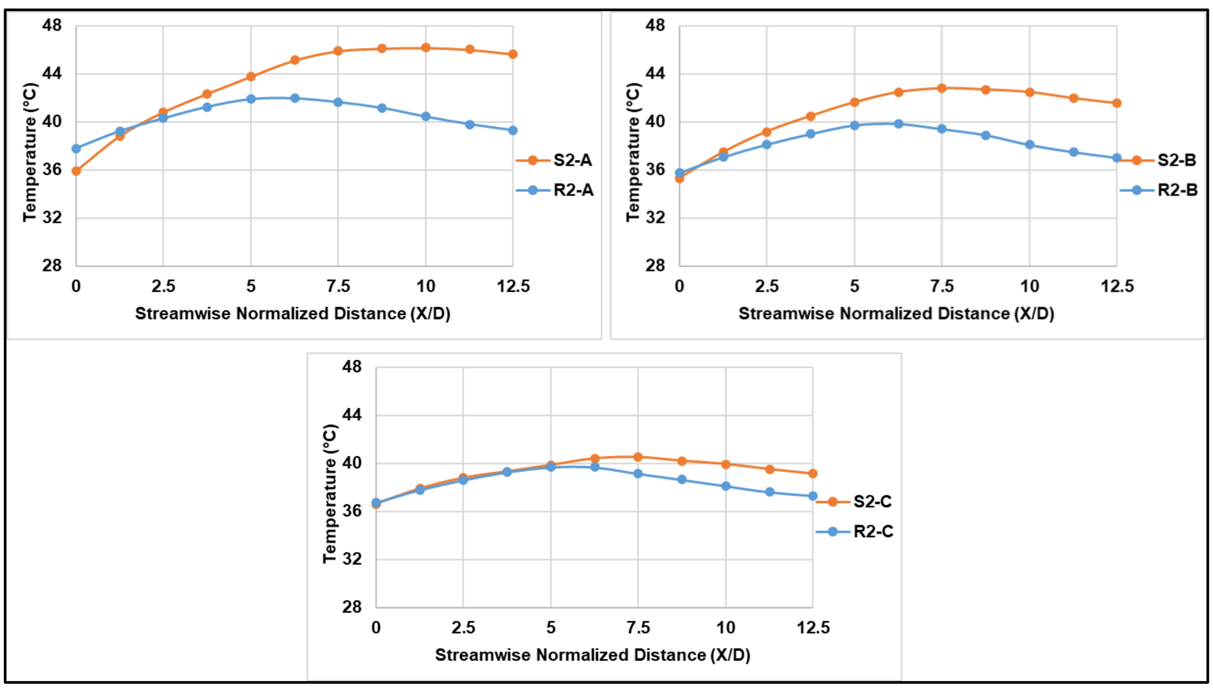

Figure 7-8: Line-averaged temperature profile comparison at R2 and different $\boldsymbol{Re_j}$

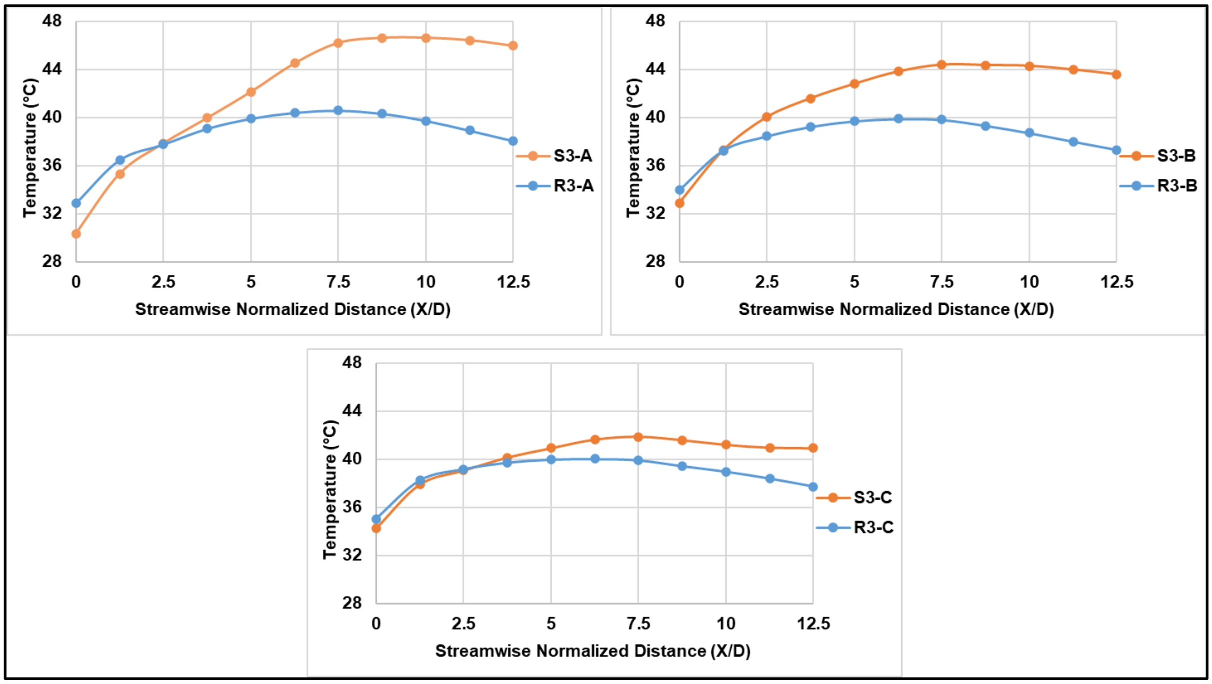

Figure 7-9: Line-averaged temperature profile comparison at R3 and different $\boldsymbol{Re_j}$

7.3.2 Normalized Line-Averaged Nusselt Number Analysis

As discussed in the previous sections, it is not practical to compare the temperature profiles of all cases since the heat flux profile can differ for each test run. Therefore, all cases have been normalized according to equation 7-8. The results are plotted in Figure 7-11, Figure 7-12, and Figure 7-13. Force analysis is essential to understand how the rotation influenced the heat transfer and the flow field. The force balance diagram shown in Figure 7-10 suggests the main components of the forces acting on the fluid's control volume. The crossflow-induced force was extensively studied previously in Chapters 5 and 6.

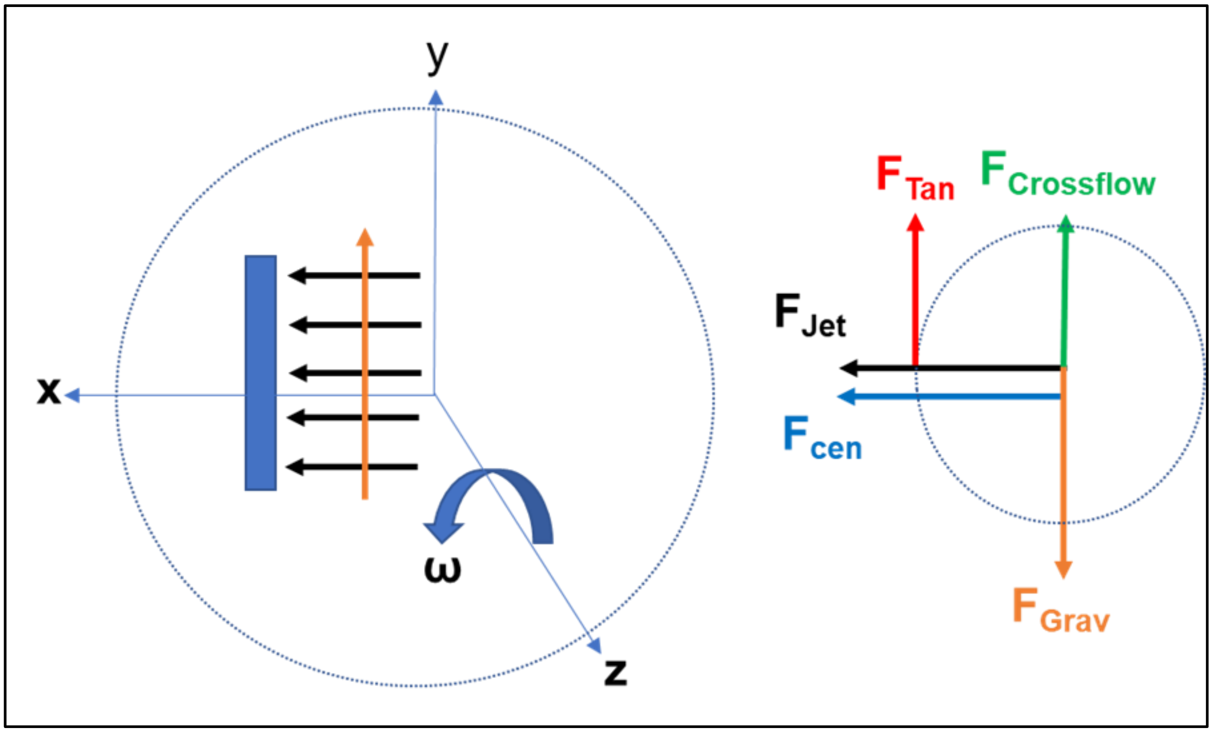

Figure 7-10: Force balance diagram

This force is countered by the gravitational force that has a minimal effect and can be ignored because of the small volume of the cooling air. Since the system can be imagined rotating (circular motion) and sliding (linear motion) at the same time, Coriolis force can also be considered. However, the Coriolis force has a minimal effect on the cooling air control volume. Therefore, the jet force, the tangential force (the reaction force), and the centrifugal force components govern the flow field. The radial forces components (the centrifugal and the jet momentum) act in the same direction towards the positive x-direction (outwards the circle), while the tangential force acts along the streamwise direction (y-direction). When the rotational speed increases, it results in a higher tangential force component that diverts the jets further towards the leading edge. This effect leads to delivering higher air flow to the leading edge compared to the trailing edge. The normalized Nusselt number curves shown in Figure 7-11, Figure 7-12, and Figure 7-13, are overlapped in the X/D region of 0 – 2.5. The overlapping seemed to reduce as the cooling air flowrate increased (increase in jet force) and it occurs in a shorter normalized distance. Additionally, this overlapping is increased as the rotational speed increases as the higher rotational speed exerts a higher tangential force component, therefore, the jets react in the opposite direction jets experience a higher tangential force component.

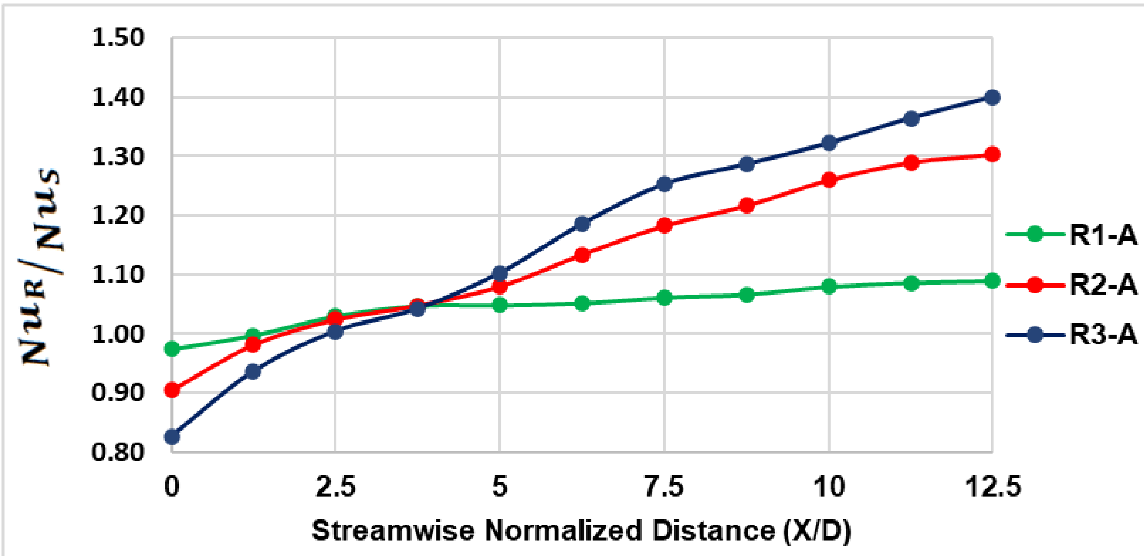

Figure 7-11: Normalized Nusselt number at $\boldsymbol{Re_j}$ = 9,484 and different rpms

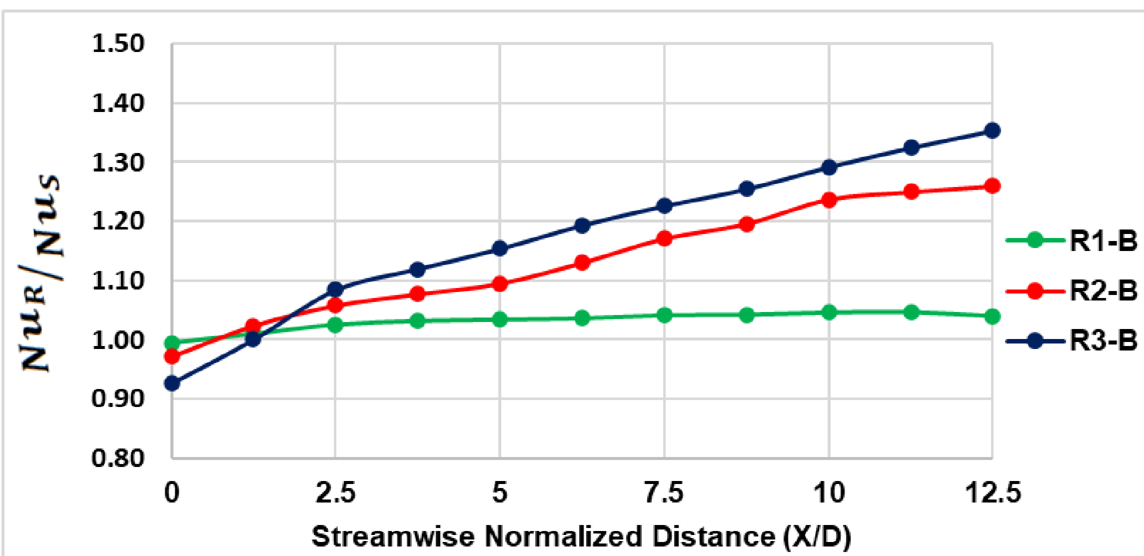

Figure 7-12: Normalized Nusselt number at $\boldsymbol{Re_j}$ = 16,676 and different rpms

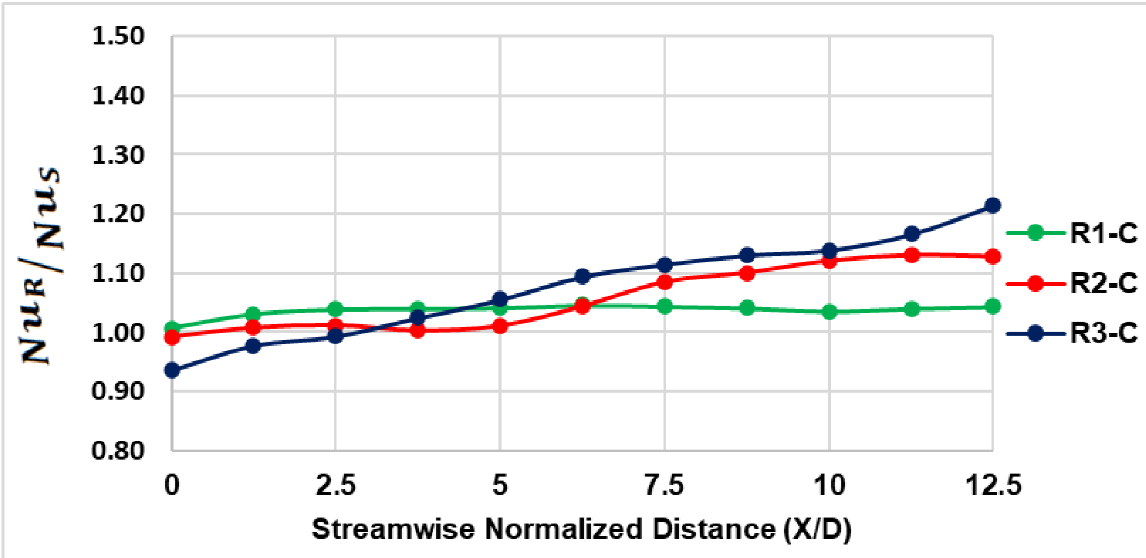

Figure 7-13: Normalized Nusselt number at $\boldsymbol{Re_j}$ = 28,492 and different rpms

7.4 Summary of Rotation Effects

The effect of rotation was experimentally studied under three rotational speeds (rpms) and three different Reynolds numbers (Re_j) in the turbulent flow regime and under non-uniform heat flux conditions. A comparison of subsequent stationary and rotational heatmaps was provided along with streamwise line-averaged temperature profiles and normalized line-averaged Nusselt number. The results showed that the rotation caused increased heat transfer rates on the target plate's leading edge compared to the trailing edge due to the jet diversion.

As the rotational speed increased, the jet diversion was increased due to the increased tangential force component. This diversion in jets was minimized as the jets' momentum increased (increase in jet Reynolds number).

CHAPTER 8: CONCLUSIONS AND FUTURE RECOMMENDATIONS

8.1 Conclusions

Experimental and numerical studies were conducted to better understand the main geometrical features that affect jet impingement cooling by investigating the heat transfer characteristics of a double exit crossflow scheme. A range of Reynolds number of 2,500 – 12,500 was covered to study the effect of Reynolds number on the heat transfer performance and to correlate the Nusselt number with Reynolds number for turbulent flow regime.

The increase in Reynolds number commonly resulted in a higher stagnation Nusselt number, peaking underneath the jets' middle row. The side rows of jets experienced higher spent air crossflows that resulted in redirecting and bending the jet flow streamline. Hence, it led to a degradation in Nusselt number along the streamwise direction. A cooling regression exponent (m) was found to match the available literature.

Comparing different stand-off distances for each flow case showed reduced Line-averaged and area-averaged Nusselt numbers as the stand-off distance increased. The reduction in Nusselt number was justified by the entrainment of the surrounding air that caused the loss of jets' momentum. Furthermore, jet active cooling regions were shifted further downstream as the stand-off distance increases due to the higher crossflow accumulations interacting more with the jet cores and each pair of jets before the impingement. It was also concluded that the in-line nozzle configuration could achieve higher heat transfer rates, especially at shorter stand-off distances. This is due to the more protection of the jets from the upstream row of jets as the spent air crossflow is given less distance to accelerate before striking the next row of jets. In the staggered arrangement, the influence of the crossflow is stronger as the crossflow accelerates and directly impacts the jets.

The jet-to-jet spacing effect was also studied. It was concluded that as the open area ratio decreases, the heat transfer performance decreases because of the larger area the nozzles cover.

Since the crossflow causes a great deal of jet distortion, bending, and Nusselt number degradation, it is worth looking into methods to minimize its effects. Therefore, the next chapter addresses the crossflow effects and proposes solutions to control them.

In this study, several crossflow mitigation techniques were also investigated. Two methods were achieved by attaching small and easy-to-manufactured crossflow diverters and circular jet extensions to protect jet cores from upstream crossflows and, therefore, enhance the heat transfer performance. The third technique was carried out by varying the jet diameter towards the channel exit. Three diverter shapes (cylinder, rectangle, and rib type) and two jet extensions (fixed height extended jets (EXTF) and variable height extended jets (EXTV)) were studied within a 25-jet array under laminar and turbulent flow regimes (Re of 2,500 – 10,000). Furthermore, three jet diameter increments of 5%, 10%, and 20% were examined.

The crossflow diverters and the extended jets affected the heat transfer performance such that the line-averaged Nu number distributions showed higher values than the baseline case. They also showed less to no shifted stagnation points at the downstream jets, where jet distortion is the most severe in the baseline case due to jet-to-jet interactions and the buildup of the crossflow. One drawback was the jet mass flux being less uniform than the baseline model. However, the Nusselt number peaks were unaffected by the air mass flux variation.

As the diverter was extended further into the flow field, more jet protection was achieved across all diverter shapes. The enhancement in Nusselt number peaked at an average of 10.5%, 11.3%, and 11.3% for cylindrical, rectangular, and ribbed shapes, respectively. The extension of the diverters' height posed an additional pressure drop that was quantified by normalizing the friction factor. For the extended jets, the enhancement in the Nusselt number peaked with an average of 18.2 and 15.7 for the EXTF and the EXTV, respectively. The EXTV Posed a slightly higher pressure drop.

As higher-pressure drops require higher pumping powers to drive the flow, the net heat transfer performance coefficient was introduced to correlate the desired enhancement in the Nusselt number with the pressure loss penalty. All diverters and extended jets showed above-unity values indicating that the enhancement in the Nusselt number dominated the pressure drop. The TQL cylindrical diverter offered a 5.2% increase in the net heat transfer performance, outperforming all other diverter shapes and heights. Overall, the cylindrical-shaped diverters showed better flow aerodynamics as they smoothly diverted the crossflows to form channels between every two rows of jets. This behavior was concluded according to the friction factor and flow pressure contours. Finally, the rectangular diverters were outperformed by cylindrical and ribbed, which is reasonable due to the less favorable aerodynamics because of the sharp edge geometry.

The EXTF showed the highest net heat transfer enhancement among all other techniques, and it offered an average of 13.4% net enhancement, while the EXTV offered 10.4%. Not only the extended jets showed higher net heat transfer enhancement, but they also resulted in less pressure drops and higher heat transfer with better mass flux distribution across all jet rows and more uniform heat loads. Finally, all heat transfer effectiveness results can be found in Figure 6-20, Figure 6-21, and Figure 6-22.

As the TQL cylindrical diverter showed the best heat transfer and flow field characteristics, a comparison between the extended jets and the TQL cylindrical diverter is shown in Figure 6-23. The comparison showed that the extended jets further enhance the heat transfer with less pressure drop penalty.

The variable jet diameter showed a minimal enhancement of Nusselt number not exceeding 2.09 % for the 5% increase in the jet diameter, and therefore no pressure loss analysis was performed. Also, as the jet diameters increased by 20%, they showed an adverse effect leading to a nonuniform heat distributions and less heat transfer rates of 2.76%.

The effect of rotation was experimentally studied under three rotational speeds (rpms) and three different Reynolds numbers (Re) in the turbulent flow regime and under non-uniform heat flux conditions. A comparison of subsequent stationary and rotational heatmaps was provided along with streamwise line-averaged temperature profiles and normalized line-averaged Nusselt number. The results showed that the rotation caused increased heat transfer rates on the target plate's leading edge compared to the trailing edge due to the jet diversion.

As the rotational speed increased, the jet diversion was increased due to the increased tangential force component. This diversion in jets was minimized as the jets' momentum increased (increase in jet Reynolds number).

8.2 Future Recommendations

The investigation of jet impingement cooling can be further extended to provide a complete platform that covers a wide variety of designs, variables, and data acquisition techniques. The below recommendations should be considered in future investigations:

A. Experimental task:

A.1. Enhance the current experimental setup to accommodate a wider range of variables such that higher values of Reynolds number and more elevated temperatures can be achieved, as well as providing better control over the stand-off distance, jet-to-jet spacing, and exit orientations in the existing setup.

A.2. Explore different cooling mediums that have desirable heat transfer properties (e.g.: heat capacity and thermal conductivity) such as glycol, nanofluids, and phase change coolants.

A.3. Investigate the end surface and tip conditions of the jets, such as the surface roughness and explore surface treatment opportunities and coatings to improve the aerodynamic performance and minimize the friction penalties.

A.4. Investigate curved and more complex geometries of the target plates and the fluid domain as the geometrical consideration can highly influence the design of cooling circuits.

B. Numerical task

B.1. Conduct numerical studies and simulations to mimic and simulate the rotational effects discussed in Chapter 7.

B.2. Explore and utilize more complicated models that can capture complex turbulence and solve for a higher scale level leading to a better understanding of the flow structures.

B.3. Introduce additional models to accommodate conduction and convection heat transfer.

REFERENCES

[1] F. Zhou, E. M. Dede and S. Joshi, "Modular jet impingement assemblies with passive and active flow control for electronics cooling". USDOE Patent 9445526, 13 09 2016.

[2] M. M. Rahman, "Investigation of Jet Impingement Cooling Using High Prandtl Number Fluids and Ammonia For Military Applications," Propulsion Directorate and Air Force Research Laboratory, Tampa, FL, 2004.

[3] D. Montorfano, A. Gaetano, M. C. Barbato, G. Ambrosetti and A. Pedretti, "CPV Cells Cooling System Based on Submerged Jet Impingement: CFD Modeling and Experimental Validation," in *AIP Conference Proceedings*, Switzerland, 2014.

[4] C. Soares, "Chapter 2: Historical Development of the Gas Turbine," in *Gas Turbines: A Handbook of Air, Land and Sea Applications*, Elsevier Inc., 2008.

[5] S. Patel, "A Brief History of GE Gas Turbines," POWER, 2019.

[6] Learn Engineering, 2020. [Online]. Available: https://engineeringlearn.com/gas-turbine-components-and-principle/. [Accessed 03 05 2022].

[7] I. Publishing, "Axial Flow Compressor," [Online]. Available: https://firecontrolman.tpub.com/14104/css/Axial-Flow-Compressor-91.htm. [Accessed 22 6 2021].

[8] H. Zinjala, "Heat Transfer Analysis of The Cooling Ring in Gas Turbine Combustor," 2010.

[9] A. H. Jaaz, H. A. Hasan, K. Sopian, A. H. Kadhum, T. S. Gaaz and A. A. Alamiery, "Outdoor Performance Analysis of a Photovoltaic Thermal (PVT) Collector with Jet Impingement and Compound Parabolic Concentrator (CPC)," *Materials*, vol. 10, no. 8, p. 888, 2017.

[10] C. Han, S. Dutta and S. Ekkad, Gas Turbine Heat Transfer and Cooling Technology, Second Edition, 2nd ed., vol. 1, Taylor & Francis, 2013.

[11] H. C. Hyung, M. K. Kyung and S. Jiwoon, "Applications of Impingement Jet Cooling Systems," *Engineering and Applications, Nova Science Publishers, Inc,* pp. 37-67, 2011.

[12] B. Kwon, T. Foulkes, T. Yang, N. Miljkovic and W. P. King, "Air Jet Impingement Cooling of Electronic Devices Using Additively Manufactured Nozzles," *IEEE Transactions on Components, Packaging and Manufacturing Technology*, vol. 10, no. 2, pp. pp. 220-229, 2020.

[13] J. Lee, Z. Ren, P. Ligrani, M. D. Fox and H. K. Moon, "Crossflows from Jet Array Impingement Cooling: Hole Spacing, Target Plate Distance, Reynolds Number Effects,," *International Journal of Thermal Sciences*, pp. 7-18, 2015.

[14] Y. Xing and B. Weiganad, "Optimum Jet-to-Plate Spacing of Inline Impingement Heat Transfer for Different Crossflow Schemes," *ASME. J. Heat Transfer*, vol. 135, no. 7, 2013.

[15] D. E. Metzger, L. Florschuetz, D. Takeuchi, R. Behee and R. A. Berry, "Heat Transfer Characteristics for Inline and Staggered Arrays of Circular Jets with Crossflow of Spent Air," *Journal of Heat Transfer,* vol. 101, no. 3, pp. 526-531, 1979.

[16] W. H. Makatar, T. Perapong and C. Nuntadusit, "Influence of Nozzle Arrangement on Flow and Heat Transfer Characteristics of Arrays of Circular Impinging Jets," *Songklanakarin Journal of Science and Technology,* vol. 35, no. 2, p. 203 – 212, 2013.

[17] L. W. Florschuetz, C. R. Turman and D. E. Metzger, "Streamwise Flow and Heat Transfer Distributions for Jet Array Impingement with Crossflow," in *ASME 1981 International Gas Turbine Conference and Products Show*, 1981.

[18] J. M. Miao, C. Y. Wu and P. H. Chen, "Numerical Investigation of Confined Multiple-Jet Impingement Cooling Over a Flat Plate at Different Crossflow Orientations," *Numerical Heat Transfer, Part A: Applications: An International Journal of Computation and Methodology,* vol. 55, no. 11, pp. 1019-1050, 2009.

[19] J. Y. San and J. J. Chen, "Effects of Jet-to-Jet Spacing and Jet Height on Heat Transfer Characteristics of An Impinging Jet Array," *International Journal of Heat and Mass Transfer,* vol. 71, no. 0017-9310, pp. 8-17, 2014.

[20] J. Y. San, Y. M. Tsou and Z. C. Chen, "Impingement Heat Transfer of Staggered Arrays of Air Jets Confined in A Channel," *International Journal of Heat and Mass Transfer,* vol. 50, no. 19-20, pp. 3718-3727, 2007.

[21] X. Wang, R. Liu and X. Bai, "Numerical Study on Flow and Heat Transfer Characteristics of Jet Impingement," in *ASME Turbo Expo, GT2011-45287*, Vancouver, British Columbia, Canada, 2011.

[22] P. Brevet, C. Dejeu, E. Dorignac, M. Jolly and j. j. Vullierme, "Heat Transfer to a Row of Impinging Jets in Consideration of Optimization," *International Journal of Heat and Mass Transfer,* vol. 45, no. 20, pp. 4191-4200, 2002.

[23] J. San and W. Z. Shiao, "Effects of Jet Plate Size and Plate Spacing on the Stagnation Nusselt Number for a Confined Circular Air Jet Impinging on a Flat Surface," *International Journal of Heat and Mass Transfer,* vol. 49, no. 19-20, pp. 3477-3486, 2006.

[24] F. Nourin, A. R. Salem and R. Amano, "Investigation of Jet Impingement Cooling for Gas Turbine Blade with In-line and Staggered Nozzle Arrays," *International Journal of Energy for a Clean Environment,* vol. 21, no. 2, pp. 169-182, 2020.

[25] A. R. Salem, F. Nourin, M. Abousabae and R. Amano, "Experimental and Numerical Study of Jet Impingement Cooling for Improved Gas Turbine Blade Internal Cooling with In-Line and Staggered Nozzle Arrays," *ASME. J. Energy Resour. Technol,* vol. 143, no. 1, 2021.

[26] E. M. Olsson, L. M. Ahrne and A. C. Tragardh, "Flow and Heat Transfer From Multiple Slot Air Jets Impinging On Circular Cylinders," *Journal of food engineering*, vol. 67, no. 3, pp. 273-280, 2013.

[27] C. Nuntadusit, W. H. Makatar, P. Tekasakul and S. Eiamsa-ard, "Local Heat Transfer Characteristics of Array Impinging Jets from Elongated Orifices," *International Communications in Heat and Mass Transfer,* vol. 39, no. 8, pp. 1154-1164, 2012.

[28] M. Keenan, R. S. Amano and S. Ou, "Study of An Impingement Cooling Jet Array for Turbine Blade Cooling with Single and Double Exit Cases," in *ASME Turbo Expo 2013: Turbine Technical Conference and Exposition,* 2013.

[29] M. Chaudhari, B. Puranik and A. Agrawal, "Effect of orifice shape in synthetic jet based impingement cooling," *Experimental Thermal and Fluid Science,* vol. 34, no. 2, pp. 246-256, 2009.

[30] D. Violato, A. Ianiro, G. Cardone and F. Scarano, "Three-Dimensional Vortex Dynamics and Convective Heat Transfer in Circular and Chevron Impinging Jets," *International Journal of Heat and Fluid Flow,* vol. 37, no. 0142-727X, pp. 22-36, 2012.

[31] R. H. Martin and J. M. Buchlin, "Jet Impingement Heat Transfer from Lobed Nozzles," *International Journal of Thermal Sciences,* vol. 50, no. 7, pp. 1199-1206, 2011.

[32] T. Guan, J. Z. Zhang and Y. Shan, "Conjugate Heat Transfer on Leading Edge of A Conical Wall Subjected to External Cold Flow and Internal Hot Jet Impingement from Chevron Nozzle – Part 2: Numerical Analysis," *International Journal of Heat and Mass Transfer,* vol. 106, no. 0017-9310, pp. 339-355, 2017.

[33] J. L. Rutledge, P. I. King and R. B. Rivir, "Influence of Film Cooling Unsteadiness on Turbine Blade Leading Edge Heat Flux," *ASME J. Eng. Gas Turbines Power,* vol. 134, p. 071901, 2012.

[34] V. J. Zimmer, J. L. Rutledge, C. Knieriem and S. Ou, "The Influence of Coolant Unsteadiness on Impingement Heat Transfer," in *ASME Turbo Expo 2014: Turbine Technical Conference and Exposition*, 2014.

[35] H. Herwig and G. Middelberg, "The Physics of Unsteady Jet Impingement and its Heat Transfer Performance," in *Acta Mechanica*, 2008.

[36] M. Zukowski, "Heat Transfer Performance of A Confined Single Slot Jet of Air Impinging on A Flat Surface," *International Journal of Heat and Mass Transfer,* vol. 57, no. 2, pp. 484-490, 2013.

[37] M. Kristiawan, A. Meslem, I. Nastase and V. Sobolik, "Wall Shear Rates and Mass Transfer in Impinging Jets: Comparison of Circular Convergent and Cross-Shaped Orifice Nozzles," *International Journal of Heat and Mass Transfer,* vol. 55, no. 1–3, pp. 282-293, 2012.

[38] Y. Yamane, M. Yamamoto and M. Moto, "Effect of Jet Shape of Square Array of Multi-Impinging Jets on Heat Transfer," *Proc. ASME. GT2013,* vol. Volume 3A: Heat Transfer, 2013.

[39] A. C. Chambers, D. R. Gillespie, D. R. H. P. T. Ireland and R. Kingston, "Enhancement of Impingement Cooling in a High Cross Flow Channel Using Shaped Impingement Cooling Holes," *ASME. J. Turbomach.*, vol. 132, no. 2, 2010.

[40] S. B. Ingole and K. K. Sundaram, "Experimental Average Nusselt Number Characteristics with Inclined Non-Confined Jet Impingement of Air for Cooling Application," *Experimental Thermal and Fluid Science*, vol. 77, no. 0894-1777, pp. 124-131, 2016.

[41] A. B. Bhagwat and A. Sridharan, "Numerical Simulation of Oblique Air Jet Impingement on a Heated Flat Plate," *ASME. J. Thermal Sci. Eng. Appl.*, vol. 9, no. 1, 2017.

[42] X. Zhang, S. Yarusevych and S. D. Peterson, "Experimental Investigation of Flow Fevelopment and Coherent Structures in Normal and Oblique Impinging Slot Jets," *Exp Fluids*, vol. 60, no. 11, 2019.

[43] K. Baghel, A. Sridharan and J. Srree, "Experimental and Numerical Study of Inclined Free Surface Liquid Jet Impingement," *International Journal of Thermal Sciences*, vol. 154, no. 1290-0729, 2020.

[44] P. R. Parida, S. V. Ekkad and K. Ngo, "Experimental and Numerical Investigation of Confined Oblique Impingement Configurations for High Heat Flux Applications," *International Journal of Thermal Sciences*, vol. 50, no. 6, pp. 1037-1050, 2011.

[45] M. Attalla, H. M. Maghrabie and E. Specht, "Effect of Inclination Angle of A Pair of Air Jets on Heat Transfer Into the Flat Surface," *Experimental Thermal and Fluid Science,* vol. 85, no. 0894-1777, pp. 85-94, 2017.

[46] A. Y. Tong, "On the Impingement Heat Transfer of An Oblique Free Surface Plane Jet," *International Journal of Heat and Mass Transfer,* vol. 46, no. 11, pp. Pages 2077-2085, 2003.

[47] S. Pawar and D. K. Patel, "The Impingement Heat Transfer Data of Inclined Jet in Cooling Applications: A Review," *Journal of Thermal Science*, vol. 29, pp. 1-12, 2020.

[48] C. Nuntadusit, M. Wae-Hayee, A. Bunyajitradulya and S. Eiamsa-ard, "Visualization of Flow and Heat Transfer Characteristics for Swirling Impinging Jet," *International Communications in Heat and Mass Transfer*, vol. 39, no. 5, pp. 640-648, 2012.

[49] P. Singh, Y. Aider and A. Kaurb, "Swirl jet impingement heat transfer: Effect of jet-to-target spacing, jet Reynolds number and orientation with flat target," *International Journal of Thermal Sciences,* vol. 184, p. 107993, 2023.

[50] H. Fawzy, Q. Zheng, N. Ahmad and Y. Jiang, "Optimization of A Swirl with Impingement Compound Cooling Unit for A Gas Turbine Blade Leading Edge," *Energies* , vol. 13, no. 1, p. 210, 2020.

[51] H. Q. Yang, T. Kim, T. J. Lu and K. Ichimiya, "Flow Structure, Wall Pressure and Heat Transfer Characteristics of Impinging Annular Jet with/without Steady Swirling," *International Journal of Heat and Mass Transfer*, vol. 53, no. 19-20, 2010.

[52] M. Y. Wen, "Flow Structures and Heat Transfer of Swirling Jet Impinging on A Flat Surface with Micro-Vibrations," *International Journal of Heat and Mass Transfer,* vol. 48, no. 3-4, pp. 545-560, 2005.

[53] F. Afroz and M. A. Sharif, "Numerical Investigation of Heat Transfer from A Plane Surface Due to Turbulent Annular Swirling Jet Impingement," *International Journal of Thermal Sciences,* vol. 151, no. 1290-0729, p. 106257, 2022.

[54] R. E. Chupp, H. E. Helms, P. W. Mcfadden and T. R. Brown, "Evaluation of Internal Heat-Transfer Coefficients for Impingement-Cooled Turbine Airfoils.," *J. Aircraft*, vol. 6, no. 3, p. 203, 1969.

[55] M. Fenot, E. Dorignac and J.-J. Vullierme, "An Experimental Study on Hot Round Jets Impinging a Concave Surface," *International Journal of Heat and Fluid Flow,* vol. 29, no. 4, pp. Pages 945-956, 2008.

[56] C. Cornaro, A. S. Fleischer, M. Rounds and R. J. Goldstein, "Jet Impingement Cooling of a Convex Semi-Cylindrical Surface," *Int. J. Therm. Sci.*, vol. 40, p. 890–898, 2001.

[57] F. Selimefendigil and H. F. Öztopb, "Hybrid Nano-Jet Impingement Cooling of a Curved Elastic Hot Surface Under the Combined Effects of Non-Uniform Magnetic Field and Upper

Plate Inclination," *Journal of Magnetism and Magnetic Materials,* vol. 561, no. ISSN 0304-8853,, p. 169684, 2022.

[58] S. Dushyant, B. Premachandran and S. Kohli, "Experimental and numerical investigation of jet impingement cooling of a circular cylinder," *International Journal of Heat and Mass Transfer,,* vol. 60, no. 0017-9310,, pp. 672-688,, 2013.

[59] H. K. D. Iacovides, B. E. Launder and J. X. Z. Li, "Experimental Study of the Flow and Thermal Development of a Row of Cooling Jets Impinging on a Rotating Concave Surface," *J. Turbomach.,* vol. 127, no. 1, pp. 222-229, 2005.

[60] T. J. Craft, H. Iacovides and N. A. Mostafa, "Modelling of Three Dimensional Jet Array Impingement and Heat Transfer on a Concave Surface," *Int. J. Heat Fluid Flow,* vol. 29, no. 3, p. pp. 687–702., 2008.

[61] S. Madhavan, K. R. Ramakrishnan, P. Singh and S. Ekkad, "Jet Impingement Heat Transfer Enhancement by U-Shaped Crossflow Diverters," *ASME. J. Thermal Sci. Eng. Appl.,* vol. 12, no. 4, p. 041005, 2020.

[62] B. J. wang, S. H. Kim, W. G. Joo and H. H. Cho, "A Study on Fluid Flow and Heat Transfer of a Corrugated Structure for Crossflow Reduction of Impingement Jet," *Transactions of the Korean Society of Mechanical Engineers B,* vol. 41, no. 5, pp. 329-339, 2017.

[63] K. Yeranee, M. Wae-Hayee, I. Piya, Y. Rao and C. Nuntadusit, "The Study of Flow and Heat Transfer Characteristics of Impinging Jet Array Mounting Air-Induced Duct," in *IOP Conference Series: Materials Science and Engineering, Volume 243, 2nd International*

Conference on Computational Fluid Dynamics in Research and Industry (CFDRI 2017), Songhkla, Thailand, 2017.

[64] E. I. Esposito, S. V. Ekkad, Y. Kim and P. Dutta, "Novel Jet Impingement Cooling Geometry for Combustor Liner Backside Cooling," *ASME. J. Thermal Sci. Eng. Appl.,* vol. 1, no. 2, p. 021001, 2009.

[65] J. He, Q. Deng, K. Xiao and Z. Feng, "Heat Transfer Enhancement of Impingement Cooling by Different Crossflow Diverters," *ASME. J. Heat Transfer*, vol. 144, no. 4, p. 042001, 2022.

[66] S. N. Parbat, S. C. Siw and M. K. Chyu, "Impingement Cooling in Narrow Rectangular Channel with Novel Surface Features," in *ASME Turbo Expo: Turbomachinery Technical Conference and Exposition*, Seoul, South Korea, 2016.

[67] C. Zhongran, R. Kan, R. Jing and J. Hongde, "Experimental and Numerical Study of the Anti-Crossflows Impingement Cooling Structure," *International Journal of Heat and Mass Transfer*, vol. 64, no. 0017-9310,, pp. 567-580, 2013.

[68] A. Terzis, P. Ott, M. Cochet, V. Wolfersdorf and B. Weigand, "Effect of Varying Jet Diameter on the Heat Transfer Distributions of Narrow Impingement Channels," in *ASME. J. Turbomach.*, 2014.

[69] S. Fechter, A. Terzis, P. Ott, B. Weigand, J. V. Wolfersdorf and M. Cochet, "Experimental and Numerical Investigation of Narrow Impingement Cooling Channels," *International Journal of Heat and Mass Transfer,* vol. 67, no. 0017-9310, pp. 1208-1219, 2013.

[70] S. K. Hong, D. H. Lee and H. H. Cho, "Effect of Jet Direction On Heat/Mass Transfer of Rotating Impingement Jet," *Applied Thermal Engineering,* vol. 29, no. 14–15, pp. 2914-2920,, 2009.

[71] Q. Lu, R. Muthukumar, H. Ge and S. Parameswaran, "Numerical study of a rotating liquid jet impingement cooling system," *International Journal of Heat and Mass Transfer,* vol. 163, p. 120446, 2020.

[72] H. Li, H. Deng and L. Qiu, "Effect of Channel Orientation on Heat Transfer in a Rotating Impingement Cooling Channel,," *International Journal of Heat and Mass Transfer,* vol. 187, no. 0017-9310, p. 122493, 2022.

[73] A. Safi, M. O. Hamdan and E. Elnajjar, "Numerical Investigation on the Effect of Rotation on Impingement Cooling of the Gas Turbine Leading Edge," *Alexandria Engineering Journal,* vol. 59, no. 5, p. 3781–3797, 2020.

[74] H. Li, H. Deng and L. Qiu, "Effect of Channel Orientation on Heat Transfer in a Rotating Impingement Cooling Channel," *International Journal of Heat and Mass Transfer,* vol. 187, no. 0017-9310, p. 122493, 2021.

[75] M. S. Saravani, N. J. DiPasquale, S. Beyhaghi and R. S. Amano, "Heat Transfer in Internal Cooling Channels of Gas Turbine Blades: Buoyancy and Density Ratio Effects," *ASME. J. Energy Resour. Technol.* , vol. 141, no. 11, p. 112001, 2019.

[76] F. Nourin and R. Amano, "STUDY ON HEAT TRANSFER ENHANCEMENT OF GAS TURBINE BLADES," *International Journal of Energy for a Clean Environment,* vol. 21, no. 2, pp. 91-106, 2020.

[77] F. Nourin, B. L. Blum and R. S. Amano, "Exploring the Effects of Guide Vane on Dimpled Cooling Channel of Gas Turbine Blade," *ASME. J. Energy Resour. Technol.*, vol. 145, no. 5, p. 051702, 2023.

[78] M. S. Saravani, R. S. Amano, N. J. DiPasquale, J. Halmo and W, " Turning Guide Vane Effect on Internal Cooling of Two-Passage Channel With Parallel Ribs," *ASME. J. Energy Resour. Technol.*, vol. 142, no. 9, p. 091303, 2020.

[79] S. A. R. &. L. J. Kumar, "Numerical Simulations of Heat Transfer Distribution of A Two-Pass Square Channel with V-Rib Turbulator and Bleed Holes," *Heat Mass Transfer,* vol. 49, no. 1, p. 1141–1158, 2013.

[80] AMETEK, "Optimal Distribution," ROTRON REGENERATIVE BLOWER DR202Y9M 080564 115/230VAC 0.33 HP ONE PHASE, , [Online]. Available: https://optimaldist.com/products/dr202y9m-080564-rotron-regen-blower-115-230vac-33-hp-one-phase?utm_source=google&utm_medium=search&utm_campaign=RotronRegen&gclid=Cj0KCQiA2-2eBhClARIsAGLQ2Rn_2M63biVV8ucEWgAcZnVluw-rdOlpMHEhztgxRrvH-XHRTPwCoroaApPrEALw_wcB. [Accessed 22 5 2020].

[81] Alicat, "Instrumart," ALICAT, [Online]. Available: https://www.instrumart.com/products/48576/alicat-scientific-mq-series-mass-flow-meters?gclid=Cj0KCQiA2-2eBhClARIsAGLQ2RndM0tyUKLP5iWh27oG23DN5HyjMCX_a00EJTHji08d71wqS2AgdlIaAherEALw_wcB. [Accessed 20 3 2019].

[82] T. FLIR, "Teledyne FLIR," 2017. [Online]. Available: https://www.flir.com/products/a35/?vertical=rd+science&segment=solutions. [Accessed 20 1 2019].

[83] V. J. Zimmer, J. L. Rutledge, C. Knieriem and S. Ou, "The Influence of Coolant Unsteadiness on Impingement Heat Transfer," in *ASME Turbo Expo 2014: Turbine Technical Conference and Exposition. American Society of Mechanical Engineers Digital Collection*, 2014.

[84] A. Schroder, S. Ou and U. Ghia, "Experimental Study of Impingement Cooling Jet Array Using an Infrared Thermography Technique," *Journal of Thermophysics and Heat Transfer,* vol. 26, no. 4, pp. 590-597, 2011.

[85] R. B. Bird, W. E. Stewart and E. N. Lightfoot, Transport Phenomena, 2nd ed., W. Anderson and P. Kulek, Eds., Madison: John Wiley & Sons, Inc,, 2002.

[86] J. R. Welty, G. L. Rorrer and D. G. Foster, Fundamentals of Momentum, Heat, and Mass Transfer, 6th ed., D. Sayre, Ed., Wiley & Sons Inc., 2013.

[87] W. P. Jones and B. E. Launder, "The Prediction of Laminarization with A Two-Equation Model of Turbulence," *International Journal of Heat and Mass Transfer,* vol. 15, no. 2, pp. 301-314, 1972.

[88] B. Weigand and S. Spring, "Multiple Jet Impingement – A Review," *Heat Transfer Research,* vol. 22, no. 2, pp. pp. 201-142, 2011.

[89] J. F. Fan, W. K. Ding, J. F. Zhang, Y. L. He and W. Q. Tao, "A Performance Evaluation Plot of Enhanced Heat Transfer Techniques Oriented for Energy-Saving," *Int. J. Heat and Mass Transfer,* vol. 52, no. (1–2), p. pp. 33–44., 2009.

[90] I. VP, "VPFlowScope In-line flow meter," [Online]. Available: https://www.vpinstruments.com/product/vpflowscope-in-line-d0-d1/. [Accessed 14 11 2022].

[91] Newark, "Flexible Heater, Silicone Rubber," Omega, [Online]. Available: https://www.newark.com/. [Accessed 12 3 2022].

[92] F. Teledyne, "FLIR ONE® Edge Pro," Flir, [Online]. Available: https://www.flir.com/products/flir-one-edge-pro/. [Accessed 20 11 2022].

[93] W. M. Kays and A. L. London, Compact heat exchangers, United States, 1984.

[94] D. B. Tuckerman and R. F. W. Pease, "High-performance heat sinking for VLSI," *IEEE Electron Device Letters*, vol. 2, no. 5, pp. 126-129, 1981.

APPENDIX A: INLINE CFD PROCESSED HEATMAPS

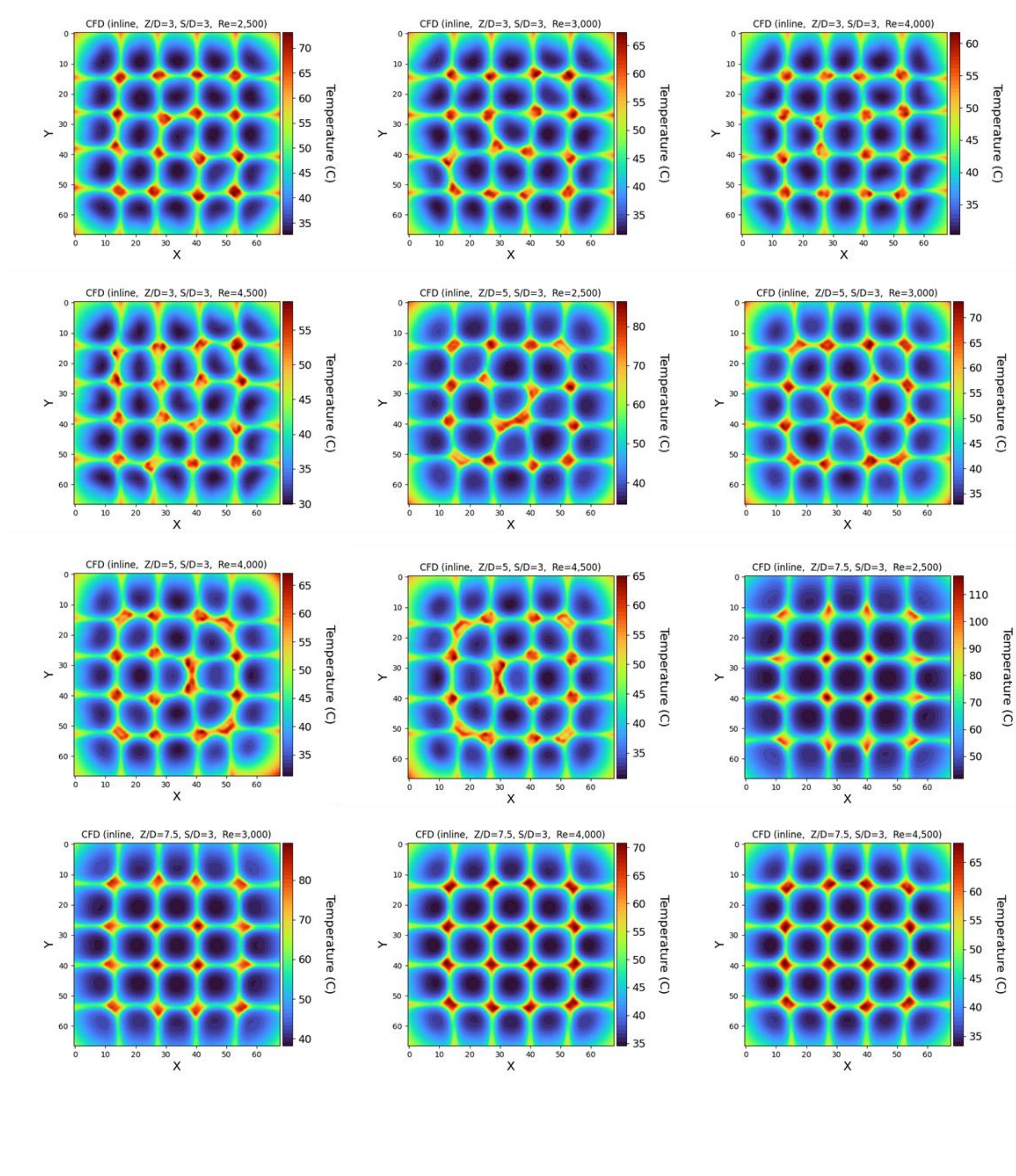

APPENDIX B: STAGGERED CFD PROCESSED HEATMAPS

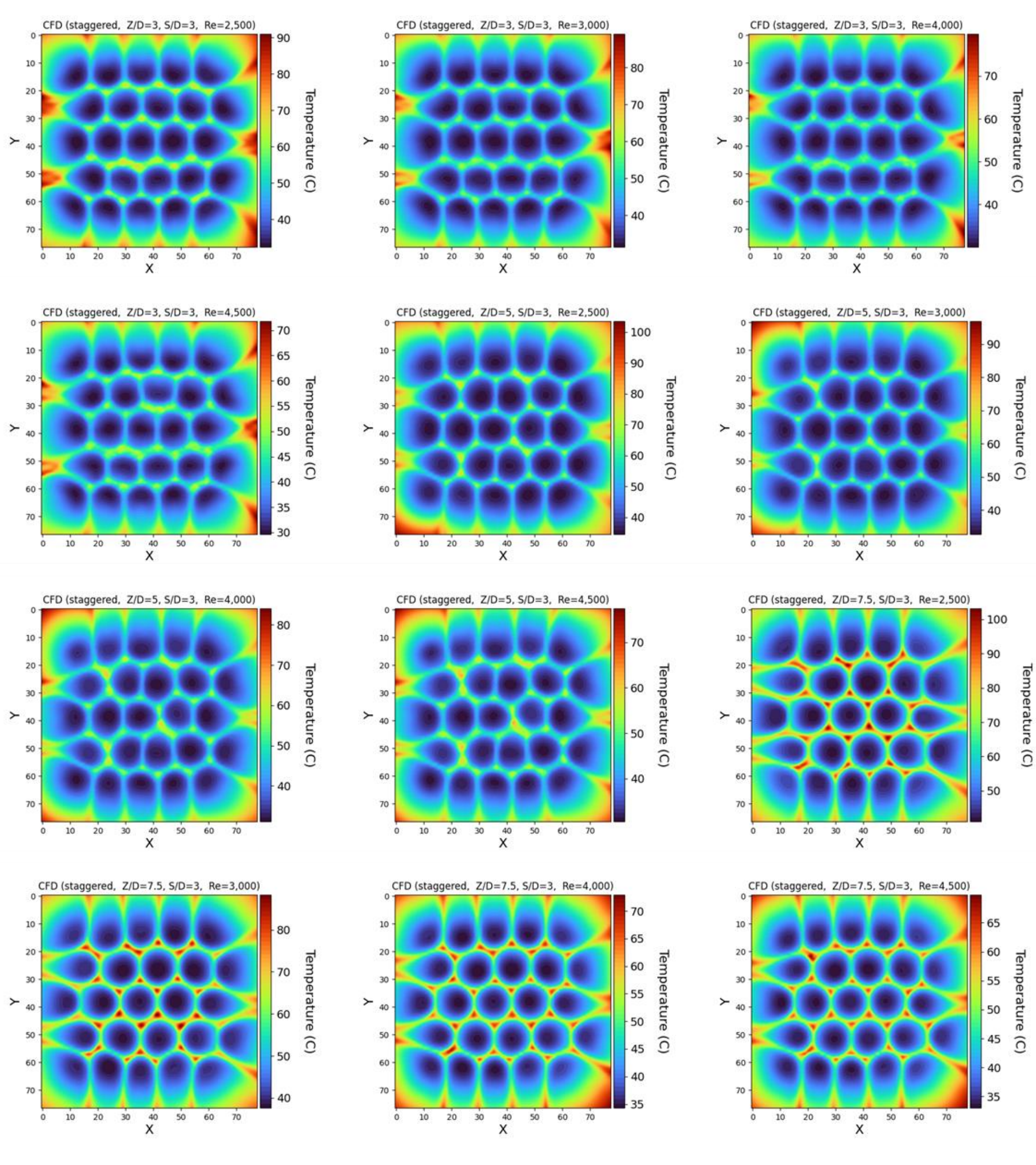

APPENDIX C: INLINE EXP PROCESSED HEATMAPS

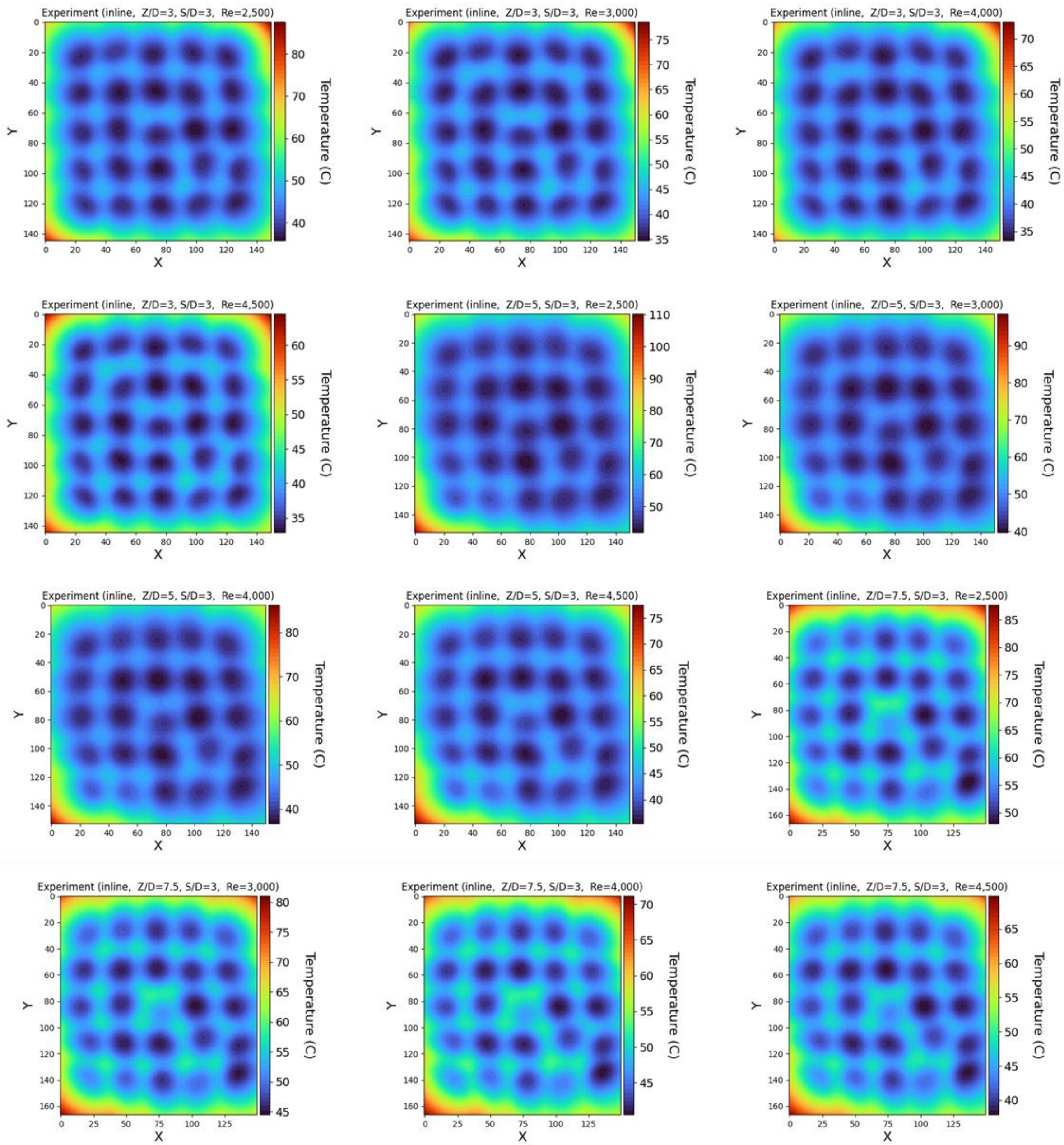

APPENDIX D: STAGGERED EXP PROCESSED HEATMAPS

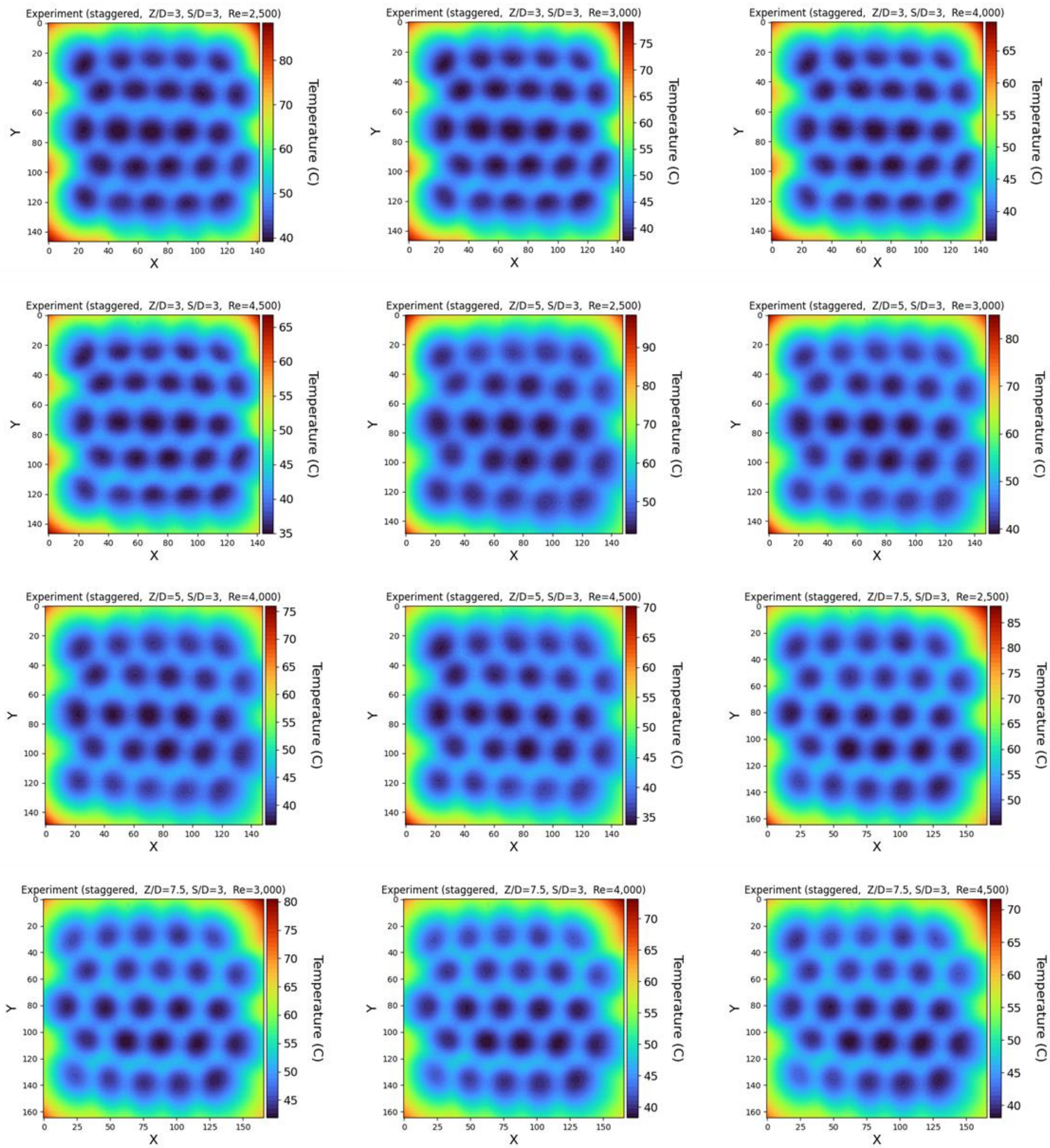

APPENDIX E: EFFECT OF Re_j - INLINE $\overline{Nu_L}$ CHARTS

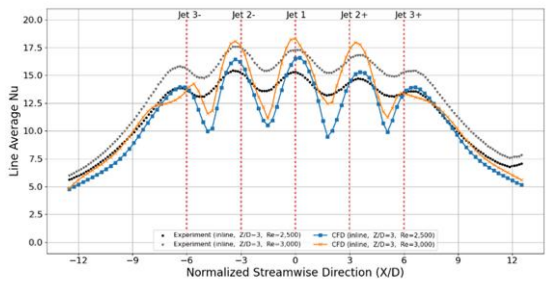

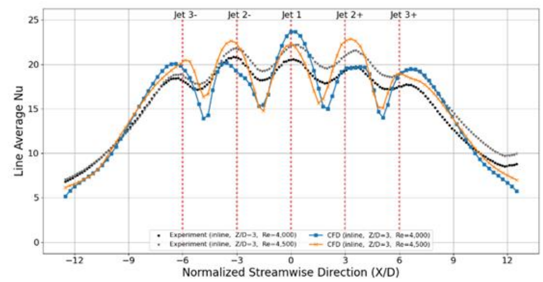

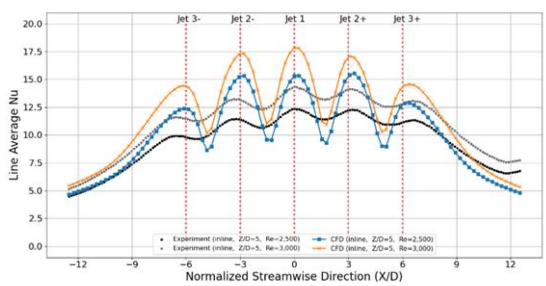

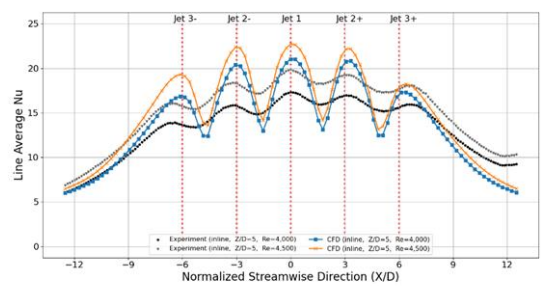

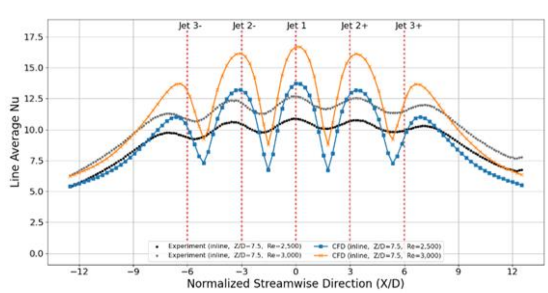

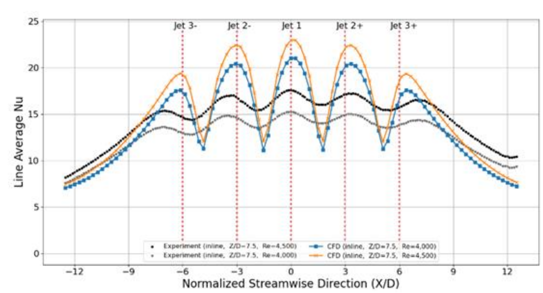

APPENDIX F: EFFECT OF Re_j - STAGGERED $\overline{Nu_L}$ CHARTS

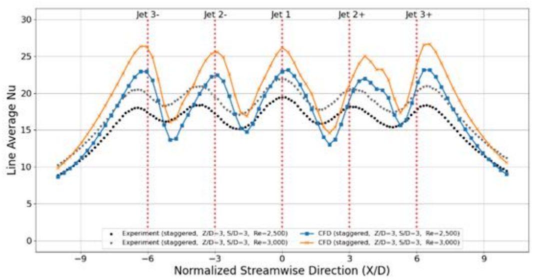

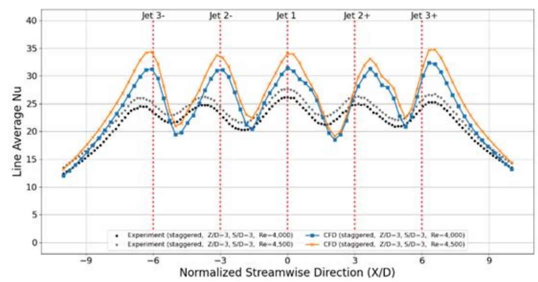

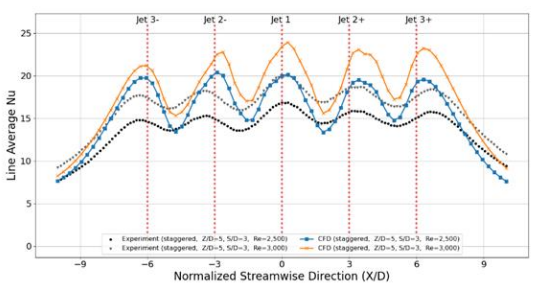

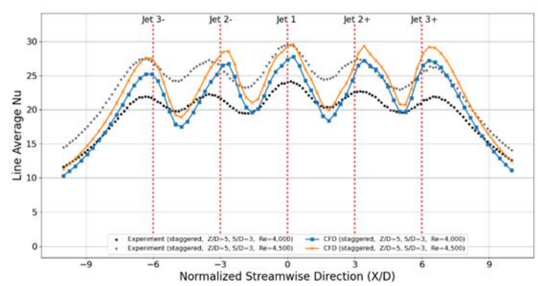

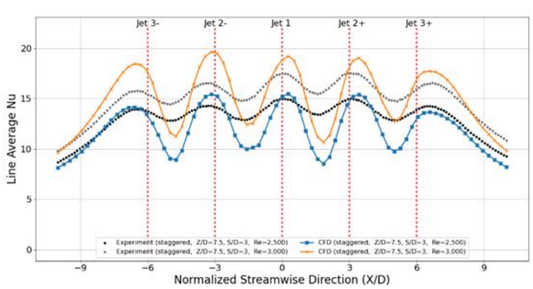

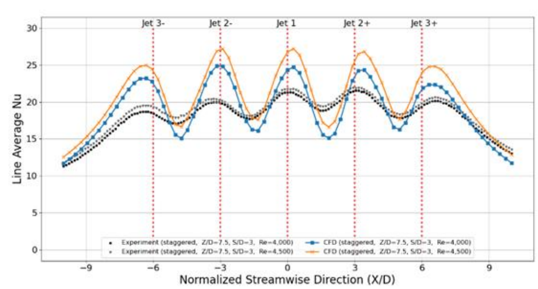

APPENDIX G: EFFECT OF Z/D - INLINE $\overline{Nu_L}$ CHARTS

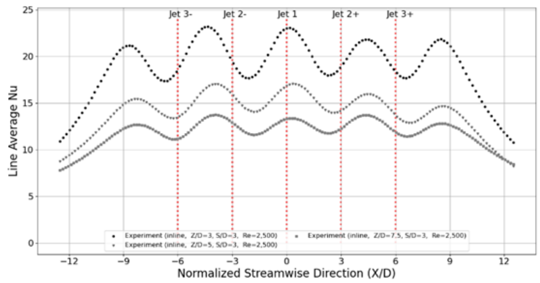

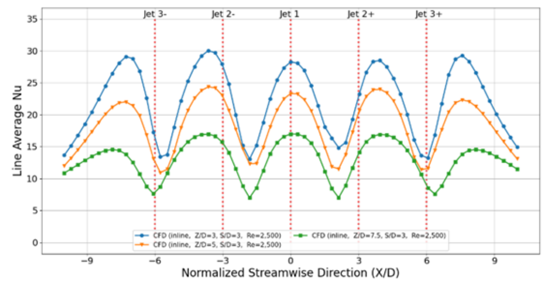

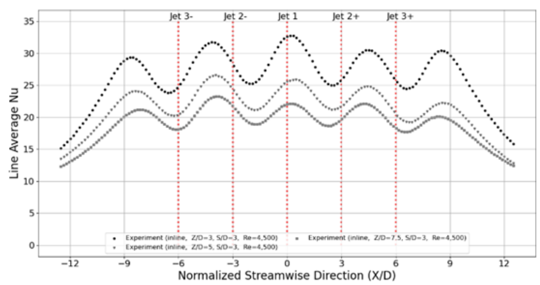

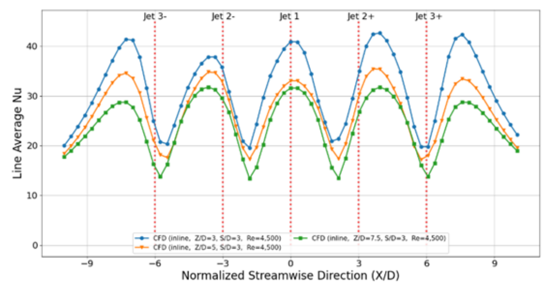

APPENDIX H: EFFECT OF Z/D - STAGGERED $\overline{Nu_L}$ CHARTS

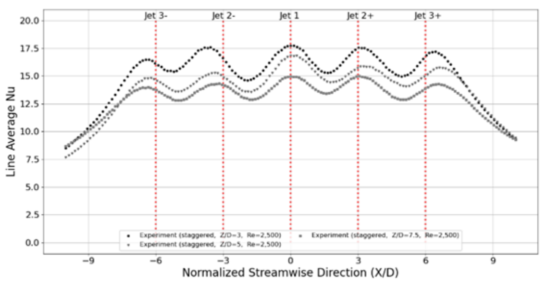

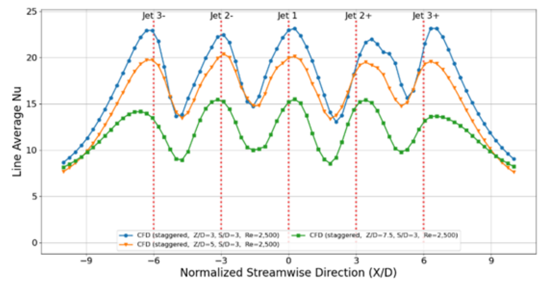

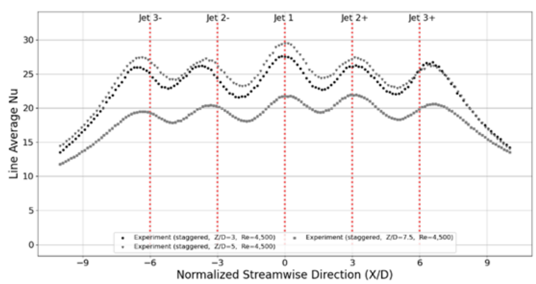

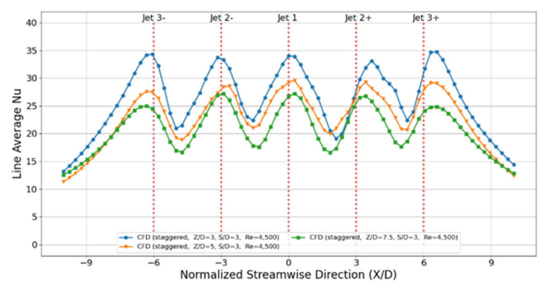

APPENDIX I: CYLINDRICAL CROSSFLOW DIVERTERS $\overline{Nu_L}$ CHARTS

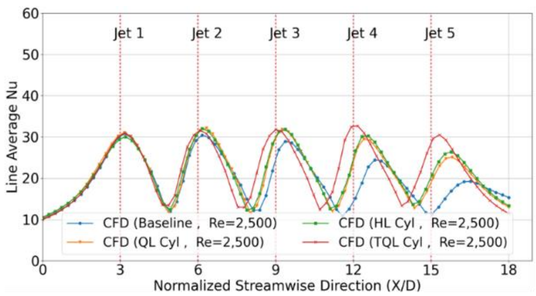

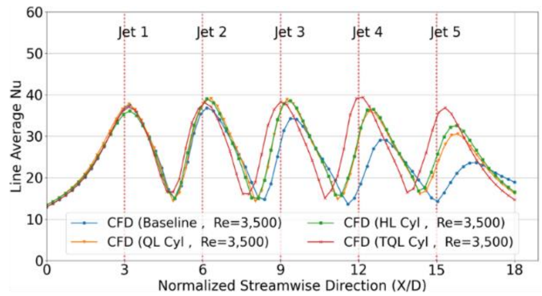

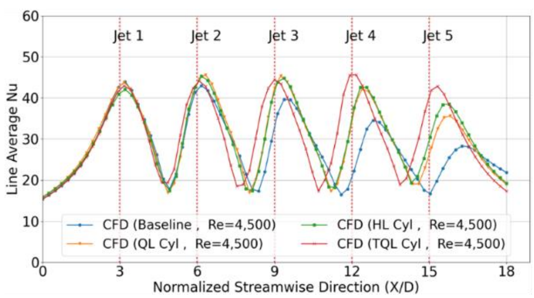

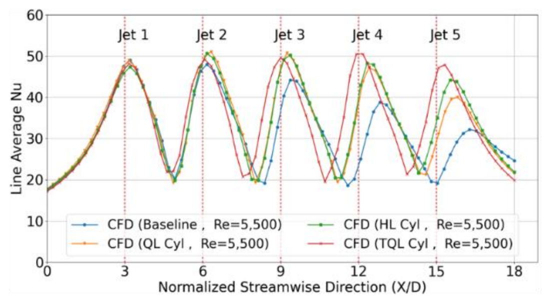

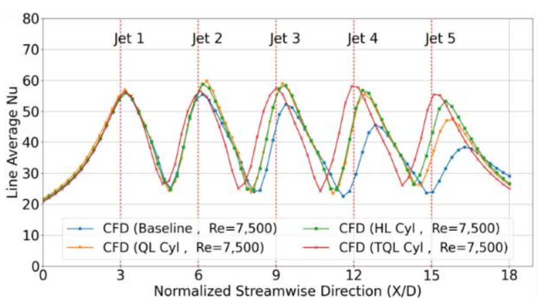

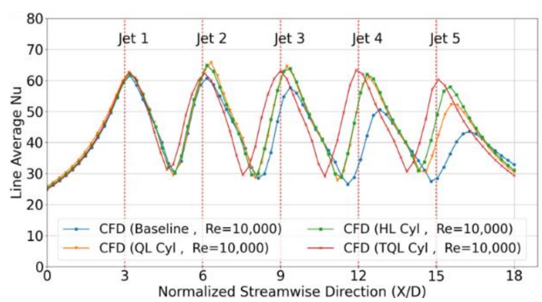

APPENDIX J: RECTANGULAR CROSSFLOW DIVERTERS $\overline{Nu_L}$ CHARTS

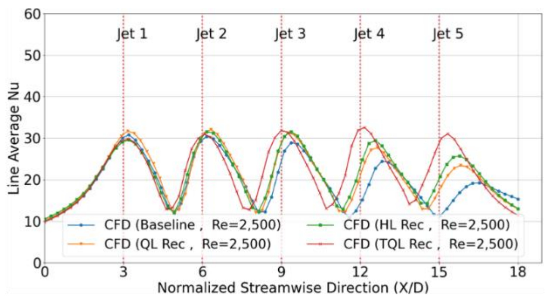

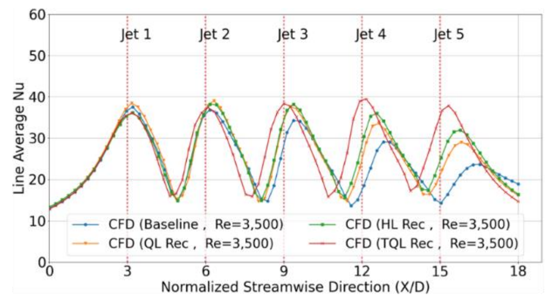

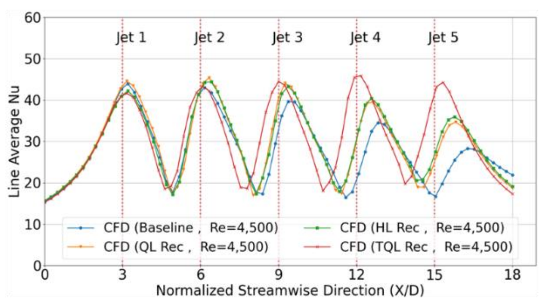

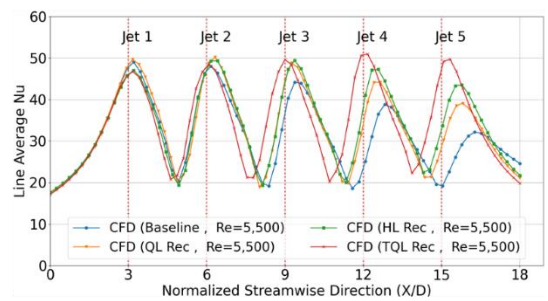

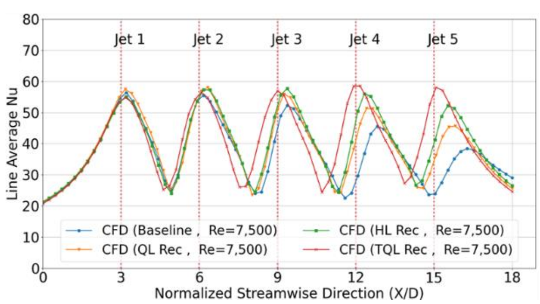

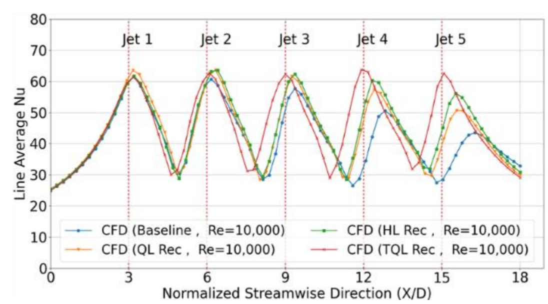

APPENDIX K: RIBBED CROSSFLOW DIVERTERS $\overline{Nu_L}$ CHARTS

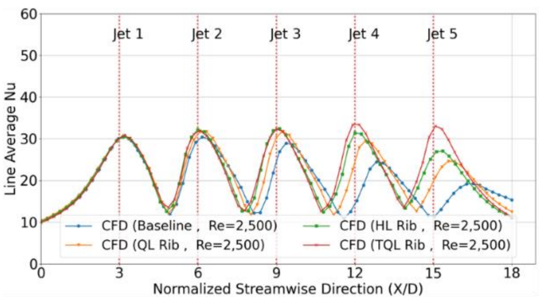

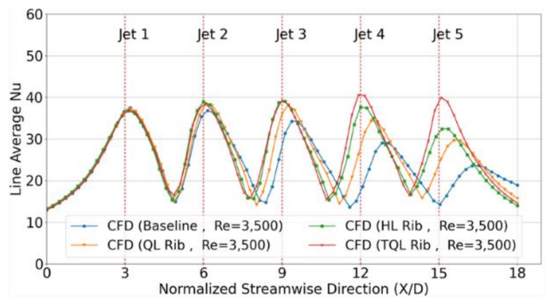

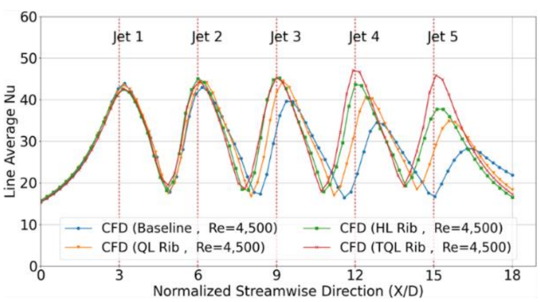

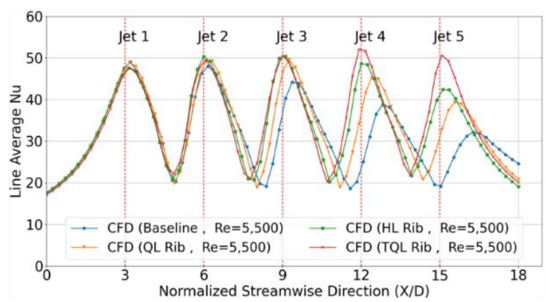

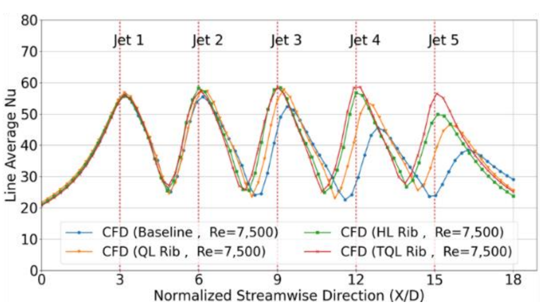

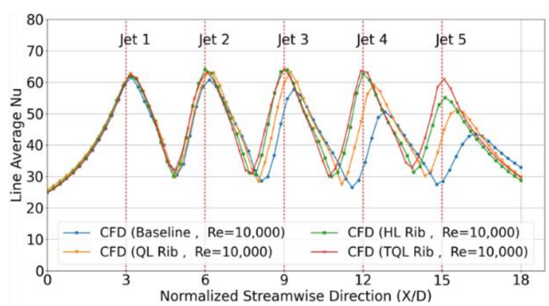

APPENDIX L: EXTENDED JETS $\overline{Nu_L}$ CHARTS

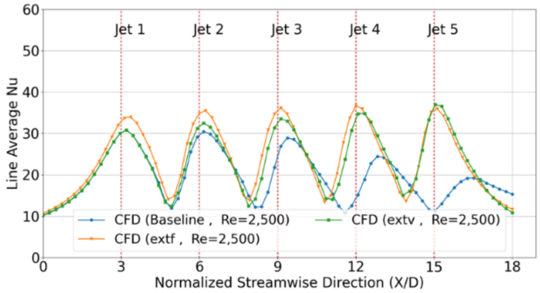

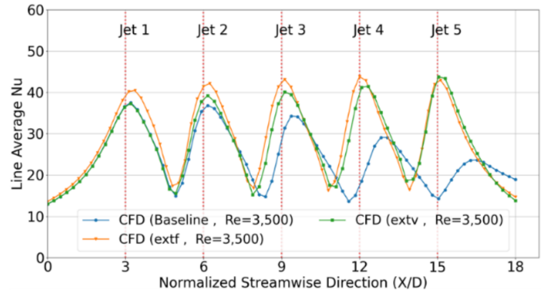

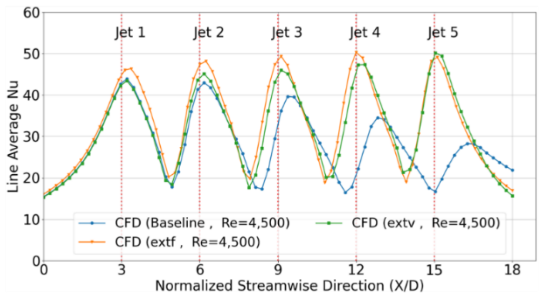

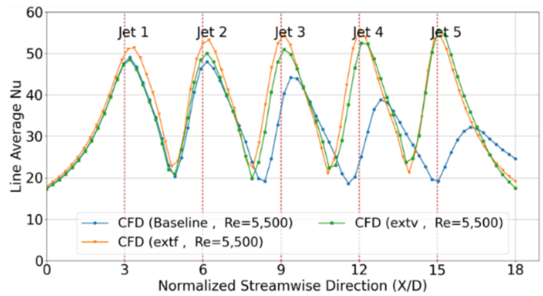

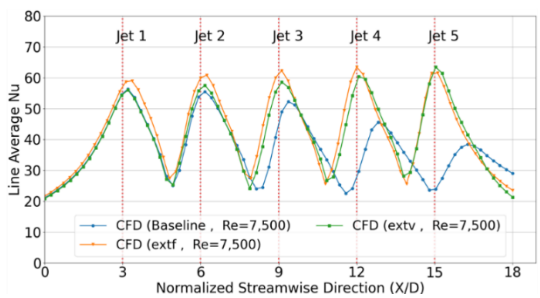

APPENDIX M: VARIABLE JET DIAMETER $\overline{Nu_L}$ CHARTS

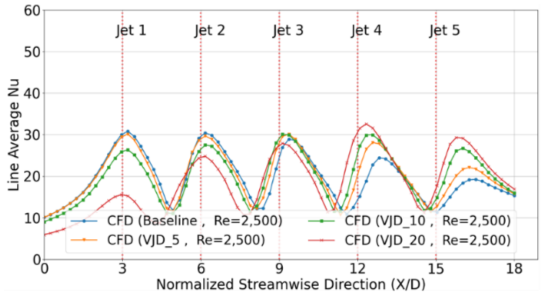

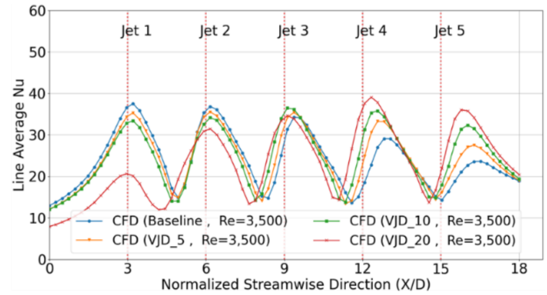

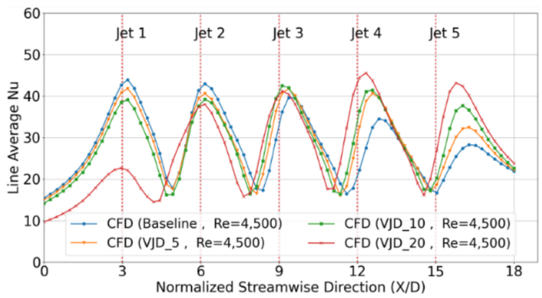

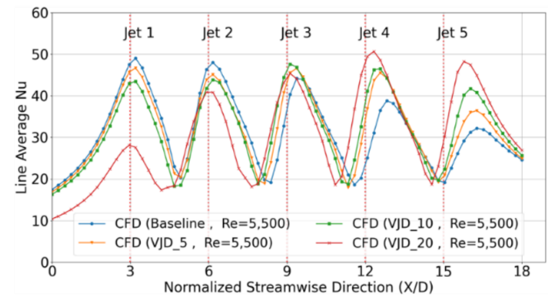

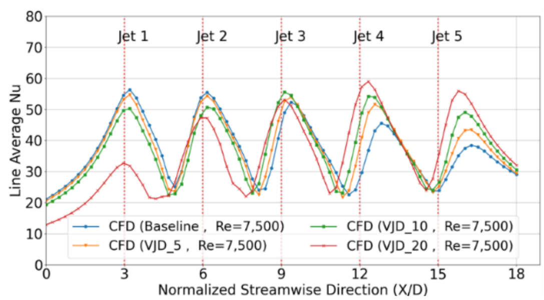

APPENDIX N: ROTATION HEAT MAPS

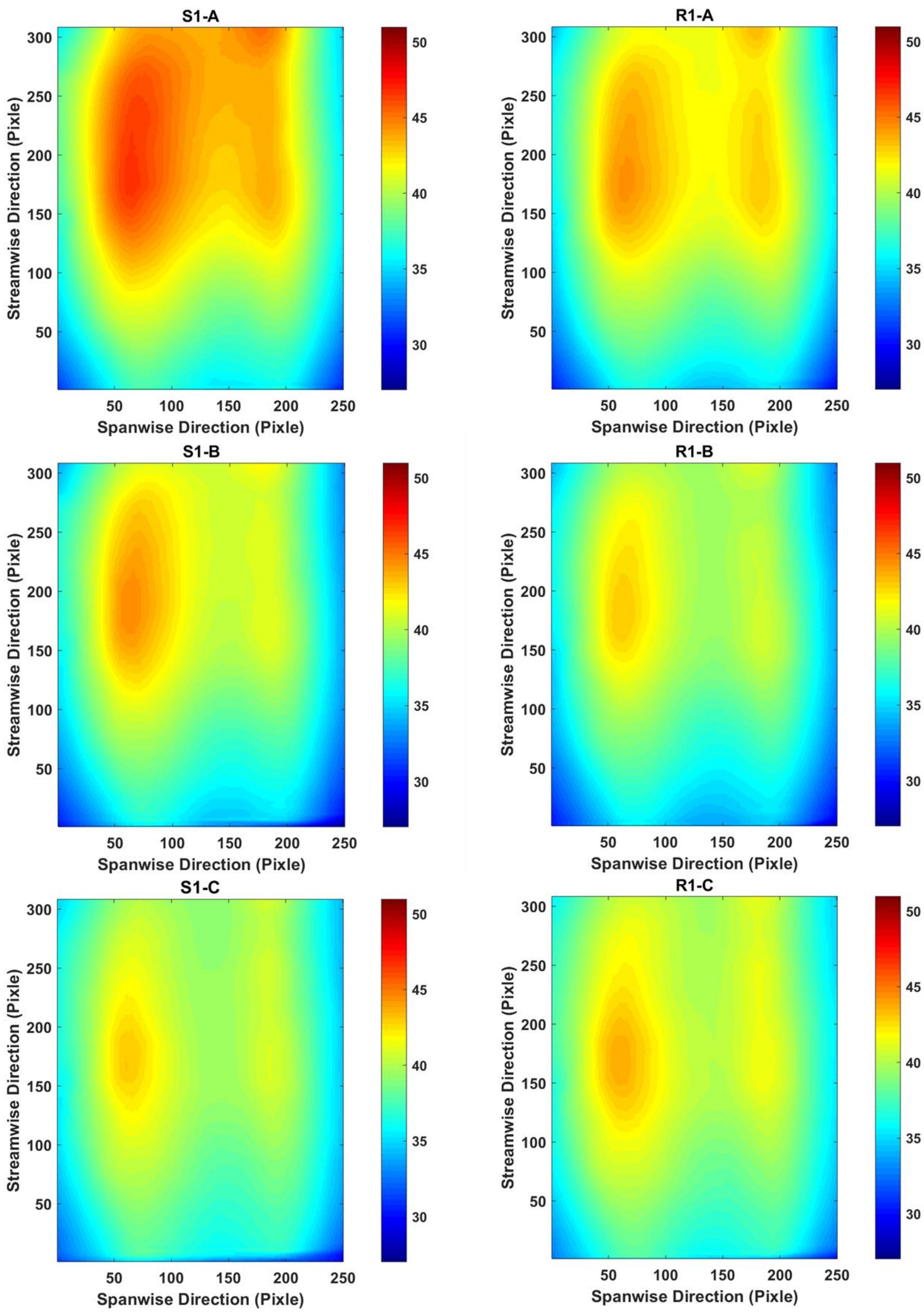

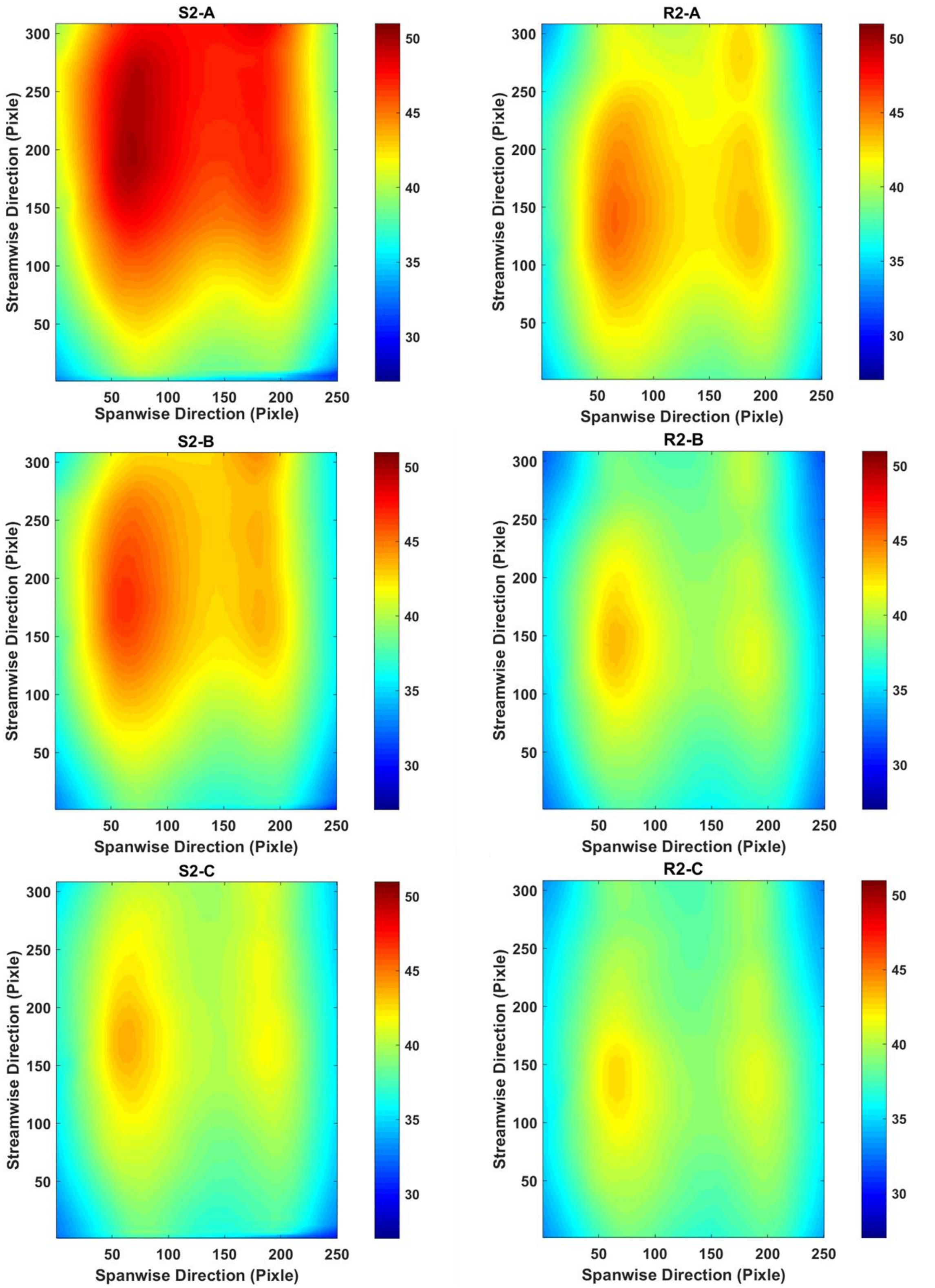
S2-A
R2-A
S2-B
R2-B
S2-C
R2-C
Streamwise Direction (Pixle)
Spanwise Direction (Pixle)
50
100
150
200
250
300
30
35
40
45
50

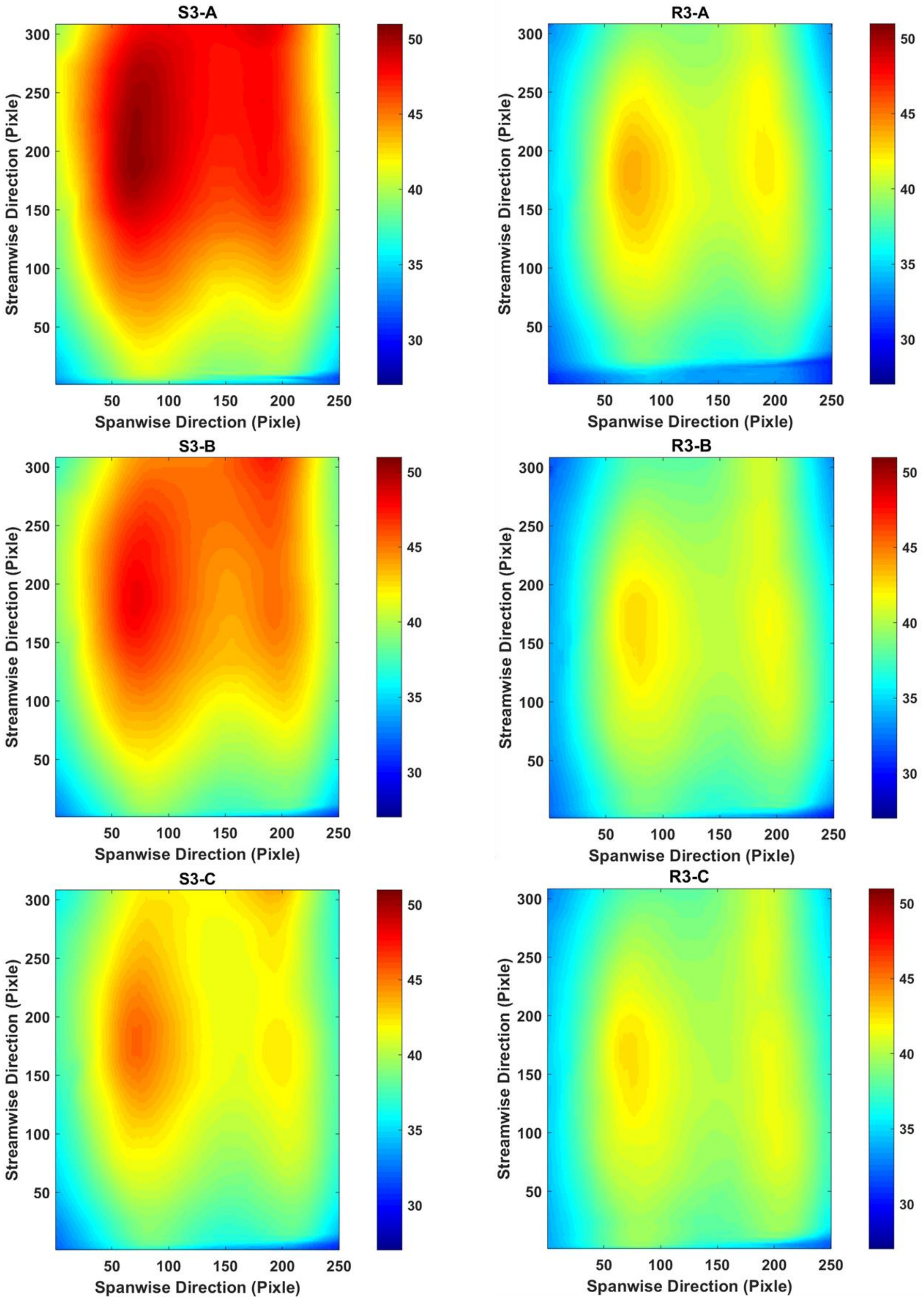
S3-A
R3-A
S3-B
R3-B
S3-C
R3-C
Streamwise Direction (Pixle)
Spanwise Direction (Pixle)
50
100
150
200
250
300
30
35
40
45
50

APPENDIX O: DATA POST-PROCESSING CODE

```
# -*- python -*-
# -*- coding: utf-8 -*-
#
#
##############################################################################

"""
DataHandling
------------
A module that supports data functionalities pertaining to: Extraction from CFD tables, Local storage, Re-structuring,
Filtering, Modeling, and Plotting.

"""
import pandas as pd
import os
from datetime import datetime
import matplotlib as mpl
from mpl_toolkits.axes_grid1 import make_axes_locatable
import numpy as np
from openpyxl import load_workbook


class Data(object):
    """
    Data class provides functionalities for handling and modeling the CFD and experiment equipment results.

    Parameters
    ----------
    task_name: str, no default,
        Label used to identify task or group of data files. This parameter is used to access the appropriate directory of
        the concerned files.
    file_name: str, no default,
        Label used to identify the name of the data file, in order to construct the full path file and load the data file.
    file_origin: str, no default,
        Label used to identify the origin of the data file in order to call the appropriate methods for handling. For
example,
        CFD-specific methods are called when this label is equal to "CFD", while experiment-specific methods are
called
        when this label is equal to "FLIR", which handles results gathered from the FLIR IR Camera.
    slice_crd: dict, default None,
        A dictionary that is used to cut the heatmap scene based on row and column coordinates.
        st_row: int, default None,
        end_row: int, default None,
        st_col: int, default None,
        end_col: int, default None,
    p: int, default None,
        Precision parameter used to round X, and Y coordinates for line average grouping.
    T: bool, default True,
        Transpose argument used to transpose the result heat map scene.
    mode: str, default "c",
        Database argument used to specify the Read/Write to the database. Use "c" for casual on the spot viewing
```

```
        without reading/writing from/to local database. Use "r" for reading the results from the local database.
        Use "w" for constructing the data from the loaded file and writing the results to the local database.

    Attributes
    ----------
    mode: str,
        Local database read/write mode.
    _data: Pandas.DataFrame,
        Heat map data table. Formatting and re-structuring overwrites the values in this table.
    dir: str,
        Files work directory.
    task_name: str,
        Name of the group of data files. Used to group different data clusters together into a category.
    filename: str,
        Data filename.
    file_origin: str,
        Origin of the data file, can be from Star-CCM+ or from FLIR IR Camera.
    _slice_Crd: dict,
        Dictionary used to specify slicing coordinates for the data file heat map.
    p: int,
        Precision used to round X, and Y coordinates in the data file heat map.
    T: bool,
        Transpose argument used to transpose the heat map of the data file.
    _line_average_data: Pandas.DataFrame,
        Table that contains the line average calculations per point on the X, or Y coordinate.
    _handler: <Data object>,
        Method that is used to load, analyze, and model the data depending on the file origin.
    """
    db_dir = 'DB'
    db_filename = 'db.json'
    db_filepath = os.path.join(db_dir, db_filename)
    os.makedirs(db_dir, exist_ok=True)

    def __init__(self, task_name, filename, file_origin, slice_crd=None, p=None, T=False, mode='c'):
        super(Data, self).__init__()
        self._access_db()
        self.mode = mode
        self._data = None
        self.dir = 'Results'
        self.task_name = task_name
        self.filename = filename
        self.file_origin = file_origin
        self._slice_crd = slice_crd
        self.p = p
        self.T = T
        self._line_average_data = None
        self.filepath = (os.path.join(self.dir, self.task_name, self.filename + '.csv')).upper()
        # Load handler depending on file origin. Each handler takes care of a specific type of formatting
        # depending on the source
        if file_origin == 'FLIR':
            self._handler = self._FLIR_handler
        elif file_origin == 'StarCCM':
            self._handler = self._StarCCM_handler
        else:
            raise ValueError('Unknown file origin = %s' % file_origin)
```

```
        # Validate slicing coordinates used to cut the correct dimensions in the heat map scene
        if self._slice_crd is None:
            pass
        elif isinstance(self._slice_crd, dict):
            pass
        else:
            raise TypeError('Slice coordinates of unknown type {}'.format(type(self._slice_crd)))

        # Local database read/write preference
        if self.mode == 'r':
            self._read_from_db()
        elif self.mode == 'w':
            self._store_to_db()
        elif self.mode == 'c':
            pass
        else:
            raise NameError('Unknown R/W mode {}'.format(self.mode))

    def _execute(self):
        """
        Method used to execute the sequence handler from the created object
        """
        self._handler()

    def _access_db(self):
        """
        Method used to read the local database file
        """
        try:
            self.db = pd.read_json(self.db_filepath)
        except Exception as e:
            self.db = pd.DataFrame()
            self.db.to_json(self.db_filepath)
        print(self.db)

    def _read_from_db(self):
        """
        Method used to read data from the local database file
        """
        try:
            locator = self.db.loc[self.db['filepath'] == self.filepath]
            if locator.empty is True:
                raise NameError('Cant find the filepath in the db {}'.format(self.filepath))
            else:
                keys = Data.default_slice_crd_keys()
                values = locator[keys].values[0]
                self._slice_crd = dict(zip(keys, values))
                self.p = locator['precision']
                self.T = locator['transpose']
        except Exception as e:
            raise e
            print('WARNING: Cannot find entry in DB {}'.format(self.filepath))

    def read_excel(filename, sheet, *args, **kwargs):
        """
        Function used to read excel xlsx files.
```

```
    Parameters
    ----------
    filename: str, no default,
        Label used to locate xlsx file.
    sheet: str, no default,
        Label used to locate sheet name within the xlsx file.

    Keyword Arguments
    ----------
    skiprows: int, default 0,
        Input used to skip first N number of rows.

    Returns
    ----------
    Pandas.DataFrame,
        A table of the excel sheet data.

    """
    # Skips N number of rows in the excel sheet
    skiprows = kwargs.pop('skiprows', 0)
    # Loads xlsx workbook
    wb = load_workbook(filename, data_only=True)
    # Load specific sheet from xlsx workbook
    ws = wb[sheet]
    data = []
    # Loop through rows within the excel workbook, and add row values to "data" list
    for row in ws:
        # Collect rows that are not hidden. Useful when using Pivot tables with filtering in excel
        if ws.row_dimensions[row[0].row].hidden is False:
            # Iterate through cells within the collected row
            row_values = [cell.value for cell in row]
            # If the first value is None, then ignore the row
            if row_values[0] is None:
                continue
            # Append the data values within the row to the "data" list
            data.append(row_values)

    # Return a dataframe that contains selected excel rows
    return pd.DataFrame(data[skiprows:], columns=data[0])

def default_slice_crd_keys():
    """
    Provides default names for slicing operations

    Parameters
    ----------
    None

    Returns
    List,
        Default names of slicing coordinates.
    """
    return ['st_row', 'end_row', 'st_col', 'end_col']

def _store_to_db(self):
```

```
        """
        Method used to store data to the local database file.

        Parameters
        ----------
        None
        """
        now = datetime.now().strftime('%Y-%m-%d %H:%M:%S')
        _data = {'filepath': self.filepath, 'file_origin': self.file_origin, 'precision': self.p,
                 'transpose': self.T, 'date_created': now}
        if self._slice_crd is None:
            _data.update(dict(zip(Data.default_slice_crd_keys(), [None] * 4)))
        else:
            _data.update(self._slice_crd)

        row = pd.DataFrame(columns=_data.keys())
        row.loc[0] = _data.values()
        if self.db.empty:
            self.db = pd.concat([self.db, row], axis=0, ignore_index=True)
        else:
            indexer = self.db['filepath'] == self.filepath

            if self.db.loc[indexer].empty is True:
                self.db = pd.concat([self.db, row], axis=0, ignore_index=True)
            else:
                _data.pop('filepath')
                for col in _data.keys():
                    self.db.loc[indexer, col] = _data[col]
        self.db.to_json(self.db_filepath)

    def dataframe_slicer(_data, st_row, end_row, st_col, end_col):
        """
        Function used to slice dataframe by slicing coordinates. This is useful to crop the given scene table.

        Parameters
        ----------
        _data: Pandas.DataFrame, no default,
            Dataframe that contains heatmap temperature data.
        st_row: int, no default,
            Slicing coordinate from the top edge downwards, in terms of rows. Must be greater than 0.
        end_row: int, no default,
            Slicing coordinate from the bottom edge upwards, in terms of rows. This number is negative, which takes
            the last N number of rows from the bottom edge. Must be lesser than 0.
        st_col: int, no default,
            Slicing coordinate from the left edge towards to the center, in terms of columns. Must be greater than 0.
        end_col: int, no default,
            Slicing coordinate from the right edge towards the center, in terms of columns. This number is negative,
which
            takes the last N number of columns from the left edge. Must be lesser than 0.

        Returns
        ----------
            _data: Pandas.DataFrame,
                Sliced heatmap temperature table.

        """
```

```
        coords = [st_row, end_row, st_col, end_col]

        if all([i is None or np.isnan(i) for i in coords]) is True:
            pass
        elif all([isinstance(i, int) or isinstance(i, float) for i in coords]):
            st_row, end_row, st_col, end_col = int(st_row), int(end_row), int(st_col), int(end_col)
            _data = _data.iloc[st_row:end_row, st_col:end_col]
        return _data

    def _StarCCM_handler(self):
        """
        Method used to handle loading operations for StarCCM+ result files and wraps the function handler of the
same.
        """
        self._data = Data.StarCCM_handler(self.filepath, self._slice_crd, self.p, self.T)

    def StarCCM_handler(filepath, slice_crd=None, precision=None, transpose=False):
        """
        Function used to handle loading operations for StarCCM+ result files.

        Parameters
        ----------
        filepath: str, no default,
            Full string filepath to load the xlsx results file.
        slice_crd: dict, default None,
            Coordinates used to slice the heatmap results table.
        precision: int, default None,
            Precision parameter used to control the rounding of the X, and Y coordinates of the data file.
        transpose: bool, default False,
            Logical argument used to control the data heatmap transposition.

        Returns
        ----------
        mod_data: Pandas.DataFrame,
            Formatted temperature dataframe.

        """
        # Used columns in StarCCM+ internal table
        usecols = ['Temperature (C)', 'X (m)', 'Y (m)']
        # Rename columns to more code friendly names
        newcols = ['T', 'X', 'Y']
        # Read CSV file, rename df, and sort values by the X coordinate
        _data = pd.read_csv(filepath, usecols=usecols)
        rename_cols = dict(zip(usecols, newcols))
        _data = _data.rename(columns=rename_cols)
        _data = _data.sort_values(['X'], ascending=False)
        # Rounding operation performed mainly to control X and Y coordinates, for easier clustering of coordinates
        if precision is not None:
            _data = _data.round(int(precision))

        # Create empty dataframe to populate later
        mod_data = pd.DataFrame()
        # Loop through grouped X coordinates so that we can create a two dimensional heatmap style table
        # Rows are the X coordinate, and columns are the Y coordinate
        for x, x_a in _data.groupby(['X']):
            x_a = x_a.sort_values(['Y'])
```

```
        x_a = x_a.T
        y_vals = x_a.iloc[2:3]
        x_a.columns = y_vals.values[0]
        row = x_a.iloc[0:1]
        mod_data = pd.concat([mod_data, row], axis=0, ignore_index=True)

    # Tranpose the coordinates to make Y the rows, and X the columns
    mod_data = mod_data.T

    # Validating the slicing coordiantes and performing the slicing operation
    if isinstance(slice_crd, dict):
        mod_data = Data.dataframe_slicer(mod_data, st_row=slice_crd['st_row'], end_row=slice_crd['end_row'],
                                          st_col=slice_crd['st_col'], end_col=slice_crd['end_col'])
    # Transpose the table once again based on user preference
    if transpose is True:
        mod_data = mod_data.T

    # Return formatted results table
    return mod_data

def _FLIR_handler(self):
    """
    Method used as a wrapper around the FLIR IR Camera handling function.
    """
    self._data = Data.FLIR_handler(self.filepath, self._slice_crd, transpose=self.T)

def FLIR_handler(filepath, slice_crd=None, transpose=False):
    """
    Function used to handle loading operations for FLIR IR Camera result files.

    Parameters
    ----------
    filepath: str, no default,
        Full string filepath to load the xlsx results file.
    slice_crd: dict, default None,
        Coordinates used to slice the heatmap results table.
    transpose: bool, default False,
        Logical argument used to control the data heatmap transposition.

    Returns
    ----------
    _data: Pandas.DataFrame,
        Formatted temperature dataframe.

    """

    # Load the CSV temperature table
    _data = pd.read_csv(filepath, header=None)

    # Validate slicing coordinates and perform the operation
    if isinstance(slice_crd, dict):
        _data = Data.dataframe_slicer(_data, st_row=slice_crd['st_row'], end_row=slice_crd['end_row'],
                                       st_col=slice_crd['st_col'], end_col=slice_crd['end_col'])

    # Transpose the table once again based on user preference
    if transpose is True:
```

```
        _data = _data.T

    # Return formatted results table
    return _data

def _nusselt(self, ax=None, *args, **kwargs):
    """
    Method used as a wrapper around the Nusselt number calculation function.

    Parameters
    ----------
    ax: <matplotlib.pyplot object>, default None,
        Plot axis used to plot the line average results. If None is given, then there will be no plotting for this result.

    Attributes
    ----------
    _line_average_data: Pandas.DataFrame,
        Dataframe containing Line average data in terms of X coordinate, Temperature, and Nusslet number.
    Nu_avg: float,
        Average nusselt number over the entire surface.
    """
    # Variable name to call within the given dataframe
    variable = 'nusselt'
    # Calls Nusselt calculation function to calculate nusselt line average from T line average values
    self._line_average_data = Data.calculate_nusselt(self._line_average_data, **kwargs)

    # Calculates Nusslet number for every point and takes average over surface
    nusslet_per_point = (kwargs['numerator'] / (self._data - kwargs['T_a']))
    self.Nu_avg = (nusslet_per_point.sum().sum()) / (len(nusslet_per_point) * len(nusslet_per_point.columns))

    # Call the plotting function if the axis object is given
    if ax is not None:
        Data.plot_line(self._line_average_data[[variable]], ax, variable, **kwargs)

def calculate_nusselt(line_average, numerator, T_a, *args, **kwargs):
    """
    Function used to calculate nusselt number over a line average. The equation for nusselt is given by:
        Nu = (numenator) / (T_i - T_a),
    Where,
        numenator: grouped constant variables in the nusselt equation.
        T_i: temperature per point on the line average, in C.
        T_a: Ambient temperature in C.

    Parameters
    ----------
    line_average: Pandas.DataFrame, no default,
        Dataframe containing X coordinates and temperature values for each line average point.
    numenator: float, no default,
        Grouped constant remaining variables in the nusselt equation.
    T_a: float, no default,
        Ambient temperature in C.

    Returns
    ----------
    line_average: Pandas.DataFrame,
        Dataframe of the line average results, containing X coordinate, temperature, and nusselt number
```

```
        per line average point.

    """
    line_average['nusselt'] = line_average['temperature'].apply(lambda T: numerator / (T - T_a))
    return line_average

def _heatmap(self, ax, *args, **kwargs):
    """
    Method used as a wrapper around the heatmap plotting function

    Parameters
    ----------
    ax: <matplotlib.pyplot object>, default None,
        Plot axis used to plot the line average results. If None is given, then there will be no plotting for this result.
    """
    Data.heatmap(self._data, ax, **kwargs)

def heatmap(df, ax, label=None, color_palette='turbo', palette_n=50,):
    """
    Function used to plot heat maps.

    Parameters
    ----------
    df: Pandas.DataFrame, no default,
        Dataframe used for heat map plotting.
    ax: <matplotlib.pyplot object>, default None,
        Plot axis used to plot the line average results. If None is given, then there will be no plotting for
        this result.

    """
    # Color map object defintion
    cmap = mpl.pyplot.cm.get_cmap(color_palette, palette_n)
    # Create heat map image object
    image = ax.imshow(df, norm=mpl.colors.Normalize(vmin=df.min().min(), vmax=df.max().max()),
                      cmap=cmap, interpolation='blackman', label=label)
    # Divider preferences
    divider = make_axes_locatable(ax)
    # Axis preferences
    cax = divider.append_axes("right", size="5%", pad=0.05)
    # Assign color bar object to image
    mpl.pyplot.colorbar(image, cax=cax)

def _line_average(self, ax=None, *args, **kwargs):
    """
    Method used as a wrapper around the line average calculation function.

    Parameters
    ----------
    ax: <matplotlib.pyplot object>, default None,
        Plot axis used to plot the line average results. If None is given, then there will be no plotting for
        this result.

    """
    # Variable used to access and store data into line average dataframe
    variable = 'temperature'
    # Calculate surface average temperature
```

```
        self.T_avg = (self._data.sum().sum()) / (len(self._data) * len(self._data.columns))
        # Calculate line average values for the specific variable name
        self._line_average_data = Data.calculate_line_average(self._data, variable, **kwargs)
        # If the axis object is valid, then call the plotting function
        if ax is not None:
            Data.plot_line(self._line_average_data, ax, variable, **kwargs)

    def normalize(coords, normalize_length, normalize_param):
        """
        Function used normalize coordinates over a specific length and normalization parameter.

        Parameters
        ----------
        coords: list or Pandas.Series, no default,
            Coordinates array.
        normalize_length: float, no default,
            The span of length for which normalization is performed.
        normalize_param: float, no default,
            The normalization parameter that is used as a denomenator for normalizing each point in the coordinates
array.

        Returns
        ----------
        coords: list or Pandas.Series
            Normalized coordinates with type based on the given coordinates type.

        """
        coords_len = len(coords)
        if normalize_length is not None and normalize_param is not None:
            if coords_len % 2 == 0:
                coords = coords[:-1]
            coords_len = len(coords)

            step = (normalize_length) / (coords_len - 1)
            _x = [round(i, 2) / normalize_param for i in np.arange(-normalize_length / 2, 0, step)]
            _x.extend([abs(i) for i in _x])
            _xmod = [i for i in _x if i != 0]
            _xmod.extend([0])
            _xmod.sort()
            coords = _xmod
        else:
            coords = [(x + 1) / (coords_len) for x in range(0, coords_len)]
        return coords


    def calculate_line_average(df, variable, axis=0, normalize=True, *args, **kwargs):
        """
        Function used to calculate line average for a given variable.

        Parameters
        ----------
        df: Pandas.DataFrame, no default,
            Dataframe for which the line average is calculated. Default formatting is that of a heat map style table
            with X and Y coordinates representing the index and column names.
        variable: str, no default,
            Variable label used to access and store data to the line average dataframe.
```

```
    axis: int, default 0,
        Axis argument of the Pandas concat function. 0 for row wise, and 1 for column wise looping.
    normalize: bool, default True,
        Argument used to control normalization of the line average coordinates.

    Keyword arguments
    ----------
    normalize_length: float, no default,
        The span of length for which normalization is performed.
    normalize_param: float, no default,
        The normalization parameter that is used as a denomenator for normalizing each point in the coordinates
array.

    Returns
    ----------
    line_average: Pandas.DataFrame,
        Dataframe of the line average result.

    """
    normalize_length = kwargs.pop('normalize_length', None)
    normalize_param = kwargs.pop('normalize_param', None)
    # Group heat map style table and create groups of X coordinate
    line_average = df.mean(axis=axis).reset_index().rename(columns={'index': 'X', 0: variable})
    # Perform normalization based on user preference
    if normalize is True:
        X_len = len(line_average['X'])
        if normalize_length is not None and normalize_param is not None:
            if X_len % 2 == 0:
                line_average = line_average[:-1]
            X_len = len(line_average['X'])

            step = (normalize_length) / (X_len - 1)
            _x = [round(i, 2) / normalize_param for i in np.arange(-normalize_length / 2, 0, step)]
            _x.extend([abs(i) for i in _x])
            _xmod = [i for i in _x if i != 0]
            _xmod.extend([0])
            _xmod.sort()
            line_average['X'] = _xmod
        else:
            line_average['X'] = [(x + 1) / (X_len) for x in range(0, X_len)]

    line_average = line_average.set_index(['X'])

    # Return line averaged data
    return line_average

def plot_line(data, ax, variable, label=None, annotate=True, n_window=5, *args, **kwargs):
    """
    Function used to facilitate line and scatter plotting.

    Parameters
    ----------
    data: Pandas Array, no default,
        Pandas data table or array used to create line plots.
    ax: <matplotlib.pyplot object>, no default,
        Plot axis used to plot the data.
```

```
    variable: str, no default,
        Variable label used to specify plotted variable.
    label: str, default None,
        Legend label for variable.
    annotate: bool, default True,
        Annotation option for local minima and maxima.
    n_window: int, default 5,
        Span of averaging used for calculating local minima and maxima.


    Keyword Arguments
    ----------
    m: str, default None,
        marker type from matplotlib.pyplot marker options.
    ls: float, default None,
        line style from matplotlib.pyplot line style options.
    plot_type: str, default None,
        Used to specify plot type to either "line" or "scatter".
    color: str, default None,
        Color option from matplotlib.pyplot color options.

    """
    m = kwargs.pop('marker', None)
    ls = kwargs.pop('linestyle', None)
    plot_type = kwargs.pop('plot_type', None)
    color = kwargs.pop('color', None)

    # Formatting and labeling
    if ls is not None:
        ls = ls.strip("'").strip('"')
    if variable.lower() == 'temperature':
        unit = 'C'
    else:
        unit = ''

    # Plotting of line plots
    if plot_type == "line" or plot_type is None:
        ax.plot(data, label=label, marker=m, linestyle=ls, lw=2, markersize=6, color=color)
    # Plotting of scatter plots
    elif plot_type == 'scatter':
        ax.scatter(data.index, data, label=label, marker=m, lw=2, s=6, color=color)

    # Annotation option
    if annotate is True:
        if 'X' not in data:
            data = data.reset_index().rename(columns={'index': 'X'})
        annotation = Data.find_local_extremes(data, variable, n_window=n_window)
        for index, vals in annotation.iterrows():
            x, value = vals['X'], vals[variable]
            ax.annotate('{} {}'.format(round(value, 1), unit), xy=(x, value))

def find_local_extremes(data, var, n_window):
    """
    Function used to seek and find local minima and maxima in a data array, which will be used to annotate
    matplotlib.pyplot line or scatter plots.
    The result is a dataframe that contains the index plotting coordinates, along with a variable column that
```

```
    contains Y axis values of the local minima and maxima.

    Parameters
    ----------
    data: Pandas.DataFrame, no default,
      Data that is used for minima and maxima seeking.
    var: str, no default,
      Column name for which minima and maxima seeking is performed.
    n_window int, no default,
      Span of averaging used for calculating local minima and maxima.

    Returns
    ----------
    local_extremes: Pandas.DataFrame,
      Dataframe containing coordinates of local minima and maxima. Each row is an X coordinate, and the second
column
      corresponds to the given "var" name, which contains minima and maxima values (In terms of the same unit
as the given variable)
    """
    peaks = []
    mins = []
    for index, vals in data.iloc[n_window:-n_window].iterrows():
      X_i = float(vals['X'])
      var_i = float(vals[var])
      # Perform average on forward and backward slices to decide if the iterated point is minima, maxima, or
neither
      fw_slice = data[var].iloc[index:index + 5]
      bw_slice = data[var].iloc[index - 5:index]
      fw_slice_var_max = fw_slice.max()
      bw_slice_var_max = bw_slice.max()
      fw_slice_var_min = fw_slice.min()
      bw_slice_var_min = bw_slice.min()
      if var_i >= bw_slice_var_max and var_i >= fw_slice_var_max:
        # Peaks list of dicts
        peaks.append({'X': X_i, var: var_i})
      elif var_i <= bw_slice_var_min and var_i <= fw_slice_var_min:
        # Mins list of dicts
        mins.append({'X': X_i, var: var_i})

    # Create Dataframe that contains coordinates along with Y values of local minima and maxima
    local_extremes = pd.concat([pd.DataFrame(peaks, columns=peaks[0].keys()), pd.DataFrame(mins,
columns=mins[0].keys())],
                  ignore_index=True)

    # Return dataframe of local minima and maxima values
    return local_extremes
```

CURRICULUM VITAE

Abdel Rahman Salem, Ph.D.
Thermal Systems Engineer

PROFESSIONAL SUMMARY

Experienced Computational Fluid Dynamics (CFD) engineer with +4 years of experience in developing and delivering high quality CFD simulations for thermo-fluids, heat transfer, and multi-phase complex problems. Deep knowledge in physical phenomena and skilled in the use of STAR-CCM+ for research, optimization, and product development.

EDUCATION

Ph.D. Candidate Mechanical Engineering — **Aug. 2018 – May 2023**
University of Wisconsin-Milwaukee (UWM) — Milwaukee, WI

B.Sc. Mechanical Engineering — **Aug. 2012 – Jun. 2016**
Al-Balqa' Applied University (BAU) — Amman, Jordan

EXPERINCE

CFD Research Assistant — **Aug. 2018 – Present**
University of Wisconsin-Milwaukee — Milwaukee, WI

- Developed CFD simulations for multiple projects including gas turbine blade and combustor liner cooling, wind turbine power enhancement via leading and trailing edge modifications, and hydro turbine cavitation treatment by compressed air injection.
- Evaluated and utilized multiple turbulence models (k-ε, k-ω, RST, and LES) for steady and transient with both stationary and rotating computational domains.
- Conducted detailed mesh independence studies including hexahedral, polyhedral, and tetrahedral cell shapes with utilizing surface repair tools to achieve solution-mesh independence.
- Analyzed solution convergence and provided residuals interpretations, numerical solver acceleration techniques.
- Adopted post-processing procedures to properly document results, develop CFD methodologies, and provide CFD feedback.

Energy Engineer — **Aug. 2018 – Present**
Industrial Assessment Center (IAC) at University of Wisconsin-Milwaukee — Milwaukee, WI

- Led and supervised the energy engineering team in energy assessment walk-throughs, energy calculations, data acquisition, and energy audit and verification reports.
- Completed +50 onsite energy assessments on various industries including foundries, plastic and paper manufacturing, food, wastewater treatment plants, and construction machinery.
- Evaluated and analyzed energy and utility bills for large industries (up to $50M annual production).
- Delivered over 500 assessment recommendations with 10% average savings and 40% implementation rate.
- Developed new energy efficiency and energy reclamation systems including micro-propeller in aeration basins (Recipient of Excellence in Applied Energy Engineering Research Award by the DOE, 2020).
- Accredited as a certified energy auditor by the DOE for the completion of requirements mandated by the U.S. DOE's IAC program at the University of Wisconsin Milwaukee, 2019.

CFD Methodology Engineer — **Oct. 2020 – Sep. 2022**
Research Intern at Rockwell Automation — Milwaukee, WI

- Utilized technical expertise and reverse-engineering techniques to design multiple spur and worm gearboxes.
- Developed CFD simulations to predict thermal loads on gears, shafts, and casings by programming field functions.
- Applied overset mesh, wall treatment, and multi-phase models.

Mechanical Design Engineer **Aug. 2016 – May 2017**
Internship at Omrania & Associates Amman, Jordan

- Assisted in designing mechanical systems for commercial buildings including HVAC, fire protection, and plumbing systems complying with international codes and standards.

TEACHING EXPERIENCE

Teaching Instructor / Assistant **Aug. 2018 – Jun. 2021**
University of Wisconsin-Milwaukee: Mechanical Engineering Department Milwaukee, WI

- Instructor for Fluid Mechanics Lab / Hands-on experiments involving applications of potential flows, boundary layer flows, gas dynamics, aerodynamics, fluid power, and CFD basics.
- Instructor for Design of Machine Element / Design of mechanical components under steady and fatigue loads. Design of columns, shafts, fasteners, springs, bearings, gearing, etc.
- Instructor for Computational Tools for Engineers / Introduction to the use of MATLAB, spreadsheets, and equation solvers. Basic engineering and financial applications using these tools.

Private Teacher **May. 2015 – Aug. 2018**
Science Pioneers Academy Amman, Jordan

- Teaching mechanical engineering courses including Thermodynamics, Fluid Mechanics, Heat Transfer, Dynamics, Hydraulic and Pneumatic Systems, and HVAC.

RESEARCH PROJECTS

Experimental and Numerical Studies of Jet Impingement Cooling Enhancement **Aug. 2018 – May. 2023**

- Designing, fabricating, and building test rigs to monitor the variations of the surface temperature under different boundary conditions.
- Optimizing cooling air characteristics, temperature uniformity, air nozzles design, and minimizing spent air crossflow by passive
- Establishing and evaluating numerical computational models using STAR-CCM+ and FLUENT.
- Developing thermal image processing techniques.

Power Reclamation of Utilizing Micro-Hydro Turbines in the Aeration Basins of Wastewater Treatment Plants **Jun. 2020 – Dec. 2021**

- Designing, fabricating, and building test rigs to monitor the power generation under various operating conditions.
- Upgrading the aeration basin technology and improving the oxygen transfer efficiency (OTE), while keeping the energy consumption at its minimum level.
- Optimizing operating conditions and design configurations that can maximize the power reclaimed by small hydro turbines installed above air diffusers in aeration tanks.

Net Zero Energy Model for Wastewater Treatment Plants **Jan. 2021 – Sep. 2021**

- Studying the possibility of achieving net-zero-energy wastewater treatment plants.
- Designing, improving, and utilizing energy efficiency opportunities, combined heat and power systems, and renewable energy sources, e.g., solar, hydro, and wind powers.

Optimization Procedure for Residential-Scale Wind Turbines **Jan. 2020 – Jun. 2020**

- Designing and 3D printing small Horizontal Axis Wind Turbine (HAWT) and analyzing various airfoil aerodynamic characteristics.
- Performing air velocity measurements at several transverse planes in the wake region of a single wind turbine.
- Modifying blade geometry of the blade tip and leading-edge by introducing winglet and tubercles seeking power improvement.
- Establishing, evaluating, and developing numerical computational models using STAR-CCM+.

AWARDS AND HONORS

- Outstanding International Advocate for students **At UWM in Nov. 2022**
- Prestigious Distinguished Dissertation Fellowship (DDF) **From UWM in Aug. 2022**
- Prestigious UWM Chancellor's Graduate Student Award (CGSA) **From UWM in 2022, 2021, and 2020**
- Prestigious Distinguished Graduate Student Fellowship (DGSF) **From UWM in Aug. 2021**
- Student Research Poster Competition (SRPC) 3rd place winner **From UWM in May. 2021**
- Excellence in Applied Energy Engineering Research by U.S. DOE **From DOE in Oct. 2020**

VOLUNTEERING

- AEE student chapter founder and president at UWM **Dec. 2022 - Present**
- Awards and Recognition Committee (ARC) at UWM **Oct. 2022 - Present**
- Journal Paper Reviewer at Elsevier / Total of 2 Manuscripts **Sep. 2021- Present**
- Journal Paper Reviewer at ASME / Total of 4 Manuscripts **Aug. 2021- Present**
- AIAA student organization president at UWM **Jun. 2019 – Jun. 2021**

PROFESSIONAL TRAININGS

- Computational Fluid Dynamics for Professionals **By Udemy**
- The Complete introduction to OpenFOAM **By Udemy**
- Complete Python Bootcamp **By Udemy**
- SOLIDWORKS: Simulation for Finite Element Analysis **By LinkedIn Learning**
- Fusion 360: Simulation **By LinkedIn Learning**
- Learning data governance **By LinkedIn Learning**
- MATLAB essential training series **By LinkedIn Learning**

TOP COMPUTER SKILLS

STAR-CCM+	OpenFOAM	SOLIDWORKS	CREO	SAM	HAP
FLUENT	Fusion 360	MATLAB	E-QUEST	HOMER	MEASUR

RESEARCH INTERESTS AND PUBLICATIONS

Research interests are in Fluid Dynamics, Heat and Mass Transfer, Computational Fluid Dynamics (CFD), Energy Optimization, Energy Management Systems, and Hybrid-Renewable Energy Systems.

https://scholar.google.com/citations?hl=en&user=Fk9L7wwAAAAJ https://www.researchgate.net/profile/Abdel-Rahman-Salem

JOURNALS

- **Salem, A. R.,** Hasan, A., Hadi, A. A., Al Hamad, S., Qandil, M., and Amano, R. S. (October 13, 2021). "Power Generation and Oxygen Transfer Analyses for Micro Hydro-Turbine Installed in Wastewater Treatment Aeration Tank." *ASME. J. Energy Resour. Technol.* March 2022; 144(3): 032102. https://doi.org/10.1115/1.4052538

- Hasan, A., **Salem, A. R.,** Hadi, A. A., Al Hamad, S., Qandil, M., and Amano, R. S. (October 20, 2021). "Optimizing Power Reclamation of Micro Hydro Turbines in WWTPs Aeration Basins." ASME. J. Energy Resour. Technol. January 2022; 144(1): 012109. https://doi.org/10.1115/1.4052539
- Qandil, M., D., Abbas, A., I., **Salem, A. R.**, AbdelHadi, A., I., Hasan, A. S., Nourin, F. N., Abousabae, M., Osama M. Selim, Juan Espindola, Amano, R. S. "Net Zero Energy Model for Wastewater Treatment Plants", J. Energy Resour. Technol. Dec 2021, 143(12): 122101. https://doi.org/10.1115/1.4050082
- Hasan, A. S., **Salem, A.R.**, Ahmad I. AbdelHadi, and Ryoichi S. Amano, "The power reclamation of utilizing micro-hydro turbines in the aeration basins of wastewater treatment plants", ASME. J. Energy Resour. Technol. Aug 2021, 143(8): 081301. https://doi.org/10.1115/1.4048869
- AbdelHadi, A., I., **Salem, A. R.**, Qandil, M., D., Abbas, A., I., and Amano, R. S. "Study of Energy Saving Analysis for Different Industries", ASME. J. Energy Resour. Technol. May 2021; 143(1): 012103. https://doi.org/10.1115/1.4048249
- **Salem, A. R.**, Nourin, F. N., Abousabae, M., and Amano, R. S. "Experimental and Numerical Study of Jet Impingement Cooling for Improved Gas Turbine Blade Internal Cooling with In-Line and Staggered Nozzle Arrays", ASME. J. Energy Resour. Technol. January 2021; 143(1): 012103. https://doi.org/10.1115/1.4047600
- Hasan, A. S., Abousabae, M., **Salem, A. R.,** and Amano, R. S. "Study of Aerodynamic Performance and Power Output for Residential-Scale Wind Turbines", ASME. J. Energy Resour. Technol. January 2021; 143(1): 011302. https://doi.org/10.1115/1.4047602
- **Salem, A. R**., Nourin, F. N., and Amano, R. S. "Investigation of Jet Impingement Cooling for Gas Turbine Blade with In-line and Staggered Nozzle Array", Inter. J. Ener. Clean Env., 2019; 21(2):169-182. https://doi.org/10.1615/InterJEnerCleanEnv.2020033479
- Qandil, M., D., Abbas, A., I., **Salem, A. R.**, AbdelHadi, A., I., Amano, R. S. "Energy Analysis: Ways to Save Energy and Reduce the Emissions in Wastewater Treatment Plants" Inter. J. Ener. Clean Env., 2021; 22(1):91-112. https://doi.org/10.1615/InterJEnerCleanEnv.2020035138

CONFERENCE PROCEEDINGS

- **Salem, A. R.,** Soliman, I., and Amano, R. S. "Crossflow Minimization for Jet Impingement Cooling Applications." Accepted conference manuscript, *ASME Turbo Expo 2023, Boston, MA. June 26 – 30, 2023*
- Soliman, I., **Salem, A. R.,** and Amano, R. S. "Novel Dilution Zone Jet Modifiers: An Experimental and Numerical Study of Combustor Temperature Uniformity." Accepted conference manuscript, *ASME Power 2023, Long Beach, CA. August 6 - 9, 2023*
- Nourin, F. N., **Salem, A. R.,** and Amano, R. S. "Investigation of Experimental Jet Array for Impinging Cooling of Blades". AIAA Propulsion and Energy forum, 2019-4240. https://doi.org/10.2514/6.2019-4240
- Abdelhadi, A., I., **Salem, A. R.,** Qandil, M., D., Abbas, A., I., and Amano, R. S. "Study of industrial energy assessments for different sectors", AIAA Propulsion and Energy forum, 2019-4238. https://doi.org/10.2514/6.2019-4238
- Qandil, M., D., Abbas, A., I., **Salem, A. R.**, AbdelHadi, A., I., Amano, R. S. "Energy Consumption, Energy-saving and Emissions Reduction of Wastewater Treatment Plants (WWTPs) in Wisconsin", AEE world conference and expo, 2019.